

**NASA CONTRACTOR
REPORT**

NASA CR-61348

**INTERACTION MODEL OF MICROWAVE
ENERGY AND ATMOSPHERIC VARIABLES**

By Norman E. Gaut and Edward C. Reifenstein, III

**Environmental Research and Technology, Inc.
58 Guinan Street
Waltham, Mass. 02154**

April 20, 1971

**CASE FILE
COPY**

Prepared for

**NASA-GEORGE C. MARSHALL SPACE FLIGHT CENTER
Marshall Space Flight Center, Alabama 35812**

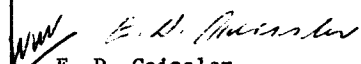
1. Report No. NASA CR-61348	2. Government Accession No.	3. Recipient's Catalog No.	
4. Title and Subtitle INTERACTION MODEL OF MICROWAVE ENERGY AND ATMOSPHERIC VARIABLES		5. Report Date April 20, 1971	
		6. Performing Organization Code	
7. Author(s) Norman E. Gaut and Edward C. Reifenstein, III		8. Performing Organization Report No.	
		10. Work Unit No.	
9. Performing Organization Name and Address Environmental Research & Technology, Inc. 58 Guinan Street Waltham, Mass. 02154		11. Contract or Grant No. NAS8-26275	
		13. Type of Report and Period Covered CONTRACTOR REPORT	
12. Sponsoring Agency Name and Address NASA Washington, D. C. 20546		14. Sponsoring Agency Code	
15. Supplementary Notes Technical Coordinator: S. C. Brown, Aerospace Environment Division, Aero-Astrodynamic Laboratory, Marshall Space Flight Center, Alabama 35812.			
16. Abstract <p>Results are presented for a study of the effects of water vapor, liquid water and ice upon radiative transfer processes at microwave frequencies and in far infrared. The fundamental processes by which these species interact with microwave energy are discussed, and their statistics analyzed in terms of their application to a range of remote sensing problems.</p> <p>Theoretical expressions for the water-vapor absorption coefficient at microwave frequencies are reviewed, and an efficient computer-oriented algorithm is presented for its computation. The Mie theory is reviewed, and the unit-volume effects of typical liquid-water and ice cloud distributions over the spectral range from 10 cm to 10 microns are examined. Characteristics of the two-dimensional distributions of water vapor, liquid water, and ice in the atmosphere have been collected on planetary, synoptic, meso-, and microscales, and are examined in terms of remote sensing applications. Extreme values of each are established as a function of scale size and related to the attenuation and noise energy produced and their fluctuations in time.</p> <p>The information content of radiosonde and cloud data, such as has been used in the 4-D Atmospheric Model and Cloud Statistics Program, is examined for its utility in simulation and predicting the influence of the atmosphere on surface observations from a space observer.</p>			
17. Key Words (Suggested by Author(s)) Water Vapor, Clouds, Atmospheric Attenuation, Microwaves, Cloud Models, Earth Observations from Space		18. Distribution Statement Unclassified-Unlimited  E. D. Geissler Director, Aero-Astrodynamics Laboratory	
19. Security Classif. (of this report) UNCLASSIFIED	20. Security Classif. (of this page) UNCLASSIFIED	21. No. of Pages 232	22. Price* \$3.00

TABLE OF CONTENTS

	Page
Chapter I Introduction	1
Chapter II The Absorption Coefficient of Atmospheric Water Vapor.	7
A. The Water Vapor Molecules	7
B. The Absorption Coefficient	9
C. The Modified Form Factor	15
D. Analysis of the Non-Resonant Spectrum	19
E. The Water Vapor Spectrum to 1350 GHz	22
F. Computational Procedure	24
Chapter III Interaction of Liquid Water and Ice Particles with Electromagnetic Energy over the Spectral Range 10 cm to 10 μ .	28
A. The Theory of Mie	31
B. Dielectric Properties of Pure Water	34
C. Mie Efficiency Factors for Water	38
D. Single Particle Properties of Ice from 10 μ to 10 cm	49

	Page
E. Dielectric Properties of Ice	50
F. Mie Efficiency Factors for Ice	50
G. Unit Volume Radiative Transfer	55
Properties of Water and Ice	
Clouds	
H. Absorption by Clouds in the	56
Rayleigh Limit	
Chapter IV Radiative Transfer Properties of	61
Clouds from 10 cm to 10 μ .	
A. Modeling Procedures for Atmos-	61
spheric Variables	
B. Models of Clear Atmospheres	65
C. Models of Cloud Cover Conditions	65
D. Unit-Volume Scattering and	72
Absorption Properties of Clouds	
Chapter V The Variability of Water Vapor in the	80
Atmosphere and Its Relationship to	
Radiometric Observations.	
A. Water Vapor in the Atmosphere	80
B. Coupling Considerations Between	107
Atmospheric Energy and Atmos-	
spheric Water Vapor	
C. Representative Absorption and	123
Noise Computations	

	Page
Chapter VI The Variability of Liquid Water and Ice in the Atmosphere and its Relation- ship to Radiometric Observations.	145
A. Liquid Water and Ice in the Atmosphere	145
B. Radiometric Studies of Clouds	155
C. Absorption, Scattering and Other Characteristics of the Clouds in the Cloud Catalogue	167
Chapter VII Conclusions and Recommendations.	168
References	171
Appendix A	175
Appendix B	177
Appendix C	195

LIST OF FIGURES

	Page
II-1. Geometrical configuration of the water vapor molecule. (Gaut, 1968)	8
II-2. Relative distribution of water vapor molecules over the first 52 energy states at 293 °K, compared with a straight Maxwell-Boltzmann distribution. (Gaut, 1968)	12
II-3. Absorption spectrum of the 22.235 GHz resonance line of water vapor together with theoretical and empirically corrected curves. (Gaut, 1968.)	21
II-4. The empirical correction term (solid line) for $P=1000$ mb, $T=300$ °K and $\rho=1$ g/m ³ , together with points derived from experimental data.	23
II-5. Water vapor spectrum from 10 to 300 GHz.	25
II-6. Water vapor spectrum from 300 to 1350 GHz.	26
III-1. Index of refraction for pure water, 10 μ to 10 cm.	35
III-2. Index of refraction for pure water, 1 GHz to 300 GHz.	37
III-3. Mie efficiency factors for scattering and extinction by pure water droplets at 10 cm.	39
III-4. Mie efficiency factors for scattering and extinction by pure water droplets at 5 cm.	40
III-5. Mie efficiency factors for scattering and extinction by pure water droplets at 1 cm.	41
III-6. Mie efficiency factors for scattering and extinction by pure water droplets at 5 mm.	42
III-7. Mie efficiency factors for scattering and extinction by pure water droplets at 1 mm.	43

	Page
III-8. Mie efficiency factors for scattering and extinction by pure water droplets at 500 microns.	44
III-9. Mie efficiency factors for scattering and extinction by pure water droplets at 100 microns.	45
III-10. Mie efficiency factors for scattering and extinction by pure water droplets at 50 microns.	46
III-11. Mie efficiency factors for scattering and extinction by pure water droplets at 10 microns.	47
III-12. Index of refraction for ice, 10 μ to 10 cm.	51
III-13. Mie efficiency factors for scattering and extinction by ice particles at 1 cm.	52
III-14. Mie efficiency factors for scattering and extinction by ice particles at 100 microns.	53
III-15. Mie efficiency factors for scattering and extinction by ice particles at 10 microns.	54
III-16. Microwave absorption by water clouds from 1 to 1000 GHz as given by the Rayleigh approximation formula of Staelin (1966).	58
III-17. Microwave absorption by ice clouds from 1 to 1000 GHz as given by tabulated data of Atlas et al. (1965).	59
IV-1. Geometries applicable to the solution of the equation of radiative transfer in a plane layered atmosphere.	62
IV-2. Temperature profiles for three model atmospheres used in the present study to represent climatic extremes.	66
IV-3. Water vapor density profiles for three model atmospheres used in the present study to represent climatic extremes.	67
IV-4. Scattering and Extinction coefficients computed for low-lying stratus as a function of wavelength with the empirical formula of Staelin (1966) shown for comparison.	73

	Page
IV-5. Extinction coefficient for three layers of a rain bearing cumulus cloud computed as a function of wavelength.	75
IV-6. Single scattering albedo for three model cloud distributions as a function of wavelength.	76
IV-7. Single scattering penetration depth for the three layers of a rain bearing cumulus cloud, with layer depths shown for reference.	78
V-1. The zonally averaged precipitable water for the summer, winter and year of the IGY.	82
V-2. The annual average of precipitable water in vapor form along 80° west longitude.	84
V-3. A meridional cross-section of the zonally averaged absolute humidity. Data are from the IGY.	85
V-4. A meridional cross-section of the mean annual distribution of water vapor along 80° west longitude.	87
V-5. The vertical distribution of the zonally averaged absolute humidity for the IGY.	88
V-6. A meridional cross-section of the zonally averaged temporal standard deviation of the absolute humidity.	89
V-7. The annual mean distribution of precipitable water in vapor form over the northern hemisphere.	91
V-8. The mean distribution of precipitable water in vapor form over the northern hemisphere during summer.	93
V-9. The mean distribution of precipitable water in vapor form over the northern hemisphere during winter.	94
V-10. The annual mean distribution of precipitable water in vapor form over the southern hemisphere.	95

		Page
V-11.	The mean distribution of precipitable water in vapor form over the southern hemisphere during summer. Units are gm/cm^2 . Data are from the IGY (1958). (Courtesy of Dr. J. P. Peixoto, M.I.T.)	97
V-12.	The mean distribution of precipitable water in vapor form over the southern hemisphere during winter. Units are gm/cm^2 . Data are from the IGY (1958). (Courtesy of Dr. J. P. Peixoto, M.I.T.)	98
V-13.	The mean annual distribution of precipitable water in vapor form over the African continent. Units are gm/cm^2 . Data are from the IGY (1958). (Peixoto and Obasi, 1965.)	100
V-14.	The mean distribution of precipitable water in vapor form over the African continent in summer. Units are gm/cm^2 . Data are from the IGY (1958).	101
V-15.	The mean distribution of precipitable water in vapor form over the African continent in winter. Units are gm/cm . Data are from the IGY (1958).	102
V-16.	Precipitable water over the U.S. on 16 March 1969 as reported by the U.S. Weather Bureau.	103
V-17.	Hypothetical curves describing the maximum precipitable water in vapor form and maximum variation of this parameter over two scale sizes as a function of scale size.	108
V-18.	Weighting function WF_1 for absorption versus height for 19.0, 21.9 and 22.235 GHz. Values have been normalized.	111
V-19.	The stability of the weighting function WF_1 at 19.0 GHz for various standard atmospheres over the earth.	112
V-20.	Weighting function WF_2 for brightness temperature, looking at the zenith ² at 19.0, 21.9, and 22.235 GHz as a function of height.	115
V-21.	Stability of the weighting function WF_2 at 19.0 GHz for various standard atmospheres over the earth.	116

	Page
V-22. The percentage of total energy received versus height at 183.310 GHz is several standard atmospheres.	118
V-23. The brightness temperature as seen by a satellite based radiometer in the vicinity of the 183 GHz line in a tropical and mid-latitude atmosphere.	119
V-24. The weighting function WF_2 , the mean tropical water vapor distribution, and the emission ($WF_2 \times \rho$) as a function of height.	121
V-25. The effect of surface versus space observations on the expected signal variability caused by hypothetical variations in the precipitable water of the atmosphere.	124
V-26. The opacity due to atmospheric water vapor between 10 and 350 GHz for 0.5, 2.5 and 4.5 gm/cm ² .	125
V-27. The absorption spectrum between 10 and 350 GHz for: (1) the mean annual atmospheric conditions near La Jolla, California; and (2) for the one sigma deviations from these atmospheric conditions.	127
V-28. Atmospheric opacity due to water vapor alone versus precipitable water in vapor form for 12, 22, 32, 97, 182, 222 and 322 GHz.	129
V-29. Atmospheric brightness temperature due to water vapor alone of a zenith viewing radiometer versus precipitable water in vapor form for 12, 22, 32, 97, 182, 222 and 322 GHz.	130
V-30. The mean annual distribution over the Northern Hemisphere of total atmospheric opacity τ due to water vapor alone at 12 GHz, for a zenith viewing radiometer.	133
V-31. The mean annual distribution over the Southern Hemisphere of total atmospheric opacity τ due to water vapor alone at 12 GHz, for a zenith viewing radiometer.	134
V-32. The mean annual distribution over the Northern Hemisphere of total atmospheric opacity τ due to water vapor alone at 32 GHz, for a zenith viewing radiometer.	135

		Page
V-33.	The mean annual distribution over the Southern Hemisphere of total atmospheric opacity τ due to water vapor alone at 32 GHz, for a zenith viewing radiometer.	136
V-34.	The mean annual distribution over the Northern Hemisphere of total atmospheric opacity τ due to water vapor alone at 97 GHz, for a zenith viewing radiometer.	137
V-35.	The mean annual distribution over the Southern Hemisphere of total atmospheric opacity τ due to water vapor alone at 97 GHz, for a zenith viewing radiometer.	138
V-36.	The mean annual distribution over the Northern Hemisphere of brightness temperature T_B due to water vapor alone at 12 GHz.	139
V-37.	The mean annual distribution over the Southern Hemisphere of brightness temperature T_B due to water vapor alone at 12 GHz.	140
V-38.	The mean annual distribution over the Northern Hemisphere of brightness temperature T_B due to water vapor alone at 32 GHz.	141
V-39.	The mean annual distribution over the Southern Hemisphere of brightness temperature T_B due to water vapor alone at 32 GHz.	142
V-40.	The mean annual distribution over the Northern Hemisphere of brightness temperature T_B due to water vapor alone at 97 GHz.	143
V-41.	The mean annual distribution over the Southern Hemisphere of brightness temperature T_B due to water vapor alone at 97 GHz.	144
VI-1.	Relative drop size distributions for fair weather cumulus, cumulus congestus and nimbostratus.	150
VI-2.	Hypothetical curves describing the maximum precipitable water in cloud droplet and rain droplet forms as a function of scale size.	156
VI-3.	Cloud opacity weighting functions in the mid-latitude atmosphere for three frequencies.	158

		Page
VI-4.	Liquid water content for which the opacity is unity as a function of frequency and nadir angle, with typical cloud types shown for reference.	160
VI-5.	Brightness temperature of the calm sea surface through low-lying stratus.	162
VI-6.	The function $W (dT_p/dw)$ vs. cloud liquid water content at 19.35 GHz and 37 GHz.	163
VI-7.	Trace from measurements by the Convair 990 19.35 GHz radiometer over clouds in the Gulf of Mexico.	166

LIST OF TABLES

	Page
IV-1 Properties of Standard Cloud Models	68
VI-1. Cloud Liquid Water Characteristics	148
VI-2. Measured droplet concentrations	152

I. INTRODUCTION

Radio astronomers and atmospheric physicists have been interested in the microwave properties of the atmosphere by necessity or inclination for many years. Designers of communication systems have relentlessly moved to utilize higher microwave frequencies as the lower ones become more crowded each year. Their interest in the interaction between microwaves and the atmosphere has therefore increased. Now the National Aeronautics and Space Administration has placed a great deal of emphasis upon earth observations and it is clear microwaves offer a potentially highly useful means of investigating surface properties. Therefore, from NASA's viewpoint, it is imperative to learn more about how the atmosphere will affect surface observations made from space.

In an attempt to illuminate certain aspects of the relationship between microwaves and atmospheric water and clouds, this study was undertaken. It is directed especially towards the problems of remote sensing of the surface from space but in answering questions concerning this application it will no doubt be useful for other purposes.

A. Objectives

The objectives of this study can be listed as follows:

1. To establish a mathematical link between the molecular processes and the bulk electromagnetic properties of atmospheric water vapor, liquid water, and ice, over the spectral range from 10cm to 10μ in wavelength.
2. To develop explicit formulation and methods to compute atmospheric spectra for arbitrary atmospheric configurations of pressure, temperature, water vapor, liquid water drops and ice over the range 10cm to 10μ .
3. To examine the variability of water vapor and clouds in the atmosphere and relate this to radiometer signal variability.
4. To establish methods for applying the techniques and information developed in 1 through 3 to world wide statistics of water vapor and clouds.

B. Approach

The objectives for this study were ambitious for the amount of funds allocated. Therefore, it has been necessary to carefully select the most vital parts of each objective and to concentrate our research on them. An example of the approach which we adopted, taking these restrictions into account, is illustrated below in the case of computing the absorption of atmospheric water vapor:

Water vapor spectra have been computed for many years. As far as we know the most accurate calculations between 1mm and 100 μ have relied upon computing the contribution to a given frequency interval from all or most spectral lines within a wide spectral interval. The process, however, is expensive in computer time, and, up to now, no matter what line shape was chosen, has been systematically inaccurate for all spectral intervals not falling on or near to the resonant frequency of a spectral line. However, to study atmospheric spectra over the very wide range which this study calls out, it is essential that these computations be accurate and economical to carry out. In preparing this section, therefore, considerable effort was expended to determine a new, more economical method for computing absorption by atmospheric water vapor. The result is an efficient new algorithm applicable to the microwave spectrum at least to 1000 GHz.

This same philosophy has been applied to each well defined subarea of the study. The essential considerations have been brought out and then the most economical methods employed to achieve accurate and meaningful results.

C. Limitations

This study in no way exhausts the subject matter discussed. In

fact various economies were required to cover the broad ground over which the study was carried out. One of the subjects which simply could not be explored was band models which could be used to compute spectra from the region from around 200μ down to 10μ over spectral bandwidths typical of instrumentation available for measurements in this region. Since the principal objective was to examine the microwave region, which is usually limited to wavelengths longer than one mm, the technique best suited for the microwave region was developed and applied as far into the infrared as it seemed useful. The computational method which evolved was the differential bandwidth method which, even though it is accurate in any part of the spectrum, loses its significance for infrared detectors, all of which have bandwidths that include many individual spectral lines.

A further limitation exists for the application of the spectral computational methods to worldwide statistics. Methods were developed to provide a means for establishing the statistics of atmospheric attenuation, emission and variability due to water vapor over the entire earth for seasonal and yearly conditions. Examples are given for a very limited set of frequencies and geographical locations because of the rapid multiplication in time and effort needed to produce these maps. However, corollary graphs and explanations make it possible to extrapolate the results to many other spectral regions.

We have not attempted to analyze surface emission or the effect of surface reflectivity on atmospheric emission. The primary subject matter is atmospheric attenuation and emission and therefore results are presented for that contribution only.

Another fundamental limitation in applying the methods to compute cloud attenuation and scattering is the lack of quantitative data on liquid water and ice distributions in the atmosphere. So far, world cloud information is limited to cloud cover statistics. No data exist to define the global distribution of liquid and frozen water. Our approach, therefore, has been to establish representative cloud models which could be related to the cloud descriptions in the 29 homogeneous cloud regions defined in the world-wide cloud studies already performed for NASA/Marshall, analyze these models and suggest which models might be appropriate for each region.

D. Uses of the Study

This report has attempted to bring together certain tools which can be used to assess the impact of water vapor and clouds on earth-space communications and observations. It can be used to establish planning data where knowledge of the statistical properties of atmospheric attenuation, noise energy and scattering processes are needed. If more detailed calculations are needed, it provides the algorithms and general procedures which can be programmed to compute the detailed

structure of the atmosphere. It outlines procedures for utilizing world wide statistics on the distribution of water vapor and clouds as they are now known and analyzes the origin and magnitude of the variability which can be expected in these quantities.

The most important use of this study may be to provide the foundation upon which specific mission oriented studies can be constructed.

II. THE ABSORPTION COEFFICIENT OF ATMOSPHERIC WATER VAPOR

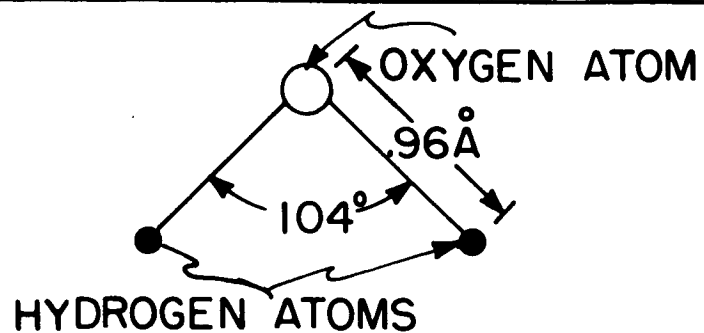
A. The Water Molecule

Associated with gas molecules are several forms of energy, among which are the following: the kinetic energy of translation, the energy associated with rotation about the principal molecular axes, the energy of vibration, and the energy associated with the atomic orbital electrons. The last three forms are quantized and interact with the ambient radiation field. Each form can be considered as an approximately independent domain of energy.

The rotational and vibrational modes of the water molecule are shown in Figure II-1. The quantized states of lowest energy correspond to those for which the molecule is not vibrating, and are called pure rotational energy states. Transitions can occur between some of these states, and thus give rise to spectral lines of absorption, if the final state is at a higher energy level than the initial state, or to spectral lines of emission, if the final state is at a lower energy level.

Energy states for asymmetric molecules like H_2O , that is, molecules whose three moments of inertia have different values, are designated in one of two ways. In the most explicit method, the quantum number J associated with the total angular momentum is expressed with two subscripts K_{-1} and K_{+1} . These last two numbers are internal quantum numbers associated with limiting prolate and oblate symmetrical

THE WATER VAPOR MOLECULE (H_2O)



ROTATIONAL MOTIONS

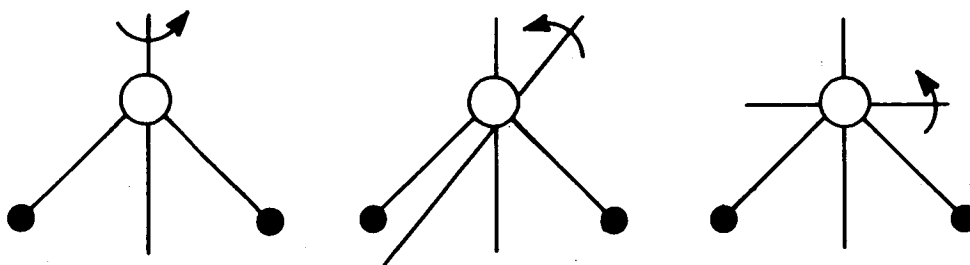


Figure II-1. Geometrical configuration of the water vapor molecule. (Gaut, 1968.)

molecules rotating in a manner similar to the asymmetric one of interest.

More concise is the J_τ notation. J remains the quantum number associated with the total angular momentum, but it now has a single subscript. This subscript is associated with the order of the energy level in question in the possible $(2J+1)$ levels which can occur for the same total angular momentum. If K_- and K_+ are known, τ may always be found from the expression $\tau = K_- + K_+$.

In the J_{K_-,K_+} notation, the transition producing the lowest frequency water vapor line occurring at 22.2 GHz line is produced by the transition between the energy states $5_{2,3} \rightarrow 6_{1,6}$. The 183.3 GHz line is produced by the transition between the energy states $2_{1,2} - 3_{1,3}$. In the J_τ notation, these transitions are $5_- \rightarrow 6_-$ and $2_+ \rightarrow 3_+$, respectively.

B. The Absorption Coefficient

The absorption coefficient for radiation is found from quantum mechanical considerations to be dependent upon the following factors: (1) the transition frequency, given by Eq. 2-1; (2) the intrinsic line strength of the transition; (3) the distribution of molecules among the states which can participate in a transition; and (4), the line shape factor.

Many excellent treatments of the theory of water vapor absorption

exist in the literature (see, for example Townes and Shawlow, 1955; Herzberg, 1966). The discussion given here summarizes the analysis of Gaut (1968).

The frequency at which spectral lines appear is directly related to the energy difference between the initial and final energy states of a transition and is approximately given by the Bohr relationship:

$$\nu_{ij} = \frac{|E_j - E_i|}{h} \quad (2-1)$$

where the subscripts i, j refer to the initial and final states, ν_{ij} is the resonant frequency of the transition between energy levels i and j with energy values E_i and E_j , and h is Planck's constant. The general expression for the absorption coefficient resulting from the transition of molecules between the energy states i and j is given by

$$\gamma_{ij} = \frac{8\pi^3\nu}{3hc} |f(\nu_{ij}, \nu)| \left\{ N_i |\mu_{ij}|^2 - N_j |\mu_{ji}|^2 \right\} \quad (2-2)$$

in which γ_{ij} is the absorption coefficient for the transition $i \rightarrow j$; ν_{ij} is the frequency of the incident radiation, N_i and N_j are the number densities of molecules in the lower and higher energy states,

respectively; $|\mu_{ij}|^2$ is the square of the dipole matrix element associated with the transition $i \rightarrow j$, and $f(\nu_{ij}, \nu)$ is the line shape factor.

Eq. 2-2 demonstrates the dependence of the absorption coefficient upon the populations of the two energy levels. Transitions occur from one energy level to the other and absorption takes place only when $|\mu_{ij}|^2 N_i > |\mu_{ji}|^2 N_j$. This situation occurs under conditions of thermodynamic equilibrium only when 'i' represents the state of lower energy. When the reverse condition exists, and $|\mu_{ij}|^2 N_i < |\mu_{ji}|^2 N_j$, again with 'i' representing the lower energy state, energy is added through emission to the ambient radiation field. Within the atmosphere, thermodynamic equilibrium exists for water vapor well into the mesosphere allowing the population of levels to be found from the Boltzmann theory, in which the population of any given level is proportional to $\exp \{-E/kT\}$ where 'k' is Boltzmann's constant and 'T' the absolute temperature. As an example, the term (energy) values of the first 52 rotational energy levels of the water molecule are shown in Figure II-2 together with their relative populations. Also for comparison shown in Figure II-2 is a straight Maxwell-Boltzmann distribution at 293° K. The deviation of the actual population from the Maxwell-Boltzmann distribution is a result of statistical weighting factors for degenerate space and nuclear spin.

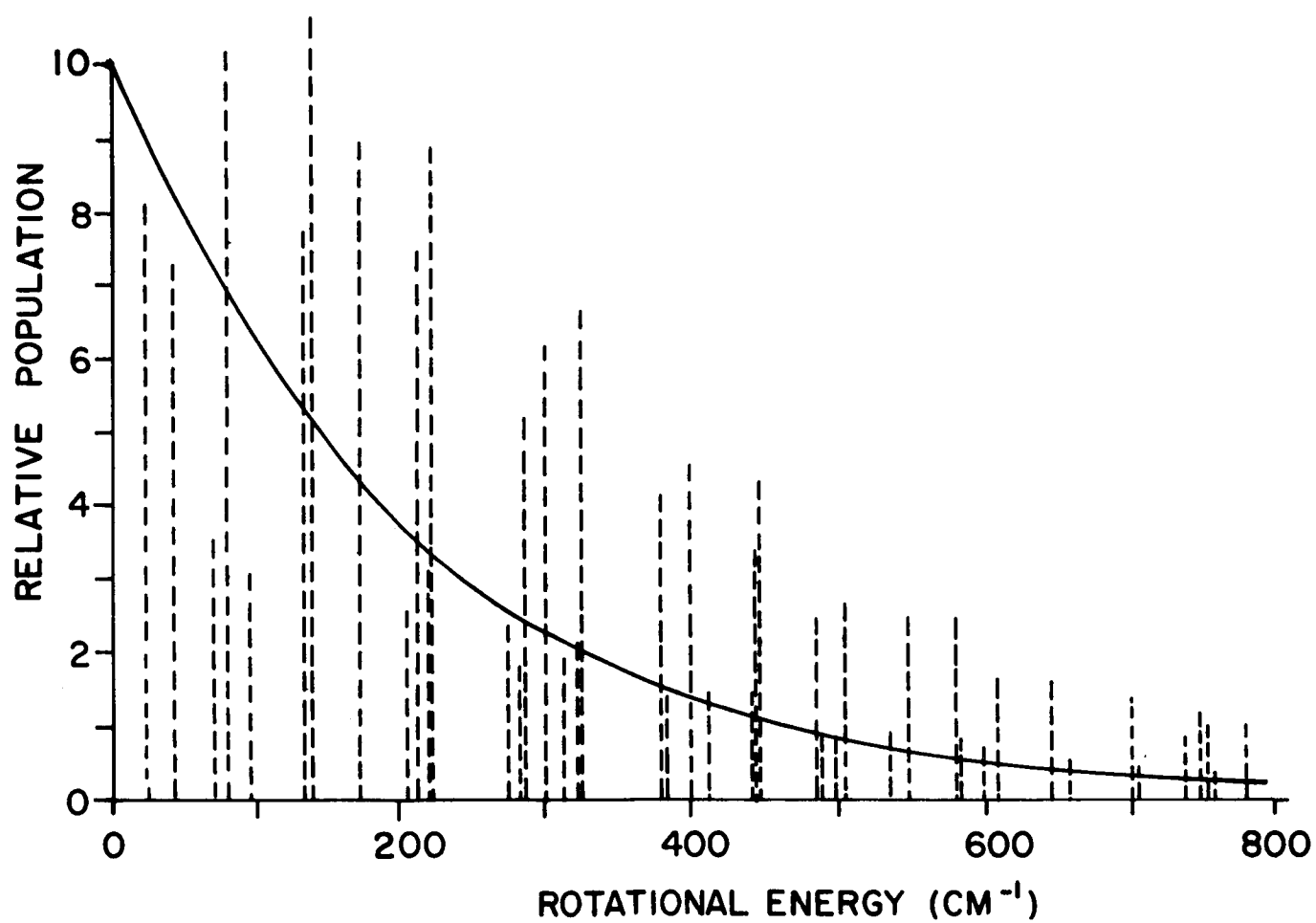


Figure II-2. Relative distribution of water vapor molecules over the first 52 energy states at 2930K, compared with a straight Maxwell-Boltzmann distribution. (Gaut, 1968.)

Making use of the approximation of Van-Vleck (1947) for the partition function for water, the expression for the absorption coefficient becomes

$$\gamma_{ij}(\nu) = \frac{8\pi^3 N \mu^2 \nu}{3hc} \frac{g_{ij} S_{ij}}{0.0344 T^{3/2}} \left\{ e^{-E_i/kT} - e^{-E_j/kT} \right\} |f(\nu, \nu_{ij})| \quad (2-3)$$

where μ is the permanent dipole moment of the water molecule, g a statistical weighting factor equal to 1 when τ is even or 3 when τ is odd, S_{ij} the "transition strength" or "line strength" representing the effective dipole moment of the transition $i \rightarrow j$ (relative to μ), and $f(\nu, \nu_{ij})$ the line-shape factor defined such that

$$\int f(\nu, \nu_{ij}) d\nu = 1 \quad (2-4)$$

For the purposes of computation, it is convenient to express Eq. 2-3 in terms of a single constant term together with parameters appropriate to water vapor absorption by the atmosphere:

$$\gamma_{ij}(\nu) = \frac{1.97 \times 10^5 \rho}{T^{3/2}} g_{ij} S_{ij} [F(\nu, \nu_{ij})] \left\{ e^{-E_i/kT} - e^{-E_j/kT} \right\} \quad (dB/km) \quad (2-5)$$

where ρ = water vapor density, g/m³
 g = 1,3 for = even, odd
 S = line strength
 T = absolute temperature in °K
 E_{ij} = term values (energy values) of the
 lower and upper states, in cm⁻¹
 k = Boltzmann's constant, in cm⁻¹ °K⁻¹

and $F(\nu, \nu_{ij})$ is a "Modified Form Factor" (no longer normalized by Eq. 2-4), containing the frequency dependence in the vicinity of the single line. According to the definitions of Eqs. 2-3 and 2-5,

$$F(\nu, \nu_{ij}) = \pi \nu |f(\nu, \nu_{ij})| \quad (2-6)$$

where $|f(\nu, \nu_{ij})|$ is the normalized line-shape factor. We shall discuss the line shape and Form Factor in greater detail below.

One further simplification to Eq. 2-5 obtains in the microwave spectral region when the Rayleigh-Jeans approximation ($h\nu/kT \ll 1$) is valid. In this case the term in brackets containing the two exponentials becomes, (making use of Eq. 2-1):

$$\left\{ e^{-E_i/kT} - e^{-E_j/kT} \right\} \longrightarrow e^{-E_i/kT} \left(\frac{h\nu_{ij}}{kT} \right) \quad (2-7)$$

and Eq. 2-5 may be replaced by

$$\gamma_{ij}(\nu) = \frac{9.45 \times 10^3 \rho g_{ij} S_{ij}}{T^{5/2}} \left[\nu_{ij} F(\nu, \nu_{ij}) \right] \left\{ e^{-E_i/kT} \right\} \quad (\text{dB/km}) \quad (2-8)$$

where all quantities are as defined above and ν, ν_{ij} are in GHz.

C. The Modified Form Factor

The finite breadth of spectral lines is the result of a combination of the following: (1) the "natural" line width related to the radiative transition lifetime by the uncertainty principle; (2) the "Doppler" line width arising from the distribution of velocities of molecules in random thermal motion; and, (3) the "collision" line width resulting from interactions between nearby molecules during collisions.

Of these mechanisms only Doppler and collision broadening processes need be considered for atmospheric studies at microwave frequencies. Radiational transition lifetimes of the order of seconds, typical of electric dipole transitions at microwave frequencies lead to natural line widths of order 1 Hz. Atmospheric temperatures yield, for water vapor at 22 GHz, Doppler line widths of order 10 kHz. Finally, atmospheric pressures lead to collisional line widths of 2 GHz at a frequency of 22 GHz. We shall therefore restrict ourselves in this discussion to the collisional, or pressure-broadening process.

The exact treatment of the problems of collisional broadening requires detailed knowledge of the interacting forces and processes occurring during collisions, not all of which are well known.

Derivations of theoretical line-shapes for collision-broadened lines have been done by Lorentz (1906), Van Vleck and Weisskopf (1945), Gross (1955), Zhevakin and Naumov (1963) and others. Additional interest has resulted, in recent years from the increased availability of data in the microwave region in the vicinity of the water-vapor lines at 22, 183 and 323 GHz. A recent review of the current status of the theory of collision broadening in the neighborhood of the 183 and 323 GHz lines has been given by Ulaby and Straiton (1970). [Note that the Modified Form Factor as defined by these last authors differs from that of Eq. 2-6, as used in this discussion by the factor (π/ν_{ij})].

At present, the most commonly used expressions are those of Van Vleck and Weisskopf (1945) who were led by conceptual difficulties with the original Lorentz theory at low frequencies to a reformulation of the theory. In the Van Vleck and Weisskopf approach, two assumptions are utilized: (1) rotating molecules can be treated as classical oscillators of natural frequency ω_0 driven by the external field to oscillate at ω ; and, (2) collision between rotating molecules leave the oscillator variables (position and velocity) dis-

tributed according to a Boltzmann distribution corresponding to the applied field at the time of collisions. An undesirable consequence of this approach is the large oscillator velocities required to redistribute the oscillators in position.

In the more recent theory of Gross (1955), the Van Vleck Weisskopf theory is modified by assuming that the oscillator positions are unchanged as a result of a collision, but that their velocities are altered to values appropriate to a Boltzmann distribution corresponding to the time of impact.

The "Modified Form Factors" as defined by Eq. 2-6 for the two theories are given below:

$$F_{VV}(\nu, \nu_{ij}) = \frac{\nu^2 \Delta\nu}{\nu_{ij}} \left[\frac{1}{(\nu_{ij} - \nu)^2 + \Delta\nu^2} + \frac{1}{(\nu_{ij} + \nu)^2 + \Delta\nu^2} \right] \quad (2-9)$$

and

$$F_G(\nu, \nu_{ij}) = \frac{4\nu^2 \nu_{ij} \Delta\nu}{(\nu_{ij}^2 - \nu^2)^2 + 4\nu^2 (\Delta\nu)^2} \quad (2-10)$$

in which ν is the observation frequency, ν_{ij} the resonant frequency of the transition, and $\Delta\nu$ the linewidth, as given by Gaut (1968):

$$\Delta\nu = (\Delta\nu)_0 \left(\frac{P}{1000} \right) \left(\frac{T}{300} \right)^{-n} \left(1 + \frac{\alpha_P T}{P} \right) \quad (2-11)$$

with $(\Delta\nu)_0$ the line width at 1000 mb pressure, 300⁰K temperature and the water vapor density $\rho \rightarrow 0$. The constant n is a line-dependent exponent describing the temperature dependence of the line width, and α is a factor that is a measure of the enhanced effectiveness of H₂O molecules for broadening water-vapor lines relative to nitrogen molecules

At resonance, both formulations

$$F(\nu, \nu_{ij}) = \frac{\nu_{ij}}{\Delta\nu}, \quad \nu = \nu_{ij} \quad (2-12)$$

The following dependencies away from resonance obtain for the Van Vleck Weisskopf case:

$$F_{vv}(\nu, \nu_{ij}) \approx \frac{2 \nu^2 \Delta\nu}{\nu_{ij}^3} \quad \nu \ll \nu_{ij} \quad (2-13)$$

$$F_{vv}(\nu, \nu_{ij}) \approx \frac{2 \Delta\nu}{\nu_{ij}} \quad \nu \gg \nu_{ij}$$

and for the Gross line-shape factor

$$F_G(\nu, \nu_{ij}) \approx \frac{4 \nu^2 \Delta \nu}{\nu_{ij}^3} \quad \nu \ll \nu_{ij}$$

$$F_G(\nu, \nu_{ij}) \approx \frac{4 \nu_{ij} \Delta \nu}{\nu^2} \quad \nu \gg \nu_{ij}$$

(2-14)

D. Analysis of the Non-Resonant Spectrum

Experimental data in the microwave region, confined largely to the three lowest lines at 22, 183 and 323 GHz show good agreement with these and other theories at resonance but are in error by as much as a factor of 5 (see Gaut, 1968 and Ulaby and Straiton, 1970) in the far wings of the lines.

Zhevakin and Naumov (1963) used the Gross line-shape factor for the calculation of atmospheric water vapor absorption over the spectral range 10 μ to 2 cm. Although the agreement between observed values and those calculated by summing the contributions of all the lines is better for the Zhevakin and Naumov expression than for the Van Vleck-Weisskopf theory, the disagreement still exists. Burch (1968) has reviewed the available data for atmospheric water vapor in addition to making laboratory measurements to 36 cm^{-1} (278 microns) demonstrating the presence of the discrepancy in the wings of the lines over the entire range.

One would at first assume that, since the calculated values are too low, the error results from not summing over enough lines, i.e., the contribution of a large number of strong lines at much higher frequencies is non-negligible. This assumption was tested by Gaut (1968) for the 183 GHz line, comparing the profile obtained with a single resonance to that obtained by summation of the contribution of the first 53 lowest rotational resonances, using the Van Vleck-Weisskopf line shape. The inclusion of the additional lines reduced the error between observed and calculated values by only 15%.

In practice, the solution to the dilemma is the adoption of an empirical term describing the difference between the observed values and those obtained by summation over the nearby lines. This approach has been adopted by Gaut (1968) who finds that, for the 22 GHz line, additive term of magnitude 4 times the uncorrected non-resonant background is needed. This is illustrated in Figure II-3. Similarly, Burch (1968) adopts an empirical "continuum" obtained by fitting the computed values to the experimental points.

In the present study, the spectrum was computed over the range from 10 to 1000 GHz making use of the Gross line shape and summations over the first 53 lines, at 1000 mb pressure, 300°K temperature, with water vapor density $\rho = 1 \text{ g/m}^3$. The experimental data of Becker

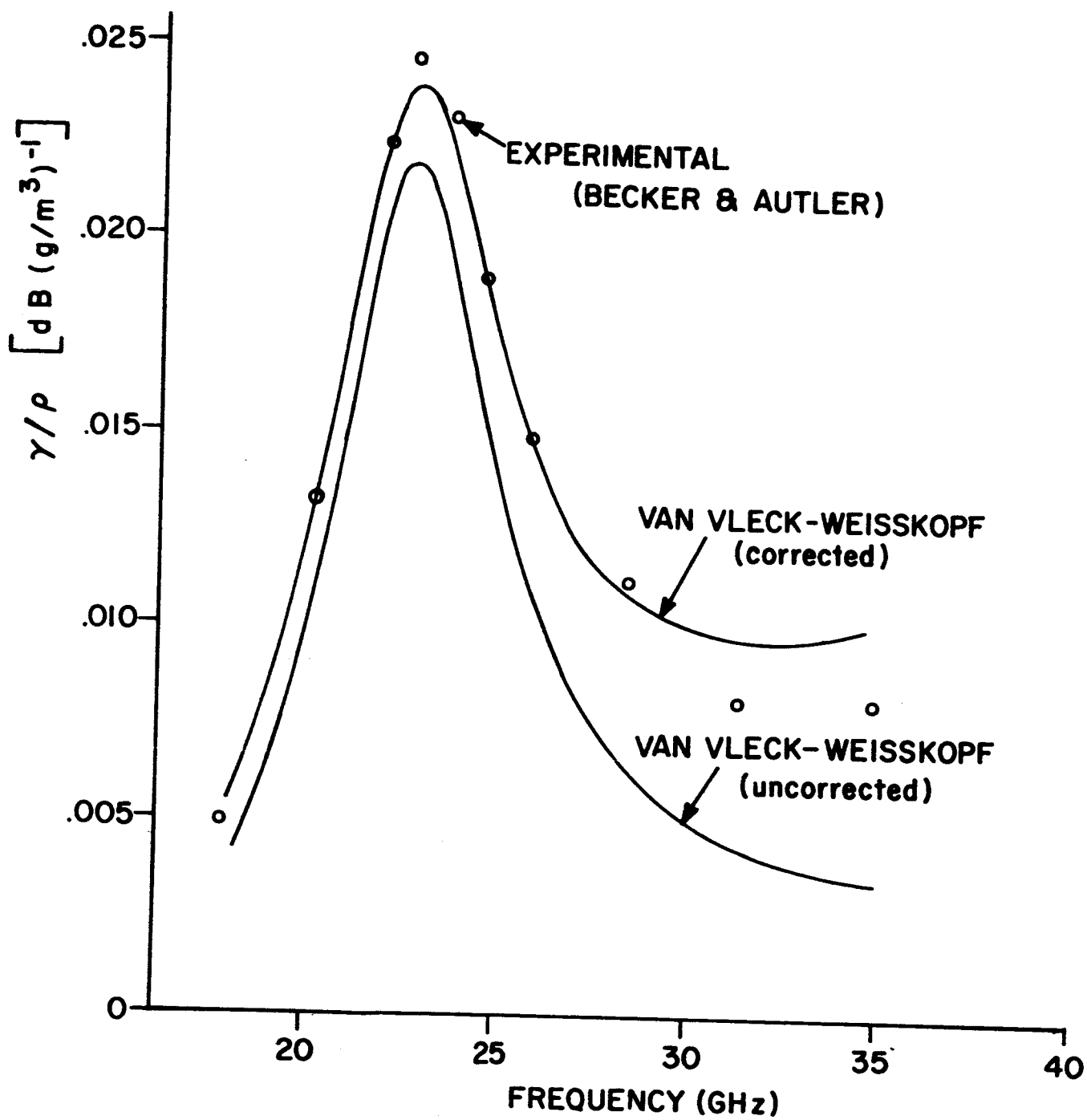


Figure II-3. Absorption spectrum of the 22.235 GHz for two pressures, at constant temperature. (Gaut, 1968.)

and Autler (1946), Frenkel and Woods (1966) and Burch (1968) were reduced to equivalent conditions, and the difference between the observed and computed values plotted in Figure II-4.

The contribution of lines at higher frequencies is proportional to ν^2 as seen from Eq. 2-14, and hence an expression of the form

$$\gamma_{\text{corr.}}(\nu) = C \left(\frac{300}{T} \right)^{n'} \left(\frac{P}{1000} \right) \nu^2 \quad (2-15)$$

was adopted for the correction term, with the parameter C and the exponent n' to be determined. In Figure II-4 the solid line represents the best fit of the points derived from the data corresponding to $C = 4.7 \pm 1.0 \times 10^{-6}$ for n' in GHz. For the temperature exponent, the values used by Gaut (1968) for the 22 and 183 GHz lines were generalized by taking

$$n' = 3/2 + n \quad (2-16)$$

where n is the temperature exponent in the line width $\Delta\nu$ as defined in Eq. 2-11. This assumption leads to $n' = 2.126, 2.10$ and 2.110 for the 22, 183 and 323 GHz lines.

E. Water Vapor Spectrum to 1350 GHz

The theoretical spectrum, making use of the above empirical correction term was calculated over the frequency range 10 to 1350 GHz,

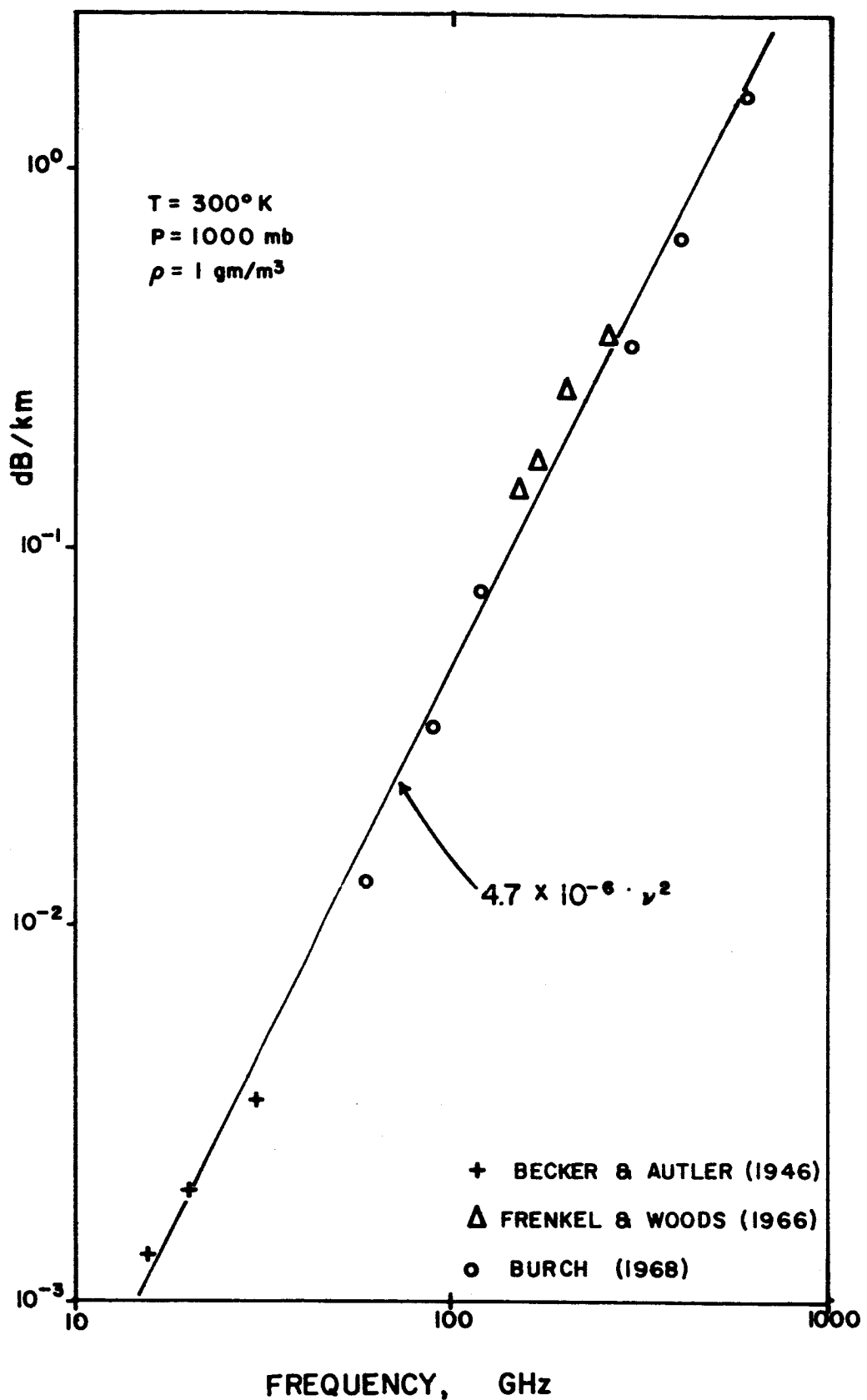


Figure II-4. The empirical correction term (solid line) for $P=1000 \text{ mb}$, $T=300^{\circ}\text{K}$ and $\rho=1\text{gm/m}^3$, together with points derived from experimental data.

using the Gross line shape factor and including at each point the nearest five lines above and below the given frequency. The resulting spectrum is shown in Figures II-5 and II-6, with experimental values added for comparison. The constants used in Eqs. 2-5, 2-10 and 2-11 are those tabulated by Gaut (1968) and are given for reference in Appendix A. The calculated spectrum appears to agree with the experimental points to within ~10% in nearly all cases, up to 1000 GHz. The validity of the assumed temperature and pressure dependence of the empirical correction term has not been determined nor has the correction itself been validated above 1000 GHz, due to lack of experimental data.

F. Computation Procedure

The computer algorithm used in the calculation of the spectrum is embodied in an IBM 360 subroutine. The routine is designed for efficient computation of many points without the necessity of an extended summation over the entire set of rotational lines. The number of lines actually summed is dependent upon the pressure; at 1000 mb, the nearest five lines above and below the given frequency are summed, and the effective contribution of those outside this range is included using the correction term of Eq. 2-15. The advantages of this procedure for the study of the microwave properties of the terrestrial environment are twofold:

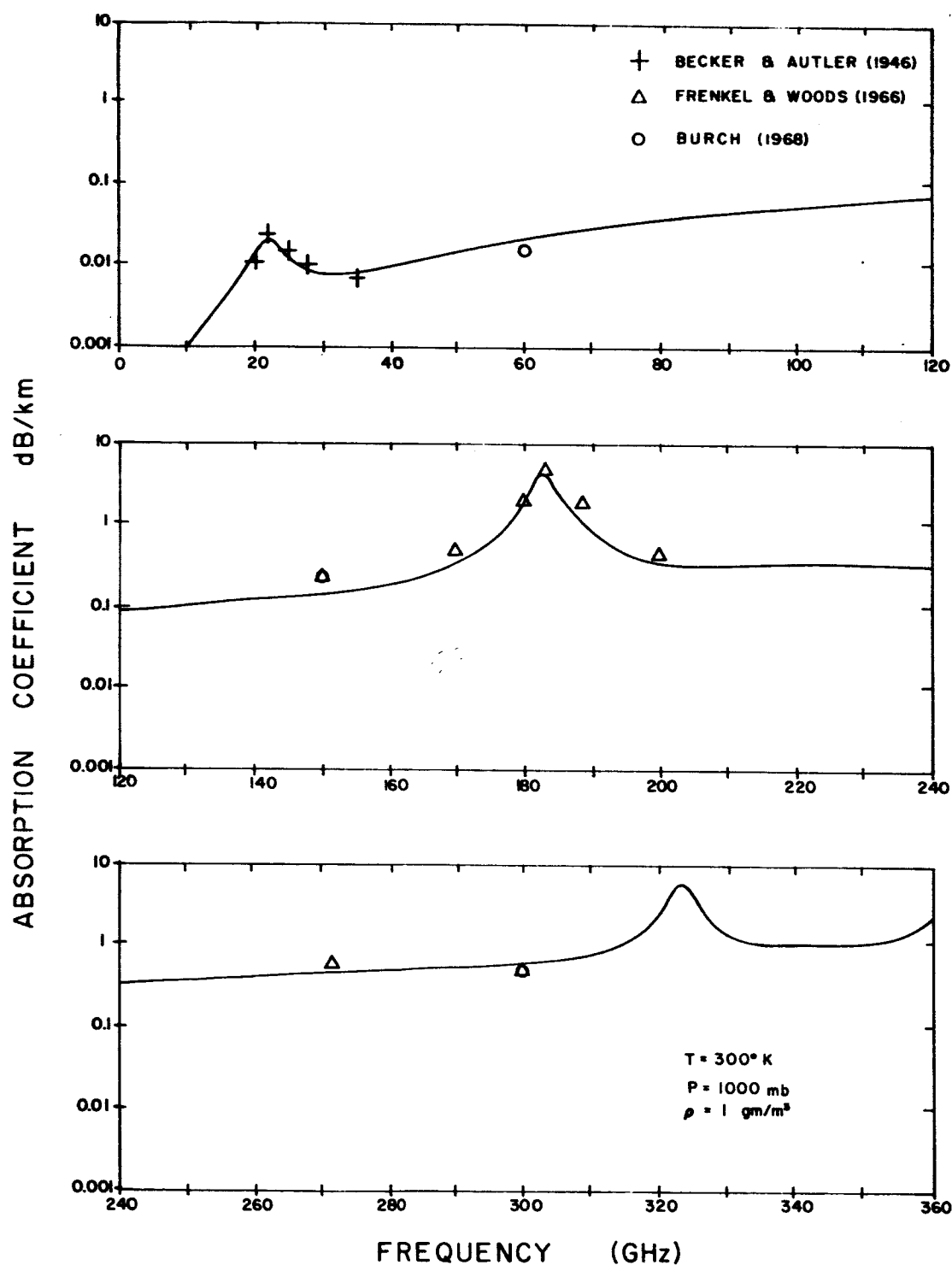


Figure II-5. Computed atmospheric water vapor spectrum from 10 to 360 GHz at 1000 mb pressure, 300°K temperature and 1 g/m³ density, with experimental values added for comparison.

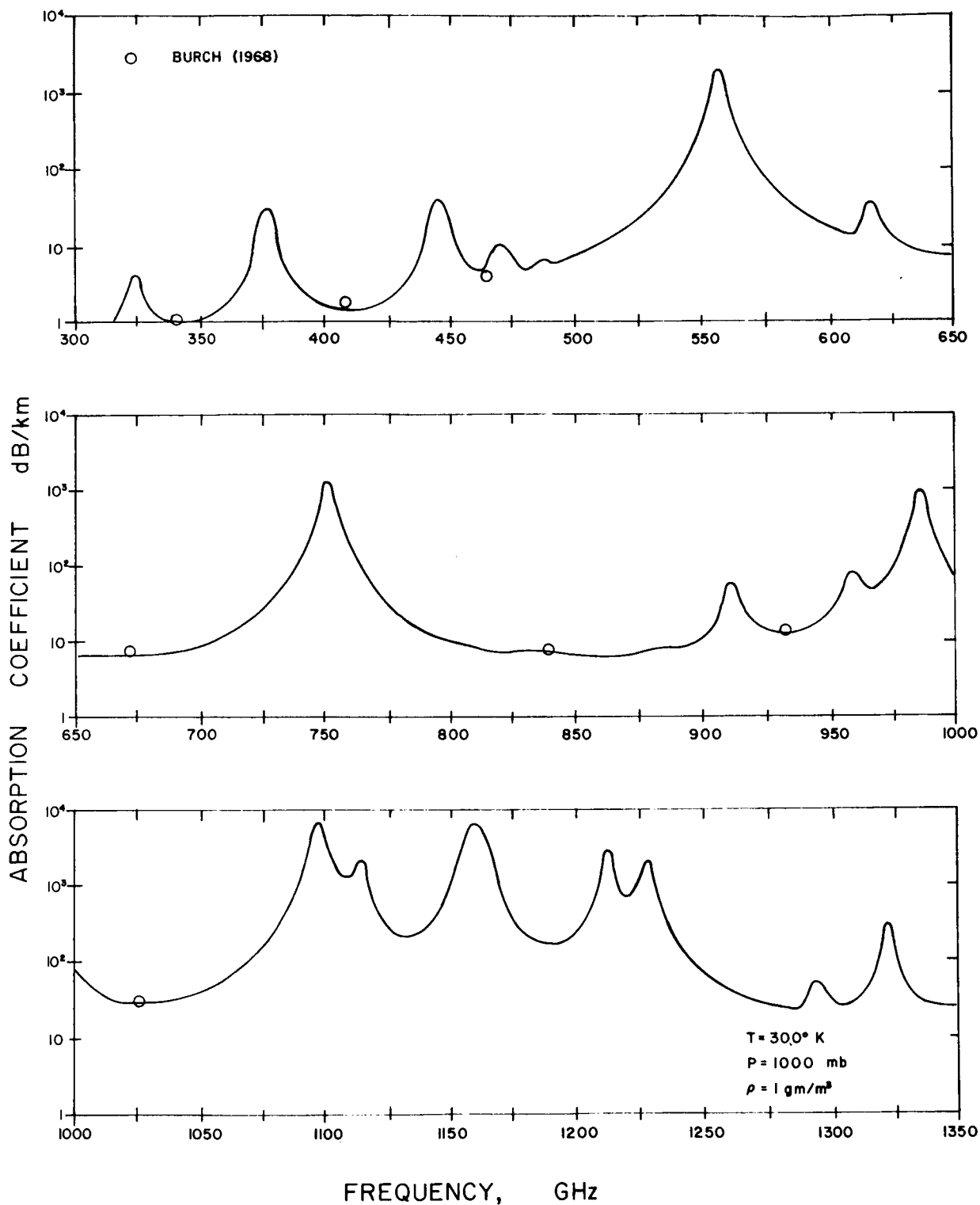


Figure II-6. Computer atmospheric water vapor spectrum from 300 to 1350 GHz at 1000 mb pressure, 300°K temperature and 1 g/m³ density, with experimental values added for comparison.

(1) The number of basic cycles in the computation is $10 \times N_p$ where N_p is the number of sets of parameters (T, P, ρ, ν) computed, instead of $N_L \times N_p$ where N_L is the number of lines. The reduction in execution time is thus $\sim N_L/10$ or ~ 100 for the entire set of about 1000 rotational lines from 22 GHz to 10 microns; and

(2) The empirical background affords sufficient accuracy to model the spectrum, at least at 1000 mb pressure and 300°K temperature, in agreement with experiment to $\sim 10\%$ over the studied range.

III. INTERACTION OF LIQUID WATER AND ICE PARTICLES WITH ELECTRO- MAGNETIC ENERGY OVER THE SPECTRAL RANGE 10 CM TO 10 MICRONS.

The absorption and emission properties of atmospheric water vapor are the result of resonant transitions from one energy state to another. The variability of these properties at any given frequency is influenced primarily by the large-scale distribution of this gas. The range of the absorption coefficient of water vapor at any given geographical location and frequency is typically one order of magnitude, as will be seen in Chapter V. In the case of clouds, however, local variations in the distribution of particles, and the size of these particles can introduce variations in extinction which greatly exceed this range.

Clouds at microwave and far infrared wavelengths interact with the radiation field through scattering and absorption by individual particles. Since there are in general no coherent relationships between the individual particles, the effect of a large-scale ensemble is obtained by algebraic summation over their individual effects, assuming that the shadowing of one particle by another may be neglected.

To examine the effect of water and ice clouds upon radiative measurements we must therefore: (1) examine the interaction of individual water and ice particles with electromagnetic radiation over the spectral range of interest; (2) define a suitable set of particle

distributions representative of cloud types likely to be found over the earth; (3) obtain for each cloud distribution the unit-volume absorption, scattering and extinction properties; and (4) making use of the climatological distribution of the selected cloud types, determine their overall impact upon remote-sensing experiments. The first and second of these steps are the purpose of this Chapter, the third will be discussed in Chapter IV, and the last in Chapter VI.

An electromagnetic wave incident upon a material particle causes an interaction with the free and bound charges present within the material by subjecting them to a force due to the incident electric field. The charges, moving under the action of this force, generate new fields which propagate within the material or are carried away as outgoing radiation. The resulting electromagnetic field outside the particle consists of the vector superposition of the incident field and the re-radiated or "scattered" field. The result of this interaction is a redistribution of the incident energy in such a manner as to attenuate the forward traveling wave. This attenuation, or "extinction" actually consists of two parts: that which reappears as scattered radiation; and that which is absorbed due to the fact that the moving charges within the medium experience damping forces which transfer their mechanical energy to the surrounding medium. In addition, the medium itself emits thermal radiation characteristic of its equilibrium temperature.

The effect of a single particle upon the external field depends

critically upon the ratio of the particle size, r , to the wavelength, λ of the radiation. In the so-called "long-wavelength limit", this ratio is small, and the electromagnetic field is effectively uniform throughout the droplet. The motion of the constituent charges is, therefore, coherent throughout the droplet and the re-radiated field is that of an induced dipole oscillating at the frequency of the incident field. This limit is referred to as the "Rayleigh-scattering limit" due to the λ^4 dependence of the power radiated by an oscillating dipole.

At the opposite extreme lies the short-wavelength or "geometrical limit" for which $r \gg \lambda$. In this case, the motion of charges within the droplet is coherent only along a wavefront of the exciting radiation, and the secondary fields are propagated within the medium in such manner as to interfere destructively except at these points. The laws of reflection and refraction apply, and a ray of incident radiation is decomposed at each surface of the droplet into reflected and refracted rays which then constitute the "scattered" radiation.

Between these two extremes, the long and short-wavelengths limits, the electromagnetic fields are best regarded as super-positions of partial waves which represent, physically, the modes of excitation of the dielectric sphere. Thus, in the simplest case, corresponding to the long-wavelength limit, only the lowest order mode--the induced dipole--is significant. As the radius of the sphere is increased successively higher multipoles--quadropole, octupole, etc--become significant.

A. The Theory of Mie

The rigorous solution for the diffraction of a plan monochromatic wave by a homogeneous dielectric sphere of arbitrary radius was first obtained by G. Mie (1908), followed shortly by P. Debye (1909). The discussion which follows summarizes the more detailed development of the theory found in the literature (see for examples, Van de Hulst, 1957; Stratton, 1941; Born and Wolf, 1964).

Consider a uniform dielectric sphere of radius r and complex index of refraction \tilde{n} in the presence of a linearly polarized monochromatic plane wave with wave vector magnitude $k=2\pi/\lambda$ and electric field vector \vec{E}^i . The fields \vec{E} and \vec{H} observed at a distance $R \gg r$ from the sphere are:

$$\vec{E} = \begin{bmatrix} E_1 \\ E_2 \end{bmatrix} = \vec{E}^i + \underset{\sim}{S} \vec{E}^i \frac{\exp(ikR)}{ikR} \quad (3-1)$$

$$\vec{H} = \frac{i}{k} (\nabla \times \vec{H})$$

where E_1 and E_2 are the electric field vector components parallel and perpendicular to the plane scattering and $\underset{\sim}{S}$ is the scattering matrix

$$\underset{\sim}{S} = \begin{bmatrix} S_2 & 0 & 0 \\ 0 & S_1(\theta) \end{bmatrix} \quad (3-2)$$

whose elements $S_1(\theta)$ and $S_2(\theta)$ are given by

$$S_1(\theta) = \sum_{l=1}^{\infty} \frac{2l+1}{l(l+1)} \{ a_l \pi_l(\cos\theta) + b_l \tau_l(\cos\theta) \}$$

$$S_2(\theta) = \sum_{l=1}^{\infty} \frac{2l+1}{l(l+1)} \{ a_l \pi_l(\cos\theta) + b_l \pi_l(\cos\theta) \}$$

The solution takes the form of an expansion in multipole fields with the coefficients a_l and b_l for each multipole in the expansion determined

by the boundary and the angular dependence of each multipole expressed in the functions:

$$\pi_\ell(\cos\theta) = \frac{dp_\ell(\cos\theta)}{d\cos\theta} \quad (3-4)$$

$$\tau_\ell(\cos\theta) = \cos\theta \pi_\ell(\cos\theta) - \sin^2\theta \frac{d\pi_\ell(\cos\theta)}{d\cos\theta}$$

with $P_\ell(\cos\theta)$ the Legendre Polynomial of order of ℓ . The complex coefficients a_ℓ and b_ℓ in the expansion are:

$$\begin{aligned} a_\ell &= \frac{\psi'_\ell(\tilde{n}, \alpha) \psi_\ell(\alpha) - \tilde{n} \psi_\ell(\tilde{n}, \alpha) \psi'_\ell(\alpha)}{\psi'_\ell(\tilde{n}, \alpha) \zeta_\ell(\alpha) - \tilde{n} \psi_\ell(\tilde{n}, \alpha) \zeta'_\ell(\alpha)} \\ b_\ell &= \frac{\tilde{n} \psi'_\ell(\tilde{n}, \alpha) \psi_\ell(\alpha) - \psi_\ell(\tilde{n}, \alpha) \psi'_\ell(\alpha)}{\tilde{n} \psi'_\ell(\tilde{n}, \alpha) \zeta_\ell(\alpha) - \psi_\ell(\tilde{n}, \alpha) \zeta'_\ell(\alpha)} \end{aligned} \quad (3-5)$$

where the primes denote differentiation with respect to the argument and $\alpha = kr = 2\pi r/\lambda$. The Ricatti-Bessel functions $\psi_\ell(\alpha)$ and $\zeta_\ell(\alpha)$ are related to the spherical Bessel functions by:

$$\psi_\ell(\alpha) = \alpha j_\ell(\alpha) \quad (3-6)$$

$$\zeta_\ell(\alpha) = \alpha h_\ell^{(2)}(\alpha)$$

The Mie efficiency factors for scattering, extinction and absorption are defined as the ratio for the actual cross section to the geometrical cross section:

$$Q_j(\tilde{n}, \alpha) = \chi_j(\tilde{n}, \alpha) / \pi r^2 = S, A, E \quad (3-7)$$

and are expressed in terms of the coefficients a_ℓ and b_ℓ and the drop size parameter as:

$$\begin{aligned} Q_S &= \frac{2}{\alpha^2} \sum_{\ell=1}^{\infty} (2\ell+1) \{ |a_\ell(\tilde{n}, \alpha)|^2 + |b_\ell(\tilde{n}, \alpha)|^2 \} \\ Q_E &= \frac{2}{\alpha^2} \sum_{\ell=1}^{\infty} (2\ell+1) \operatorname{Re}\{a_\ell(\tilde{n}, \alpha) + b_\ell(\tilde{n}, \alpha)\} \end{aligned} \quad (3-8)$$

$$Q_A = Q_E - Q_S$$

where the primes denote differentiation with respect to the argument and $\alpha = kr = 2\pi r/\lambda$. The Ricatti- Bessel functions $\psi_\ell(\alpha)$ and $\zeta_\ell(\alpha)$ are related to the spherical Bessel functions by :

$$\psi_\ell(\alpha) = \alpha j_\ell(\alpha) \quad (3-6)$$

$$\zeta_\ell(\alpha) = \alpha h_\ell^{(2)}(\alpha)$$

The Mie efficiency factors for scattering, extinction and absorption are defined as the ratio of the actual cross section to the geometrical cross section:

$$Q_j(\tilde{n}, \alpha) = \chi_j(\tilde{n}, \alpha) / \pi r^2_j = S, A, E \quad (3-7)$$

and are expressed in terms of the coefficients a_ℓ and b_ℓ and the drop-size parameter α as:

$$\begin{aligned} Q_S &= \frac{2}{\alpha^2} \sum_{\ell=1}^{\infty} (2\ell+1) \{ |a_\ell(\tilde{n}, \alpha)|^2 + |b_\ell(\tilde{n}, \alpha)|^2 \} \\ Q_E &= \frac{2}{\alpha^2} \sum_{\ell=1}^{\infty} (2\ell+1) \operatorname{Re}\{a_\ell(\tilde{n}, \alpha) + b_\ell(\tilde{n}, \alpha)\} \\ Q_A &= Q_E - Q_S \end{aligned} \quad (3-8)$$

B. Dielectric Properties of Pure Water

From the foregoing discussion it is clear that the complex index of refraction must be known before the efficiency factors, and hence the cross sections for scattering and extinction may be determined. The polarizability of liquid water is the result of dipole rotation at microwave frequencies and to ionic and electronic interactions in the infrared and optical regions of the spectrum respectively. For this reason, the values of the real and imaginary parts of the complex index of refraction, shown in Figure III-1, vary appreciably over the range from 10 cm to 10 microns. The data used in the preparation of Figure III-1 (curve "A") is taken from the comprehensive literature survey of infrared properties of water and ice by Irvine and Pollack (1968) who present values from 1 to 200 microns. In the microwave region, the index of refraction due to dipole rotation is given

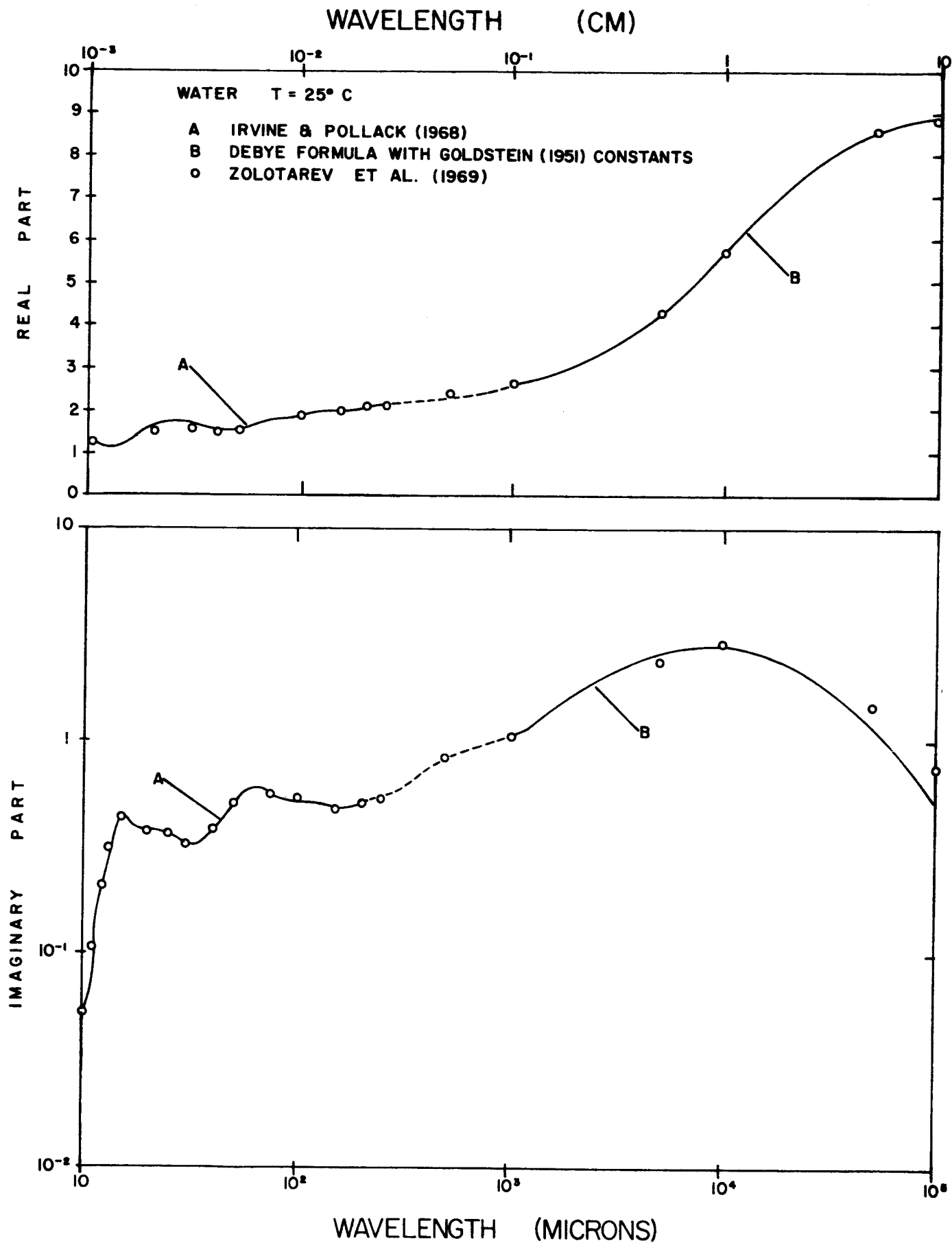


FIGURE III-1. Index of refraction for pure water, 10 μ to 10cm.

accurately by the Debye (1929) formula:

$$n^2 = \frac{\epsilon_0 \epsilon_\infty}{1 + i(\lambda_0/\lambda)} + \epsilon_\infty \quad (3-9)$$

where ϵ_0 and ϵ_∞ are the static and optical dielectric constants and λ_0 is the Debye relaxation wavelength, resulting from damping effect in the liquid. The real and imaginary parts of the index of refraction have been computed using the Debye formula together with the constants ϵ_0 , ϵ_∞ , λ_0 given for pure water as a function of temperature by Goldstein (1951) and are shown in Figure III-1 as curve "B". Also shown for comparison in Figure III-1 are recent data of Zolotarev et. al. (1969) who tabulate the index of refraction of water from 1 micron to 1 meter, at 25°C.

The strong temperature dependence of the microwave properties of cloud particles may be seen in Figure III-2, in which the Debye formula has been used, together with the Goldstein constants to compute the real and imaginary parts of the index of refraction over the range from 1 to 300 GHz for several temperatures from 273°K to 313°K. The temperature dependence of the real part is a maximum in the range from 10 to 100 GHz, while for the imaginary part the temperature dependence is a minimum in this same interval. Note that for frequencies less than 10 GHz, the imaginary part decreases by almost an order of magnitude

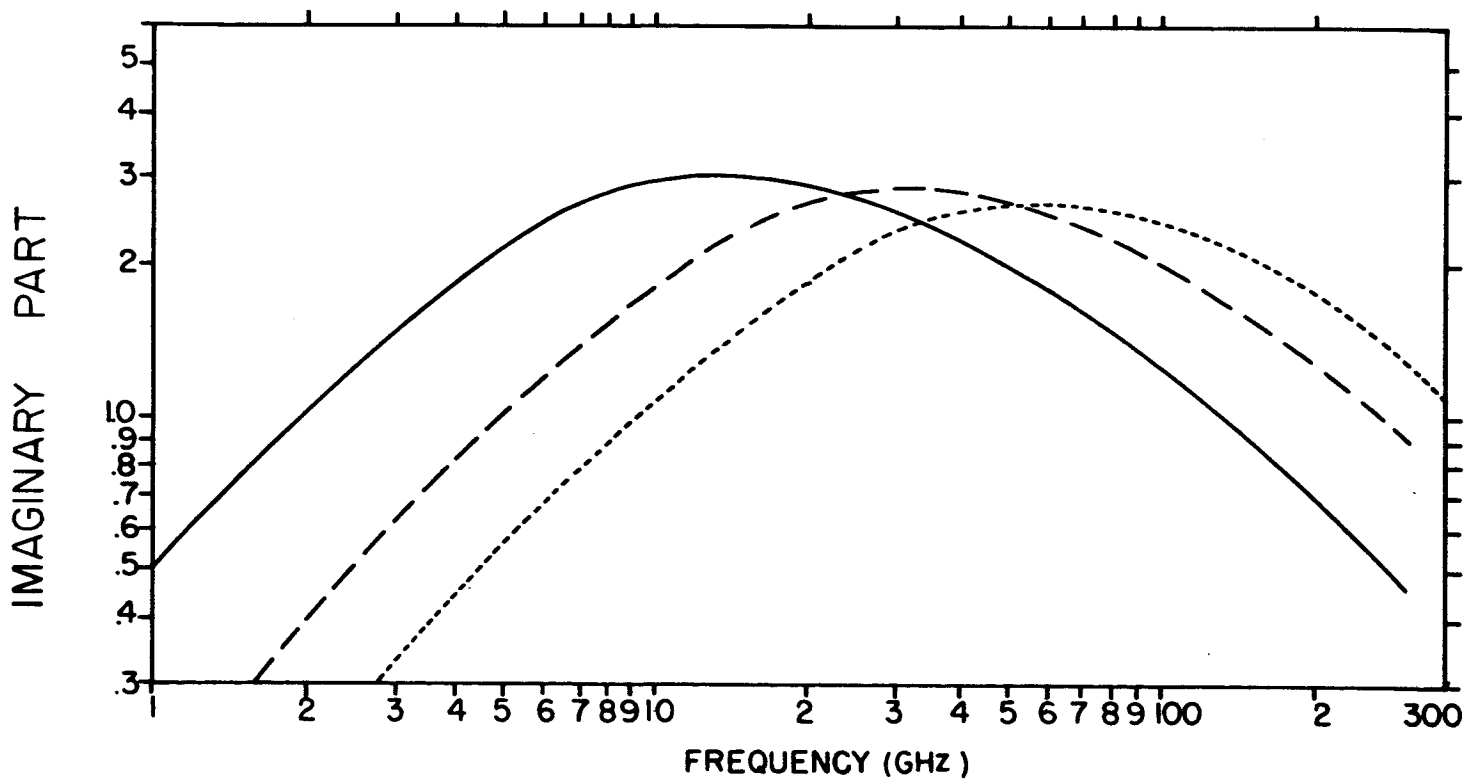
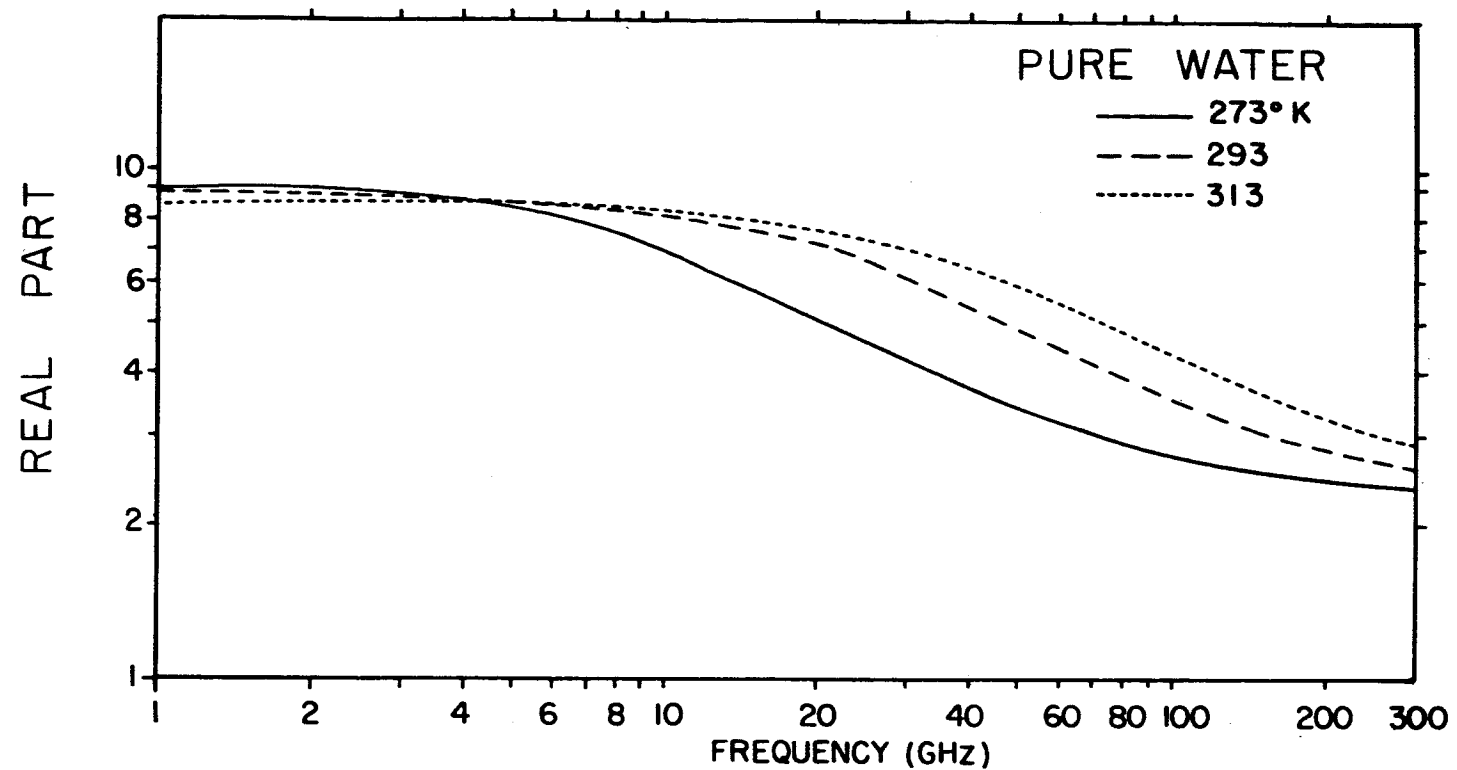


FIGURE III-2. Index of refraction for pure water, 1 GHz to 300 GHz.

over this temperature range. Above 100 GHz, a direct variation of approximately half an order of magnitude occurs.

C. Mie Efficiency Factors Water, 10 μ to 10 cm

The Mie efficiency factors for scattering and extinction by pure water have been computed as a function of drop radius for 9 wavelengths in the range from 10 microns to 10 cm, and are shown in Figs III-3 through III-11. The index of refraction data used are those of Zolotarev et. al. (1969). For each wavelength, the efficiency factors were computed over a range of drop-size parameters α from 0.01 to 50.0, to demonstrate in each case the drop sizes for which the long and short wavelength limits are appropriate, respectively. The former "Rayleigh" limit is of particular interest in the present application; since it is in this limit that scattering may be neglected and clouds treated as purely absorbing media. In the Rayleigh limit, $\alpha \ll 1$ the efficiency factors Q_S and Q_E of Eq. 3-8 take the form

$$\begin{aligned} Q_S &= \frac{8\alpha^4}{3} |K|^2 + \dots \\ Q_E &= 4\alpha \operatorname{Im}\{-K\} + \frac{8\alpha^4}{3} |K|^2 + \dots \quad (3-10) \\ Q_A &= 4\alpha \operatorname{Im}\{-K\} + \dots \end{aligned}$$

$$\text{where} \quad K = \frac{n^2 - 1}{n^2 + 2} \quad (3-11)$$

WATER AT 298. K, DATA FROM ZOLATAREV ET AL (1969)

LAMDA= 1.00000E 01 CM, ETA= 8.856-0.740 I, PRECISION= 1.000E-04

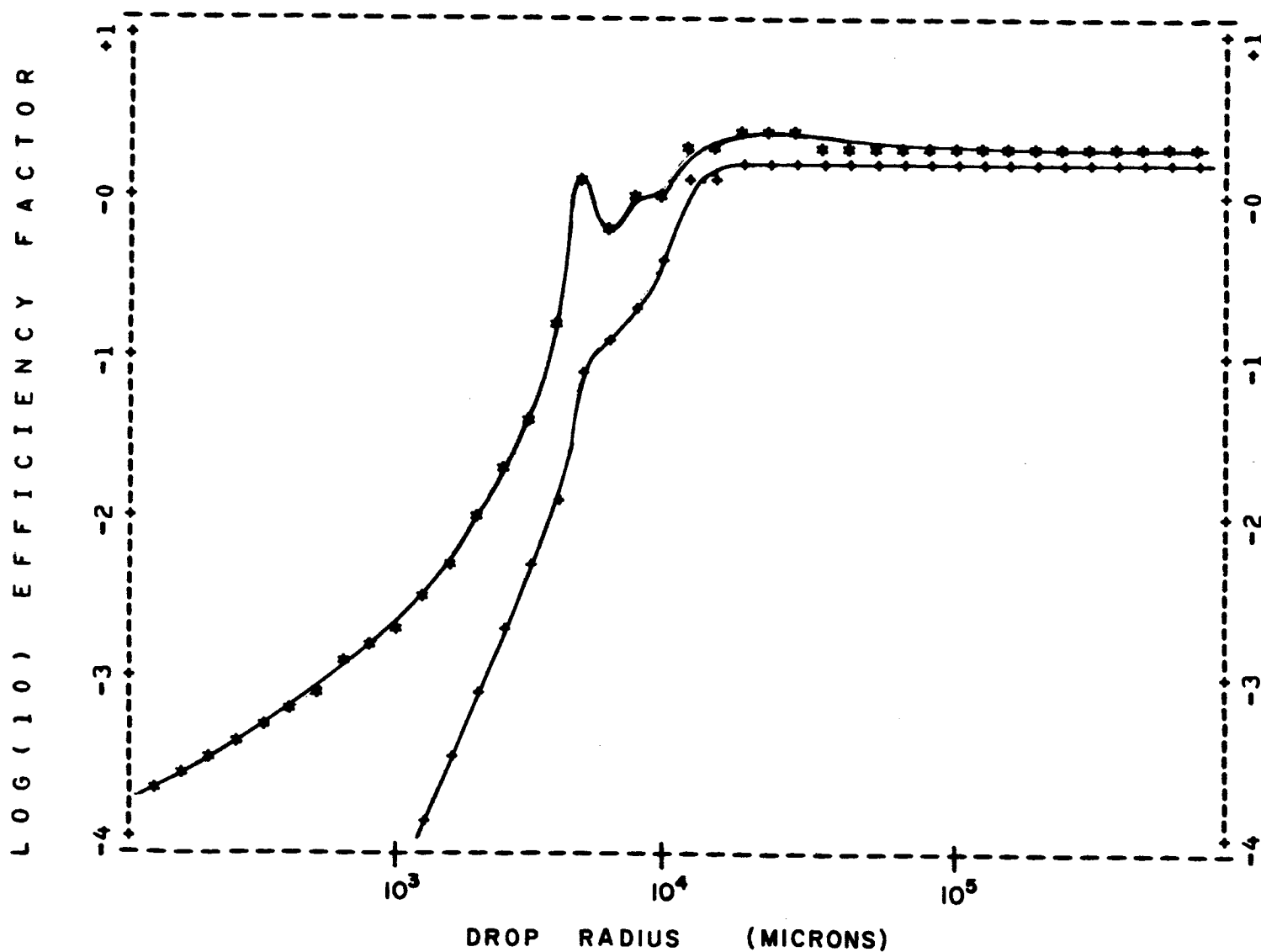


Figure III-3. Mie efficiency factors for scattering and extinction by pure water droplets at 10 cm.

WATER AT 298. K, DATA FROM ZOLATAREV ET AL (1969)

LAMDA= 5.00000E 00 CM, ETA= 8.553-1.480 I, PRECISION= 1.000E-04

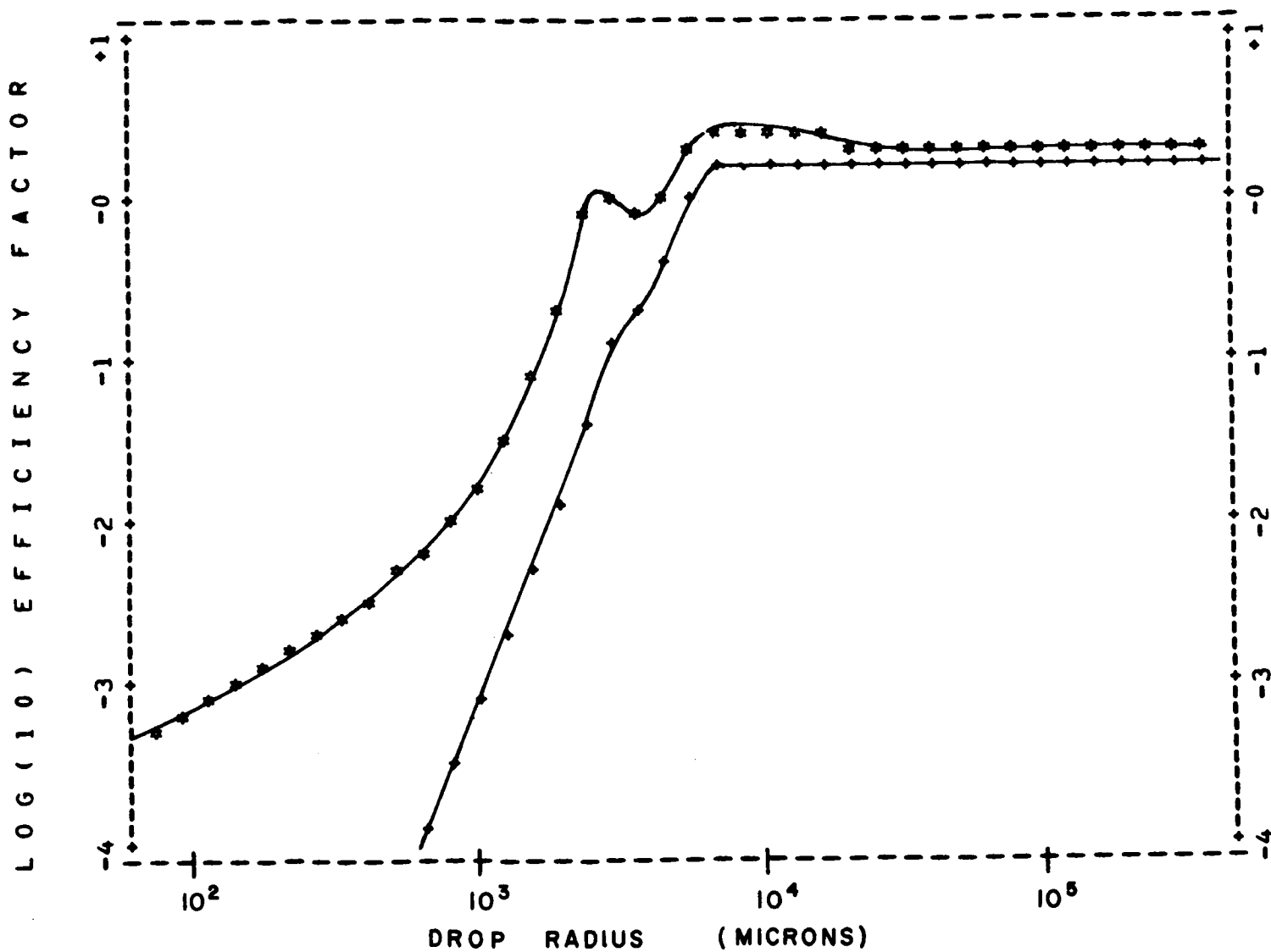


Figure III-4. Mie efficiency factors for scattering and extinction by pure water droplets at 5 cm.

WATER AT 298. K, DATA FROM ZOLATAREV ET AL (1969)

LAMDA= 1.00000E 00 CM, ETA= 5.697-2.900 I, PRECISION= 1.000E-04

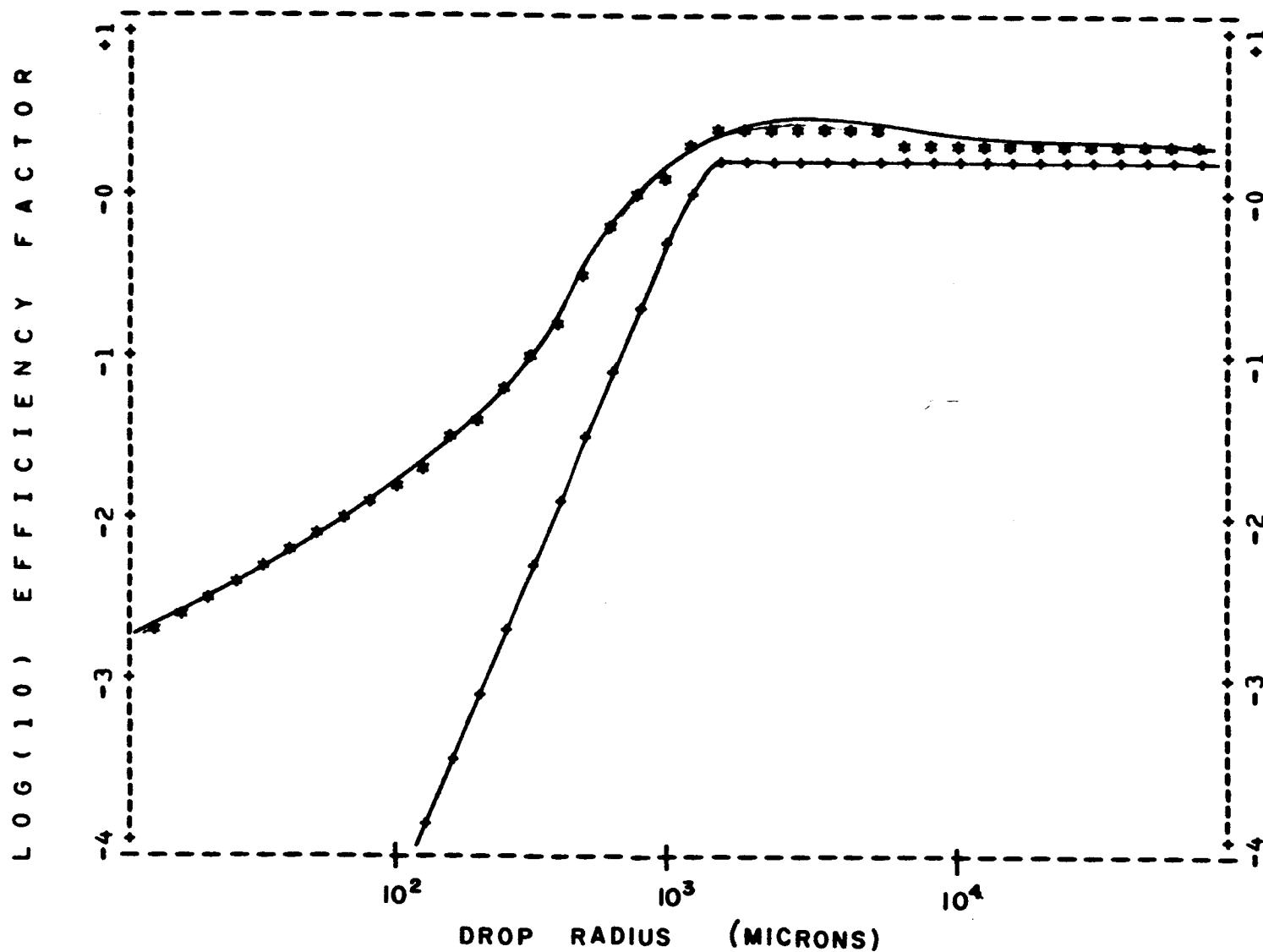


Figure III-5. Mie efficiency factors for scattering and extinction by pure water droplets at 1 cm.

WATER AT 298. K, DATA FROM ZOLATAREV ET AL (1969)

LAMDA= 5.00000E-01 CM, ETA= 4.162-2.330 I, PRECISION= 1.000E-04

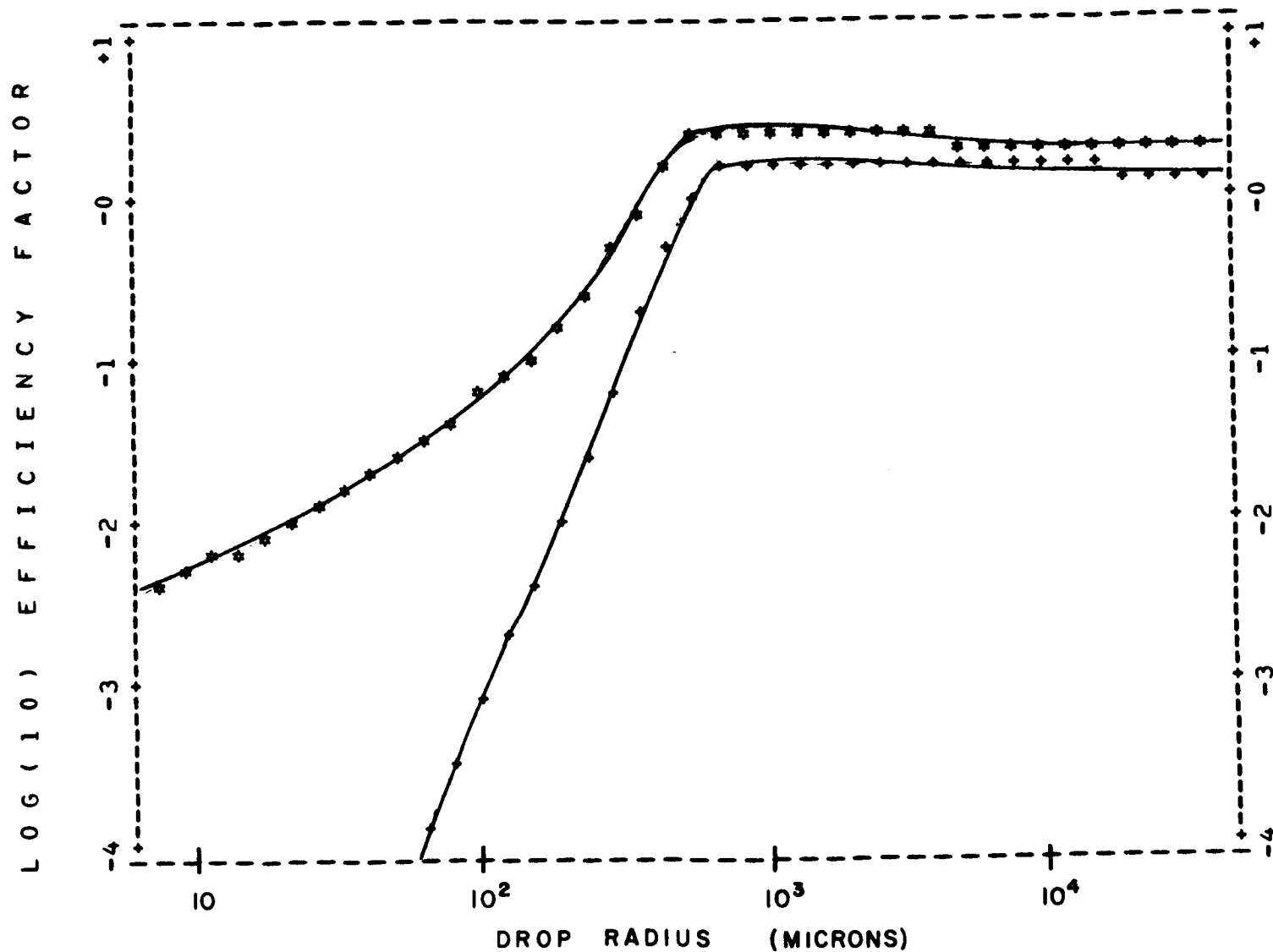


Figure III-6. Mie efficiency factors for scattering and extinction by pure water droplets at 5 mm.

WATER AT 298. K, DATA FROM ZOLATAREV ET AL (1969)

LAMDA= 1.00000E-01 CM. ETA= 2.663-1.020 I, PRECISION= 1.000E-04

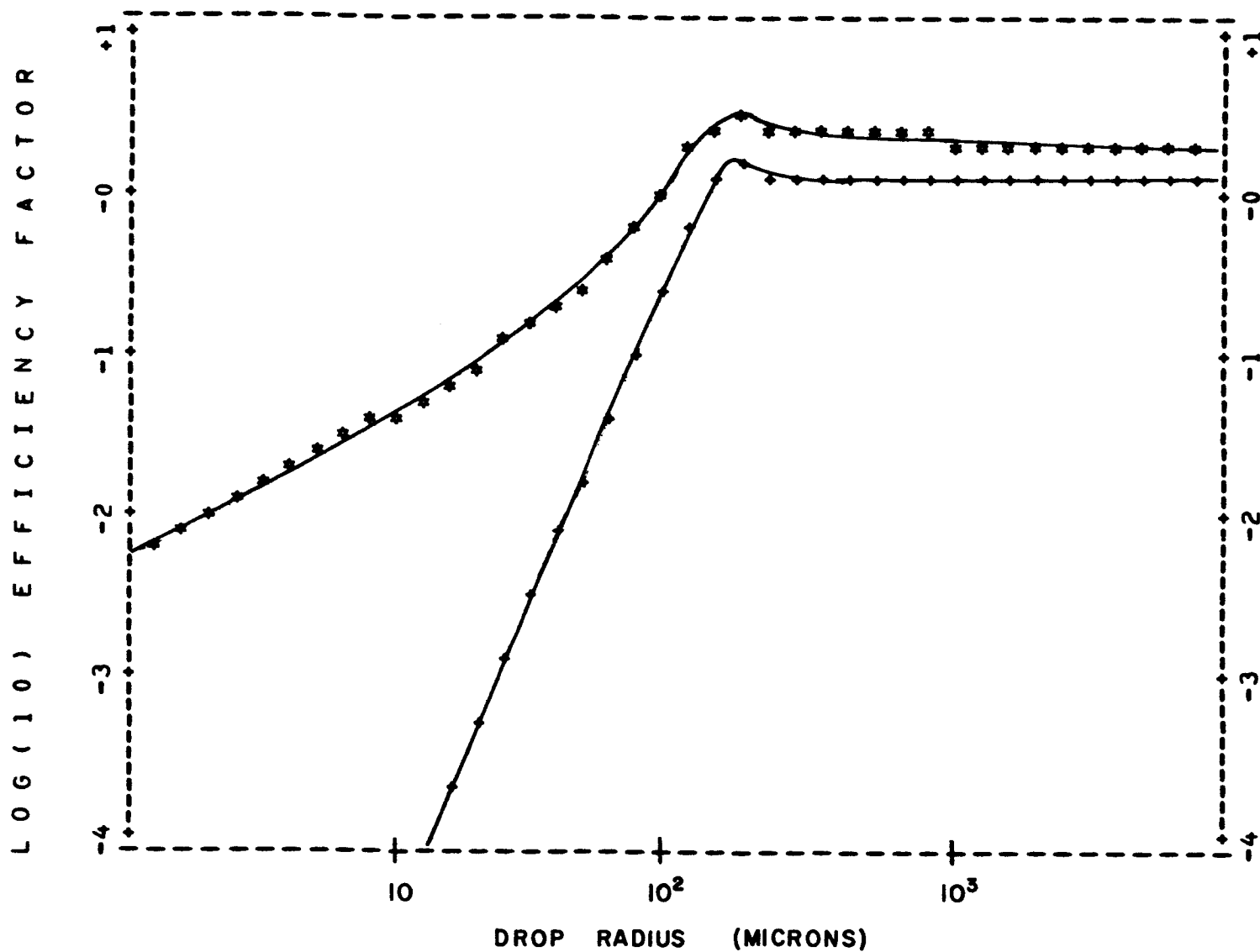


Figure III-7. Mie efficiency factors for scattering and extinction by pure water droplets at 1 mm.

WATER AT 298. K, DATA FROM ZOLATAREV ET AL (1969)

LAMDA= 5.00000E-02 CM, ETA= 2.409-0.740 I, PRECISION= 1.000E-04

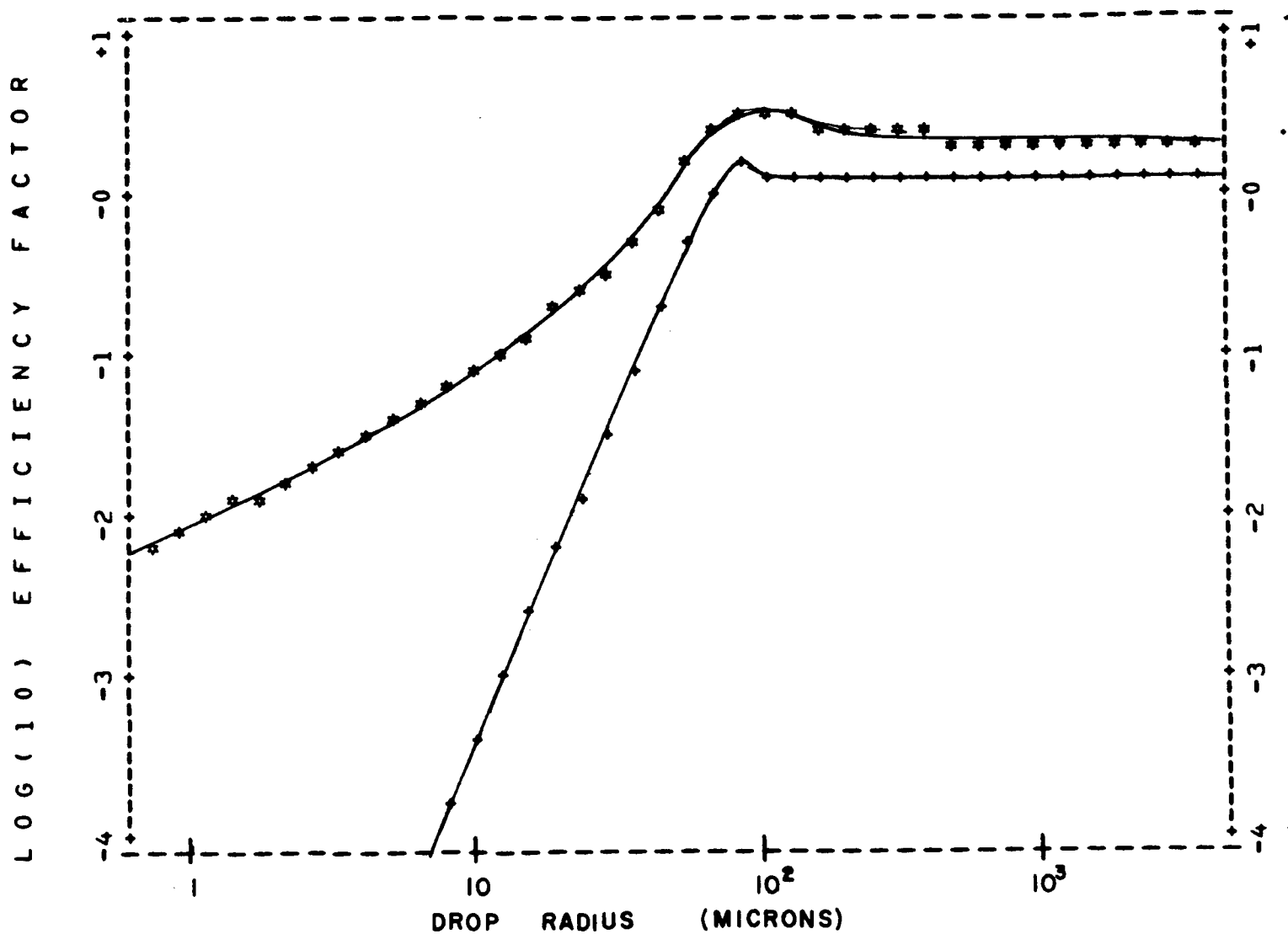


Figure III-8. Mie efficiency factors for scattering and extinction by pure water droplets at 500 microns.

WATER AT 298. K, DATA FROM ZOLATAREV ET AL (1969)

LAMDA= 1.00000E-02 CM, ETA= 1.986-0.527 I, PRECISION= 1.000E-04

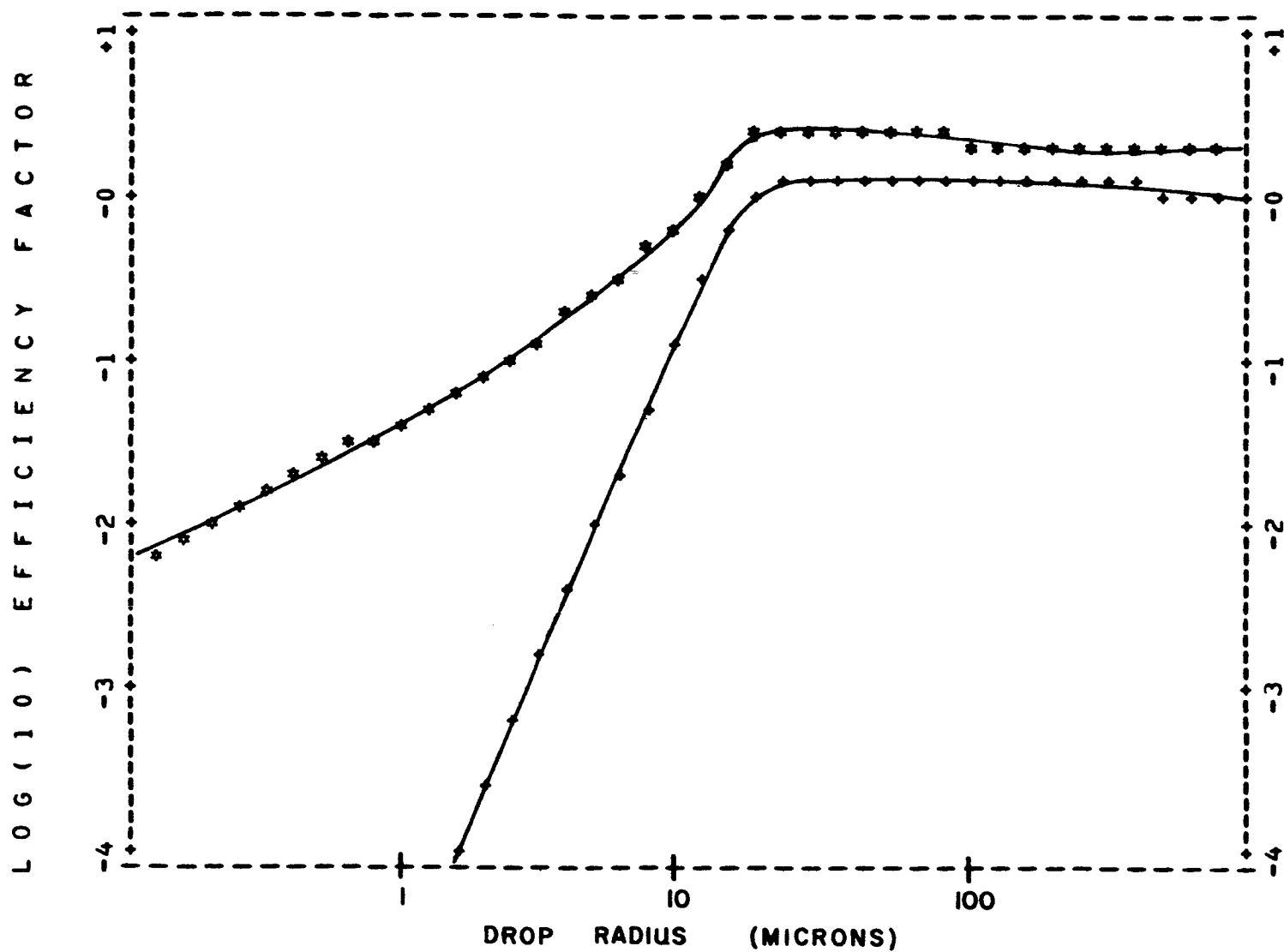


Figure III-9. Mie efficiency factors for scattering and extinction by pure water droplets at 100 microns.

WATER AT 298. K, DATA FROM ZOLATAREV ET AL (1969)

LAMDA= 5.00000E-03 CM, ETA= 1.582-0.503 I, PRECISION= 1.000E-04

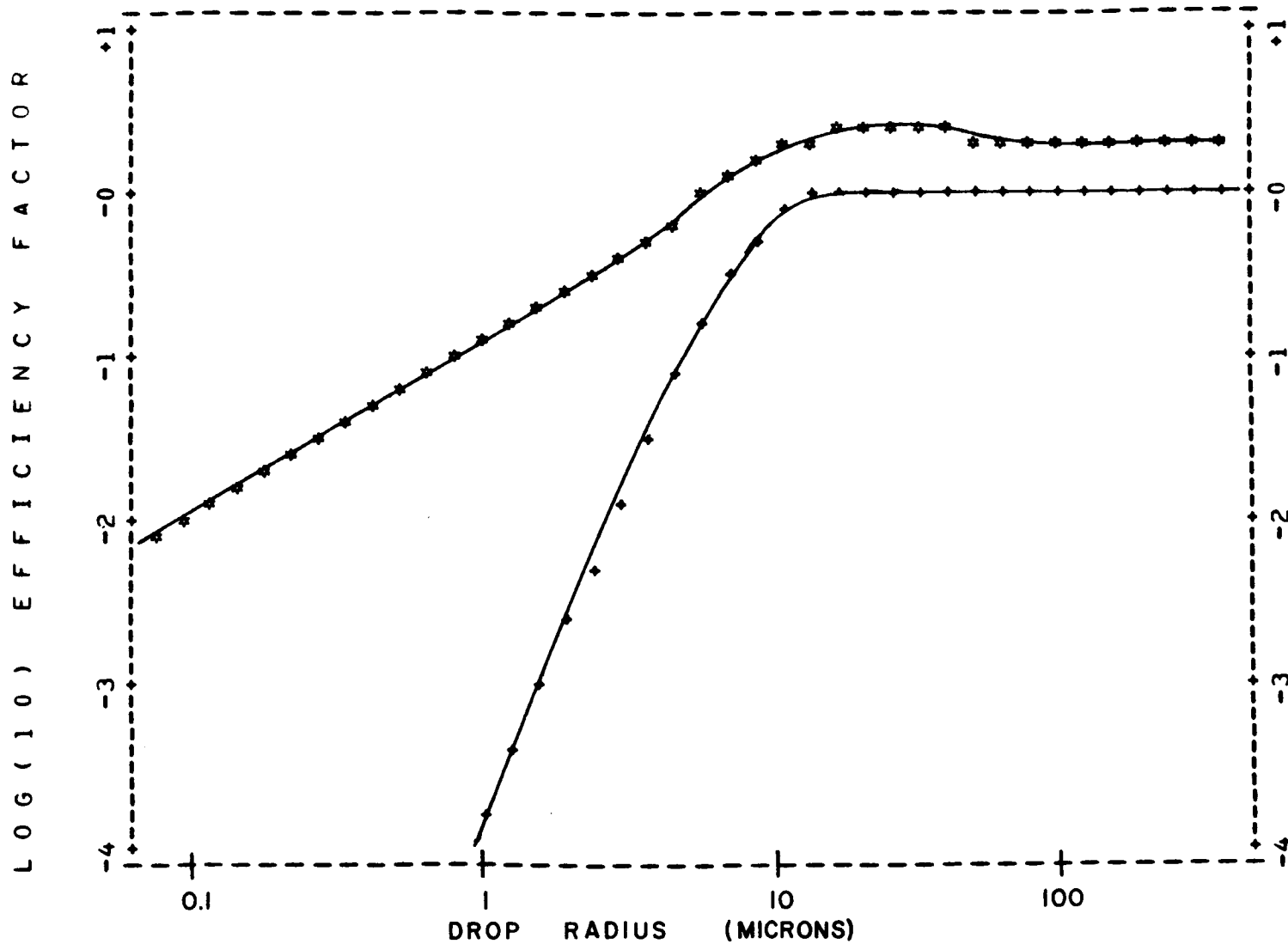


Figure III-10. Mie efficiency factors for scattering and extinction by pure water droplets at 50 microns.

WATER AT 298. K, DATA FROM ZOLATAREV ET AL (1969)

LAMDA= 1.00000E-03 CM, ETA= 1.208-0.054 I, PRECISION= 1.000E-04

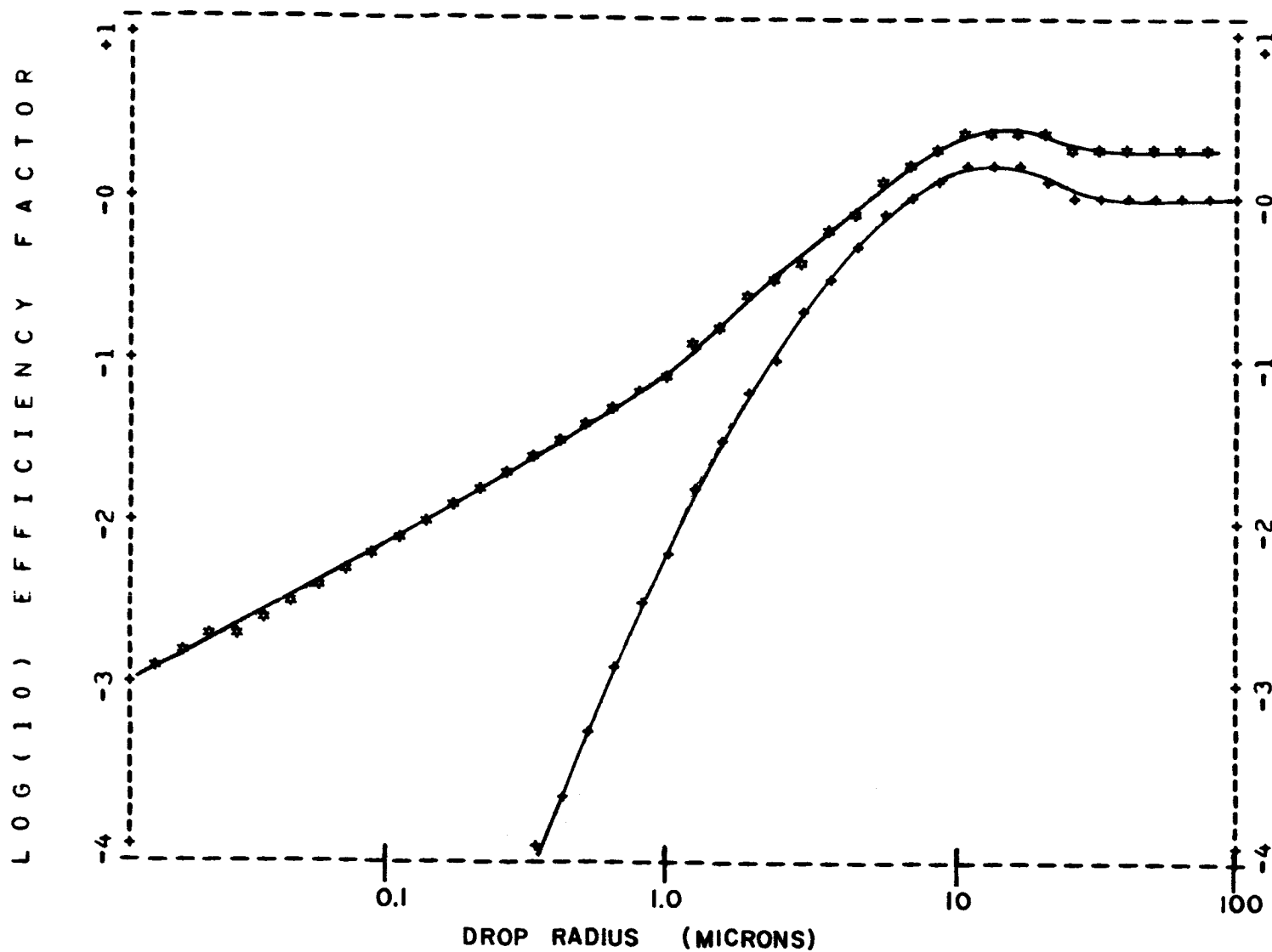


Figure III-11. Mie efficiency factors for scattering and extinction by pure water droplets at 10 microns.

Examination of Figures III-3 through III-11 indicate that there exists at each wavelength a range of drop sizes for which the extinction factor Q_E is linear in the drop radius, i.e., for which the extinction is given accurately by the Rayleigh limit of Eq. 3-10. Two conclusions may be drawn from these results:

(1) In the Rayleigh limit, the ratio of the scattering to the total extinction cross sections χ_S/χ_E is proportional to $(r/\lambda)^3$, neglecting the wavelength dependence of K .

(2) In the Rayleigh limit the extinction cross section χ_E for a spherical droplet is proportional to r^3 and hence simply to the volume (or mass) of the droplet. The total extinction coefficient due to an ensemble of droplets is, therefore, simply proportional to the total mass of the drop ensemble, and independent of the drop size distribution.

At the short wavelength limit, also apparent in Figures III-3 through III-11, both Q_E and Q_S approach constant values, although they continue to exhibit oscillations which show up when studied to higher resolution in drop size parameter than used for the present calculations. In the limit $\alpha \rightarrow \infty$, the efficiency factor for extinction $Q_E \rightarrow 2$, corresponding to a cross section of twice the geometrical cross section of the droplet. This result is due to equal contributions, to the total extinction, of energy intercepted by the geometrical cross section and energy diffracted at the edge of the geometrical shadow.

The behavior of Q_S as $\alpha \rightarrow \infty$ is fairly complicated, and is strongly dependent upon the real and imaginary parts of the complex index of refraction. A detailed discussion of the asymptotic behavior of both Q_E and Q_S is given in Plass (1966). For the purposes of the present study, we assume that the values applicable to the regime $\alpha > 50$ are those computed for $\alpha = 50$.

D. Single-Particle Properties of Ice from 10μ to 10 cm .

The analysis of the single-particle interaction of ice particles with electromagnetic energy is complicated by the non-spherical shape of ice crystals. They exist in several forms, making solution of the field equations in terms of normal modes of oscillation of the particle possible only for special cases. Ice crystals found in cirrus clouds have been found by sampling techniques (Blau, et al., 1966; Hall, 1968) to be largely made up of prismatic columns 100 to 200 μ in length with hexagonal bases of order 30 to 50 μ . It is clear that the effect of cirrus clouds becomes highly important as one moves into the infrared, in which the ratio of a characteristic dimension, i.e. 30 μ becomes large. Since the lack of uniformity in ice crystal distributions is substantial, the effect of the irregularity of individual particle shapes becomes relatively less important, so that in practice an ensemble of spherical ice particles is used for computation purposes.

E. Dielectric Properties of Ice

At the present time, values for the index of refraction of ice covering much of the spectral range of interest are not available. The existing data for the infrared region to 200 microns have been assembled and reviewed by Irvine and Pollack (1968) and are shown in Fig. III-12 as curve "A". For the microwave region from 1 to 10 cm, the value of Herman et al, (1961) has been shown as curve "B". Between these two regions reliable published data on the index of refraction appears to be lacking. Furthermore, the data represent values at temperatures ranging from 0° C to -30° C, and information required for the examination of the temperature dependence incomplete. The index of refraction of ice over the region of interest is due to ionic and electronic polarizability, with dipole rotation occurring only at wavelengths in excess of 1 kilometer (Debye, 1929). The resulting real and imaginary parts of the index of refraction exhibit substantial variations particularly in the vicinity of the absorption bands.

F. Mie Efficiency Factors for Ice, 10 μ to 10 cm

The Mie efficiency factors for scattering and extinction have been calculated at 3 wavelengths, and are shown in Figs. III-13 through III-15, using the values of Irvine and Pollack (1968) for the index of refraction at 10 and 100 μ , and that of Herman, et al.

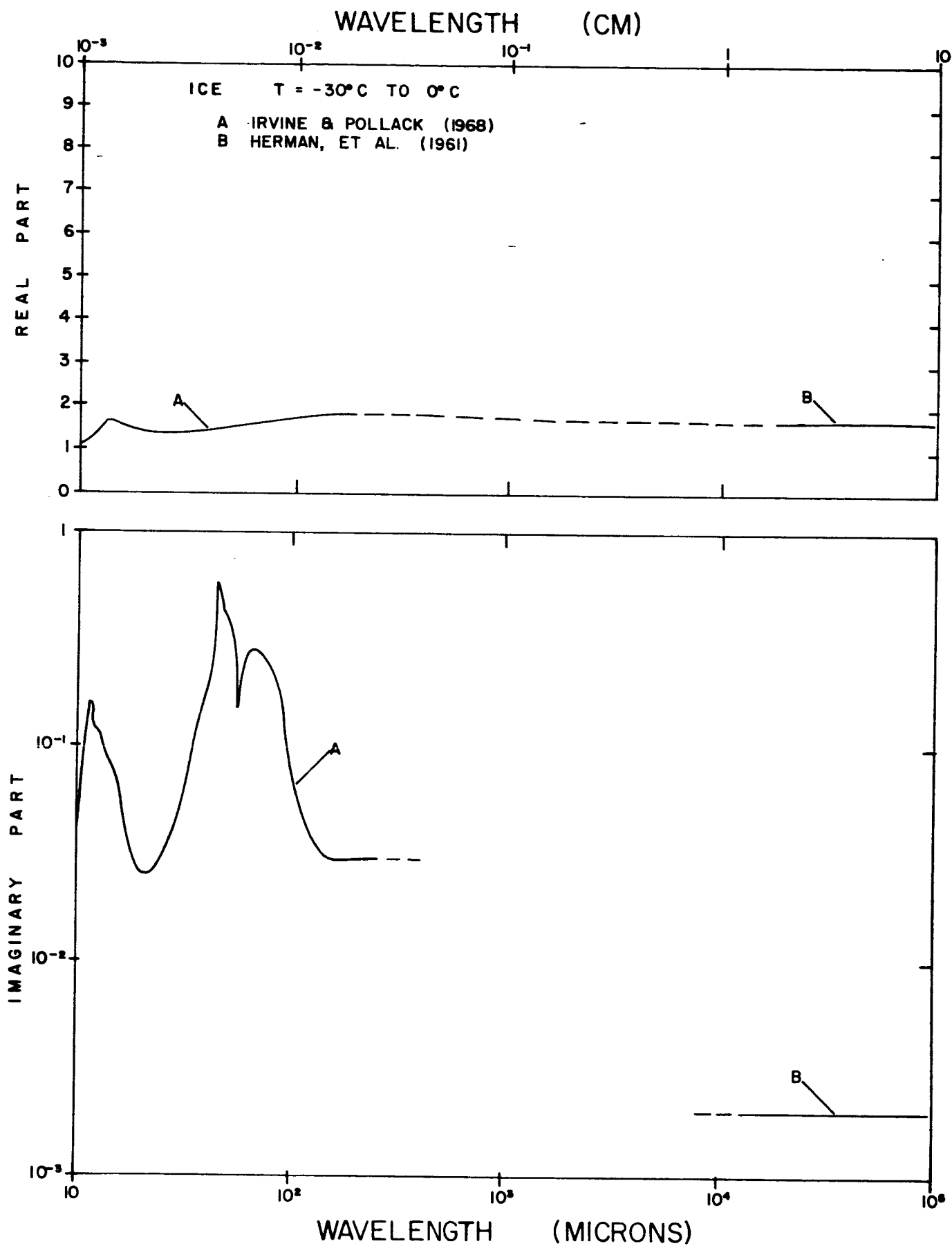


FIGURE III-12. Index of refraction for Ice, 10μ to 10cm .

ICE AT 0 DEG C, 1 TO 10 CM

LAMDA= 1.00000E 00 CM, ETA= 1.780-0.002 I, PRECISION= 1.000E-04

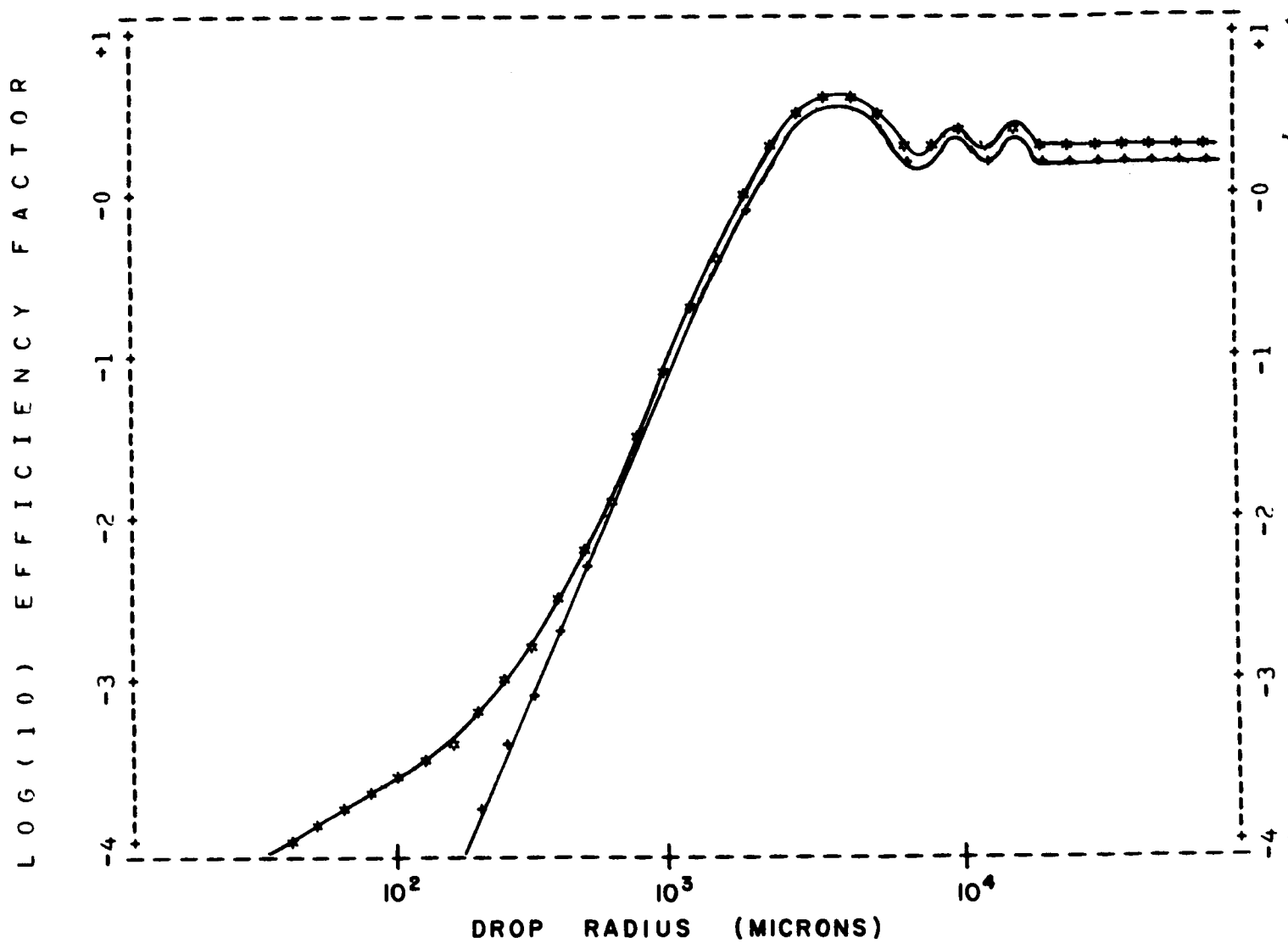


Figure III-13. Mie efficiency factors for scattering and extinction by ice particles at 1 cm.

ICE AT 0 DEG C, 3000 GHZ (100 MICRONS)

LAMDA= 1.00000E-02 CM, FTA= 1.650-0.080 I, PRECISION= 1.000E-04

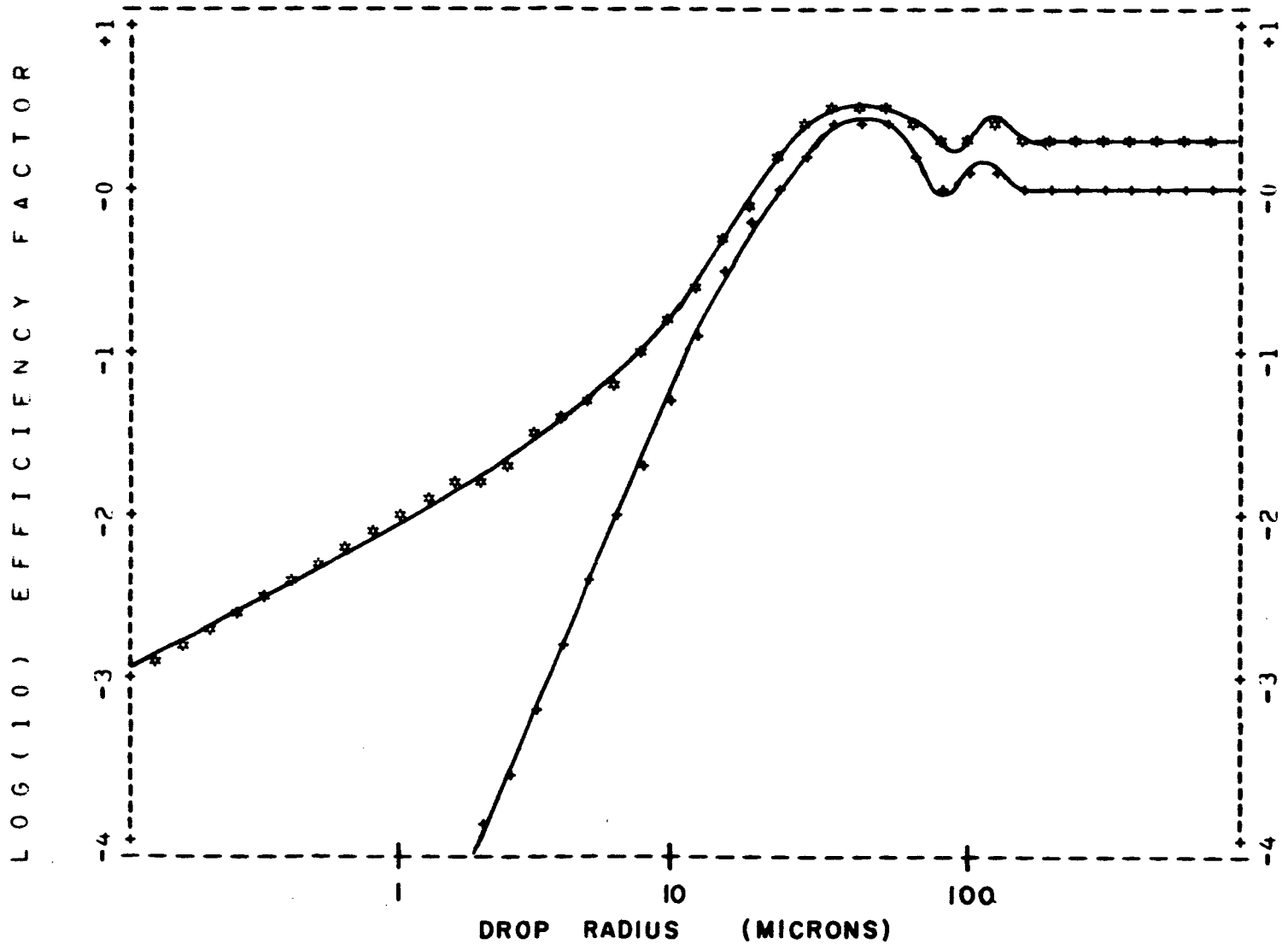


Figure III-14. Mie efficiency factors for scattering and extinction by ice particles at 100 microns.

ICE AT 0 DEG C, 30000 GHZ (10 MICRONS)

LAMDA= 1.00000E-03 CM, ETA= 1.152-0.041 I, PRECISION= 1.000F-04

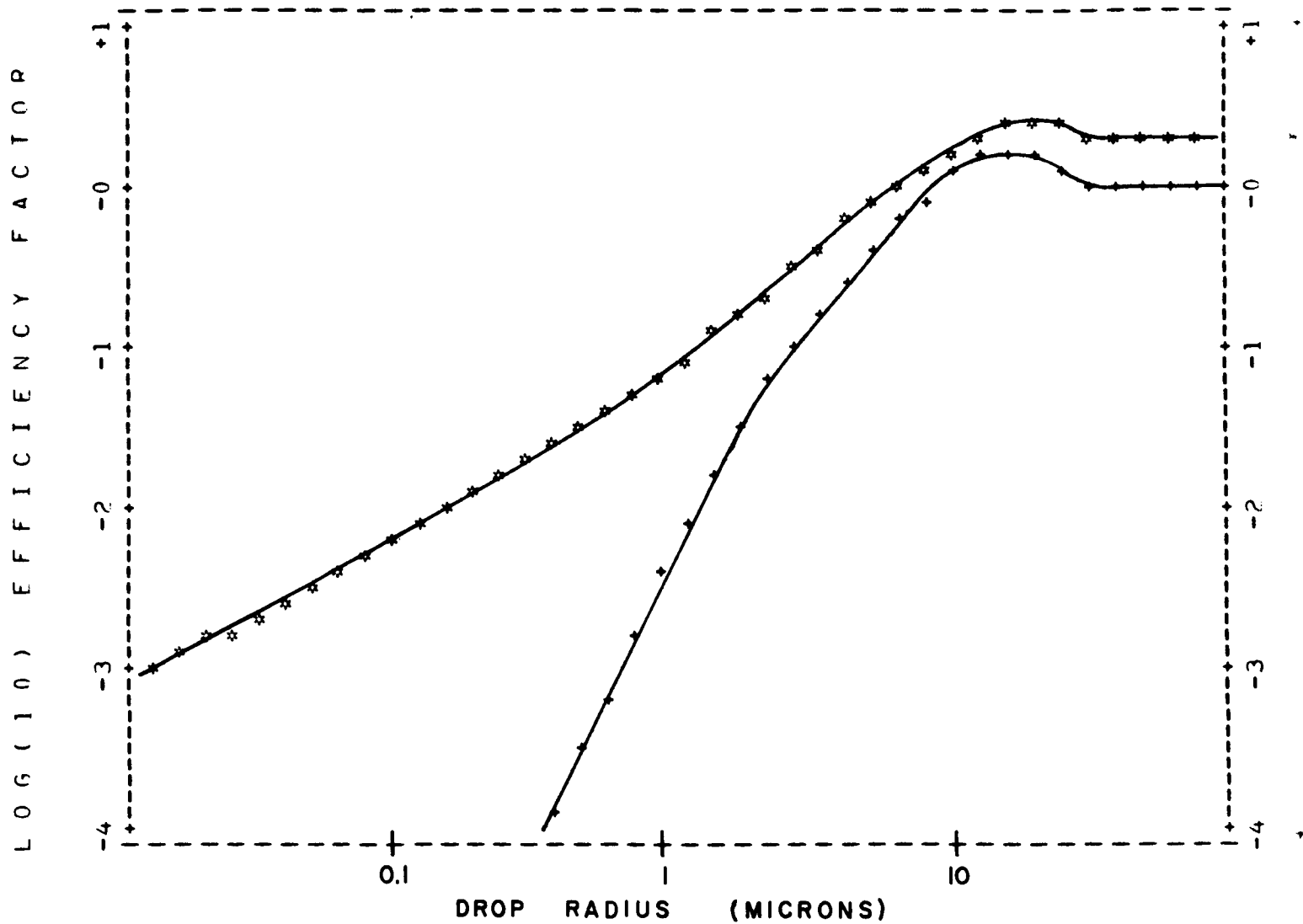


Figure III-15. Mie efficiency factors for scattering and extinction by ice particles at 10 microns.

(1961) for 1 cm. As in the case of water, the range of drop size parameters is 0.01 to 50, demonstrating both the long and short wavelength limits respectively. It is interesting to note the relatively high contribution of scattering to the total extinction cross section of ice particles in the microwave region, which is a result of the low imaginary part of the index of refraction. From Eq. 3-10 it is apparent that, even in the Rayleigh limit, scattering can become important relative to absorption if $\text{Im}\{-K\} \rightarrow 0$.

G. Unit Volume Radiative Transfer Properties of Water and Ice Clouds

The extent to which a particular cloud type affects the propagation of electromagnetic radiation within a spatially localized region depends upon the scattering, extinction and absorption coefficients, given by:

$$\begin{aligned} \gamma_j(\tilde{n}, \lambda) &= \int_{\mathbf{r}} N(\mathbf{r}) \chi_j(\tilde{n}, \lambda, \mathbf{r}) d\mathbf{r} \quad \text{neper cm}^{-1} \\ \text{with } N_T &= \int_{\mathbf{r}} N(\mathbf{r}) d\mathbf{r} \quad \text{cm}^{-3} \end{aligned} \quad (3-12)$$

where χ_j is the single-drop cross section ($j = S, A, E$) as given above and $N(\mathbf{r})$ the number of drops per cm^3 in the radius range from r to $r + dr$, with N_T the total number density at the point in the medium. Two additional parameters of interest are the single scattering albedo and the penetration depth for single scattering. The single-

scattering albedo is defined as the ratio of the scattering to total extinction coefficients:

$$\omega_0 = \gamma_S(\hat{n}, \lambda) / \gamma_E(\hat{n}, \lambda) \quad (3-13)$$

and is a measure of the fraction of energy removed from the incident radiation field due to scattering. The penetration depth for single scattering, as used in the present study, is defined as 10% of a mean free path for single scattering:

$$d_S = \frac{0.1}{\gamma_S} \quad (3-14)$$

It represents the distance in which the probability of a scattering event is less than 10%, or within which the assumption of a purely absorbing medium introduces an error of $\lesssim 10\%$. The penetration distance is of particular interest in relating the unit-volume properties of an assumed distribution of cloud droplets to their over-all effect upon radiative transfer within a cloud of a given scale size.

H. Absorption by Clouds in the Rayleigh Limit

It has already been observed that in the Rayleigh limit, the single-drop cross sections for extinction and absorption are dependent only upon the mass of the droplet. Hence, Eq. 4-1 takes the simple form

$$\gamma_E \approx \gamma_A = m F(\lambda, T) \quad (3-15)$$

where m is the mass density of the ensemble and f is a function of the wavelength and temperature. The function f has been determined empirically for water clouds by Staelin (1966) using constants from Goldstein (1951) with the result that the extinction coefficient applicable to clouds in the Rayleigh limit is given by

$$\gamma_{\text{cloud}} = \frac{4.35 \, m \, 10^{\{0.0122(291-T)-1\}}}{\lambda^2} \, \text{dB km}^{-1} \quad (3-16)$$

in which T is the absolute temperature in $^{\circ}\text{K}$, m the mass density in gm m^{-3} , and λ the wavelength in cm. Values for the absorption coefficient as given by the Staelin formula are presented as a function of frequency in Fig. III-16 for several temperatures ranging from -30°C to $+40^{\circ}\text{C}$.

A similar approach may be applied to ice, making use of tabulated data of Atlas et al. (1965) for absorption by ice clouds in the Rayleigh limit, for temperatures ranging from 0° to -20°C . These data are shown in Fig. III-17. A useful empirical relation which fits the data over the range 0° to -20° to within about 5% is given by:

$$\gamma_{\text{ICE}} = \frac{m \, 10^{-\{2.11 + 0.145(273-T)^{0.5}\}}}{\lambda} \, \text{dB km}^{-1} \quad (3-17)$$

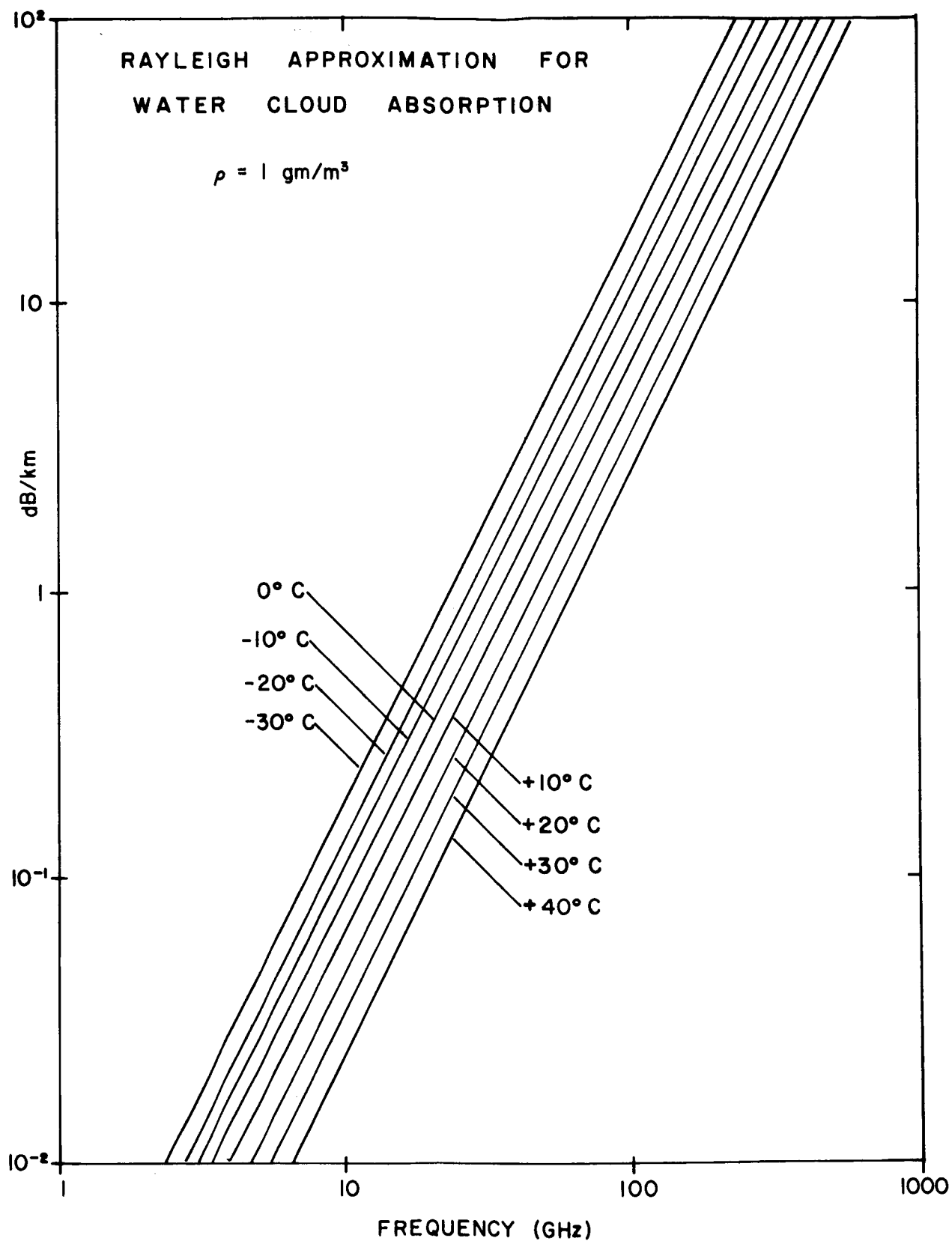


Figure III-16. Microwave absorption by water clouds from 1 to 1000 GHz as given by the Rayleigh approximation formula of Staelin (1966).

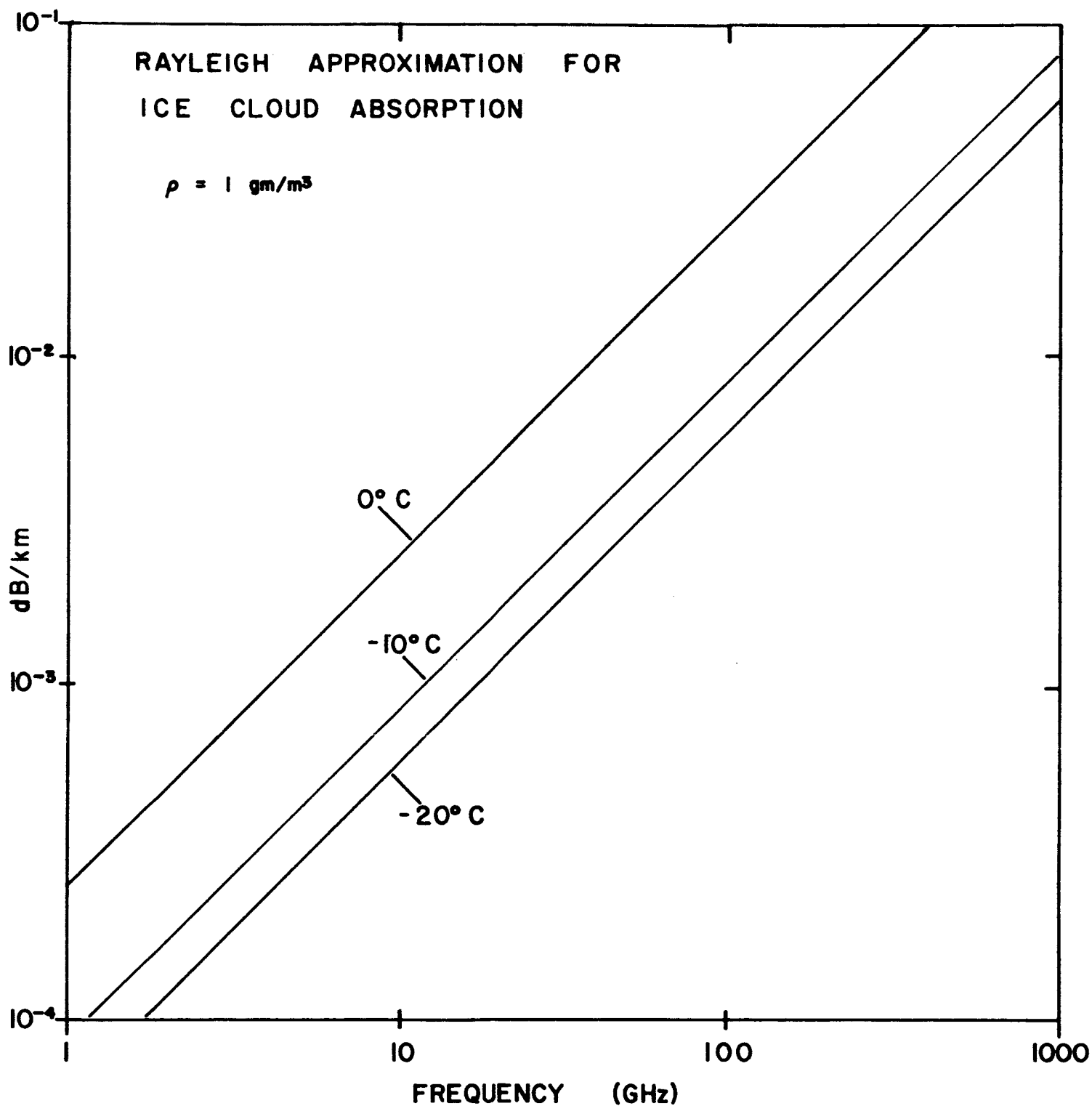


Figure III-17. Microwave absorption by ice clouds from 1 to 1000 GHz as given by tabulated data of Atlas et al. (1965).

Comparison of Eqs. 3-16 and 3-17 demonstrates the (λ^{-2}) dependence of water-cloud absorption by clouds in the microwave region, and the (λ^{-1}) dependence of ice-cloud absorption. This latter dependence results from the fact that the index of refraction for ice is constant over the microwave whereas for water it is not (see Eq. 3-10). Another noteworthy point is the temperature dependence, which is direct in the case of ice, but inverted in the case of water.

We shall examine the validity of the Rayleigh approximation further after discussion of the computational models used to describe the atmosphere and clouds, in Chapter IV.

IV. RADIATIVE TRANSFER PROPERTIES OF CLOUDS FROM 10 CM TO 10 μ

A. Modeling Procedure for Atmospheric Variables

The formal relation which describes the passage of radiation through a material medium is the equation of radiative transfer. For the purpose of simulating microwave signals received by a radiometer sensing the terrestrial environment, a numerical model is needed which solves the equation of radiative transfer at every point along the line of sight, for a medium characteristic of real atmospheric, cloud-cover and surface conditions. The purpose of this chapter is to discuss the algorithm used in the computation and the models used for representation of the clear atmosphere and for representative cloud-cover conditions.

The geometry applicable to the numerical solution of the equation of radiative transfer is shown in Figure IV-1. The atmosphere is assumed to be made up of plane layers each of which contains a uniform density of water vapor, oxygen, and liquid water at a uniform temperature and pressure. The model atmosphere is constructed by first using a set of values for temperature, pressure and water vapor density T_{atm_i} , P_i , and ρ_i corresponding to a set of N levels of altitude z_i , $i = 1, \dots, N$. Cloud layers are modeled by inserting levels corresponding to the base and top of each cloud layer, and interpolating the values of T_{atm} , P , and ρ to obtain values of these variables appropriate to the inserted levels. The liquid water density M_i for each level within the cloud

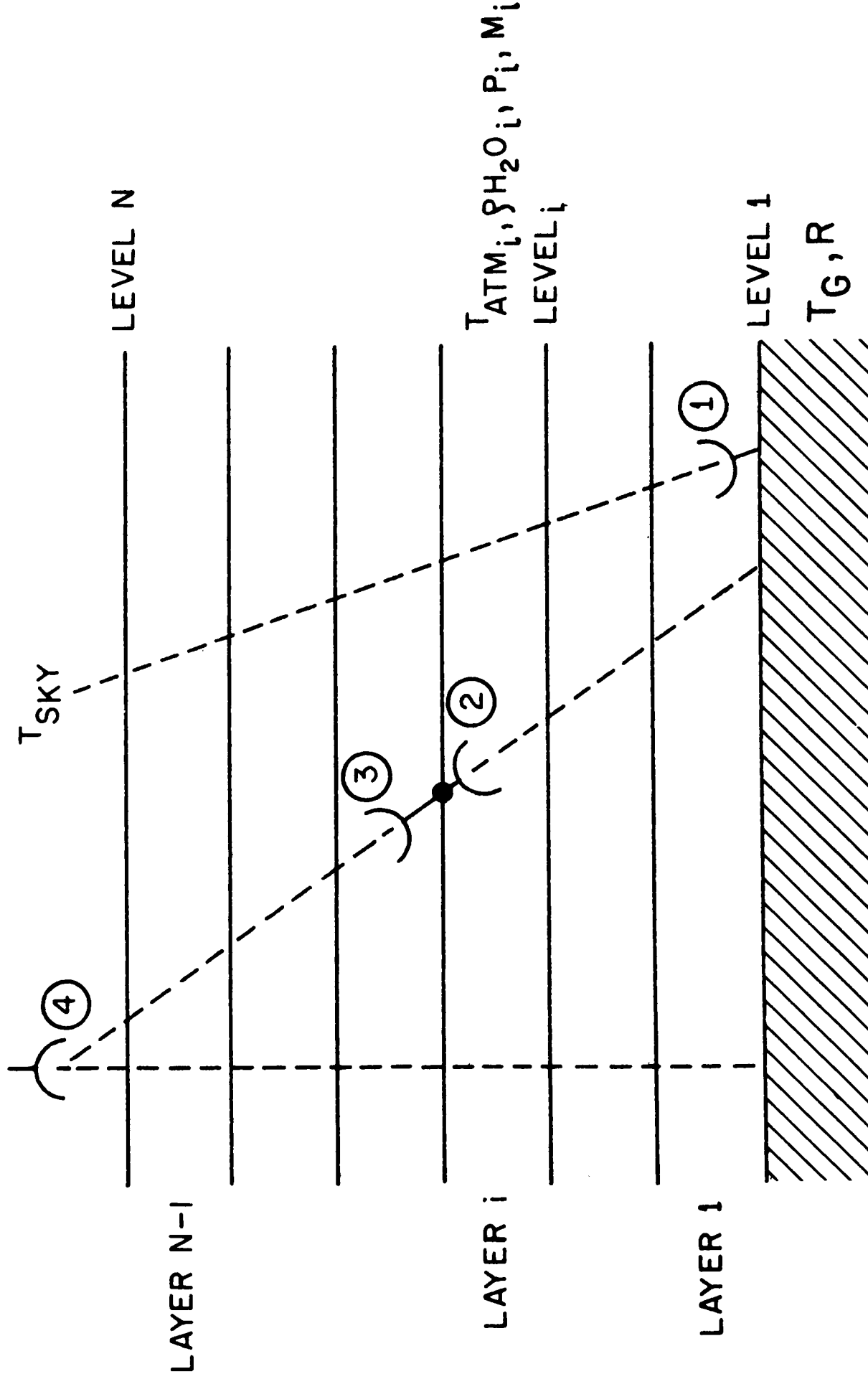


Figure IV-1. Geometries applicable to the solution of the equation of radiative transfer in a plane layered atmosphere.

layer is set to that of the cloud model, and the water vapor density to a value corresponding to 100% humidity, under the assumption that the atmosphere is fully saturated within the cloud layer.

Layers in the model atmosphere are defined as extending between two levels, such that the i -th layer extends between levels i and $i + 1$. For each of the $N - 1$ layers defined by the set of N levels, the mean temperature \bar{T} , pressure \bar{P} , water-vapor density $\bar{\rho}$, and liquid water density \bar{M} are assigned to mean the height \bar{z} of the layer. The temperature, water-vapor and liquid water density averages are obtained by linear averages, and the pressure by interpolation of the hypsometric formula.

Once the layered model of the atmosphere, with its inserted cloud layers, has been constructed, the set of extinction coefficients appropriate for water vapor, oxygen and clouds must be assigned to each layer. The absorption coefficient of water vapor is obtained using the algorithm of Chapter II, using the mean temperature, pressure and water vapor density for the layer. The absorption coefficient of oxygen is computed using the expressions of Lenoir (1968). For cloud layers, the unit-volume scattering and extinction coefficients are calculated using Eq. 3-12 of Chapter III, after first computing the single-particle cross sections $\chi(\hat{n}, r)$, and defining the drop-size distribution $N(r)$.

The problem of radiative transfer in a scattering medium is in general fairly complicated and the methods for its solution are applicable only to special cases (see Chandrasekhar, 1960; Samuelson, 1967; or Van de Hulst, 1957 for further discussion). For this reason, the unit-

volume properties of clouds are used in the present study to define those conditions for which scattering may be neglected; i.e., for which the problem of radiative transfer becomes that of a finite series of uniform absorbing layers. An important criterion for the validity of this simplified approach is that the single-scattering penetration depth, d_s defined by Eq. 3-14 of Chapter III be large in comparison to the physical path length traversed by the beam within the layer. For space-based observations at near-nadir angles in the microwave region, this assumption is valid for all but the rain-bearing cloud distributions, but as one approaches the infrared region, it becomes less and less valid. Within the context of this general approach, therefore, it is really only feasible to discuss the atmospheric opacity or brightness temperature derived by the modeling procedure for cloudy atmospheres at the longer wavelengths.

In the application of the model, the number of layers required for sufficient accuracy depends upon the minimum scale height within which the important parameters change appreciably. Since the scale height for water vapor is about 2 kilometers, spacing of levels for a clear atmosphere at about half this distance is adequate. Cloud layers, of course, may be assumed to be of any desired thickness, and hence the spacing of levels according to local change of the important parameters is accomplished by the cloud insertion procedure. In the present study, the actual computations were performed using the "Generalized Atmospheric Brightness Temperature and Weighting Function" (GABTAWF) program,

implemented for the Univac 1108 computer.

B. Models of Clear Atmospheres

Three atmospheric models suitable for use with the numerical procedure described in Section A have been used in the present study, to represent the effect of climatic variations and extremes. Their temperature profiles, shown in Figure IV-2, are the Standard Atmosphere, 1962, (mid-latitude), and the Tropical and Subarctic (summer) supplements thereto, as presented in the Handbook of Geophysics and Space Environments (Valley, 1965). The water-vapor density curves for the atmospheres, shown in Figure IV-3, are means for the latitudes represented. They are also reported (up to the 10 kilometer level) in the Handbook of Geophysics and Space Environments.

Above 10 kilometers, distributions of moisture are those constructed by Gaut (1967), making use of data of Mastenbrook and Purdy (1969) and Sissenwine et. al. (1966) up to 28 kilometers. The distributions of water vapor above 28 kilometers for each case assume constant mixing ratios of 2×10^{-6} grams of water vapor per gram of dry air.

C. Models of Cloud-Cover Conditions

A total of 19 cloud models have been taken from Reifenstein and Gaut (1971) for use in the present study, representing both fair-weather and rain-bearing cloud conditions, and including commonly-occurring categories of low, middle, high stratus and cumulus clouds. The properties of these models are given in Table IV-1. Each model is characterized by one or

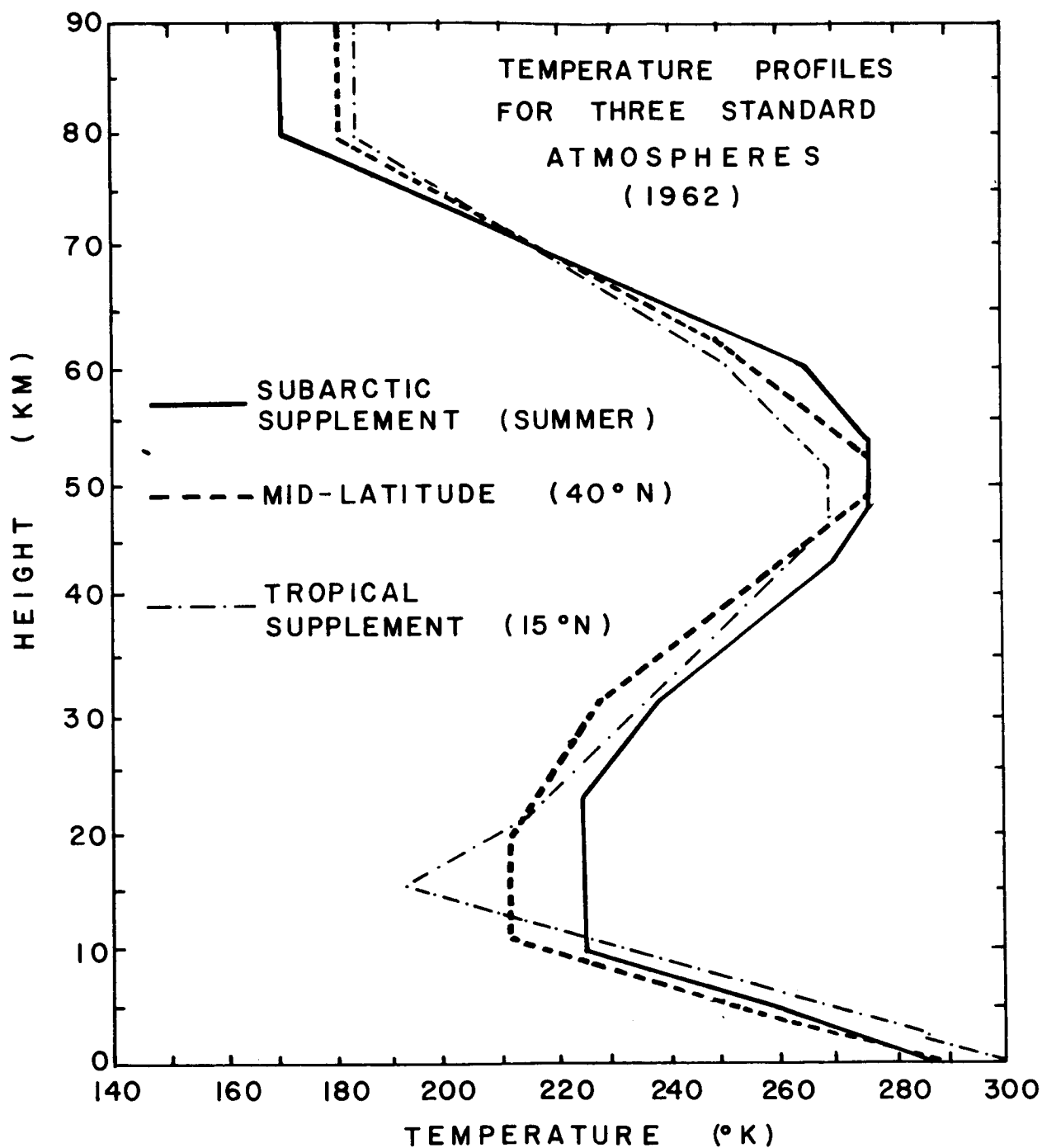


Figure IV-2. Temperature profiles for three model atmospheres used in the present study to represent climatic extremes.

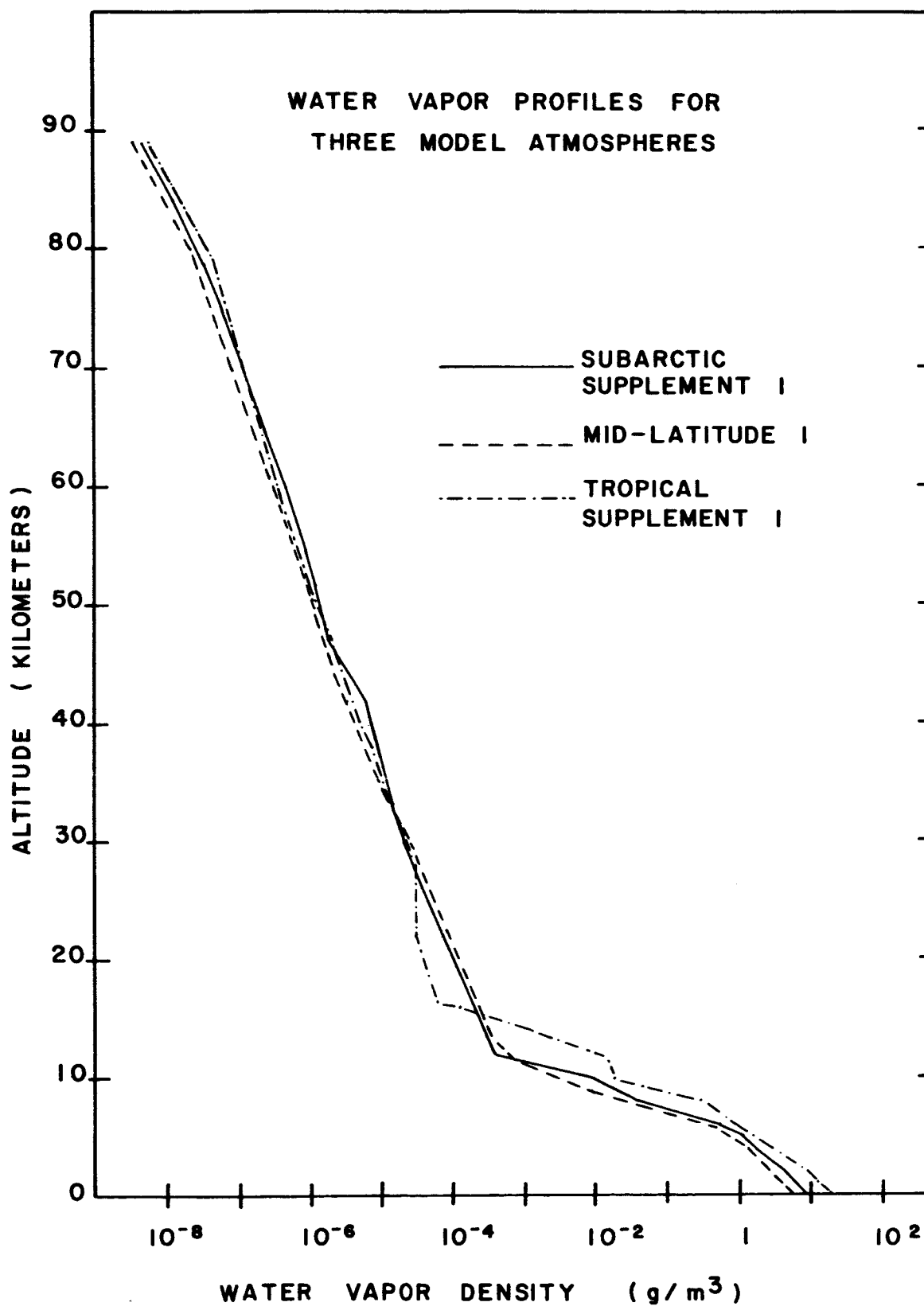


Figure IV-3. Water vapor density profiles for three model atmospheres used in the present study to represent climatic extremes.

TABLE IV-1
PROPERTIES OF STANDARD CLOUD MODELS

NUMBER	NAME	BASE (m)	TOP (m)	DENSITY (g/m ³)	r _c (μ)	C ₁	C ₂	COMP.	Ref.
1-A-1	CIRROSTRATUS, ARCTIC, 12-18 kft	4000.	6000.	0.10	40.0	6.0	0.5	ICE	1,4
1-M-1	CIRROSOTRATUS, MID-LAT., 15-21 kft	5000.	7000.	0.10	40.0	6.0	0.5	ICE	1,4
1-T-1	CIRROSTRATUS, TROPICAL, 18-24 kft	6000.	8000.	0.10	40.0	6.0	0.5	ICE	1,4
10-1	ALTO CUMULUS 8000-9650 ft	2400.	2900.	0.15	10.0	6.0	0.5	WATER	1,2,3
14-1	ALTOSTRATUS 8000-9650 ft	2400.	2900.	0.15	10.0	6.0	1.0	WATER	1,2,3
20-1	LOW-LYING STRATUS 500-2000 ft	150.	650.	0.25	10.0	6.0	1.0	WATER	1,2,3
20-2	LOW-LYING STRATUS 1500-3000 ft	500.	1000.	0.25	10.0	6.0	1.0	WATER	1,2,3
20-3	FOG LAYER, GROUND TO 150 ft	0.	50.	.15	20.0	7.0	2.0	WATER	3
20-4	HAZE, HEAVY	0.	1500.	10 ⁻³	0.05	1.0	0.5	WATER	1,5
21-1	DRIZZLE, 0.2 mm/hr	0. 500. 1000.	500. 1000. 1500.	1.00 2.00 1.00	20.0 10.0 10.0	6.0 6.0 6.0	0.5 0.5 0.5	RAIN WATER WATER	6
21-2	STEADY RAIN, 3 mm/hr	0. 150. 500. 1000.	150. 500. 1000. 1500.	0.20 1.00 2.00 1.00	200.0 10.0 10.0 10.0	5.0 6.0 6.0 6.0	0.5 0.5 0.5 0.5	RAIN WATER WATER WATER	6
21-3	STEADY RAIN, 15 mm/hr	0. 300. 1000. 2000.	300. 1000. 2000. 4000.	1.00 2.00 3.00 2.00	200.0 10.0 10.0 10.0	5.0 6.0 6.0 6.0	0.5 0.5 0.5 0.5	RAIN WATER WATER WATER	6

PROPERTIES OF STANDARD CLOUD MODELS, con't

NUMBER	NAME	BASE (m)	TOP (m)	DENSITY (g/m ³)	r _c (μ)	C ₁	C ₂	COMP.	Ref.
22-1	STRATOCUMULUS 1000-2000 ft	330	660.	0.25	10.0	6.0	0.5	WATER	1,2,3
22-2	STRATOCUMULUS 2000-4000 ft	660.	1320.	0.25	10.0	6.0	0.5	WATER	1,2,3
25-1	FAIR WEATHER CU. 1500-6000 ft	500. 1000. 1500.	1000. 1500. 2000.	0.50 1.00 0.50	10.0 10.0 10.0	6.0 6.0 6.0	0.5 0.5 0.5	WATER WATER WATER	1,2,3
25-2	CUMULUS WITH RAIN 2.4 mm/hr	0. 500. 1000.	500. 1000. 3000.	0.10 1.00 2.00	400.0 20.0 10.0	5.0 6.0 6.0	0.5 0.2 0.2	RAIN WATER WATER	3,6
25-3	CUMULUS WITH RAIN 12 mm/hr	0. 400. 1000.	400. 1000. 4000.	0.50 2.00 4.00	400.0 20.0 10.0	5.0 6.0 6.0	0.5 0.2 0.2	RAIN WATER WATER	3,6
25-4	CUMULUS CONGESTUS, 3000-9000 ft	1000. 1200. 1600. 2000. 2500.	1200. 1600. 2000. 2500. 3000.	0.30 0.50 0.80 1.00 0.50	10.0 15.0 20.0 20.0 20.0	6.0 5.0 5.0 5.0 5.0	0.5 0.4 0.3 0.3 0.3	WATER WATER WATER WATER WATER	3
26-1	CUMULONIMBUS W. RAIN 150 mm/hr	0. 300. 1000. 4000. 6000. 8000.	300. 1000. 4000. 6000. 8000. 10000.	6.30 7.00 8.00 4.00 3.00 0.20	400.0 20.0 10.0 10.0 10.0 40.0	5.0 6.0 6.0 6.0 6.0 6.0	0.2 0.2 0.2 0.2 0.2 0.5	RAIN WATER WATER WATER WATER ICE	2,3,6

REFERENCES:

1. Valley, 1965
2. Fletcher, 1966
3. Mason, 1957
4. Blau, Espinola, and Reifenstein, 1966
5. Deirmendjian, 1964
6. Crane, 1966

more horizontal layers for which the composition (water cloud, ice cloud, precipitation, etc.), the mass density, and three parameters describing the drop size distribution, are specified. In Table IV-1, column 1 contains a reference number, column 2 the most descriptive name of the model. The base height and top height are specified in meters in columns 3 and 4. (The separate specification of a base and top height for each layer allows for the possibility of layers which are physically separated or stratified in height.) The mass density m of liquid water is given in column 5, in g/m^3 . Columns 6-8 contain the parameters characterizing the cloud-dropsize distribution, $N(r)$. For this study, the analytical distribution of Deirmendjian (1964) had been used which enables a given cloud layer to be characterized by four parameters the mass density M , mode radius r_c of the distribution, and two shape parameters C_1 and C_2 :

$$N(r) = A r^{C_1} \exp \left[-B r^{C_2} \right] \quad (4-1)$$

where

$$A = \frac{m C_2 B \left[\frac{C_1 + 4}{C_2} \right]}{\frac{4}{3} \pi \times 10^6 \Gamma \left[\frac{C_1 + 4}{C_2} \right]} \quad (4-2)$$

and

$$B = \frac{C_1}{C_2 r_c^{C_2}} \quad (4-3)$$

The mode radius r_c is that drop radius at which the number density distribution function is maximum, and is tabulated in column 6 of Table IV-1. The two shape parameters C_1 and C_2 are given in columns 7 and 8. Finally, the principal composition of each cloud layer is shown in column 9, with the notation "water" indicating a cloud with liquid water (100% humidity and a continuous drop-size distribution), "ice" a layer primarily made up of ice crystals, "rain" a layer made up primarily of precipitation (less than 100% humidity, with a drop-size distribution concentrated at radii larger than 100 microns). The information necessary to construct the models has been taken largely from Valley (1965), Fletcher (1966), and Mason (1957) with data of Laws and Parsons (1943) as tabulated by Crane (1966) used for the rain-bearing layers. The three ice-cloud models represent Cirrus at three predominantly different altitude ranges, corresponding to the three different climatological conditions of the "standard" atmospheres. For modeling purposes, the ice layers have been assumed to be made up of ice spheres as discussed in Chapter III. The mode radius of 40μ was based on the work of Blau et al. (1966), with the shape parameters designed to include the effect of random-oriented crystal faces of 100μ or more. The properties of haze, included as model 20-4 have been taken from Deirmendjian (1964). The catalog does not intend to be inclusive, but instead covers a range of cloud conditions of interest in the study of remote-sensing applications.

The drop-size distributions for each layer of the liquid water clouds and the 1-M-1 Cirrus (midlatitude) model are given as computer-generated plots in Appendix B.

D. Unit-Volume Scattering and Absorption Properties of Clouds

The scattering and extinction coefficients as given by Eq. 3-12 of Chapter III have been computed for each layer of the liquid water clouds, at 5 wavelengths from 10 cm to 10 μ , and for the 1-M-1 Cirrus model at 10 cm, 100 μ and 10 μ . The results of these computations are tabulated in Appendix C.

Several interesting results emerge from these calculations, and deserve special note. First, the scattering and extinction coefficients for the low-lying stratus cloud model (20-1) are shown as a function of wavelength in Fig. IV-4. Also shown in the figure is the extinction coefficient as given by the empirical formula, (Eq. 3-16 of Chapter III) of Staelin (1966) for the Rayleigh approximation. The agreement between the Staelin formula and the computed extinction coefficient is good for frequencies less than ~ 100 GHz, with the slight discrepancy in this region due in all probability to the difference in refractive indices applicable to the two curves (the former makes use of data of Goldstein, (1951) whereas the latter uses that of Zolotarev, et al., (1969). For wavelengths shorter than ~ 5 mm, the departure of the computed extinction coefficient from the λ^{-2} dependence is evident with the scattering coefficient becoming significant for wavelengths shorter than ~ 1 mm.

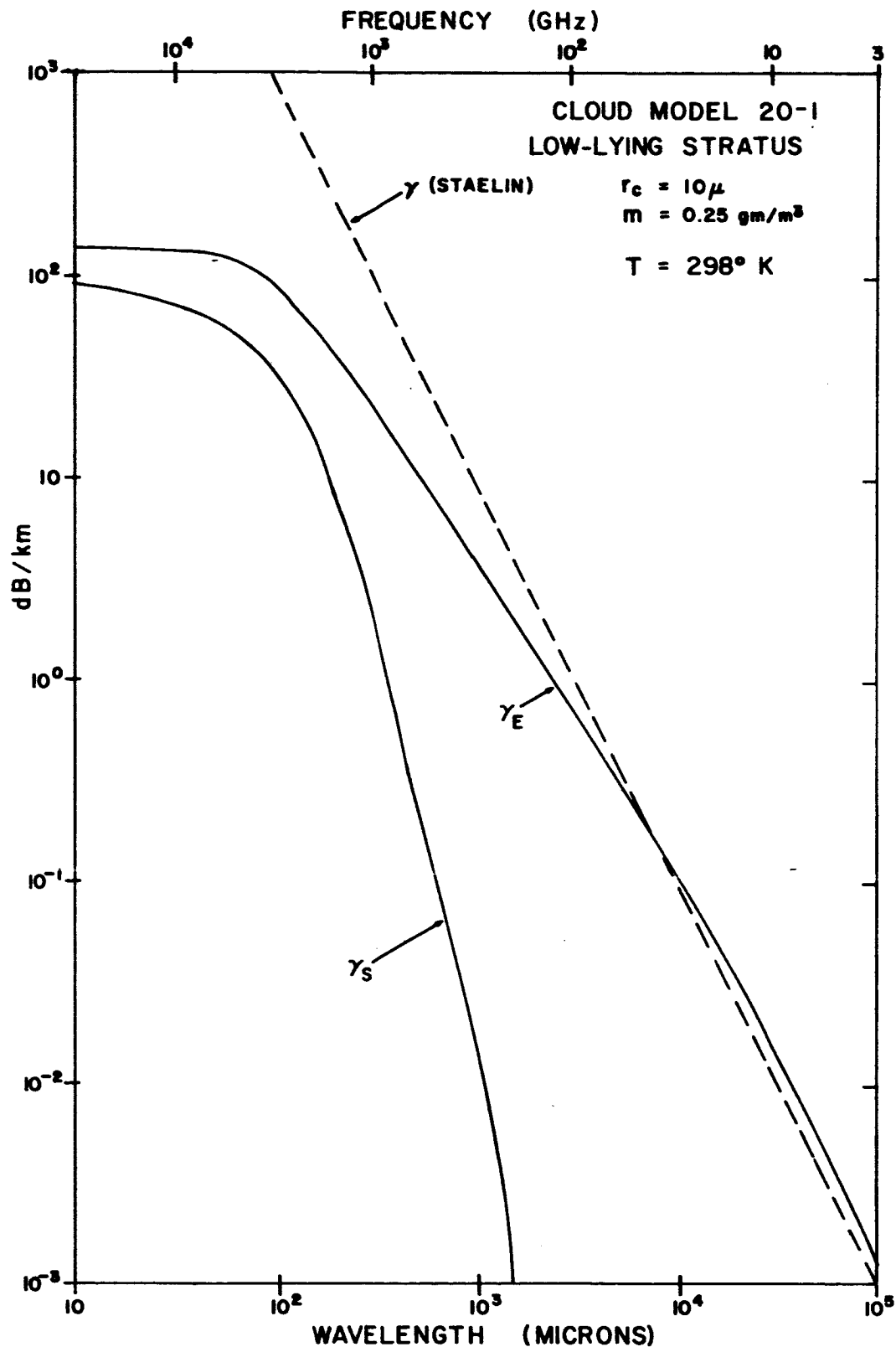


Figure IV-4. Scattering and Extinction coefficients computed for low-lying stratus as a function of wavelength with the empirical formula of Staelin (1966) shown for comparison.

For wavelengths shorter than $\sim 100 \mu$, the major portion of the drop-size distribution lies in the "short wavelength limit", of Chapter III, and the extinction coefficient approaches a constant value proportional to the mean cross section of the individual drops.

A similar presentation is given for a range of drop distributions in Fig. IV-5, in which the extinction coefficient γ_E for the three layers of a rain-bearing cloud (25-2) is shown as a function of wavelength. The three layers differ in mode radius r_c , and mass density m , as well as in their shape parameters C_1 and C_2 (see Appendix B). Each of the three curves exhibits the same characteristic saturation effect with increasing frequency observed for the low-lying stratus, but at frequencies dependent upon the mode radius of the distribution. In the microwave part of the spectrum, the λ^{-2} dependence is still present in the case of the non-raining layers (2 and 3) but not for the raining layer 1. The effect of extremely large drops in rain layers has been studied in the microwave region by Reifstein and Gaut (1971) who find that the departure from the λ^{-2} dependence can be severe in the case of thundershowers (e.g. model 26-1, layer 1) even at wavelengths longer than 1 cm.

The additional parameters of interest are the single scattering albedo and single scattering penetration depth, as defined and discussed in Chapter III. The single scattering albedo is shown in Figure IV-6 for three cloud types representing extremes of mode radius. The three

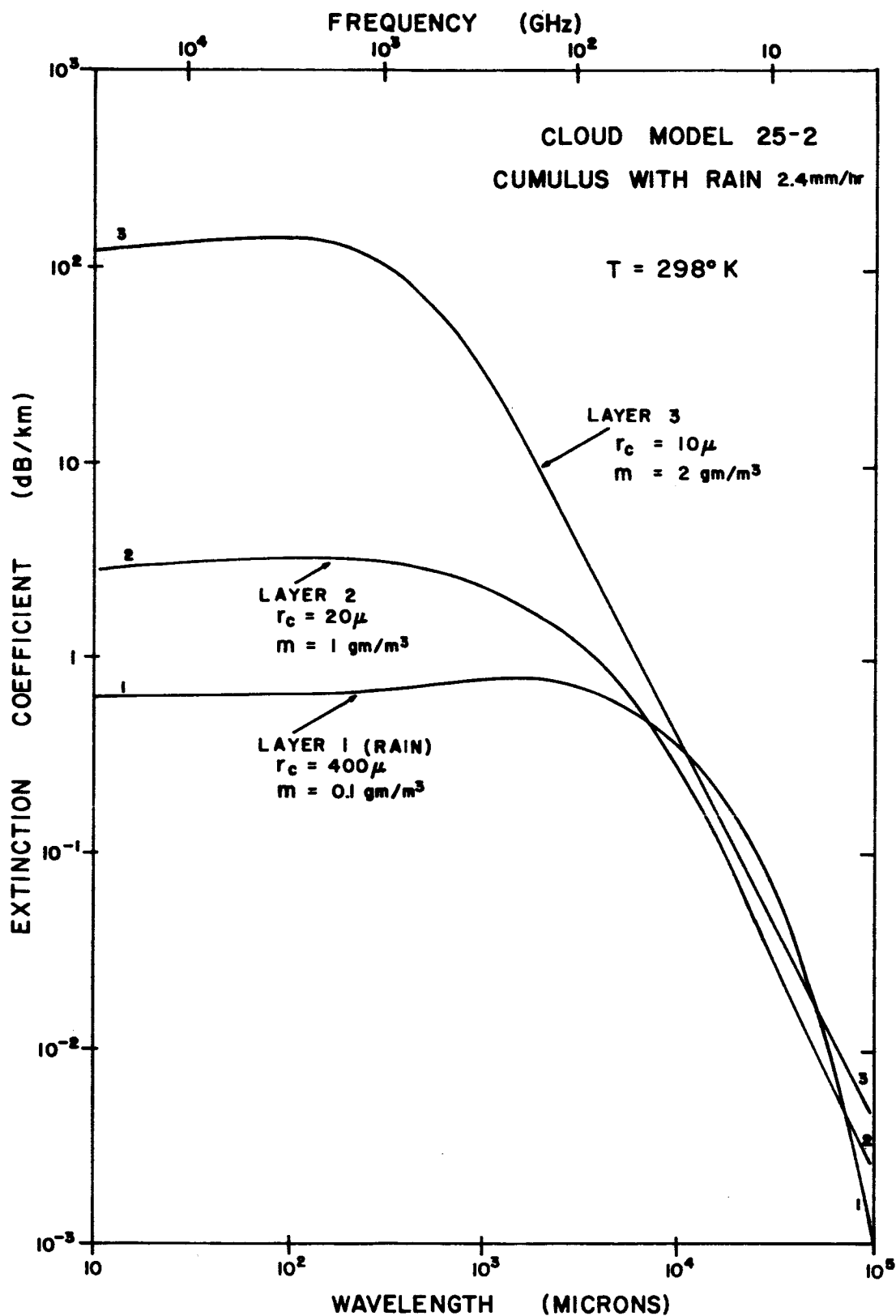


Figure IV-5. Extinction coefficient for three layers of a rain bearing cumulus cloud computed as a function of wavelength.

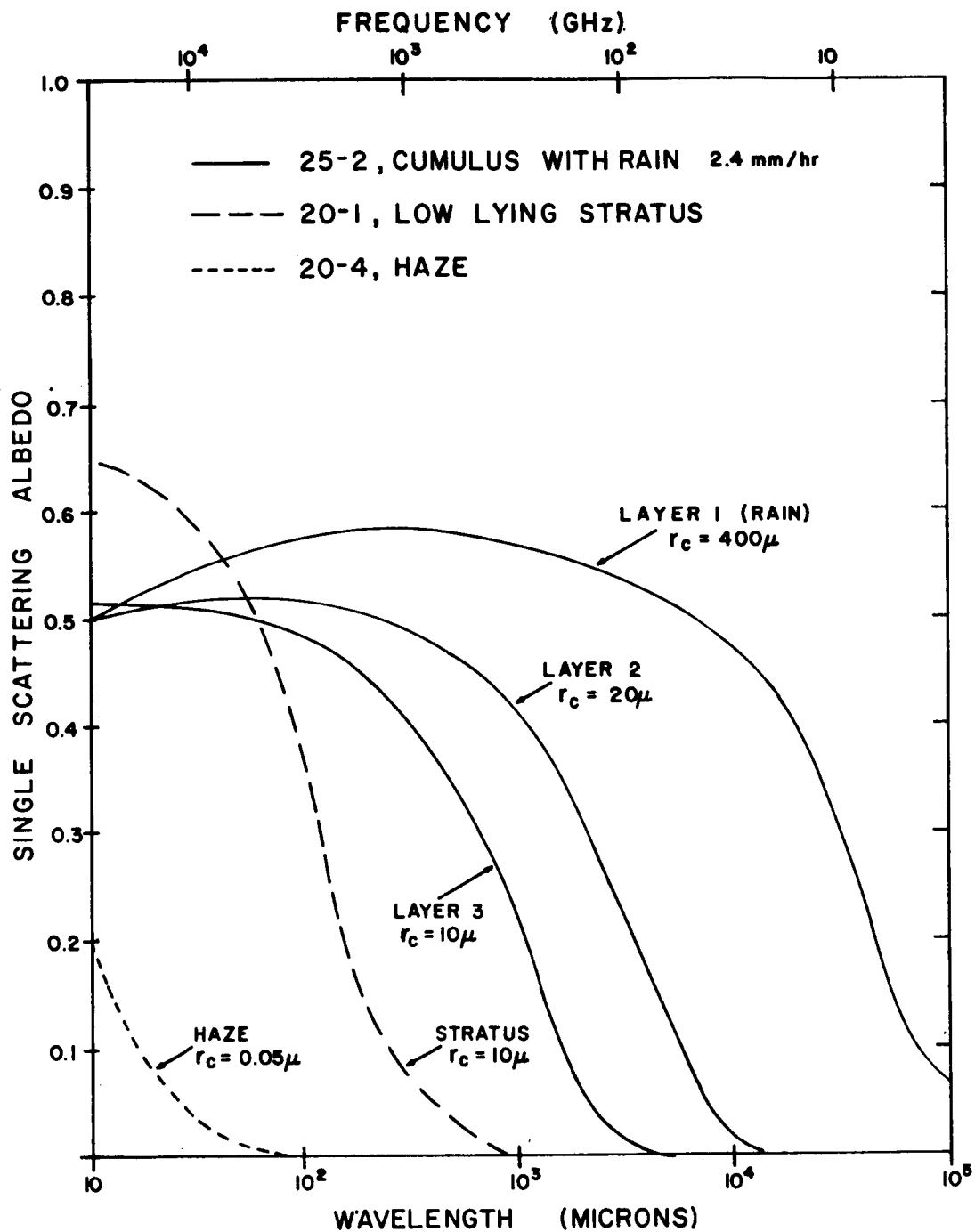


Figure IV-6. Single scattering albedo for three model cloud distributions as a function of wavelength.

layers of the rain-bearing cumulus are shown, with that for low-lying stratus and heavy haze. The domain of wavelengths for each for which scattering may be expected to be important are marked by a sharp rise in the scattering albedo. As the wavelength becomes shorter, the scattering albedo reaches a maximum corresponding to the coincidence of the peak of the Mie efficiency factors with the peak of the drop size distribution. Finally, in the "short wavelength limit", the scattering albedo reaches a constant value determined essentially by the limiting values of Q_S and Q_E , which are in turn highly dependent upon the complex index of refraction.

The single scattering penetration depth is shown for the rain-bearing cumulus model in Fig. IV-7. Also shown for comparison in Fig. IV-7 are the layer thicknesses, corresponding to the physical path-length for observations at the nadir. Since the penetration depth is equal to 10% of a mean free path for single scattering, an error of less than ~10% is made in neglecting scattering in the equation of radiative transfer if the path length is greater than the penetration depth. The wavelengths for which this criterion is met are sharply defined for layers 2 and 3. For the rain-bearing layer, however, the criterion is met over the entire range! This surprising result serves to demonstrate the important point that it is not only the distribution of drop-sizes within the path but also the number, which determines the over-all opacity. The mass density of the rain layer of model 25-2 is only 0.1 gm/m^3 (2.4 mm/hr). Since

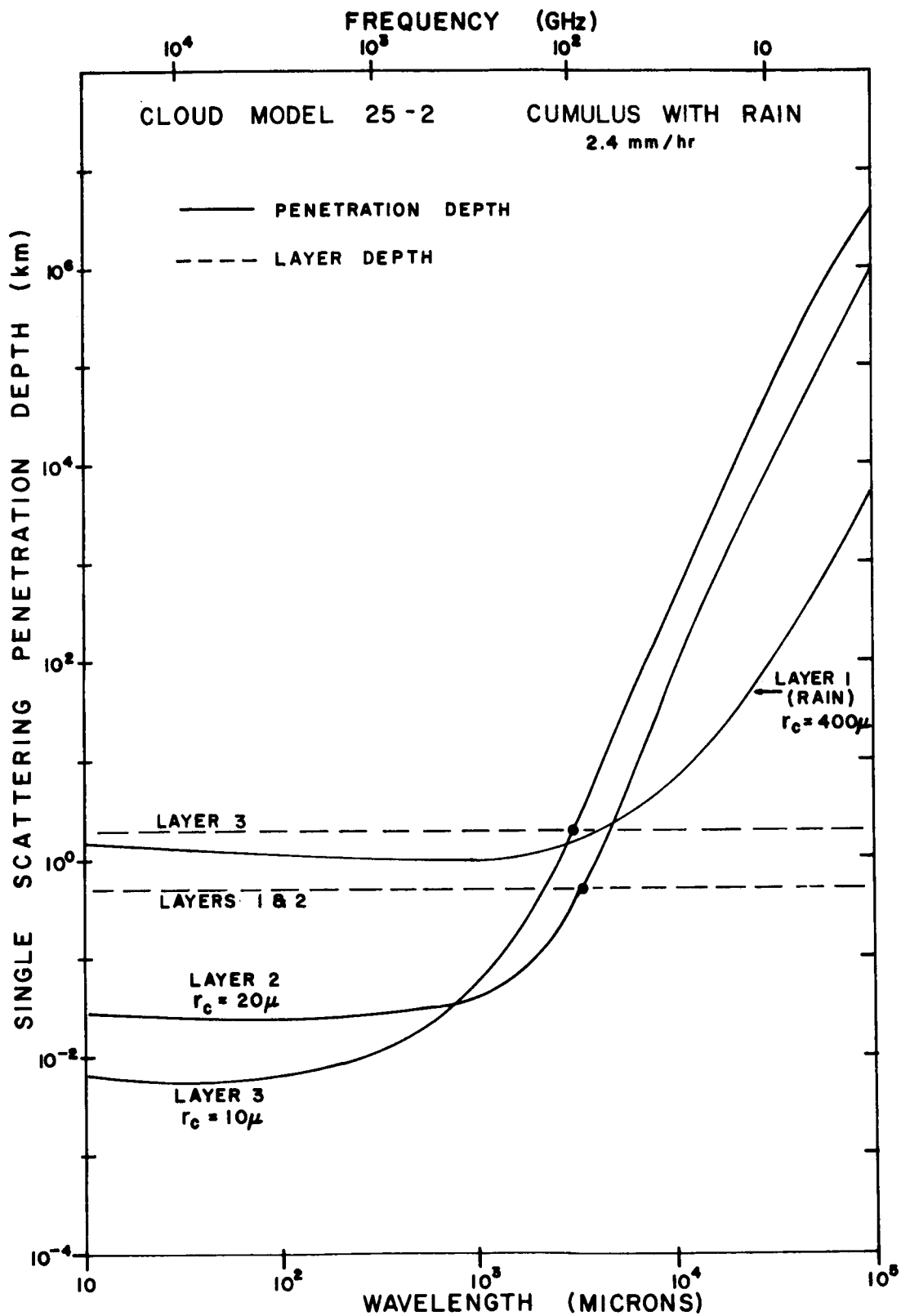


Figure IV-7. Single scattering penetration depth for the three layers of a rain bearing cumulus cloud, with layer depths shown for reference.

we have already observed that the scattering albedo reaches a maximum, it follows that the penetration depth reaches a minimum, and that this minimum defines the physical path length for which scattering may be neglected at all wavelengths. Note that for the other rain models with rain layers of 400 μ , the mass density of the layer is at least a factor of 5, and that for a layer depth of 300 meters, the criterion is violated for all wavelengths shorter than about 1 cm. For slant path observations, particularly at large nadir angles, the situation is altered drastically, and scattering must be included in computations made with most of the modeled distributions for wavelengths shorter than ~ 1 mm.

V. THE VARIABILITY OF WATER VAPOR IN THE ATMOSPHERE AND ITS RELATIONSHIP TO RADIOMETRIC OBSERVATIONS.

All observations through the atmosphere, in those spectral regions in which water vapor and clouds are not totally transparent, will show variability arising from the inhomogeneous distributions of these two absorbers. In this chapter the question of the variability of water vapor is taken up and related to some of the practical considerations of remote observations. In particular, the following three questions have been addressed to provide guideposts for the ensuing discussion:

1. What variations in water vapor can be expected for different spatial scale sizes and averaging periods?
2. What are the fundamental considerations which relate variability of an atmospheric gas to the variability of the signal recorded by a radiometer?
3. What variability due to water vapor can be expected from a radiometer observing through the atmosphere at various frequencies?

A. Water Vapor in the Atmosphere

Water in gaseous form is found in the atmosphere from close to zero percent by mass to as much as four percent in warm, moist conditions. It is highly variable from microscopic scale sizes on up to planetary scale sizes. It is variable in time for any given point in the atmosphere,

but this variability is itself a function of space and time. The maximum water vapor which the atmosphere can hold is a strong function of temperature so that the distribution of absolute humidity in the atmosphere is related to the mean atmospheric temperature distribution.

To bring out some of the more important details of the variability of water vapor, the discussion that follows addresses itself in turn to some of the features of planetary, synoptic, and meso-microscale variations in atmospheric water vapor.

(1) Planetary Scales

Figure V-1 presents the zonally averaged (around latitude circles) precipitable water as measured at approximately 450 radiosonde stations over a one year period (IGY-1958). The data was assembled and analyzed by the staff of the Planetary Circulation Project at M.I.T. The figure is taken from Peixoto (1971). Other work by the same group and reported in Peixoto (1970) is based upon five years of data for the northern hemisphere. The lengthier statistical record substantiates this basic curve. Included in Figure V-1 are the curves for summer and winter conditions to show seasonal variability.

Several points of interest related to the spatial and temporal variability of water vapor on a planetary scale should be brought out. First, it should be noted that the equator-pole variation is approxi-

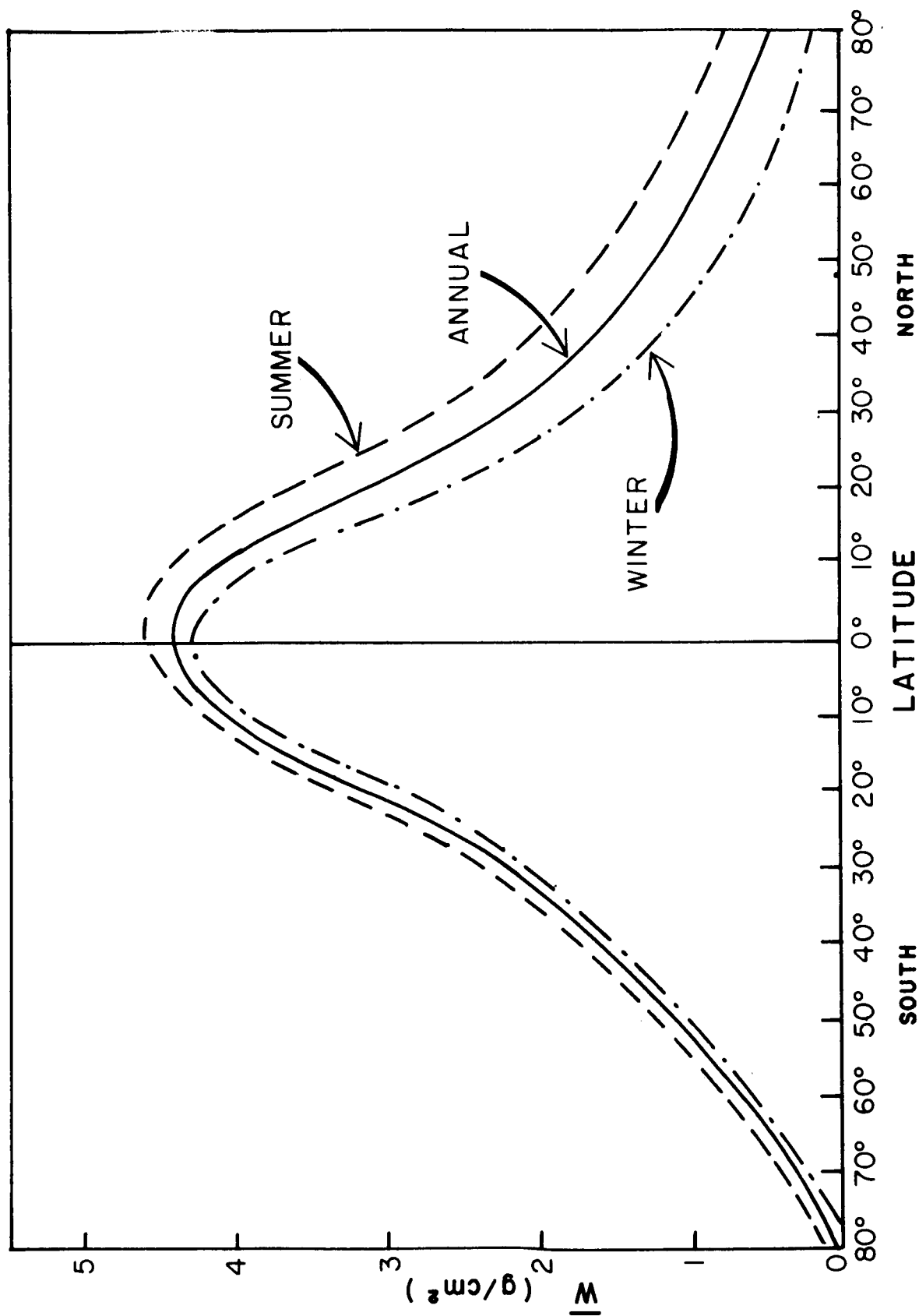


Figure V-1. The zonally averaged precipitable water for the summer, winter and year of the IGY (1958). Units are gm/cm^2 . (Peixoto, 1971.)

mately one order of magnitude ($0.2-0.5 \text{ gm/cm}^2$ at the poles to approximately 4.5 gm/cm^2 at the equator). Secondly, the winter-summer variation in these zonal averages are everywhere less than 1 gm/cm^2 with the maximum variation occurring in the mid- and higher latitudes of the northern hemisphere. The important differences between the equatorial regions and the arctic regions is a direct result of the equator-pole temperature difference. The mean precipitable water for the entire globe derived from these curves is approximately 2.6 gm/cm^2 .

If one chooses a single meridian and plots the mean annual precipitable water, some variation from the zonal mean is to be expected. Along 80° west longitude the pattern for W is that shown in Figure V-2. The maximum water vapor is both greater than the zonal mean (4.3 vs 4.9 gm/cm^2) but also displaced northward about 10° . However, it is remarkably similar in general appearance and magnitude to the zonal mean. This similarity is repeated at most longitudes.

The variation in the vertical for the zonal average of the absolute humidity is shown in Figure V-3. The units are gm/m^3 . Again the distribution is dominated by the temperature distribution found in the troposphere. Regions of warm temperatures have higher values for the average water vapor density. Equatorial regions are roughly one order of magnitude more moist than polar regions at all pressures. There is an interesting asymmetry between the northern and southern hemisphere.

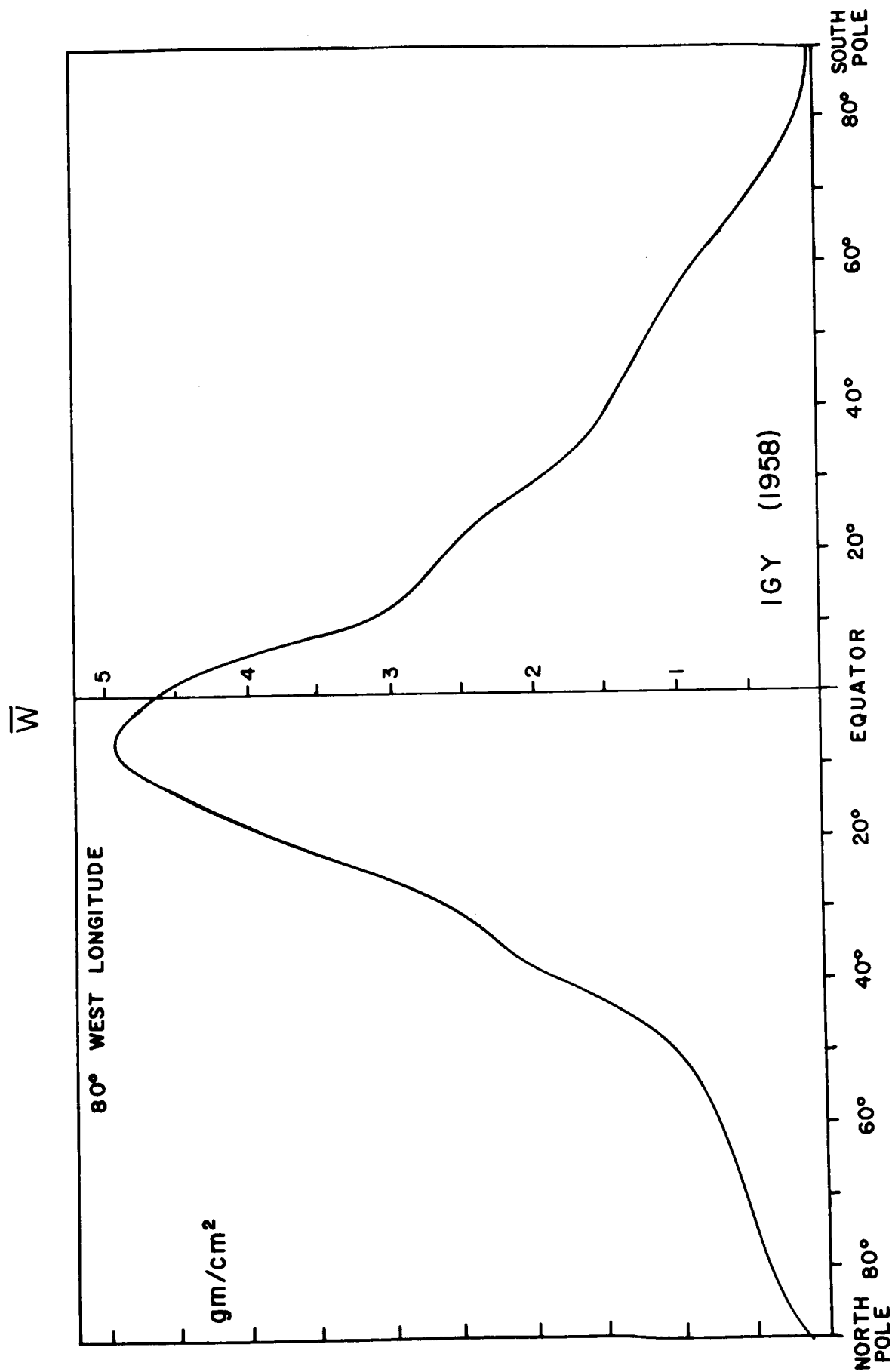


Figure V-2. The annual average of precipitable water in vapor form along 80° W. longitude. Units are gm/cm^2 . Data are from the IGY (1958).

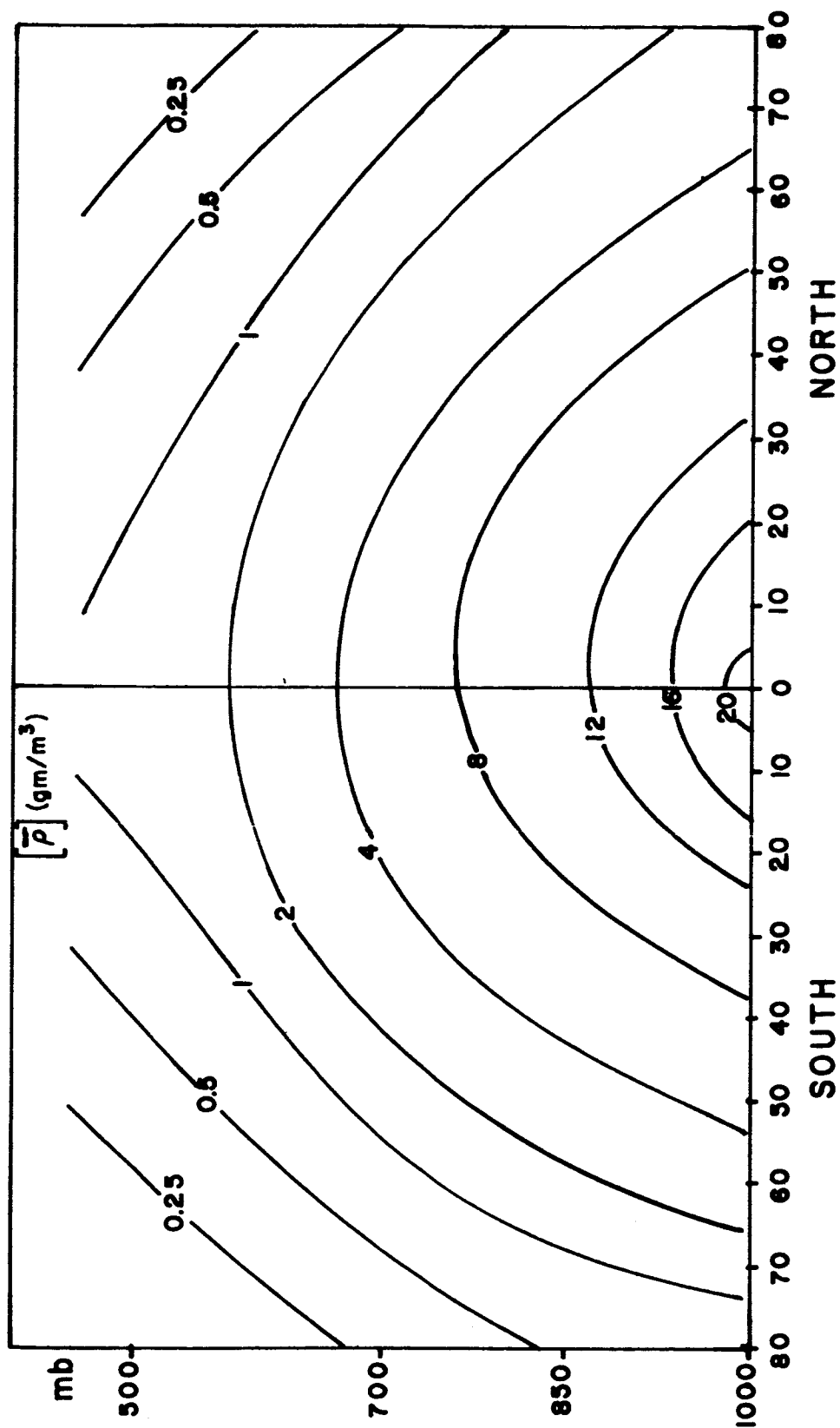


Figure V-3. A meridional cross-section of the zonally averaged absolute humidity $\bar{\rho}$. Data are from the IGY (1958) for the complete year. Units are gm/m^3 . (Adapted from Starr, Peixoto, Mckean, 1969.)

Considerably higher values of water vapor density appear in north polar regions as opposed to south polar regions.

Along 80° west longitude in the northern hemisphere, the cross-section of annual mean ρ values is as shown in Figure V-4. This supports the curve for precipitable water shown in Figure V-2. The maximum values are displaced 10° to 15° north of the equator. Other than this anomaly the values are similar to the zonal means.

Important for later discussions concerning the effect of water vapor on earth observations are the two facts that 50 percent of the water vapor is contained in the lowest 15% of the atmosphere (>850 mb) and 90 percent is found in the lowest half of the atmosphere (>500 mb). This can be better seen in Figure V-5 which gives some zonally averaged yearly profiles of absolute humidity for various representative latitudes in the northern and southern hemispheres.

Figure V-6 presents the temporal standard deviations of the zonally averaged absolute humidity. Here, a double lobed picture appears. The zones of maximum variation in time do not coincide with the zones of maximum humidity. In the northern hemisphere, the maximum occurs about 30°N. In the southern hemisphere, the maximum seems to be closer to the equator, near 20° to 22°S. It should be noted, however, that the data base for the northern hemisphere is much more extensive than the data base for the southern and it is unclear how much the difference in the

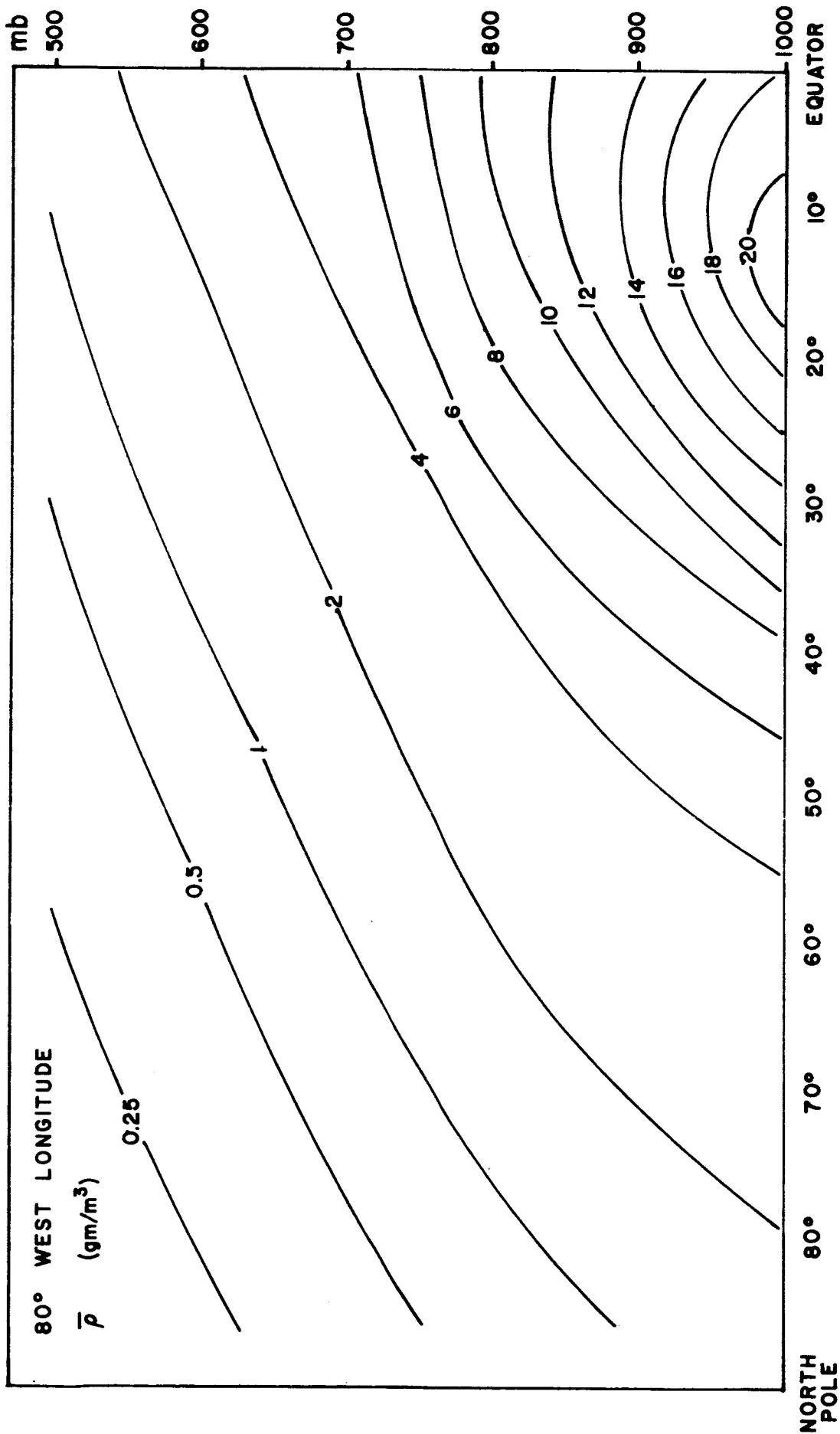


Figure V-4. A meridional cross-section of the mean annual distribution of water vapor along 80° W. longitude. Units are gm/cm². Data are from the IGY (1958).

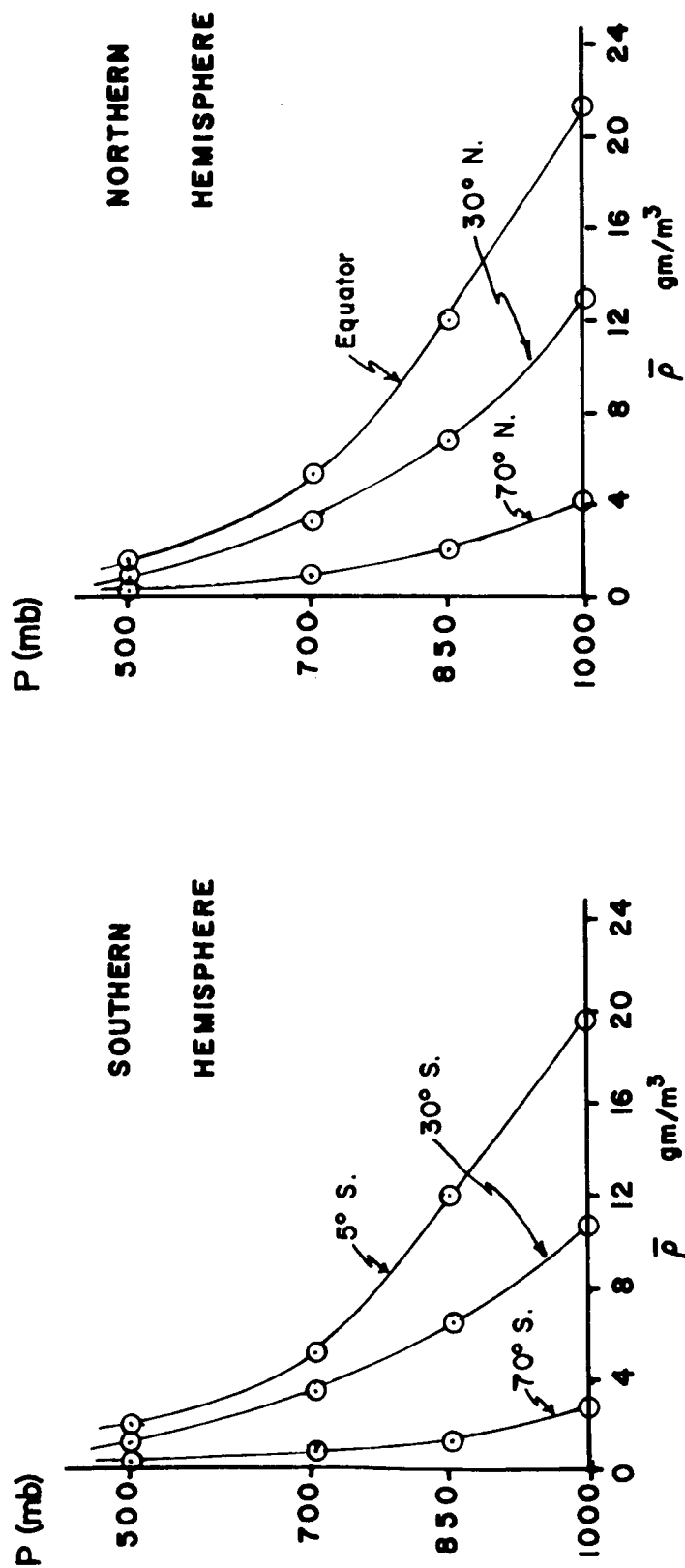


Figure V-5. The vertical distribution of the zonally averaged absolute humidity for the IGY (1958). Units are gm/m³. (Adapted from Peixoto, 1971.)

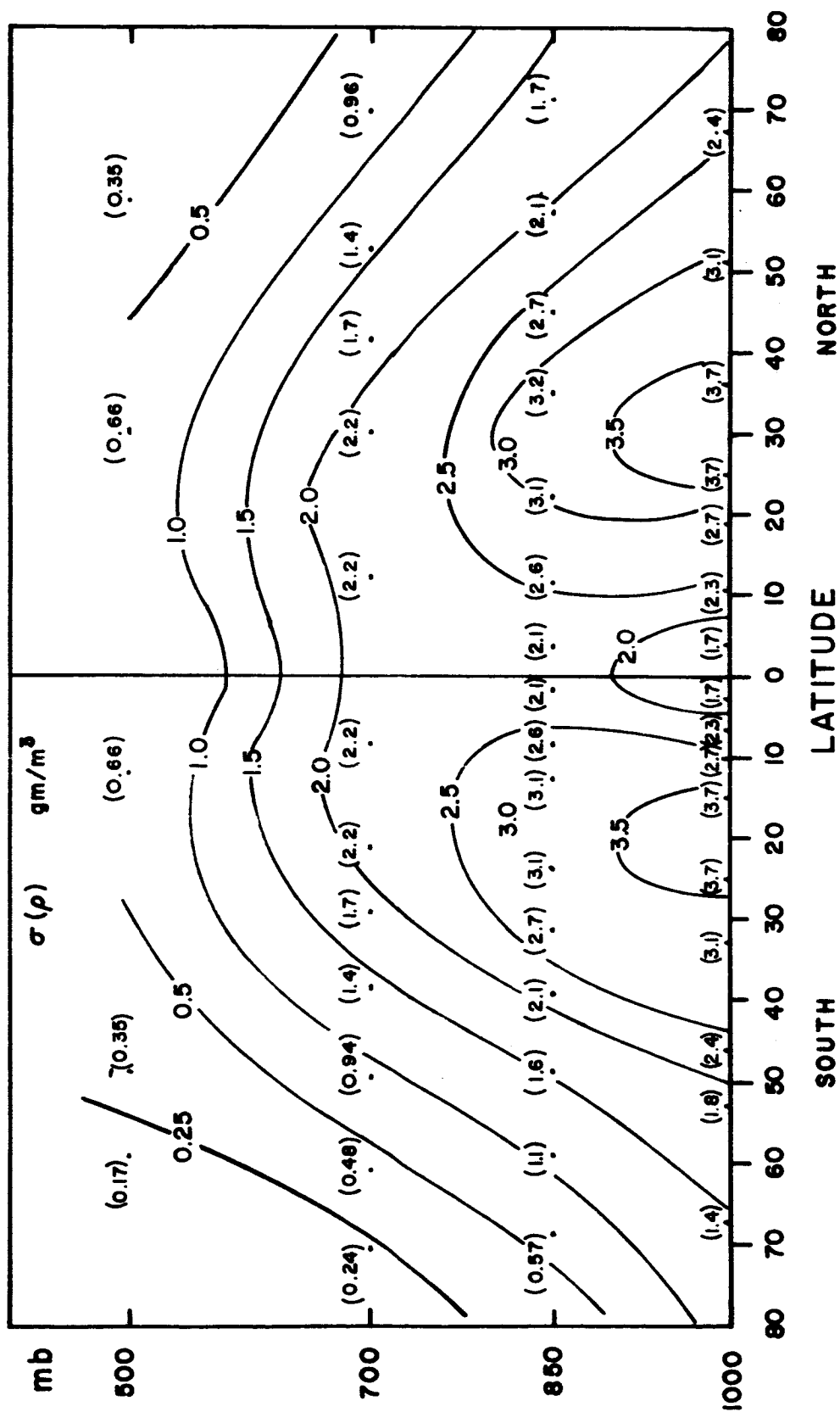


Figure V-6. A meridional cross-section of the zonally averaged temporal standard deviation of the absolute humidity $\sigma(\rho)$ in units of gm/m^3 . Data are from the IGY (1958). (Adapted from Starr, Peixoto, and McKean, 1969.)

hemispheres is due to data deficiencies in the southern hemisphere. From purely meteorological reasoning the differences appear to be real. The variability in lower middle latitudes is not surprising because it is in this region that air mass changes from one moisture condition to another take place most frequently.

The spatial variability of precipitable water averaged over one year over the northern hemisphere is shown in Figure V-7. The distribution reflects the influence of the temperature field, the large scale circulation systems, especially as they relate to convergence and divergence of the flow in the lowest part of the troposphere, and the topography. High plateaus and mountains tend to be above the warm moisture laden air and therefore less precipitable water exists above these regions on the average.

Some of the features in Figure V-7 are important to note. Most obvious and already brought out in previous figures is the general equator-pole decrease in moisture. Continental regions, which are the sources of arctic air masses, show up low in moisture content (e.g., Siberia). The east end of semi-permanent high pressure regions are lower in moisture than their western counterparts corresponding to the notion of descending diverging air in the eastern parts and ascending converging air in western parts of these features. Maxima occur over the equatorial regions of South America and the western equatorial re-

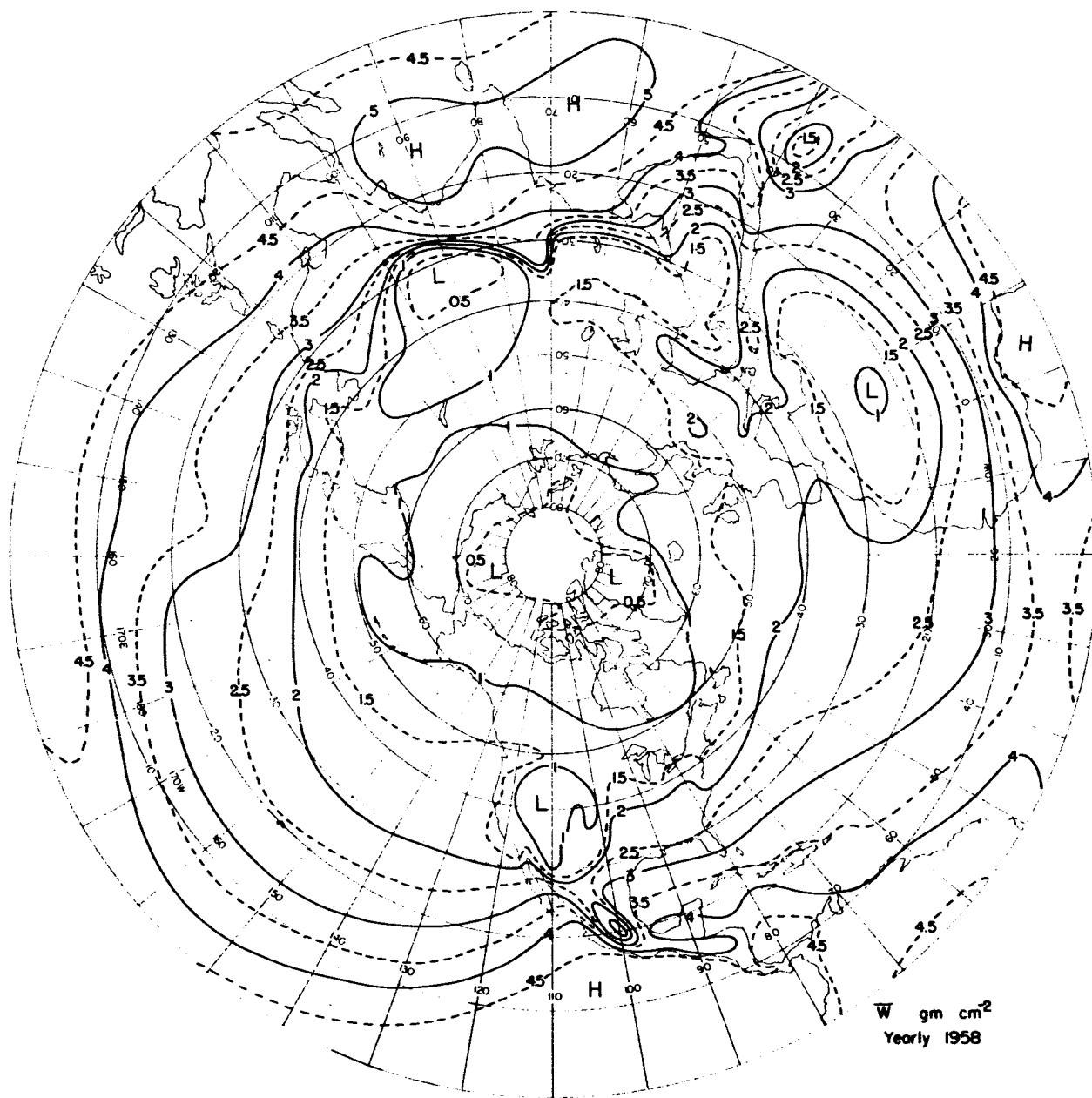


Figure V-7. The annual mean distribution of precipitable water in vapor form over the northern hemisphere. Units are in gm/cm^2 . Data are from the IGY (1958). (Peixoto and Crisi, 1965.)

gions of Africa, as well as over the southern part of India and the waters surrounding this part of the subcontinent. An arm of moisture extends up the east coast of Greenland perhaps as a result of the North Atlantic Drift. Desert regions are plainly low in moisture as evidenced by the Sahara (northern Africa), the Kalihari (southern Africa), and the Great Victoria Desert of Central Australia. Topographical influences occur in the western U.S., the west coast of South America, the Tibetan Highlands, and the Central Highlands of Mexico.

For our present purposes Figure V-7 illustrates the long term, large scale, spatial variability of atmospheric water vapor in the northern hemisphere.

Figures V-8 and V-9 give some idea of the seasonal variability of precipitable water in the northern hemisphere. They are the summer and winter equivalents to Figure V-7. The important differences to note are the general increase of water vapor everywhere during the summer period. This is reflected in the seasonal zonal averages as shown in Figure V-1. It also should be noted that there are no dramatic changes in the patterns from summer to winter. That is, dry areas remain dry and moist areas generally remain moist.

The southern hemisphere yearly mean precipitable water distribution is shown in Figure V-10. As in the northern hemisphere the patterns are

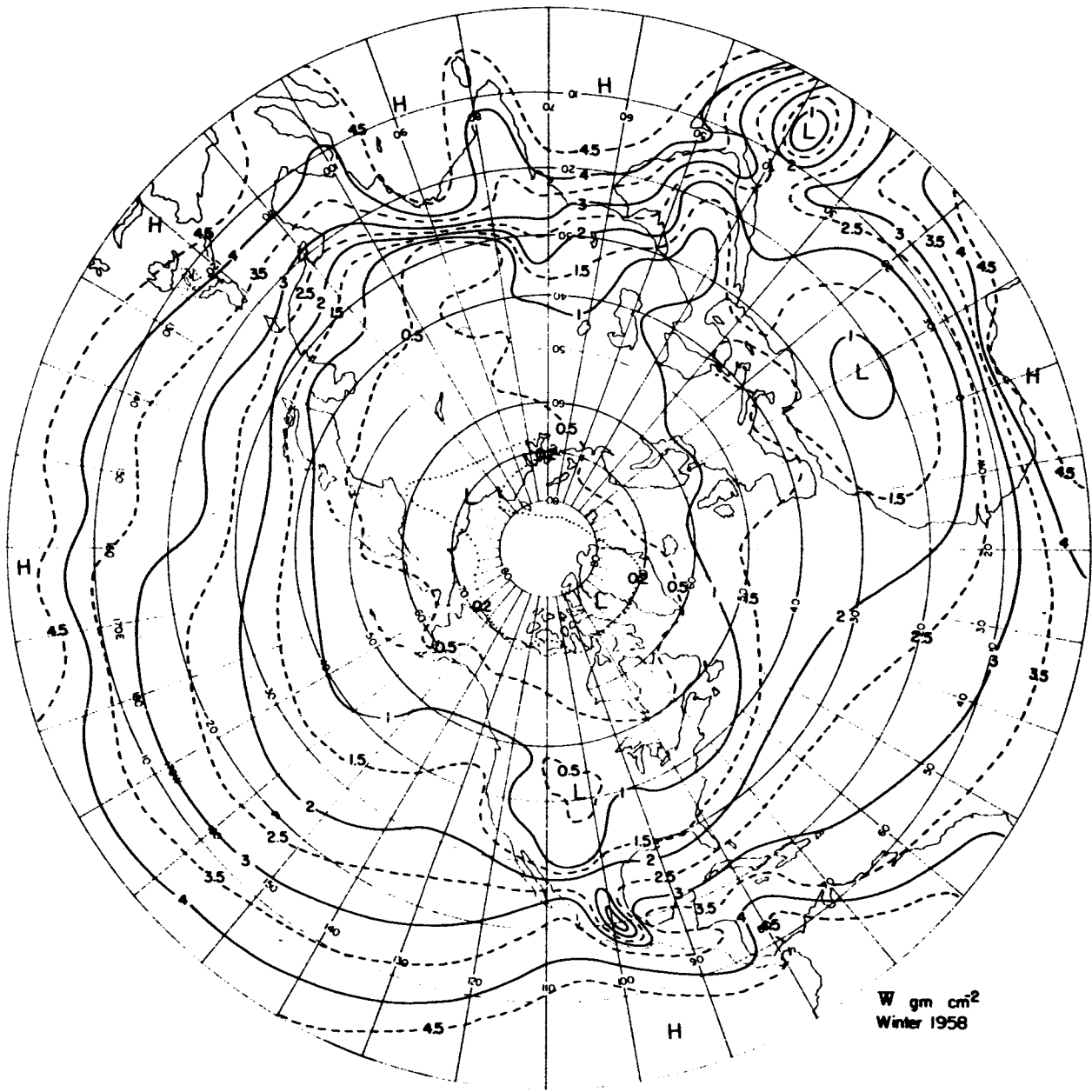


Figure V-8. The mean distribution of precipitable water in vapor form over the northern hemisphere during summer. Units are gm/cm^2 . Data are from the IGY (1958). (Peixoto, and Crisi, 1965.)

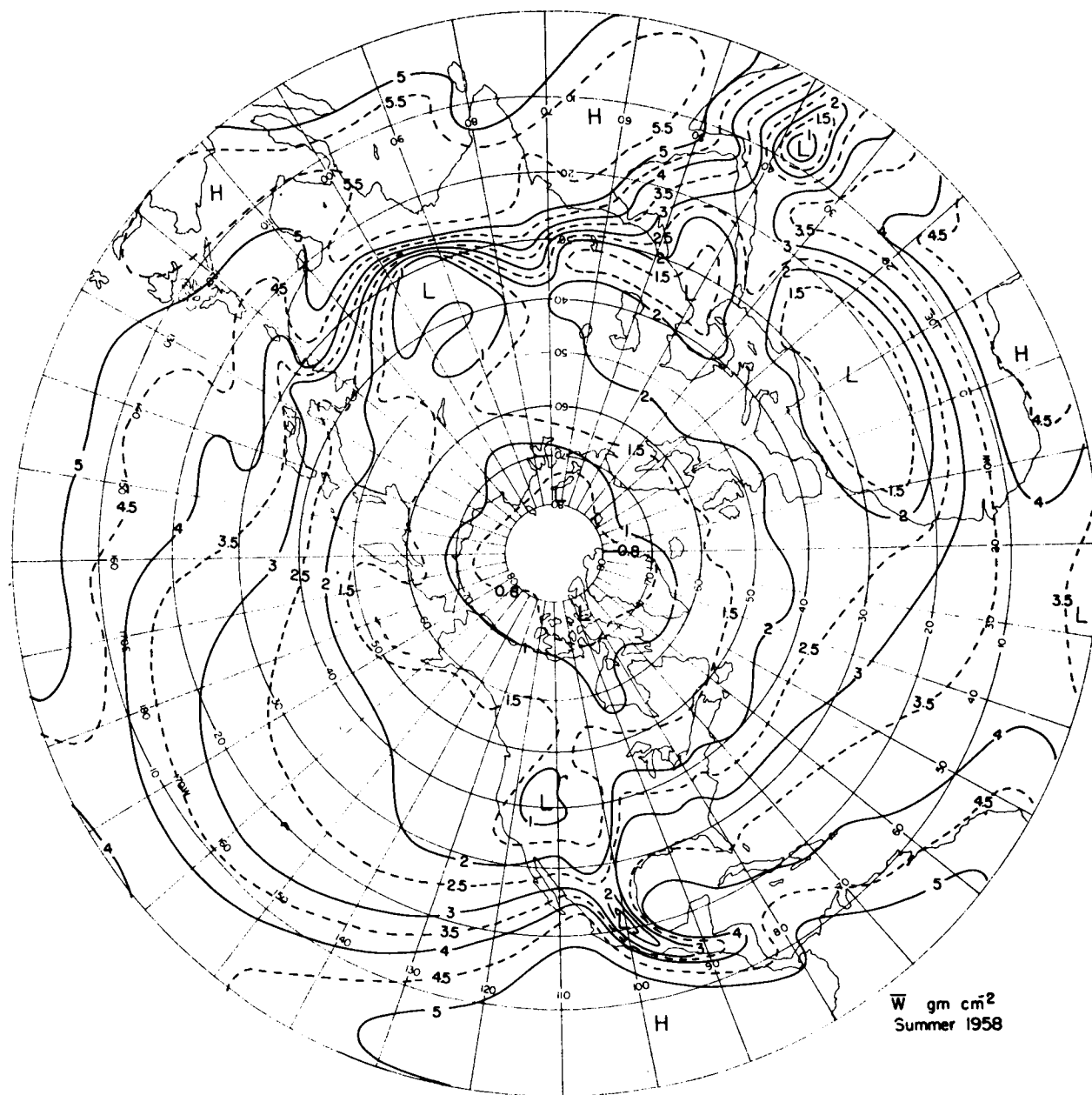


Figure V-9. The mean distribution of precipitable water in vapor form over the northern hemisphere during winter. Units are in gm/cm². Data are from the IGY (1958). (Taken from Peixoto and Crisi, 1965.)

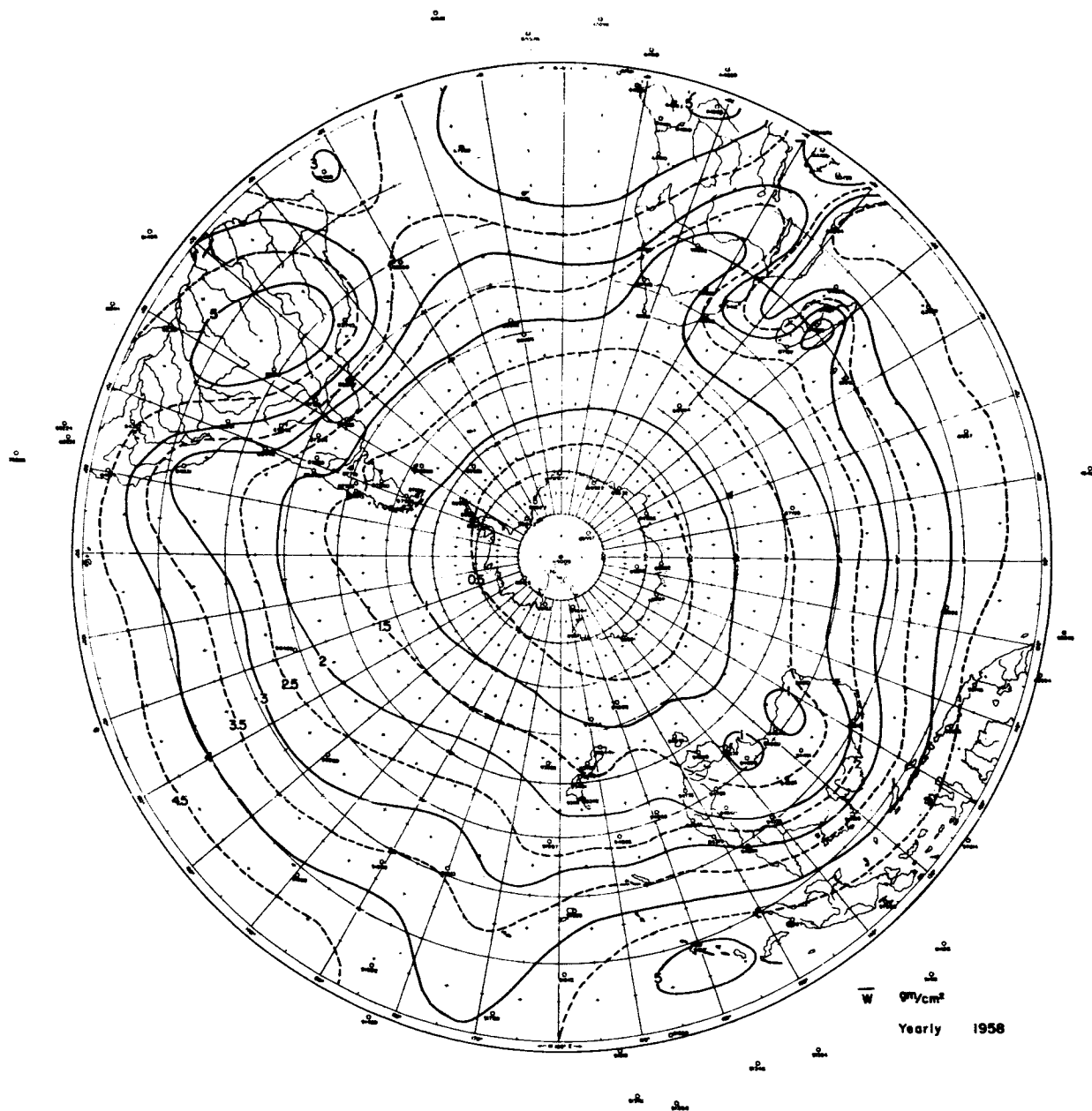


Figure V-10. The annual mean distribution of precipitable water in vapor form over the southern hemisphere. Units are gm/cm². Data are from the IGY (1958). (Courtesy of Dr. J.P. Peixoto, M.I.T.)

greatly influenced by the presence or absence of land. Patterns over water areas show a marked skewness toward the western boundaries of large land masses. The most obvious example of this being on the west coast of South America. There is less data for the southern hemisphere but the large areas of water where data is scarce would be expected to show uniform conditions as are depicted in the Figure.

The summer and winter distributions of water vapor in the southern hemisphere are depicted in Figures V-11 and V-12, respectively. The poleward trend in the isolines during summer and the equatorward trend in winter is similar to the northern hemispheric patterns. Again dry areas generally remain dry and moist areas moist from winter to summer.

(2) Synoptic Scale Variations

When we speak of synoptic scale disturbances we mean the scale upon which weather systems develop and move - of the order of 1000 to 2000 kilometers. The variations between the moisture contents of juxtaposed air masses are those which concern us. From Figure V-6 it can be seen that the major variability occurs in lower middle latitudes and subtropical latitudes. The most contrast occurs when dry arctic or continental polar air masses move equatorward to mix with moist tropical air masses moving poleward. The contrast in absolute humidity across these air masses is greatest near their common border because of the moisture carried aloft in the strong vertical motions. However, the

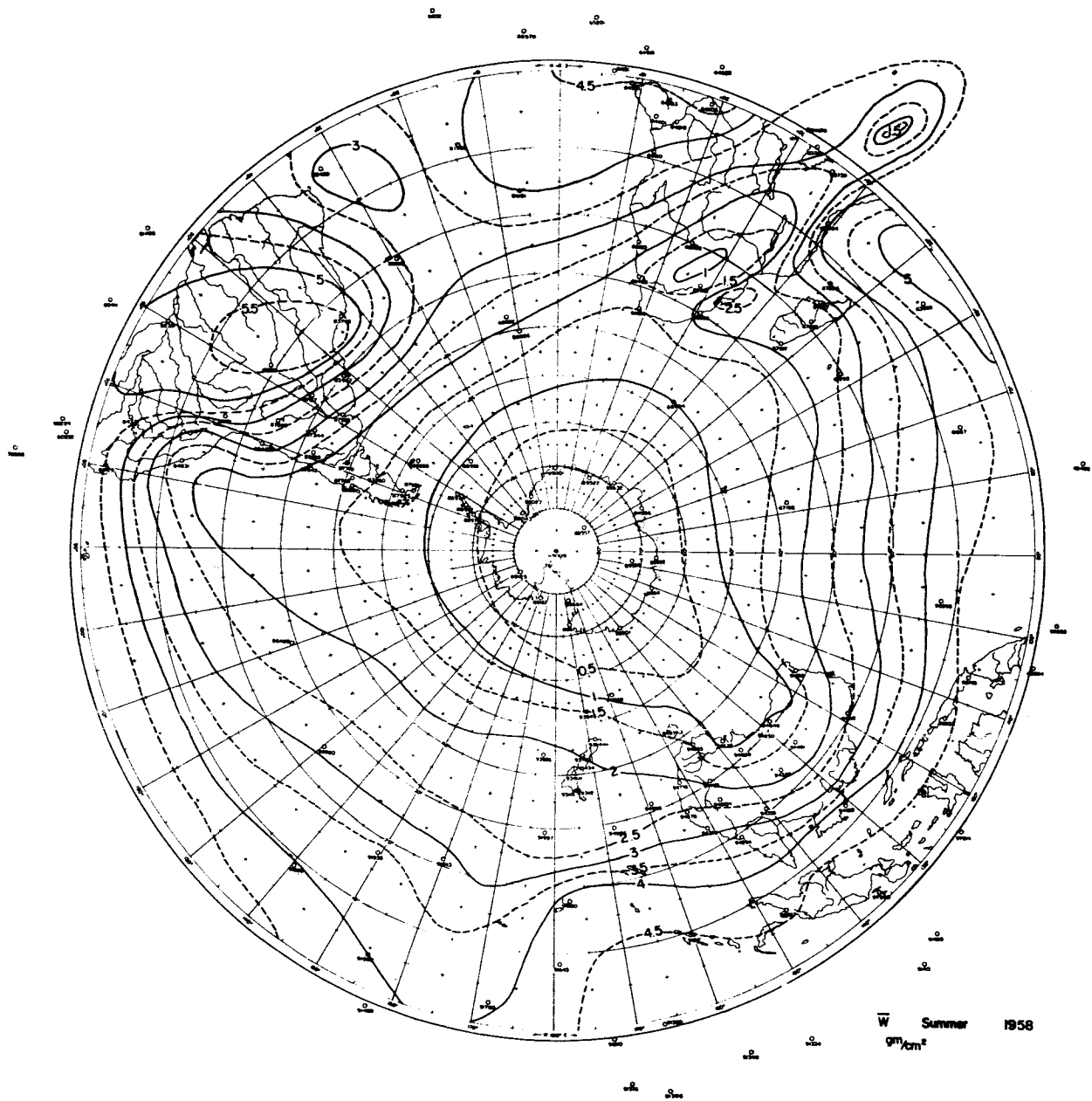


Figure V-11. The mean distribution of precipitable water in vapor form over the southern hemisphere during summer. Units are gm/cm². Data are from the IGY (1958). (Courtesy of Dr. J.P. Peixoto, M.I.T.)

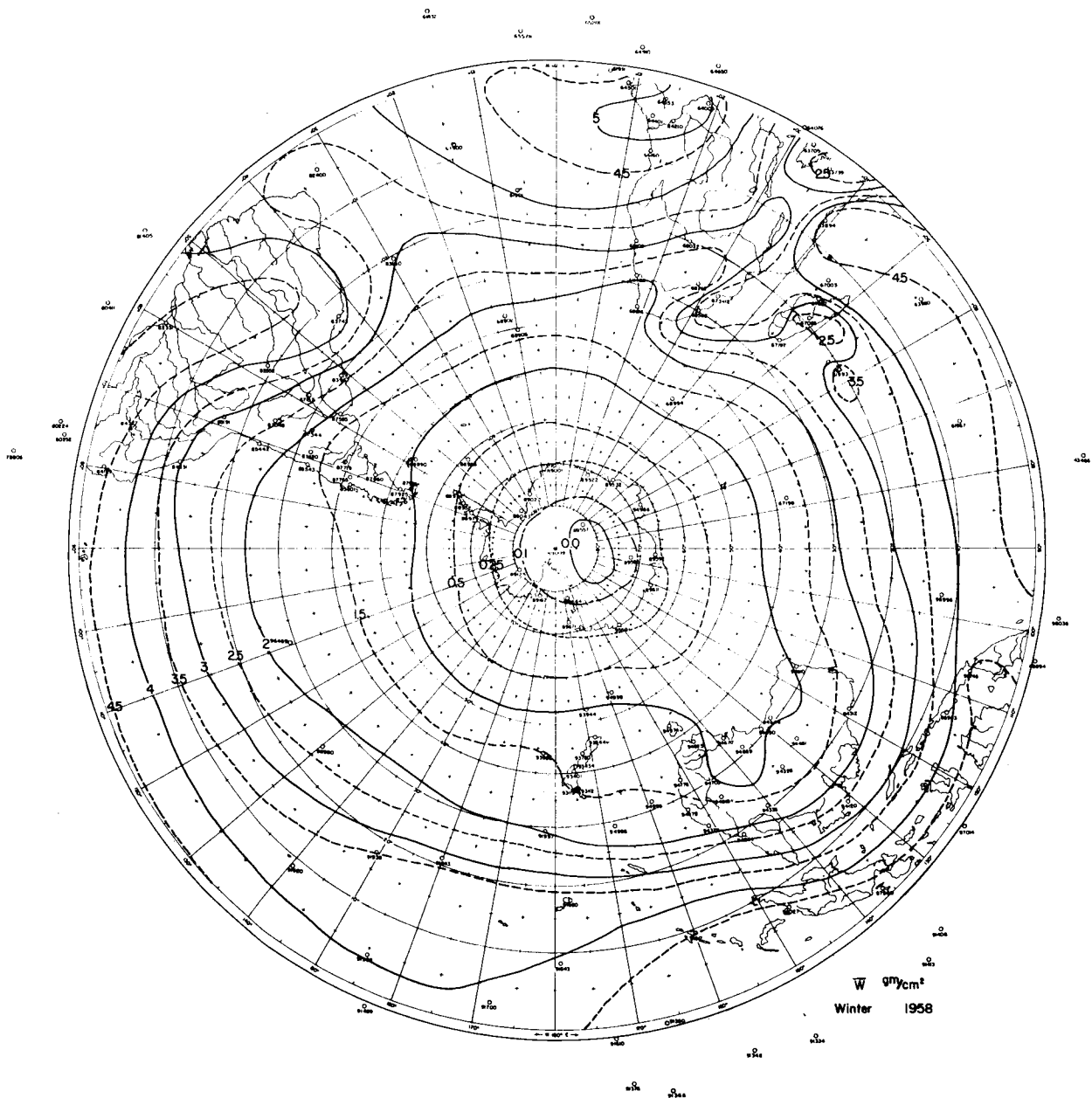


Figure V-12. The mean distribution of precipitable water in vapor form over the southern hemisphere during winter. Units are gm/cm^2 . Data are from the IGY (1958). (Courtesy of Dr. J.P. Peixoto, M.I.T.)

mean moisture in the air masses is less than these extremes. The presence of widespread cloudiness is indicative of saturated moisture conditions at the cloud levels. Extensive clouds, however, are often part of overrunning conditions along a warm frontal zone and exist over only a small area along the border between the two air masses.

The maximum precipitable water vapor for a well defined air mass appears to be about 5.5 to 6 gm/cm^2 and this occurs only in very warm tropical latitudes. Extreme values occur over the Bay of Bengal, central South America, Southern India, Central Africa and various oceanic regions along the equator.

As examples of the annual and seasonal mean conditions one can expect on the synoptic scale size Figures V-13, V-14, and V-15 are presented. They give conditons over the African continent for the year, the summer season and the winter season. Again, close inspection shows that the maximum seasonal difference is no more than approximately 2 gm/cm^2 maximum and that normally the difference is much smaller. For the African continent these maximum values occur about 25°S between the continent and the island of Mozambique.

The precipitable water in vapor form as deduced by the U.S. Weather Bureau on 16 June 1969 is shown in Figure V-16. This is a maturing extratropical storm which is still centered in the Gulf of Mexico and therefore has an excellent source of water vapor to draw from. The

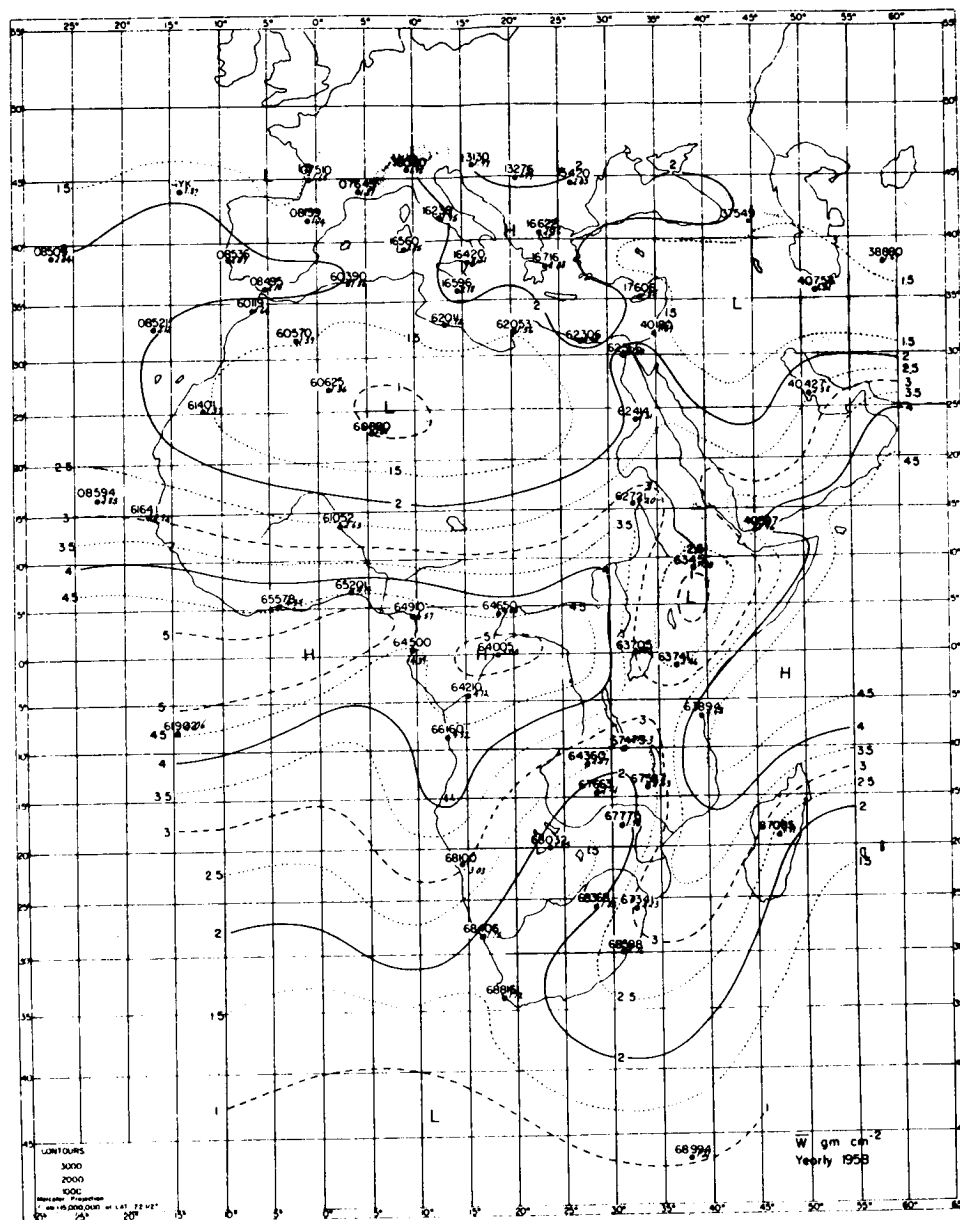


Figure V-13. The mean annual distribution of precipitable water in vapor form over the African continent. Units are gm/cm^2 . Data are from the IGY (1958). (Peixoto and Obasi, 1965.)

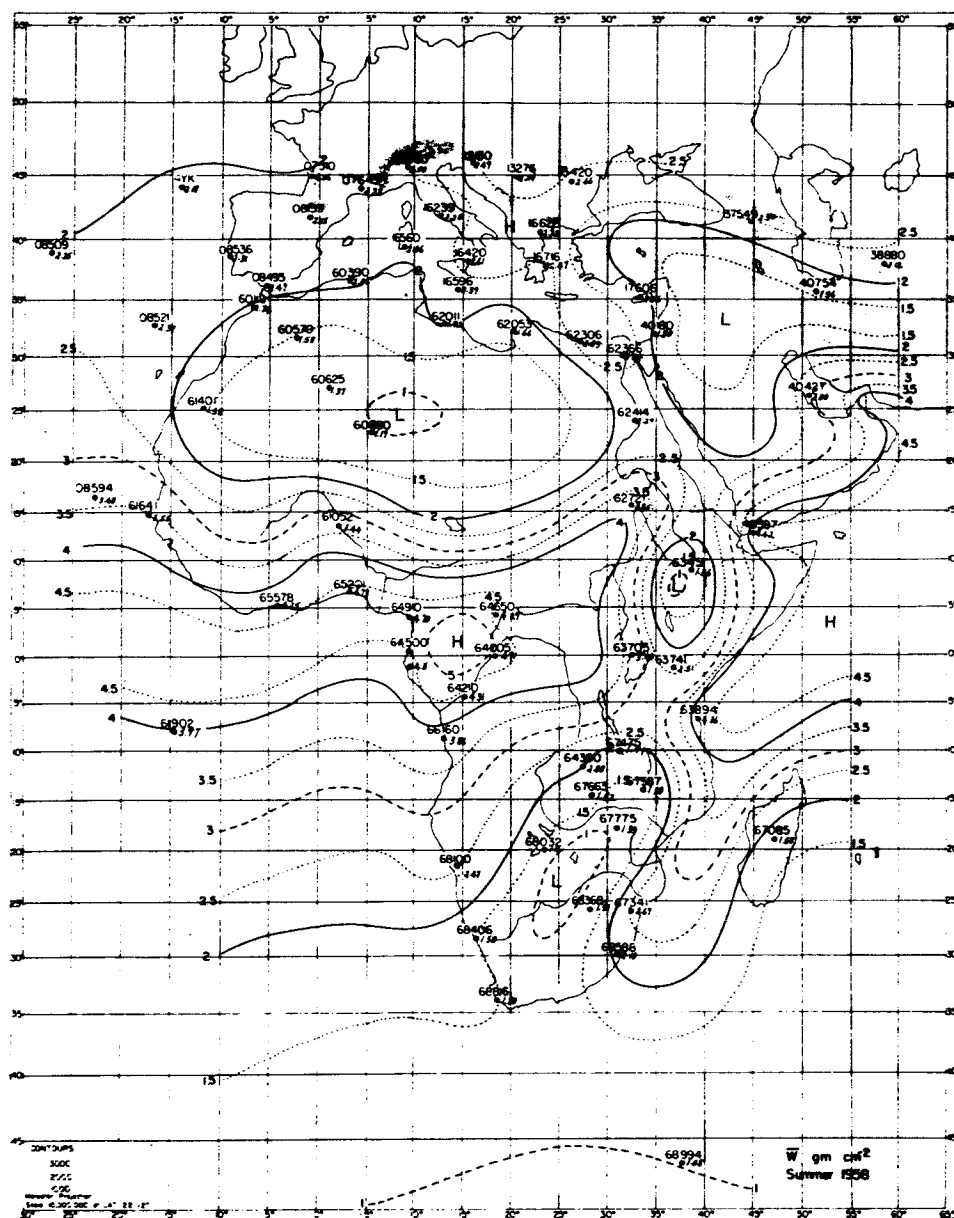


Figure V-14. The mean distribution of precipitable water in vapor form over the African continent in summer. Units are gm/cm^2 . Data are from IGY (1958). (Peixoto and Obasi, 1965.)

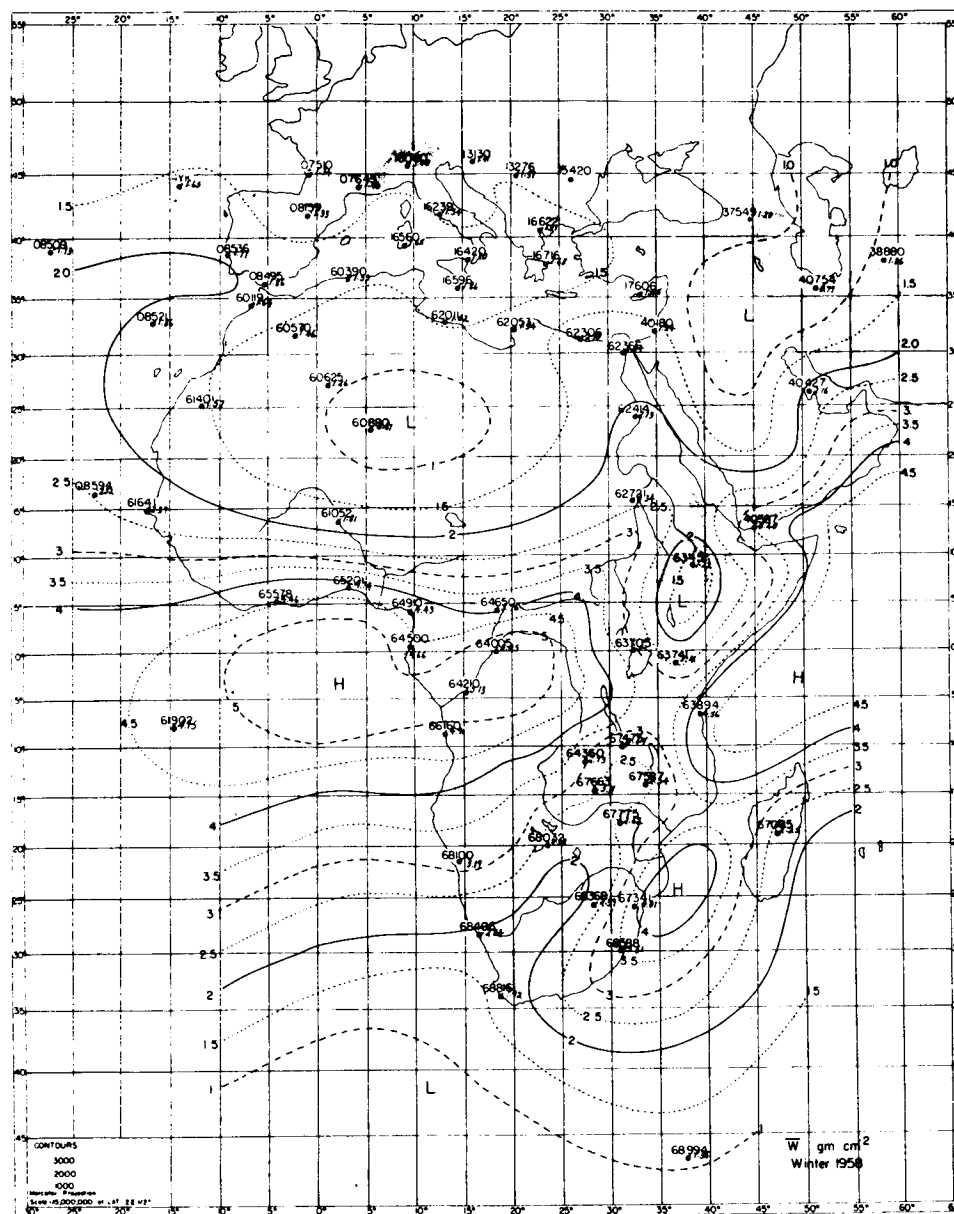


Figure V-15. The mean distribution of precipitable water in vapor form over the African continent in winter. Units are gm/cm². Data are from the IGY (1958). (Peixoto and Obasi, 1965.)

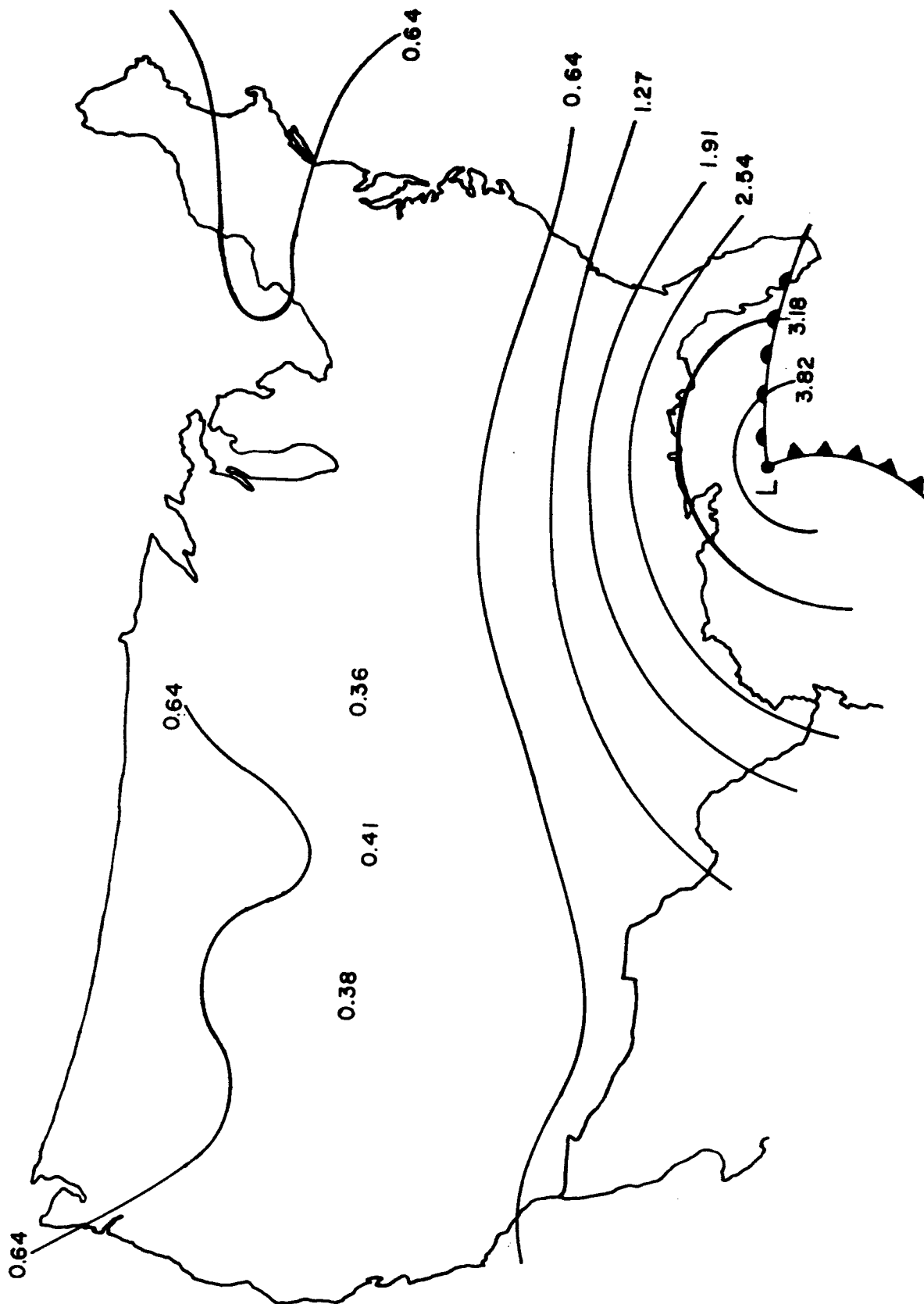


Figure V-16. Precipitable water over the U.S. in centimeters on the 16 March 1969 as reported by the U.S. Weather Bureau.

maximum value of the isopleth of precipitable water is 3.82 cm (1.5 inches) and one can expect that nearer the center of the low pressure area, the precipitable water vapor exceeds 4 cm.

The minimum value occurs out in the Midwest and is more than one order of magnitude less than the maximum over the Gulf. The lowest value reported was 0.36 cm (0.14 inches). Therefore, even for a situation which has not been chosen for its uniqueness, the contrast over synoptic scale distances exceeds three centimeters of precipitable water.

The time scale for changes in water vapor as large as those represented by the maximum and minimum in Figure V-16 is on the order of 1 to 2 days depending upon the vigor and speed of frontal movement. Typically, one can expect changes of 1 to 2 gm/cm² in periods as short as 1 to 2 hours for a fast moving cold front. Changes occurring ahead of a warm front may take, in contrast, from 6 hours to one day to change from a dry cool air mass to a warm sector type air mass through the process of overrunning.

As one more reference point, the maximum precipitable water measured over Boston in the summer of 1965 was 4.2 gm/cm², the least was 1.2 gm/cm². For the winter of 1965-66, the maximum was 3.5 gm/cm², the minimum 0.3 gm/cm². The average difference between contiguous air masses which

moved over the Boston area was of the order of 2 to 2.5 gm/cm². The general conclusion is that the maximum contrast or variability of the water vapor between air masses appears to be of the order of 3 to 4 gm/cm². Generally, however, the variability between adjacent air masses must be considerably below these values because many air masses away from equatorial zones simply do not contain this amount of precipitable water.

(3) Meso- and Microscale Variations

As one examines smaller and smaller scale sizes, the maximum precipitable water approaches the theoretical maximum which the atmosphere can hold, which is a saturated condition from the surface upward. For the Arctic Supplemental Atmosphere, (see Valley, 1965) this theoretical maximum is approximately 0.38 gm/cm². For the U.S. Standard Atmosphere the value is approximately 2.6 gm/cm², and for the Supplemental Tropical Atmosphere, the value goes as high as 6.1 gm/cm².

For similar reasoning the absolute humidity encountered will also approach a maximum as the scale decreases only being limited by the absolute temperature. In many thunderstorms, saturated conditions exist at temperatures as high as 20°C. The water vapor density can therefore be as high as 20 to 25 gm/m³ on the scale of these cloud formations. The highest recorded absolute humidity is ~30 gm/m³ corresponding to saturation at about 24°C (Valley, 1965).

The data, as presented so far, takes into account only water vapor in the troposphere and even then only in the lower part of the troposphere. Some attention should be given to the water vapor distribution above these levels.

The mixing ratio at the surface of the earth in midlatitudes is of the order of 10 to 20 grams of water vapor for every 1000 grams of dry air. The general trend is to have decreasing mixing ratios as one ascends, partially because of diminishing temperatures, and partly because the source for atmospheric water vapor is at the surface.

Few measurements of stratospheric water vapor exist, but from those which do appear to be valid, the mixing ratio in the lower stratosphere has been shown to be of the order of 2 to 3 parts per million (Mastenbrook and Purdy, 1969). That is, for every 1000 grams of dry air, approximately $2 \text{ or } 3 \times 10^{-3}$ grams of water vapor exist, about two to three orders of magnitude less than at the surface. The stratosphere appears to be very dry. Only a few measurements have been taken to establish the spatial and temporal variations in the stratosphere. They do not, as yet, show much variability from the values quoted above.

In order to bring some complete picture together out of the discussions about precipitable water vapor and its temporal and spatial

variations, Figure V-17 is presented. It is an attempt to establish some link between scale size and maximum precipitable water vapor, and between scale size and maximum variability over a distance of two scale sizes. It is hypothetical in the sense that no carefully prepared set of statistics back it up. It is drawn wholly from the information presented so far and the experience which the authors have had developing and working with atmospheric models.

B. Coupling Considerations Between Microwave Energy and Atmospheric Water Vapor

Before we attempt to combine the theoretical results of Chapter II, with the summary of the world wide water vapor distribution statistics as given in part A of this chapter, it will prove useful to review some important considerations about the coupling between the water vapor distribution and microwave energy.

(1.) Weighting Functions

A most useful concept is the weighting function. It can be defined in a number of ways, but perhaps the simplest is that for water vapor absorption given by:

$$WF_1 = \frac{\gamma_{H_2O}(v, P, T, \rho)}{\rho} \quad dB(gm/m^3)^{-1}m^{-1} \quad (5 - 1)$$

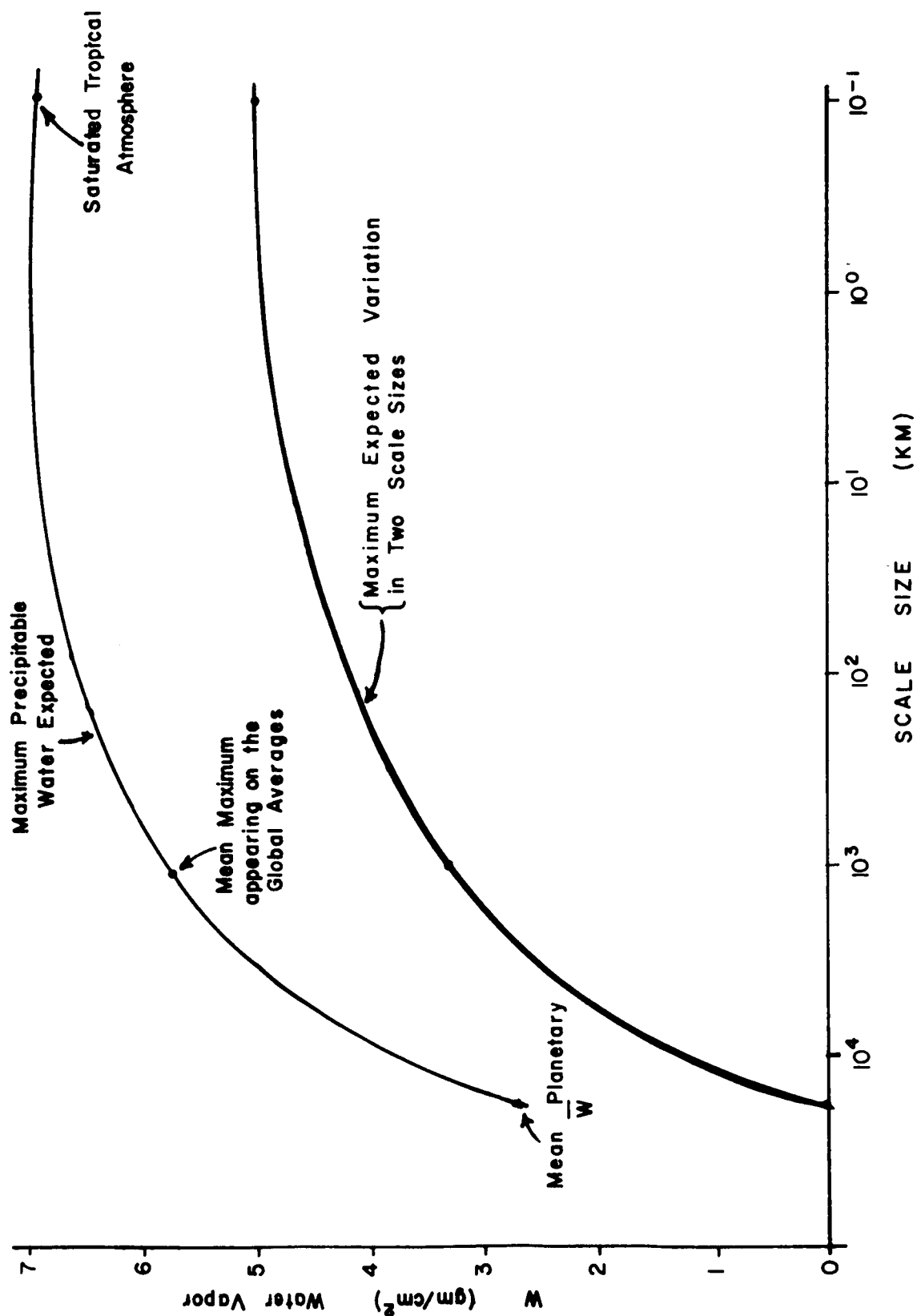


Figure V-17. Hypothetical curves describing the maximum precipitable water in vapor form and maximum variation of this parameter over two scale sizes as a function of scale size.

WF_1 is the designation for this weighting function, γ_{H_2O} is the absorption coefficient in dB/m for some frequency and set of atmospheric conditions, and ρ is the water vapor density in gm/m^3 . Essentially, it is the absorption per unit water vapor density per unit length, typically given in decibels per gram per cubic meter per meter ($dB (gm/m^3)^{-1}m^{-1}$). It is the absorption which a layer of water vapor one meter thick would cause at a density of one gram per cubic meter at ambient pressure and temperature.

There is a second order effect of water vapor on its own broadening parameter, hence there would be slight differences in WF_1 for the same pressure and temperature if γ_{H_2O} were measured at different water vapor densities. However, the difference is so slight as to be unimportant in most applications.

By the definition of WF_1 for the particular atmospheric conditions which defined γ_{H_2O} as a function of height, then the total opacity can be written as

$$\tau(\nu) = \int_0^H WF_1 \rho \, dz \quad (dB) \quad (5-2)$$

where WF_1 is in $dB(g/m^3)^{-1} m^{-1}$, ρ is in g/m^3 and z is in meters. The shape of the WF_1 curve as a function of height differs depending

upon whether the frequency chosen is on the resonant frequency of a water vapor transition, near a resonant frequency, or somewhat removed from such a resonance. The characteristic shapes of these three spectral regions is shown in Figure V-18 taken from Gaut (1967).

The curve for 22.235 GHz is exactly on the lowest water vapor rotational transition resonant frequency. WF_1 for this condition is proportional to $1/P$ and therefore increases monotonically as pressure decreases. The curve for 19.00 GHz is far enough removed from the resonant frequency to show the characteristic non-resonant behavior, that is a direct dependency upon pressure. Therefore, WF_1 for this frequency decreases monotonically with the pressure. The curve for WF_1 at 21.900 GHz shows a characteristic maximum. This occurs because of competing effects. Below the maximum the resonant effect, proportional to $1/P$, is dominant. Eventually the line narrows so much as pressure decreases that the spectral region becomes essentially a non-resonant region and decreases in direct proportion to the pressure. The height of the maximum is a function of frequency. The vertical width of the half amplitude points is typically 10 to 15 km.

The utility of the weighting function concept depends considerably upon its stability from atmospheric profile to atmospheric profile. WF_1 happens to be very stable as shown in Figure V-19 for a frequency of 19.0 GHz. If a mean value were chosen among the atmospheres represented,

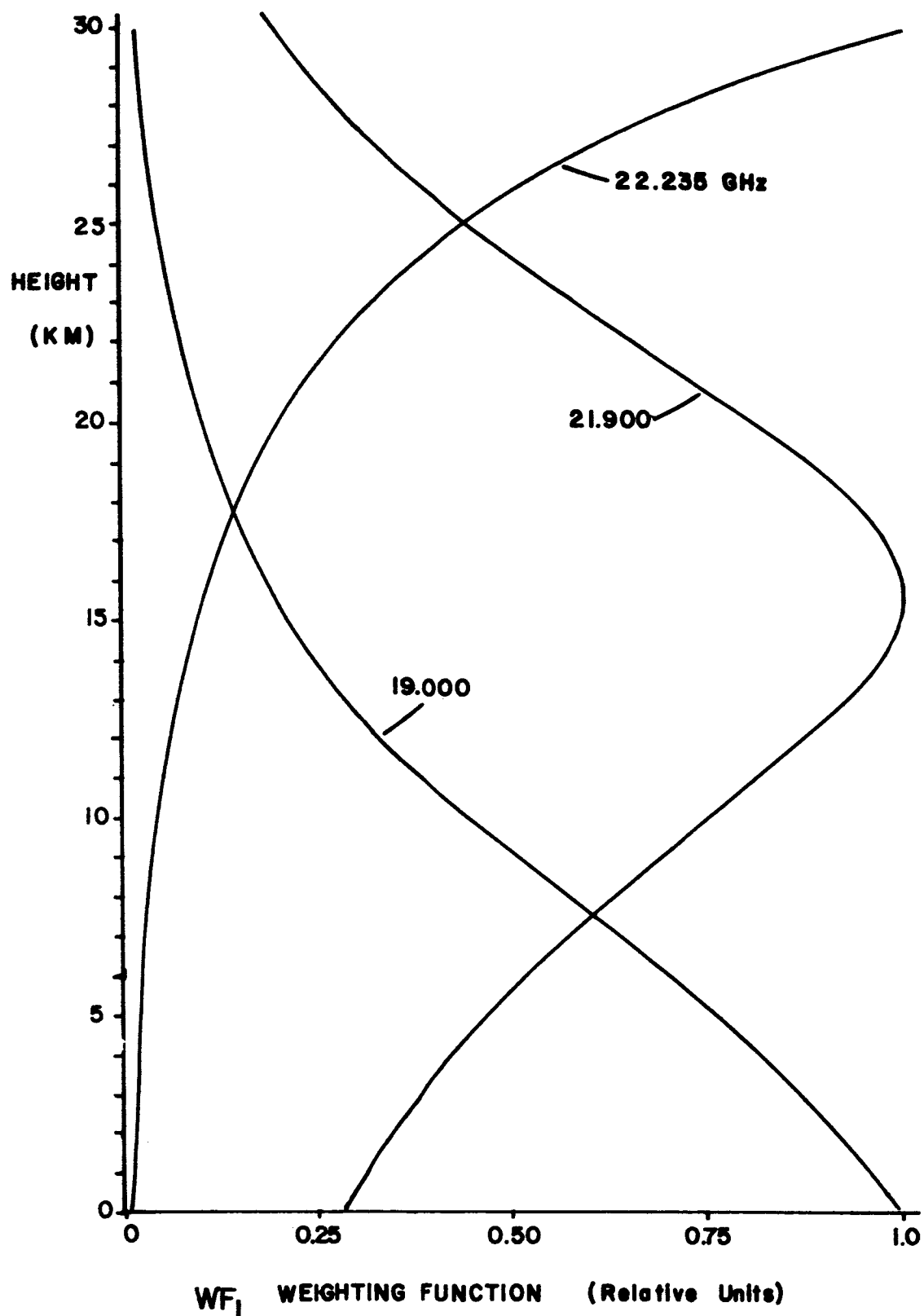


Figure V-18. Weighting function WF_1 for absorption versus height for 19.0, 21.9 and 22.235 GHz. Values have been normalized. (Gaut, 1968)

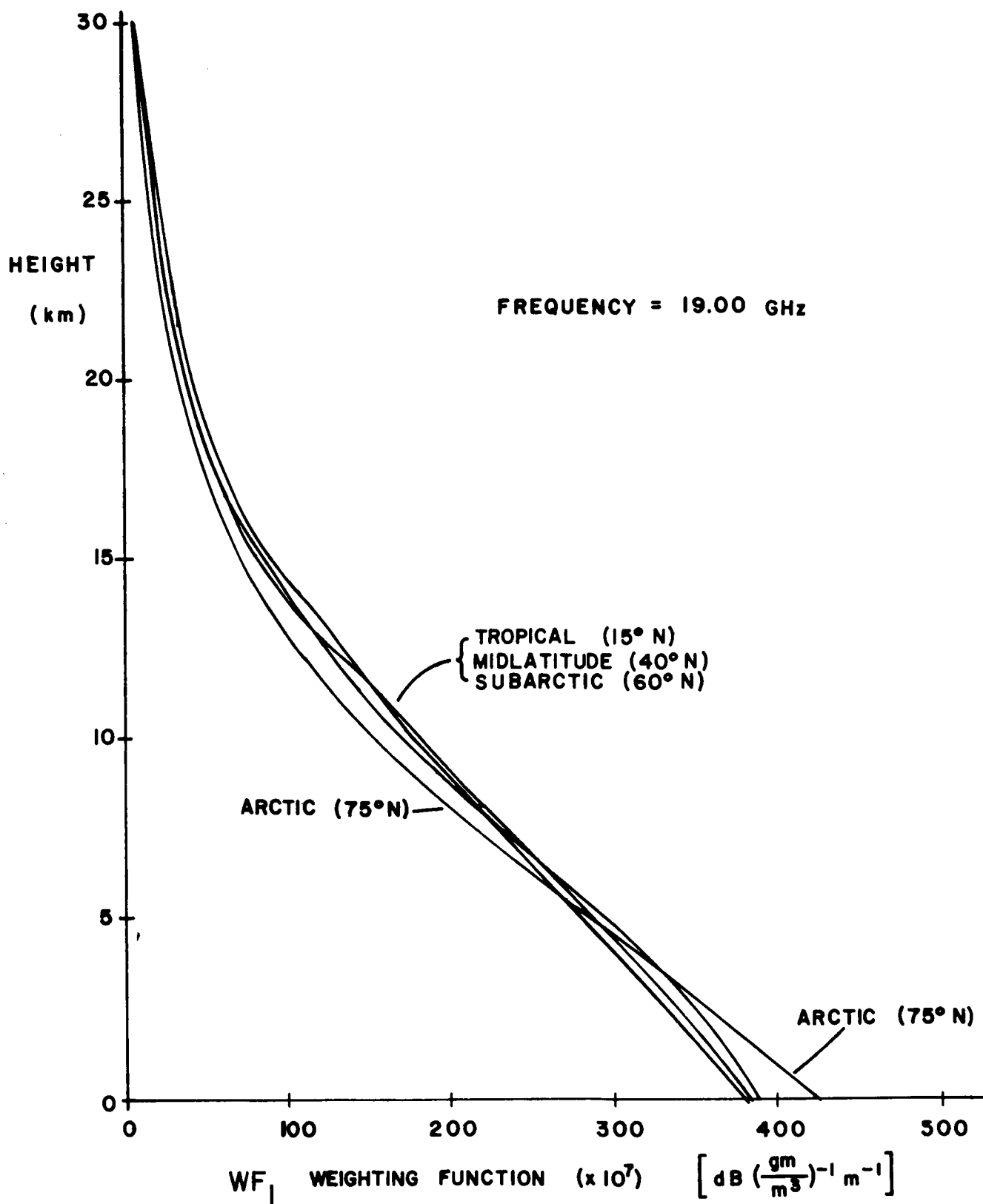


Figure V-19. The stability of the weighting function WF_1 at 19.0 GHz for various standard atmospheres over the earth. (Gaut, 1968)

the surface variation would be the greatest and would be less than $\pm 5\%$. If the extreme Arctic atmosphere is removed, the variation is approximately $\pm 1\%$. The atmospheres are those given in Valley (1965).

A second weighting function which relates the emission of noise energy by atmospheric water vapor to atmospheric conditions is that one which measures the contribution of a unit thickness of unit density water vapor at some ambient condition to the energy received by a radiometer at the ground viewing the zenith. We will call this weighting function WF_2 and define it as follows for those regions of the spectrum in which the Rayleigh-Jeans approximation may be applied:

$$WF_2 = \frac{T_{AT}(z) \gamma_{H_2O}(z) e^{-\tau_v(z,0)}}{\rho(z)} \quad (5-3)$$

in which WF_2 is the weighting function for energy received at the receiver on the surface usually given in $^{\circ}K (g/m^3)^{-1} m^{-1}$, T_{AT} is atmospheric temperature in $^{\circ}K$, γ_{H_2O} is the absorption coefficient in dB/m, ρ is water vapor density in g/m^3 and $\tau(z,0)$ is the integrated opacity in nepers between the level z and the surface.

This weighting function WF_2 is a measure of the energy emitted by a unit density, unit thick layer of water vapor at a temperature and pressure at some height, diminished by the absorption between that layer and the surface. Because it takes into account the absorption

beneath it, this weighting function is more sensitive to the actual water vapor distribution in the atmosphere than WF_1 . However, the general shape of WF_2 is remarkably similar to WF_1 in regions of the spectrum which are mostly transparent. Such a transparent region extends everywhere below 40 GHz.

Figure V-20 gives the weighting functions WF_2 for the same frequencies as used to illustrate WF_1 . The reason for the similarity is that to first order, the emission is proportional to $T_{AT}\gamma_{H_2O}$, the temperature of the atmosphere multiplied by the absorption coefficient. Since the percentage change in temperature is small the shape conforms to the γ_{H_2O} curves. The stability of the 19.000 GHz curve over different atmospheric conditions is depicted in Figure V-21.

The usefulness of WF_1 does not diminish as opacity increases. Since the weighting function for absorption does not depend upon any conditions outside the layer under consideration, the linear dependence of total absorption on ρ_{H_2O} remains within very wide bounds.

The same is not true for WF_2 . Because increasing opacity affects the percentage of energy reaching the radiometer from any given layer, the whole concept of WF_2 rapidly loses its invariance and becomes useful only for a given set of water vapor, temperature and pressure conditions. As an example of the drastic changes in the geometrical source region of

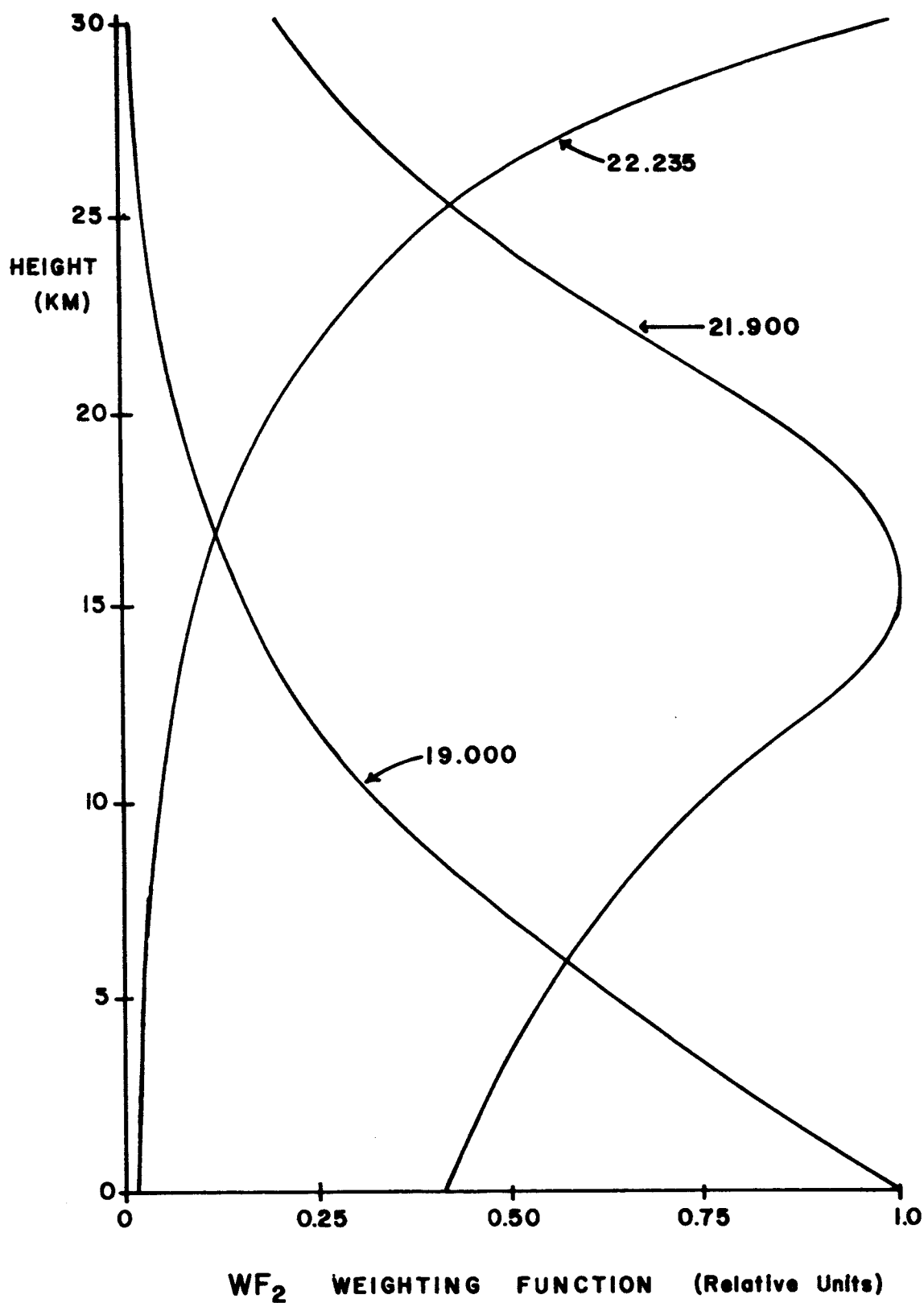


Figure V-20. Normalized weighting function WF_2 for a zenith viewing radiometer at 19.00, 21.90, and 22.235 GHz as a function of height in the U.S. Standard Atmosphere. (Gaut, 1968)

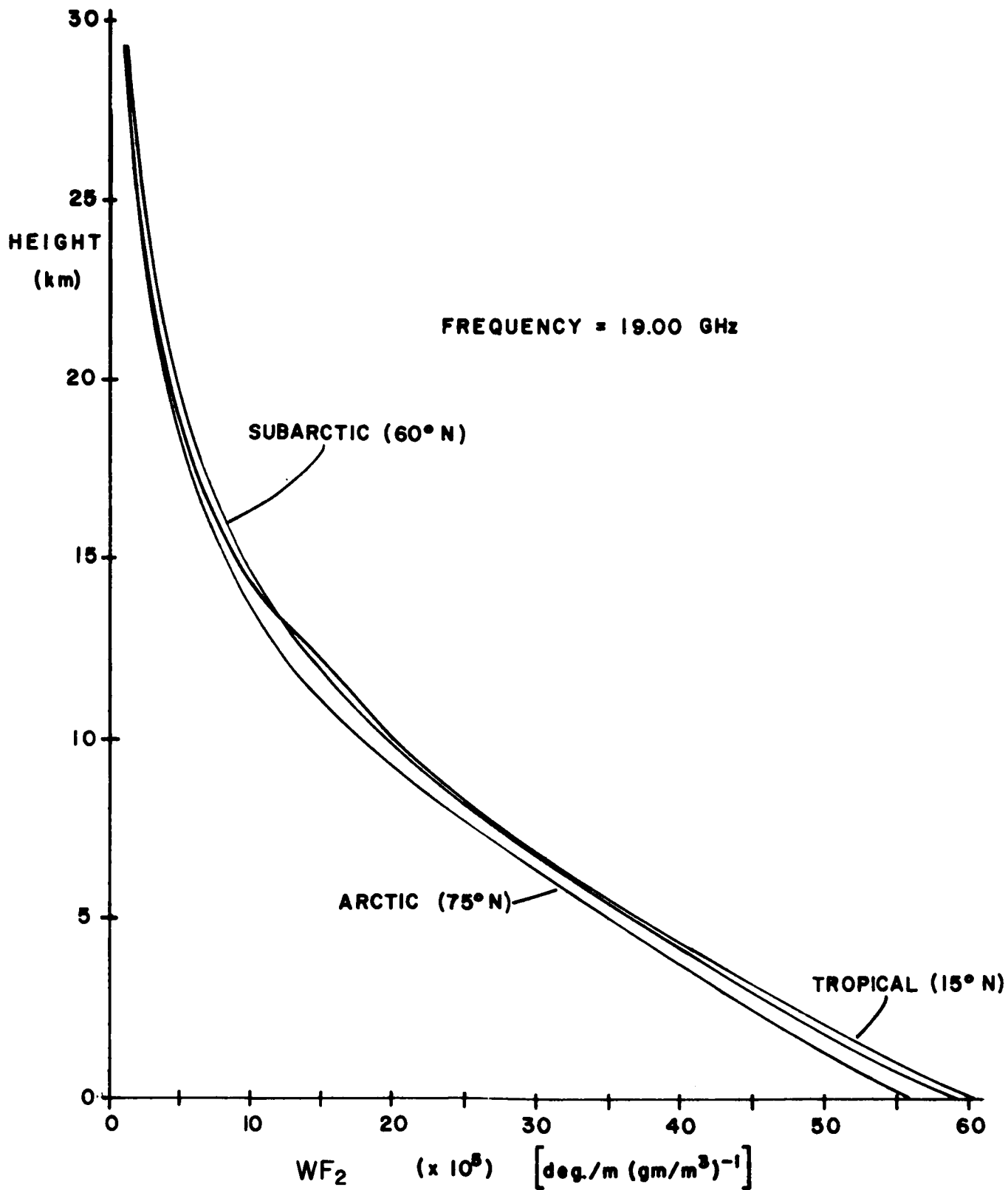


Figure V-21. Stability of the weighting function WF_2 at 190 GHz for various standard atmospheres over the earth. (Gaut, 1968)

energy received by a surface radiometer, Figure V-22 is presented. The frequency is on the resonant peak of the second lowest rotational line of water vapor at 183.310 GHz. In progressively more moist conditions the energy received is confined more and more closely to the immediate vicinity of the radiometer, reaching a minimum in the tropical example in which 90% of the energy is received from less than 125m. In the arctic atmosphere the integrated water vapor is approximately 0.30 gm/cm²; in the midlatitude atmosphere approximately 2.0 gm/cm²; and in the tropical atmosphere approximately 4.2 gm/cm². The total opacity for each of these atmospheres at this frequency is approximately 16 dB, 96 dB and 212 dB respectively.

If one looks from space toward the earth's surface in frequency intervals which exhibit large opacities, one sees only part way into the atmosphere. The absorption is so great that one sees radiation only from the top part of the atmosphere, and for the frequencies near 193 GHz this means above the stratopause. Figure V-23 shows the brightness temperature as a function of frequency for two atmospheres: the Tropical Supplemental, and U.S. Standard Atmospheres both with mixing ratios of 2×10^{-6} g/g in the stratosphere and mesosphere. The radiation in each case essentially originates in the 60 to 66 km regions. The coldest temperatures originate at the highest altitudes.

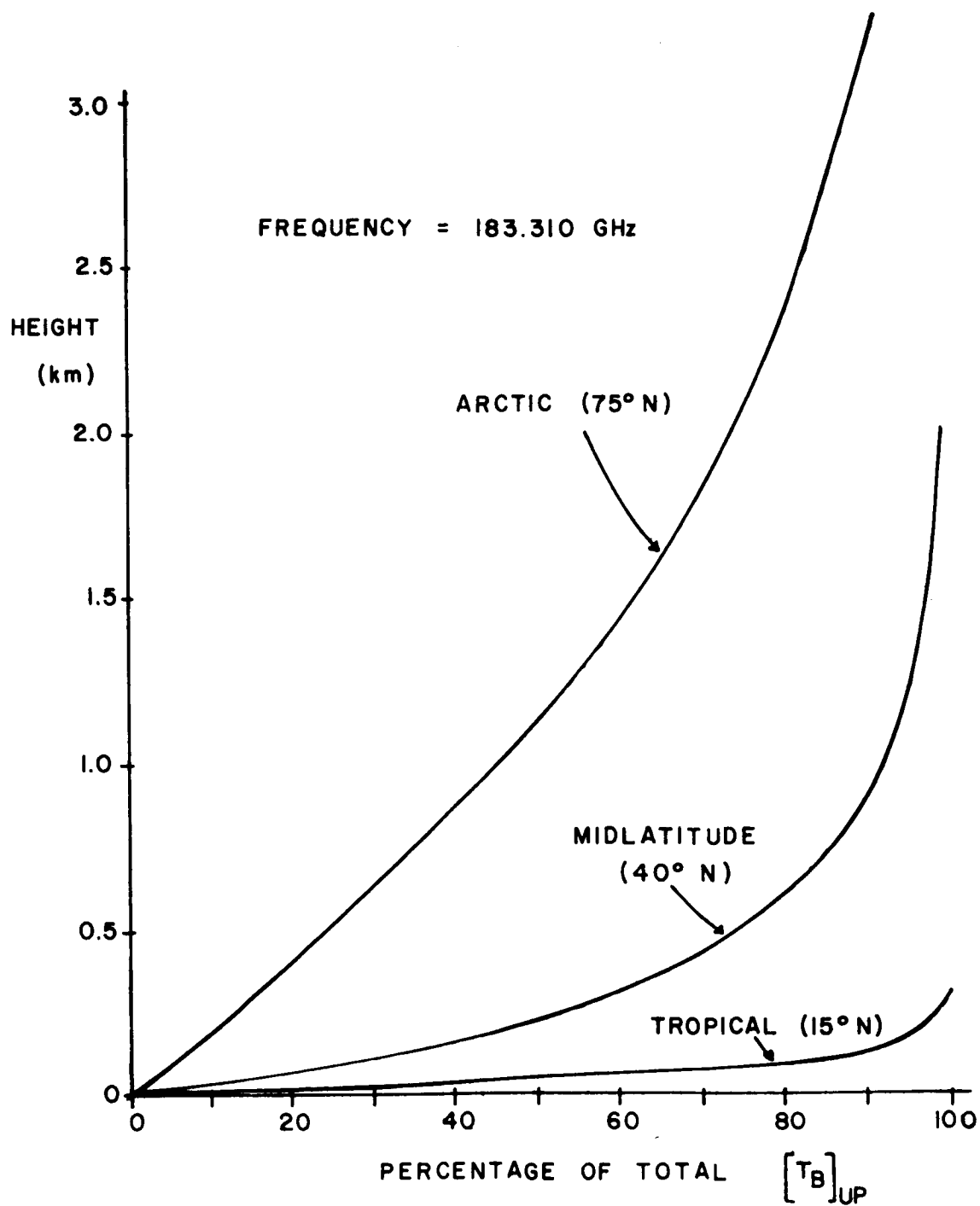


Figure V-22. The percentage of total energy received by a zenith viewing radiometer height at 183.310 GHz in several standard atmospheres. (Gaut, 1968)

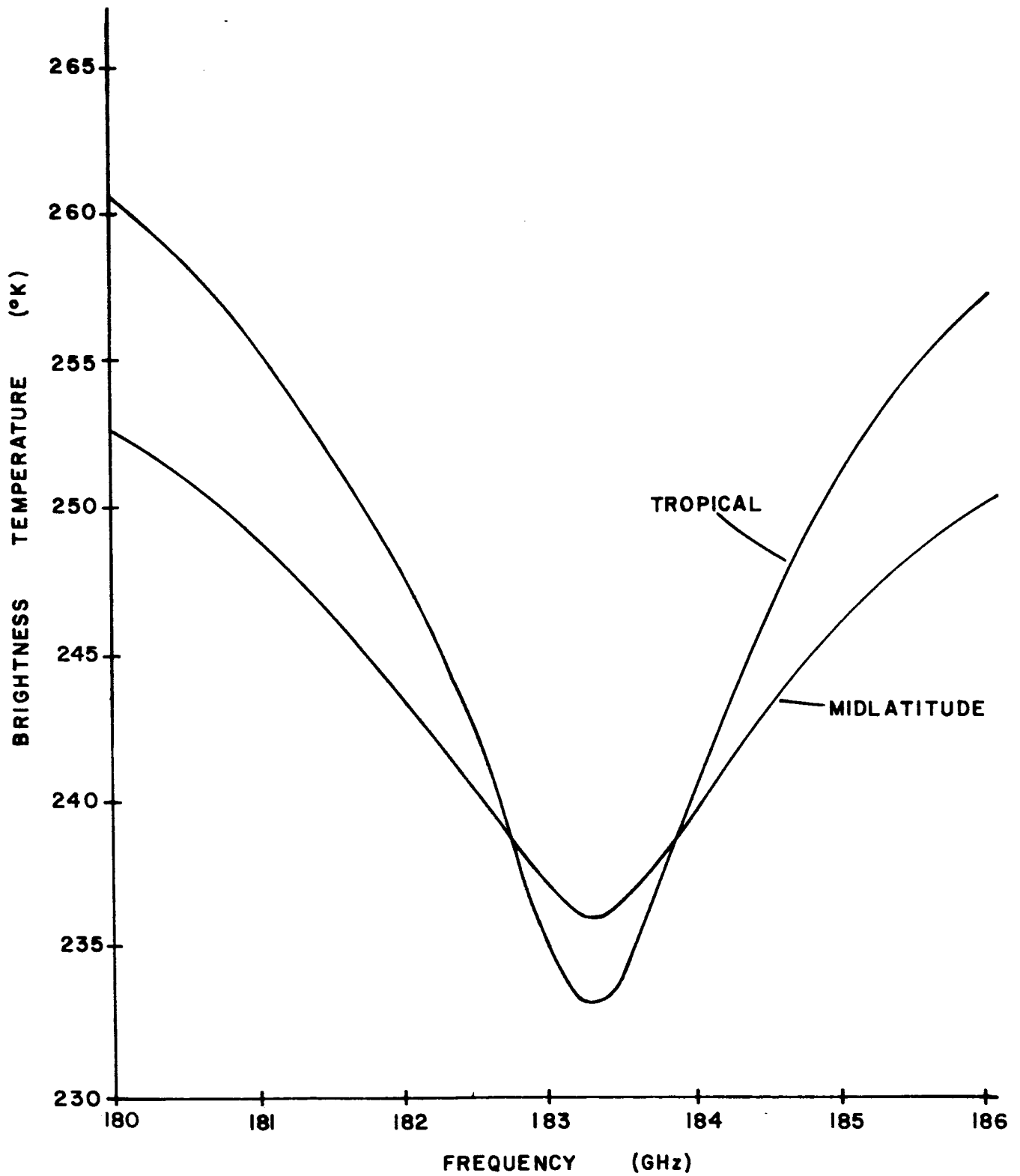


Figure V-23. The brightness temperature as seen by a satellite viewing the nadir based radiometer in the vicinity of the 183 GHz line in a tropical and midlatitude atmosphere. (Gaut, 1968)

(2.) The Relationship Between Water Vapor Variations and Variations in The Energy Received by a Radiometer

The weighting function concept is useful, with the restrictions already mentioned, to now analyze the actual origin of the energy which a radiometer receives from a hypothetical water vapor distribution and the expected coupling between variations in atmospheric water vapor and signal variations at the radiometer.

The weighting function curve is derived from unit water vapor density everywhere. The actual atmosphere, of course, normally distributes water vapor more like an exponential function so that actual energy received at frequencies removed from resonances is even more restricted to the lowest levels of the troposphere. Figure V-24 gives the example of WF_2 at 19.0 GHz multiplied by the equatorial distribution of water vapor density from Figure V-5. The result emphasizes the dominant role of the lower troposphere; more than 50% of the signal is received from below 1.5 km.

With the curve of $(WF_2 \times \rho)$ in mind, one can easily visualize the influence of fluctuations in water vapor at any level in the atmosphere. The area under this curve represents the total energy received by the radiometer, call it A. If, for example fluctuations as drastic as one hundred percent occurred in the two to three

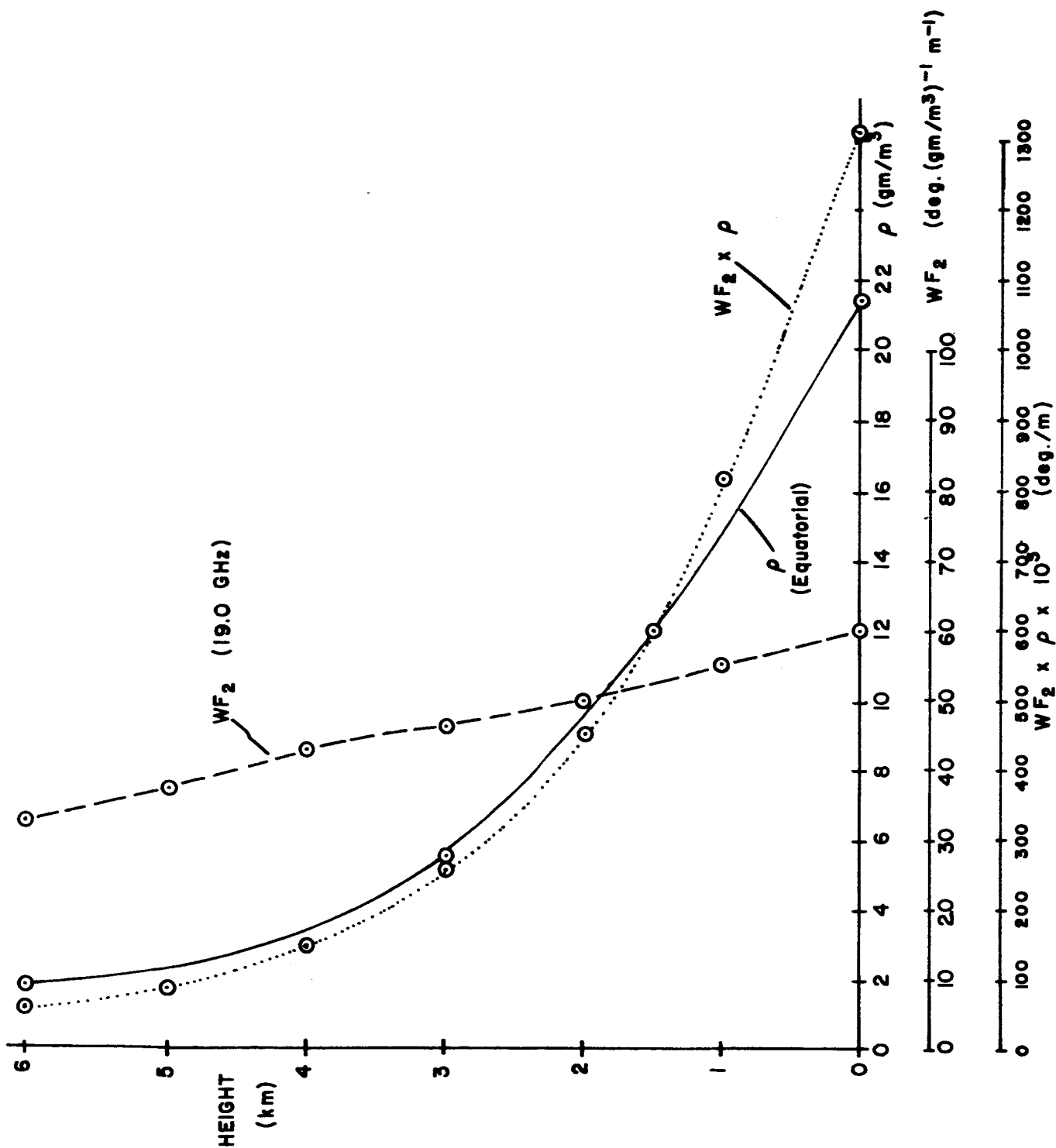


Figure V-24. The weighting function WF_2 , the mean tropical water vapor distribution, and the emission ($WF_2 \times \rho$) as a function of height.

kilometer layer the fractional change in surface signal would be proportional to a/A where 'a' is the area between the ordinate values 2 and 3 km and the curve ($WF_2 \times \rho$). In the case illustrated by Figure V-24, if 'A' is equal to unity, then 'a' is equal to 0.15. Since the signal for this example is 23.4°K, the variation caused by the one hundred percent fluctuation between 2 and 3 km is $\pm 3.5^\circ\text{K}$, and easily measurable variation.

In conditions in which the opacity is high, the simple approach outlined above is not applicable. In that case, any change in water vapor on any level will influence the radiation which originates above that level. The only sure analysis of signal fluctuations is to compute in detail the signal and weighting function for both normal and perturbed conditions. Further, since the coupling in the high opacity case is so complete, differences in temperature cannot be ignored, as brought out in Figure V-23.

(3.) The Effect of Viewing Geometry

Not only will the degree of coupling, that is the opacity, affect the signal variability for a given set of water vapor conditions, but so will the viewing geometry. For exactly the same set of water vapor variations and radiometer design, different signal variations will be evident.

To illustrate this difference refer to Figure V-25. Because the bulk of the water vapor is found in a layer only several kilometers thick, there is a drastic difference in the volume sampled by an upward looking radiometer from the surface and a downward looking radiometer from space. A radiometer with a 3° beamwidth looking up sees, at the 5 km level, a circle approximately 250m in diameter. A down looking radiometer from 160 km sees a spot 8 km in diameter at the surface. The smoothing effect for water vapor variability is very pronounced between scale sizes of 250m and 8 km.

C. Representative Absorption and Noise Energy Computations

The information so far presented on water vapor and water vapor spectra can be utilized in a number of ways. In this part of the chapter, several examples of what can be done are presented.

(1) Atmospheric Water Vapor Spectra

Basic to all computations is the requirement to compute atmospheric spectra for various atmospheres and water vapor distributions. Figure V-26 presents the opacity of the atmosphere in decibels as a function of the frequency in GHz. The atmospheres and water vapor distributions correspond roughly to the mean annual zonal average of water vapor taken from Figure V-1 at the equator (4.5 gm/cm^2), at 30° from the equator (2.5 gm/cm^2), and in the polar regions (0.5 gm/cm^2).

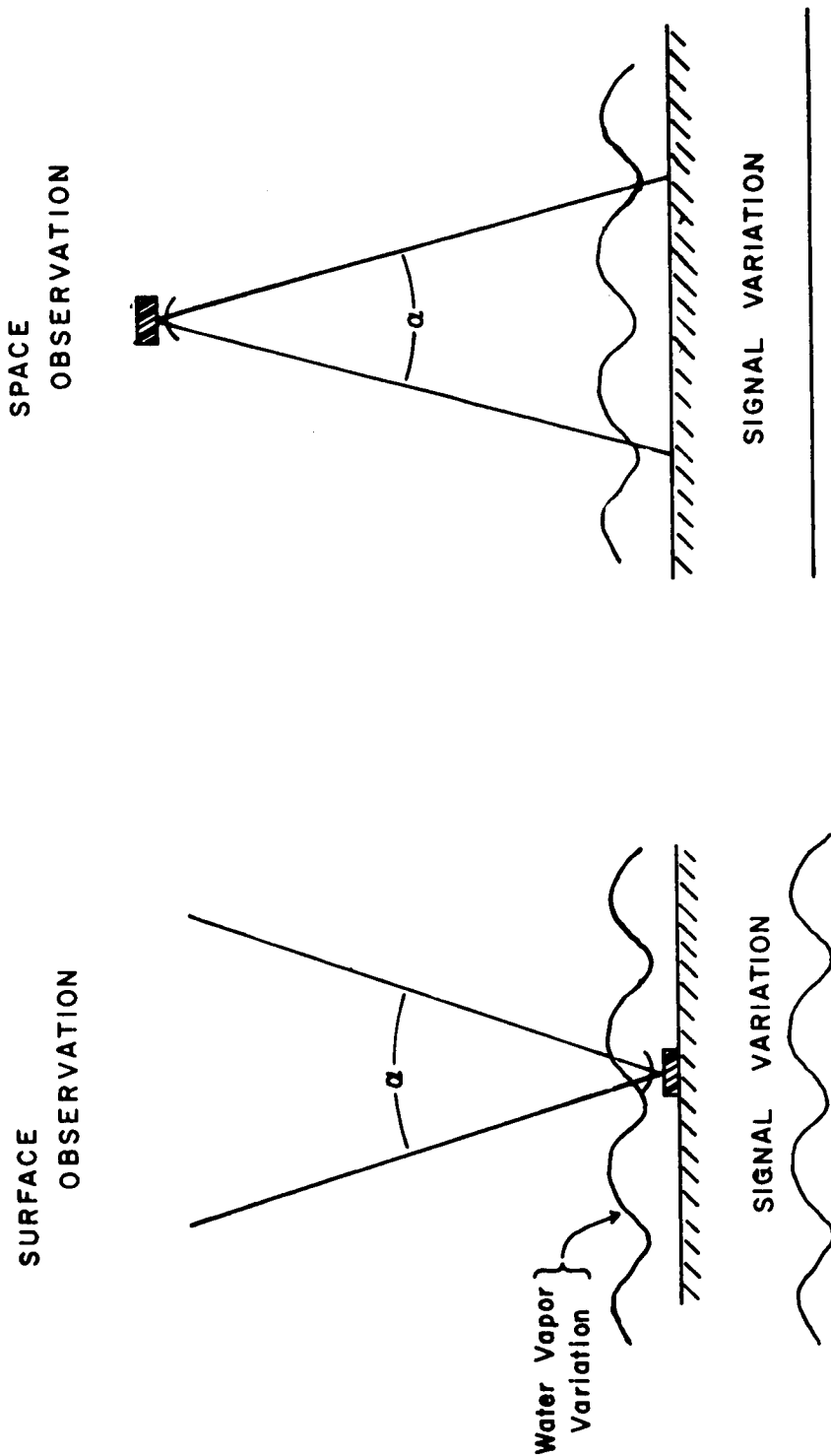


Figure V-25. The effect of surface versus space observations on the expected signal variability caused by hypothetical variations in the precipitable water of the atmosphere.

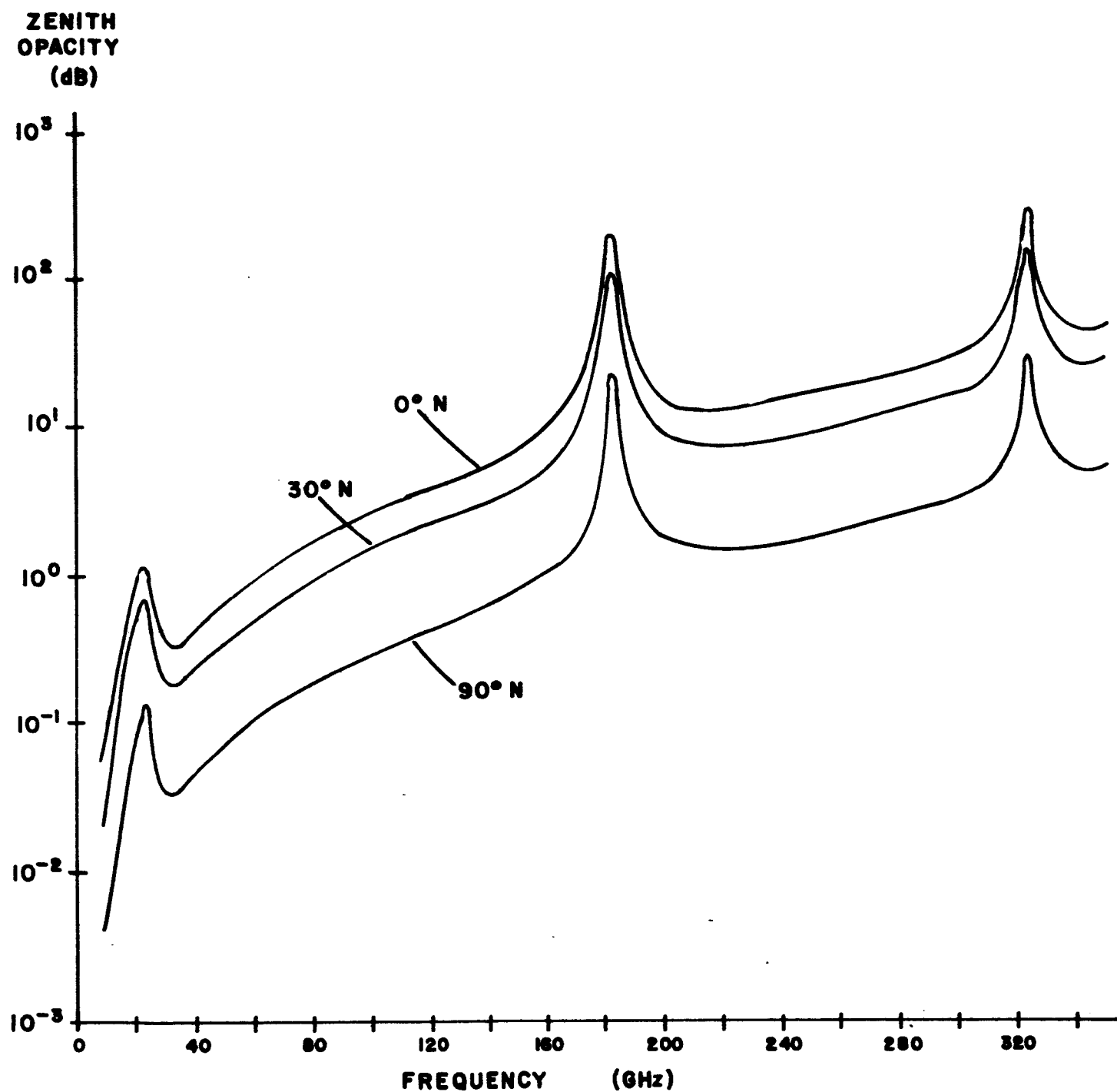


Figure V-26. The opacity due to atmospheric water vapor between 10 and 350 GHz for 0.5, 2.5 and 4.5 gm/cm², corresponding approximately to mean zonal values at 0°, 30° N and 90° N.

If we first examine the spectrum up to 300 GHz, the nominal limit for microwaves, several features can be seen: (1) the maximum opacity attained is on the peak of the 183 GHz line and exceeds 200 dB for the tropical case; (2) the minimum between the 22 GHz and 183 GHz line occurs between 29 and 35 GHz and ranges between 0.03 and 0.3 dB; the minimum between the 183 GHz and 324 GHz line occurs in the region of 210 GHz to 225 GHz and exhibits opacities between 1.5 dB and approximately 13 dB.

Above 300 GHz the minimum value expected is at 300 GHz. In the arctic case the opacity computed is 3 dB. In the tropical case at 300 GHz, the value increases to well above 20 dB.

A second useful means of presenting atmospheric absorption data can be made for a particular geographical location. Figure V-27 presents such data for La Jolla, California. For this information one year's worth of radiosonde data was analyzed for the water vapor statistics, and the absorption statistics computed from these statistics. The curves show the mean absorption and the one sigma limits about this mean for water vapor absorption alone. The contribution of clouds or oxygen were not included in these curves. Clouds will be discussed in the next chapter. It is interesting to note that the mean and the one sigma curves do not vary much from the arctic, midlatitude, and equatorial curves of Figure V-26.

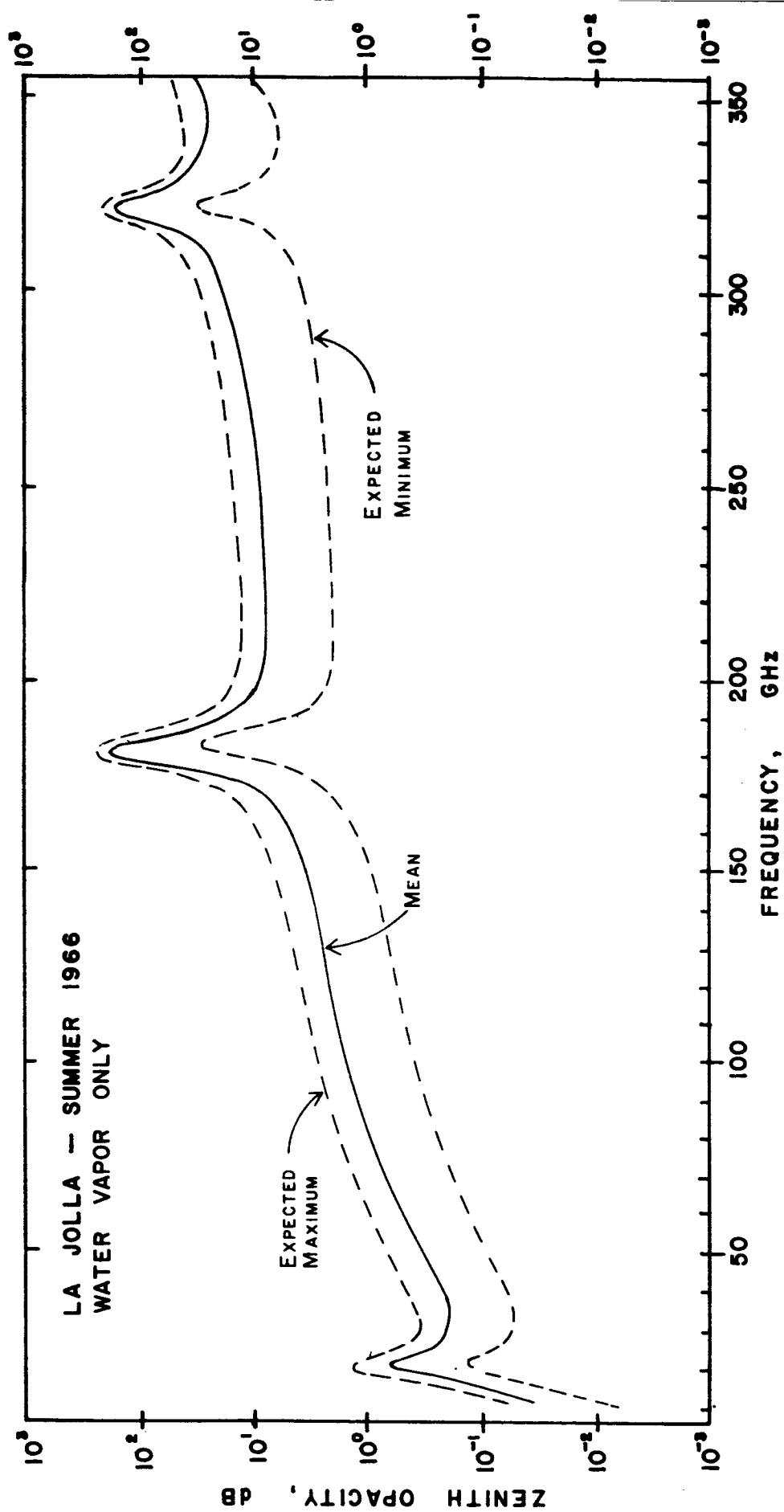


Figure V-27. The water vapor absorption spectrum between 10 and 350 GHz for: (1) the mean annual atmospheric conditions near La Jolla, California; and (2) for the one sigma deviations from these atmospheric conditions.

Rather than presenting absorption data with fixed water vapor and variable frequency, the frequency can be held constant and the water vapor varied. Figures V-28 and V-29 are plots using this latter format. Figure V-28 presents atmospheric opacity τ as a function of precipitable water W at various frequencies for a mid-latitude atmosphere. The plots show up as curves on the log-linear plot but in reality are quite linear with W . The log-linear plot was used in order to display all of the frequencies.

Figure V-29 plots the total brightness temperature due to water vapor alone for zenith viewing radiometer. This last point should be emphasized. In addition to the contribution which is shown, absorption due to oxygen must be added. For the frequencies chosen oxygen is relatively important only at 12 GHz. For those frequencies for which the atmosphere remains mostly transparent, the curves of T_B versus W are quite linear in precipitable water. At those frequencies which are more opaque the brightness temperature approaches the mean temperature of the atmosphere and saturates. At the highest frequencies, only miniscule amounts of water vapor do not produce saturation.

The frequencies displayed on Figures V-28 and V-29 were chosen to represent window and resonant peaks of the region between 10 GHz and 324 GHz. 12 GHz is well below the lowest rotational line;

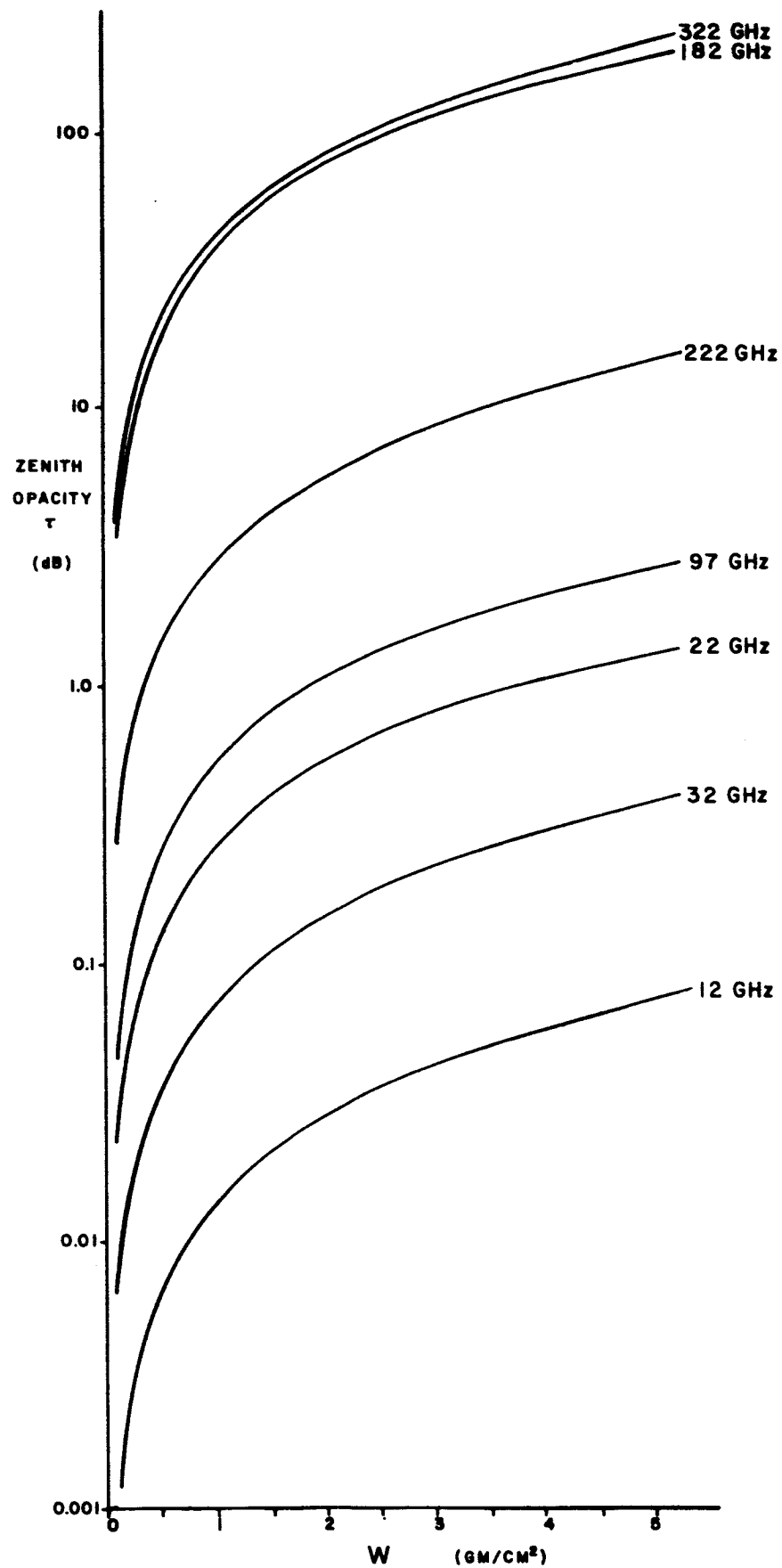


Figure V-28. Atmospheric opacity due to water vapor alone versus precipitable water in vapor form for 12, 22, 32, 97, 182, 222 and 322 GHz.

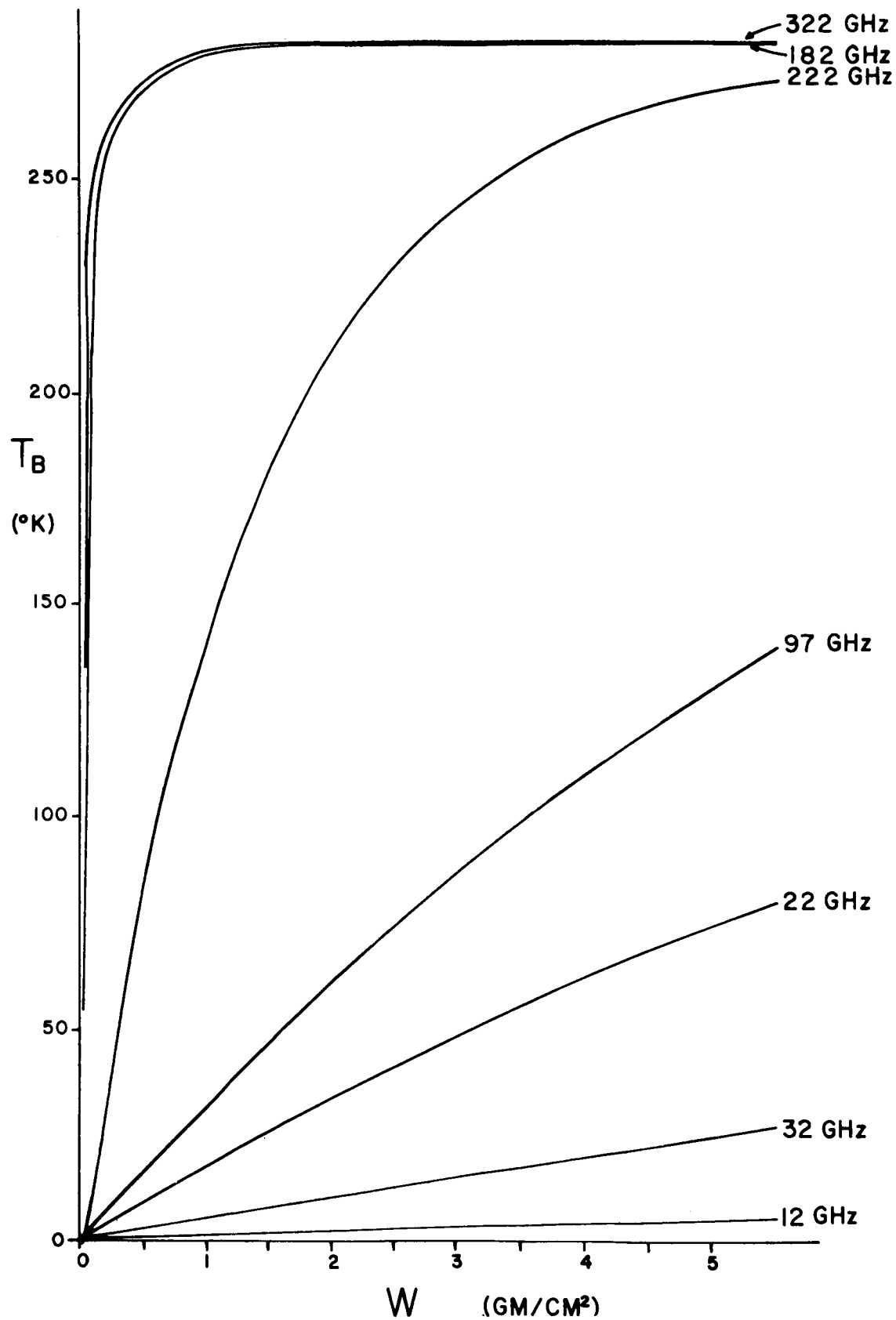


Figure V-29. Atmospheric brightness temperature due to water vapor alone of a zenith viewing radiometer versus precipitable water in vapor form for 12, 22, 32, 97, 182, 222 and 322 GHz.

22 GHz is near the lowest water vapor resonance (22.235 GHz); 32 GHz is in the region of minimum absorption between the lowest line and the next to lowest line (183.310 GHz); 97 GHz is near the minimum absorption which occurs above the oxygen complex of lines near 50-70 GHz but below the single oxygen line at 118 GHz; 182 GHz is near the peak of the second lowest frequency water vapor line; 222 GHz is near the minimum value between the 183 GHz water vapor line and the two lines near 324 GHz; and 322 GHz is near the peak of these last two lines.

A final format for the presentation of atmospheric water vapor radiation data is used in Figures V-30 through V-41. Its purpose is to bring out the spatial distribution of absorption and noise energy for mean conditions. It can be used for preliminary planning purposes both for communication design and earth observations applications. In Figures V-30 through V-41 the northern and southern hemisphere precipitable water distributions are translated into distributions of absorption and noise energy for the frequencies 12 GHz, 32 GHz and 97 GHz. At a glance one can get a feel for the range of values to be expected and their distribution over the earth.

The maximum absorptions at 12, 32 and 97 GHz are 0.08, 0.4, and

2.7 dB respectively. These translate into noise energies of 5°, 25°, and 130°K, respectively. Patterns remain the same as the corresponding precipitable water maps because at no time does the linearity seriously breakdown between water vapor and γ_{H_2O} or T_B at the frequencies chosen.

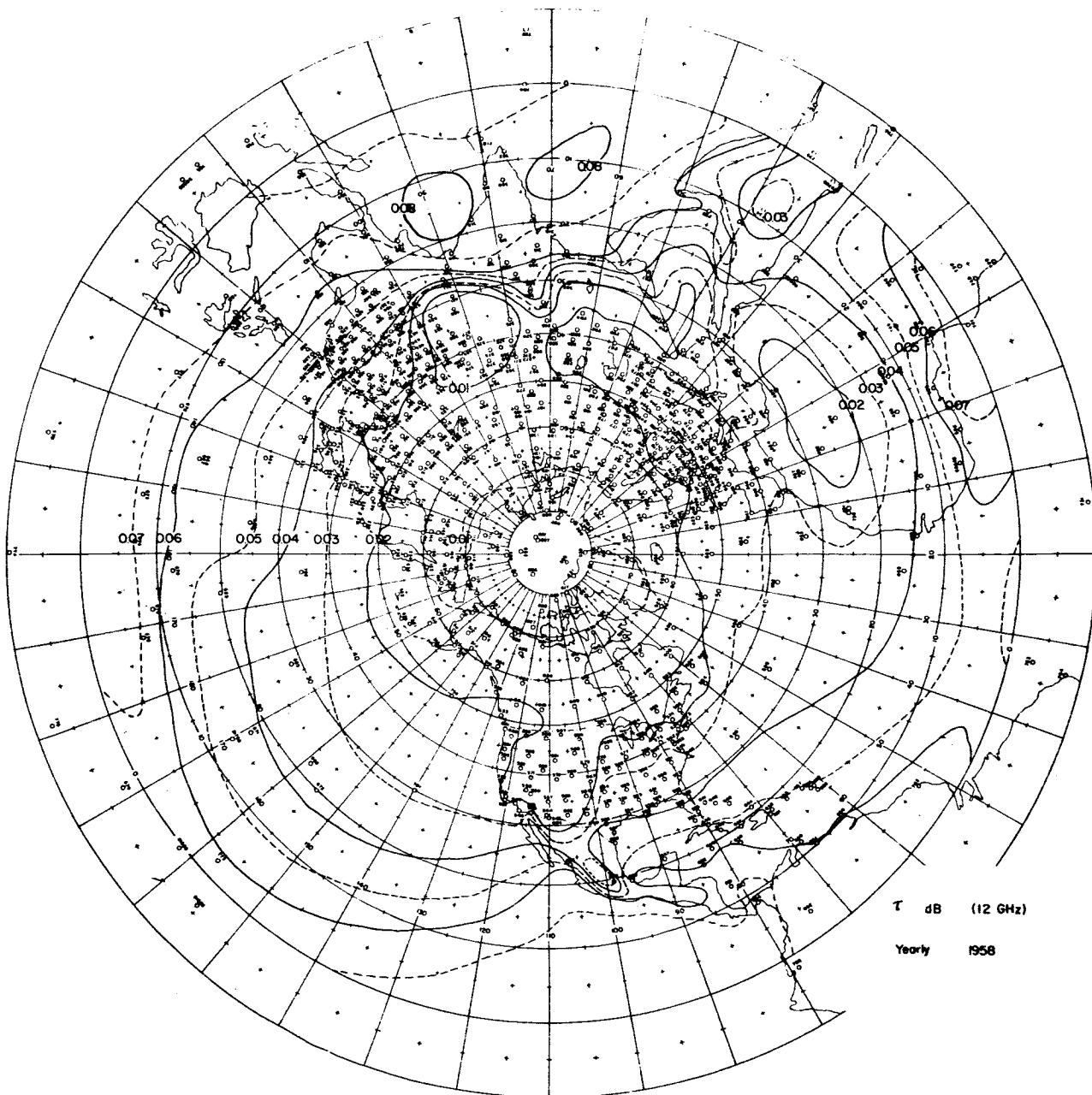


Figure V-30. The mean annual distribution over the northern hemisphere of total atmospheric opacity τ due to water vapor alone at 12 GHz, for a zenith viewing radiometer.

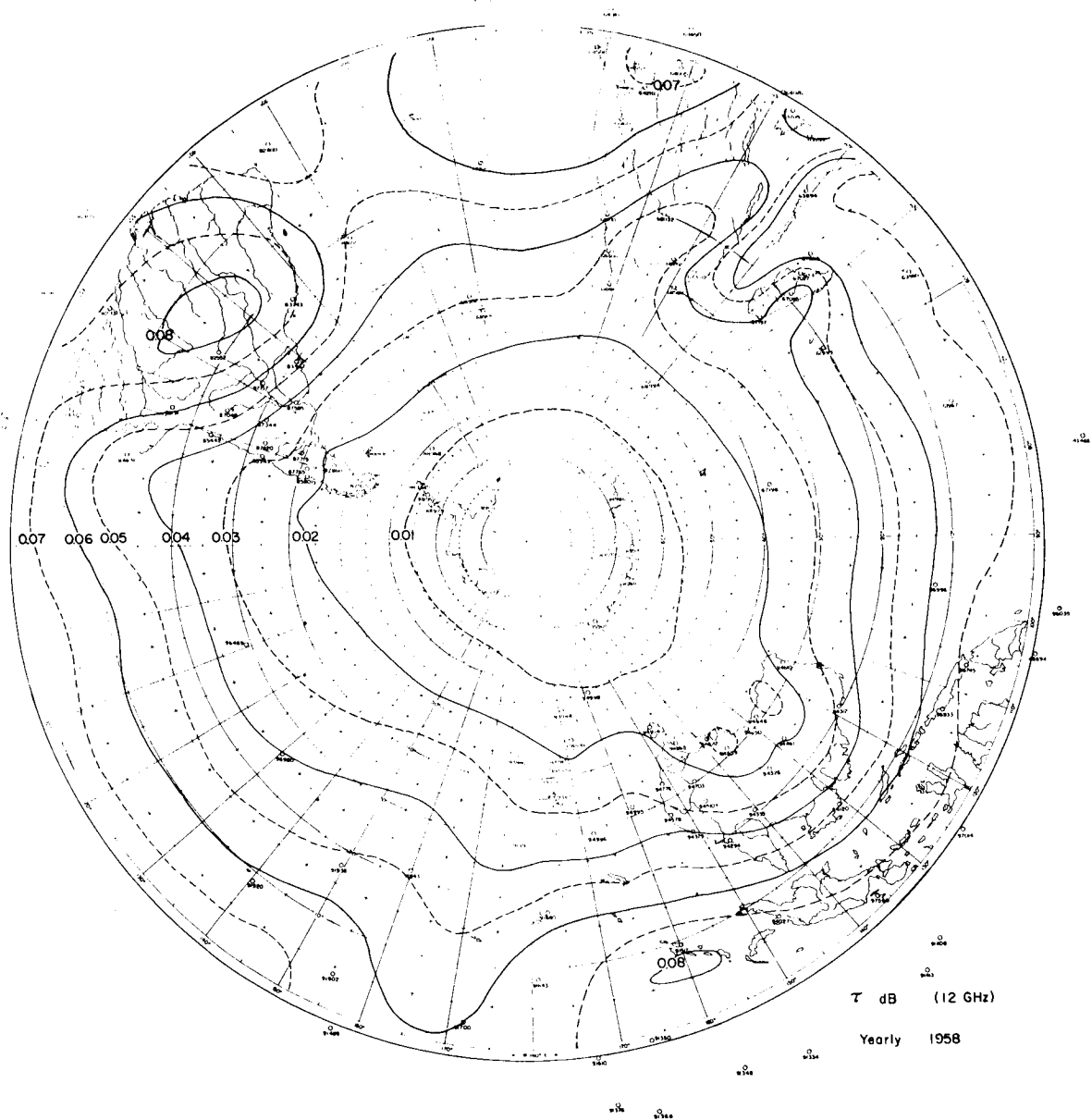


Figure V-31. The mean annual distribution over the southern hemisphere of total atmospheric opacity τ due to water vapor alone at 12 GHz, for a zenith viewing radiometer.

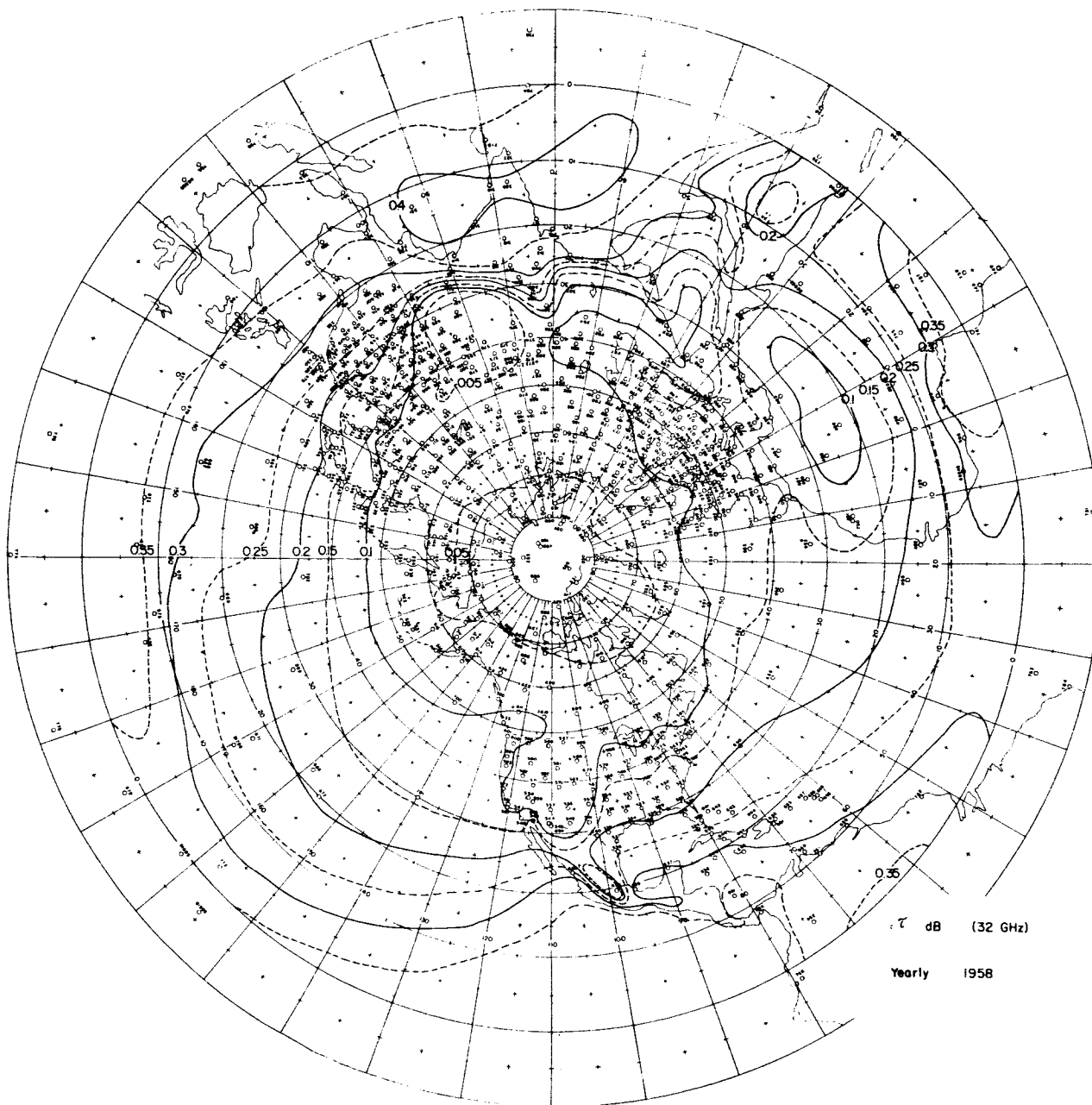


Figure V-32. The mean annual distribution over the northern hemisphere of total atmospheric opacity τ due to water vapor alone at 32 GHz, for a zenith viewing radiometer.

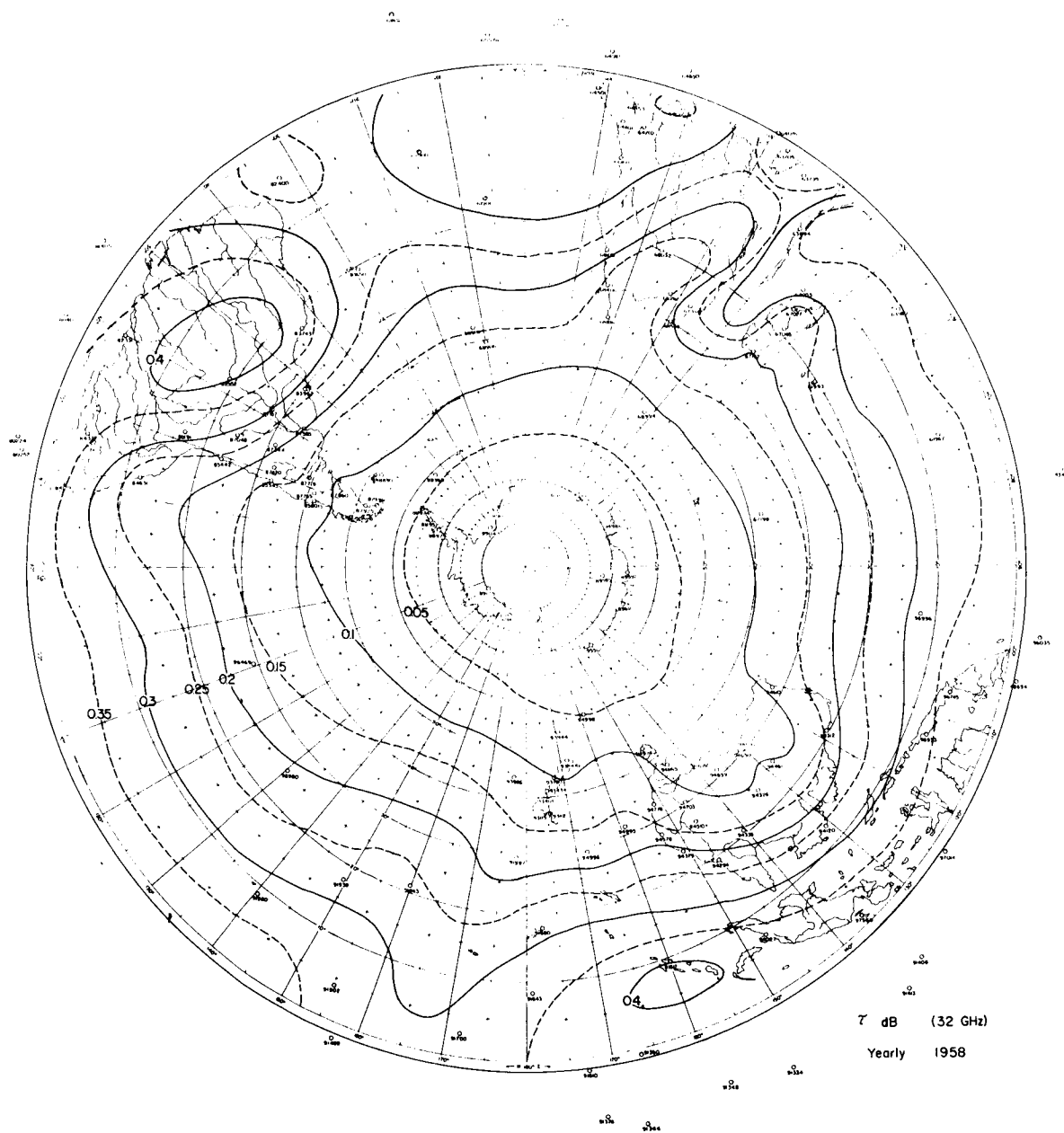


Figure V-33. The mean annual distribution over the southern hemisphere of total atmospheric opacity τ due to water vapor alone at 32 GHz, for a zenith viewing radiometer.

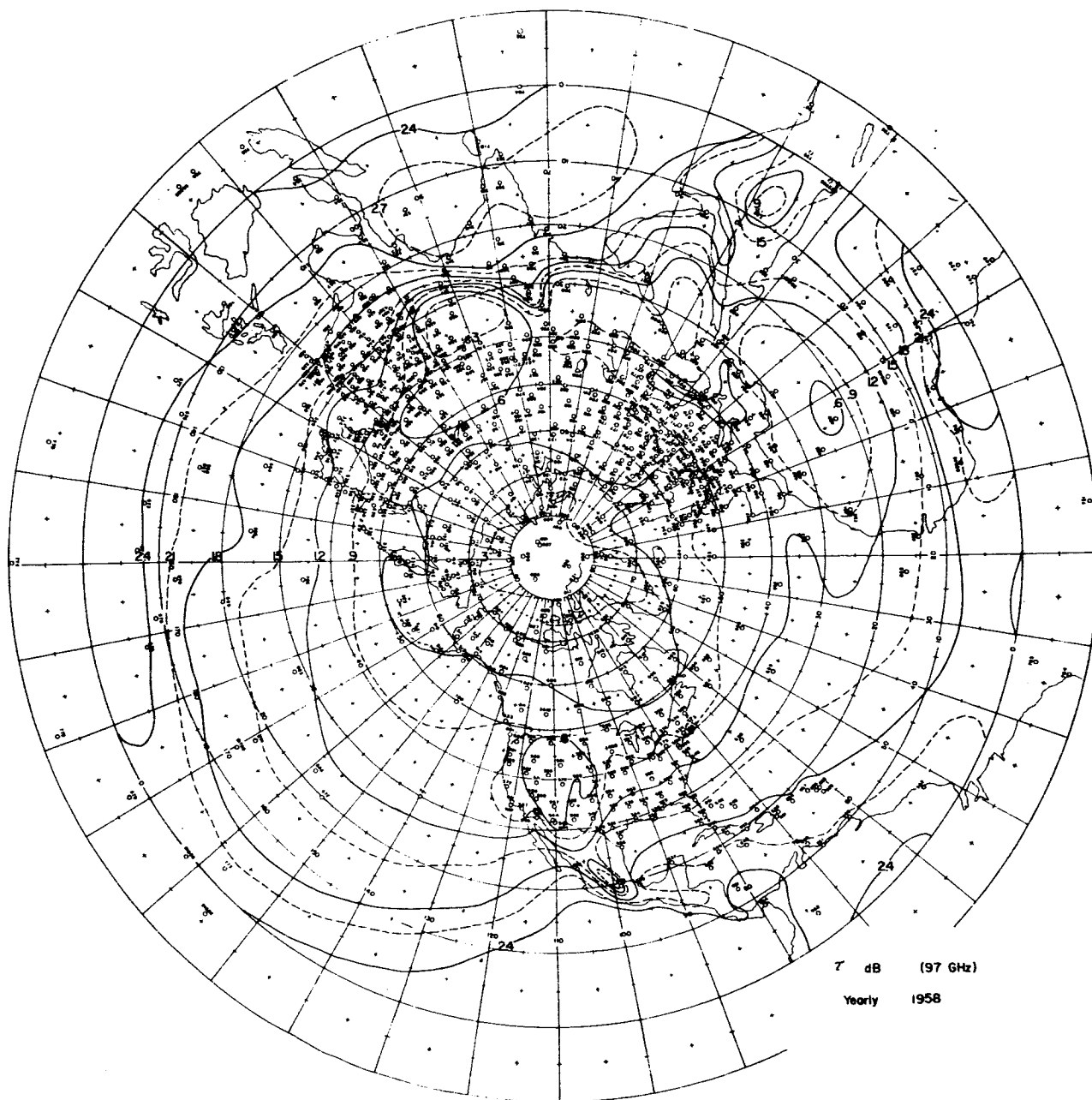


Figure V-34. The mean annual distribution over the northern hemisphere of total atmospheric opacity τ due to water vapor alone at 97 GHz, for a zenith viewing radiometer.

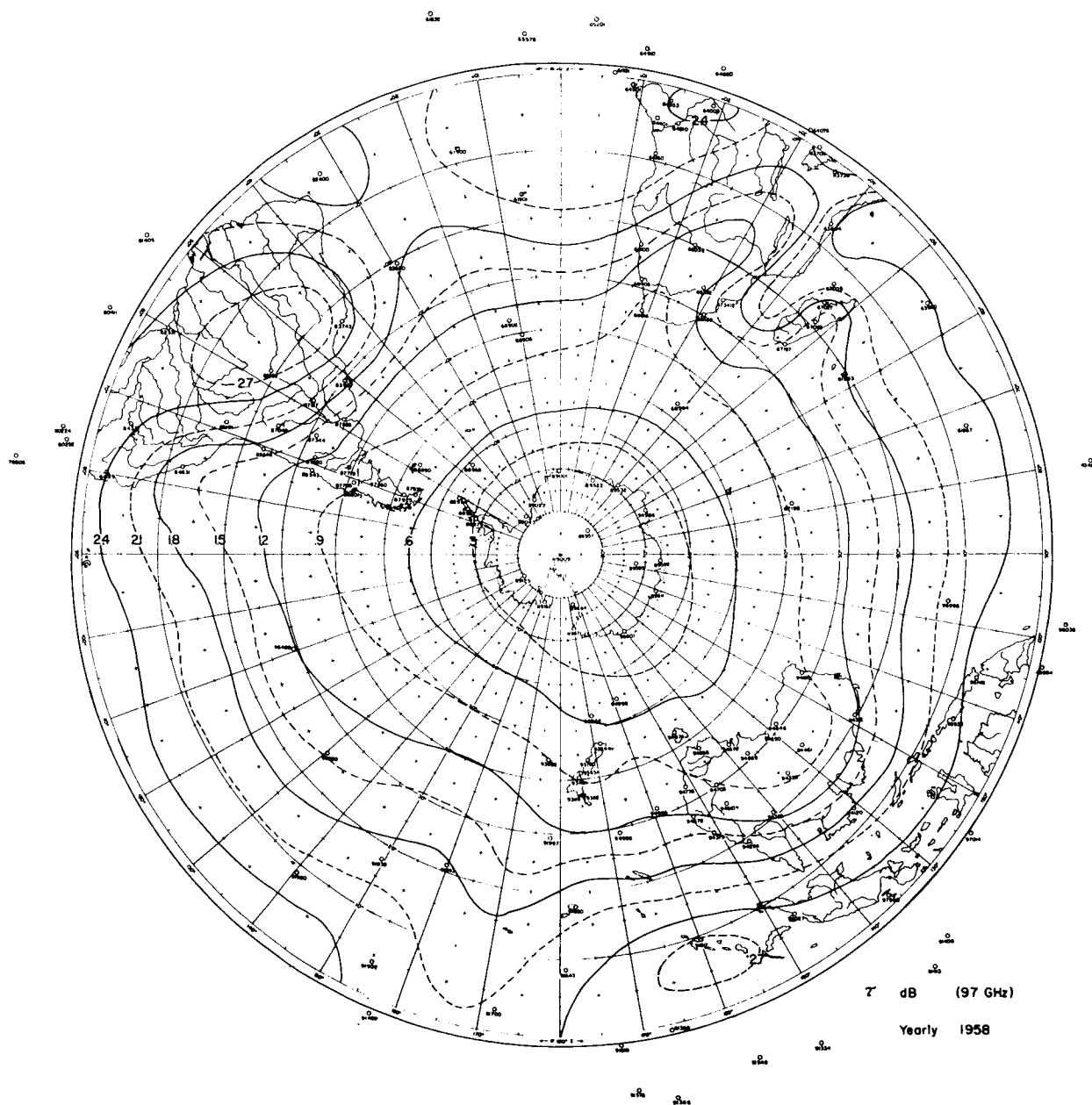


Figure V-35. The mean annual distribution over the southern hemisphere of total atmospheric opacity τ due to water vapor alone at 97 GHz, for a zenith viewing radiometer.

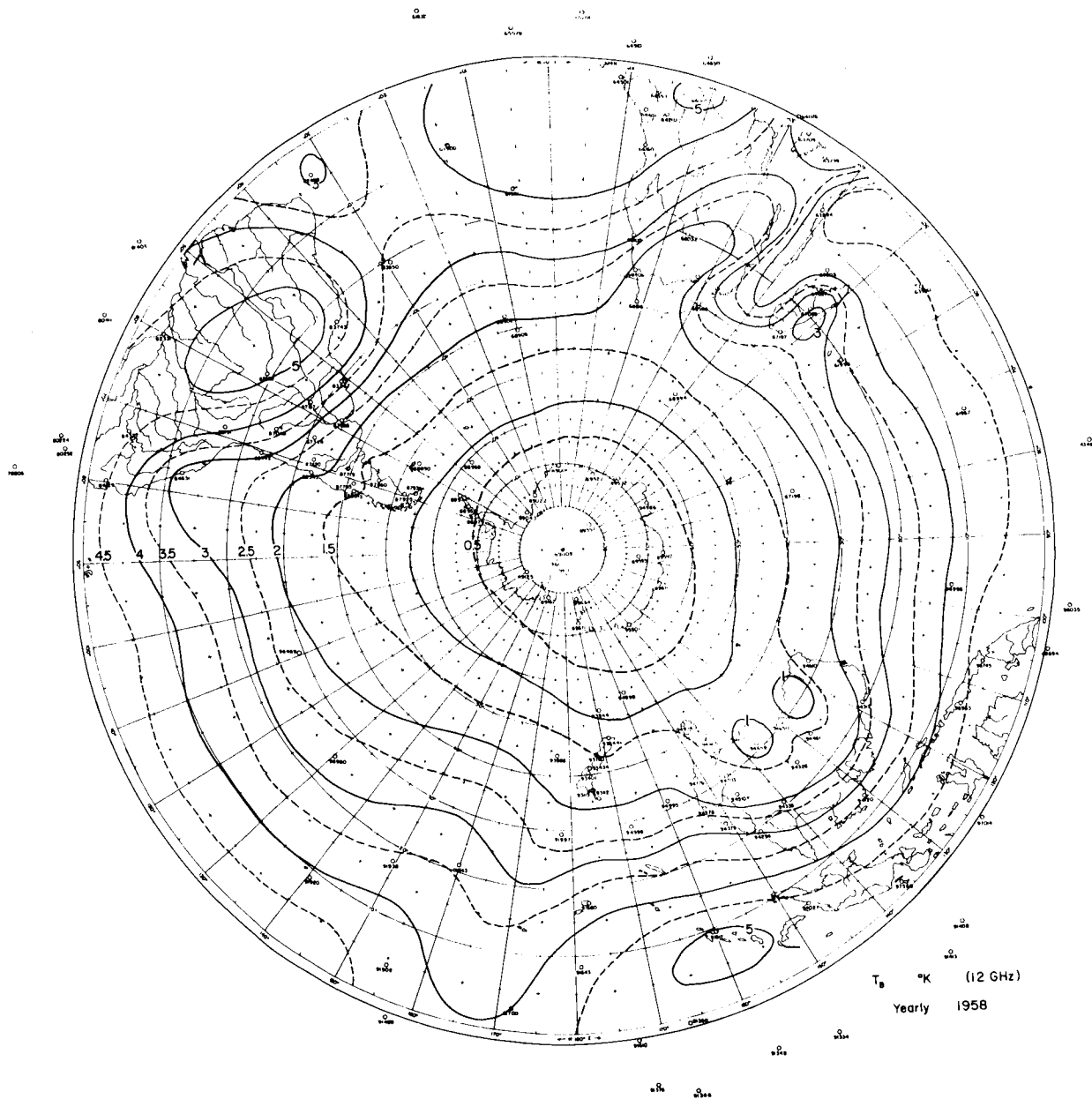


Figure V-37. The mean annual distribution over the southern hemisphere of brightness temperature T_B due to water vapor alone at 12 GHz.

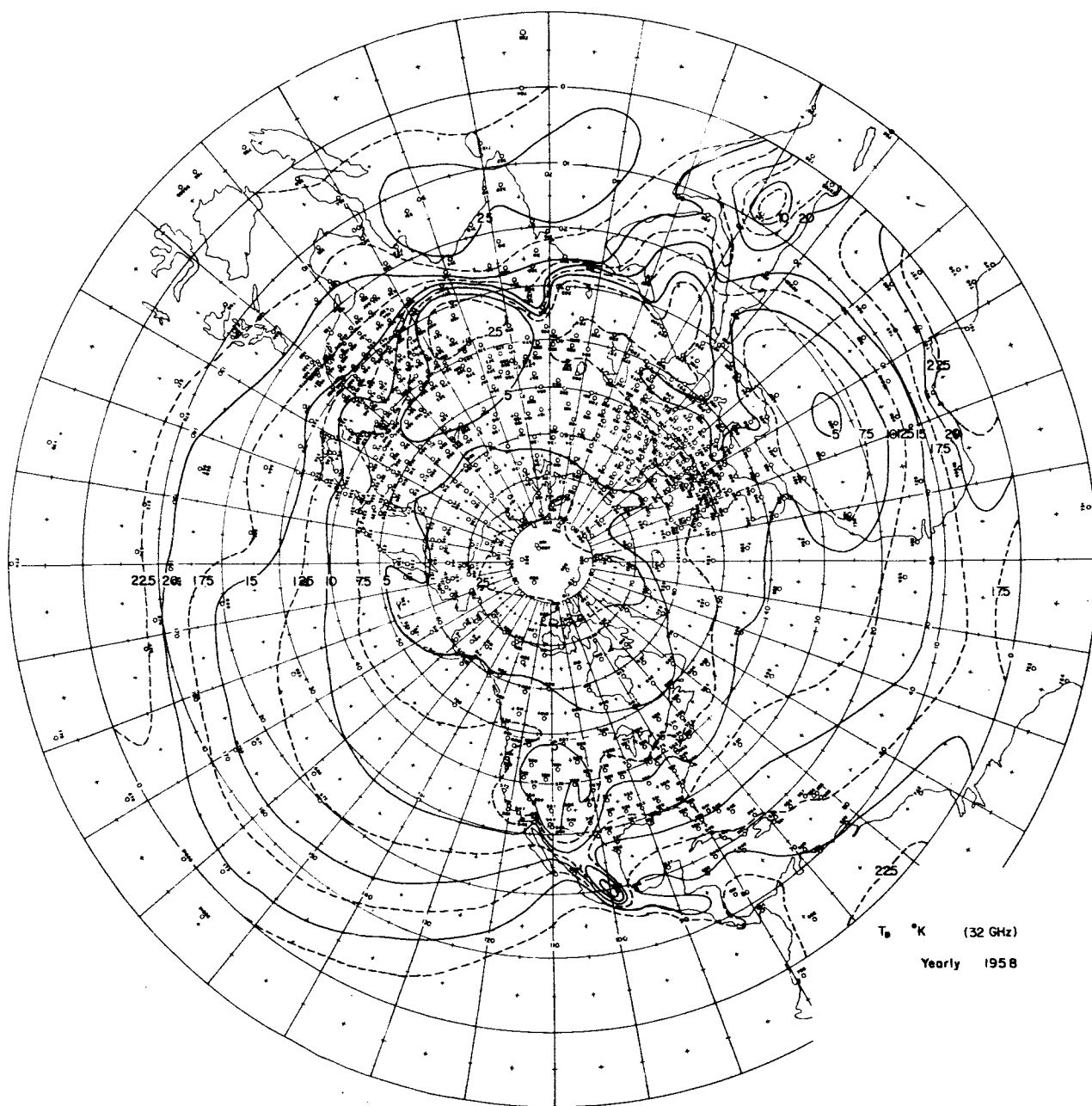


Figure V-38. The mean annual distribution over the northern hemisphere of brightness temperature T_B due to water vapor alone at 32 GHz.

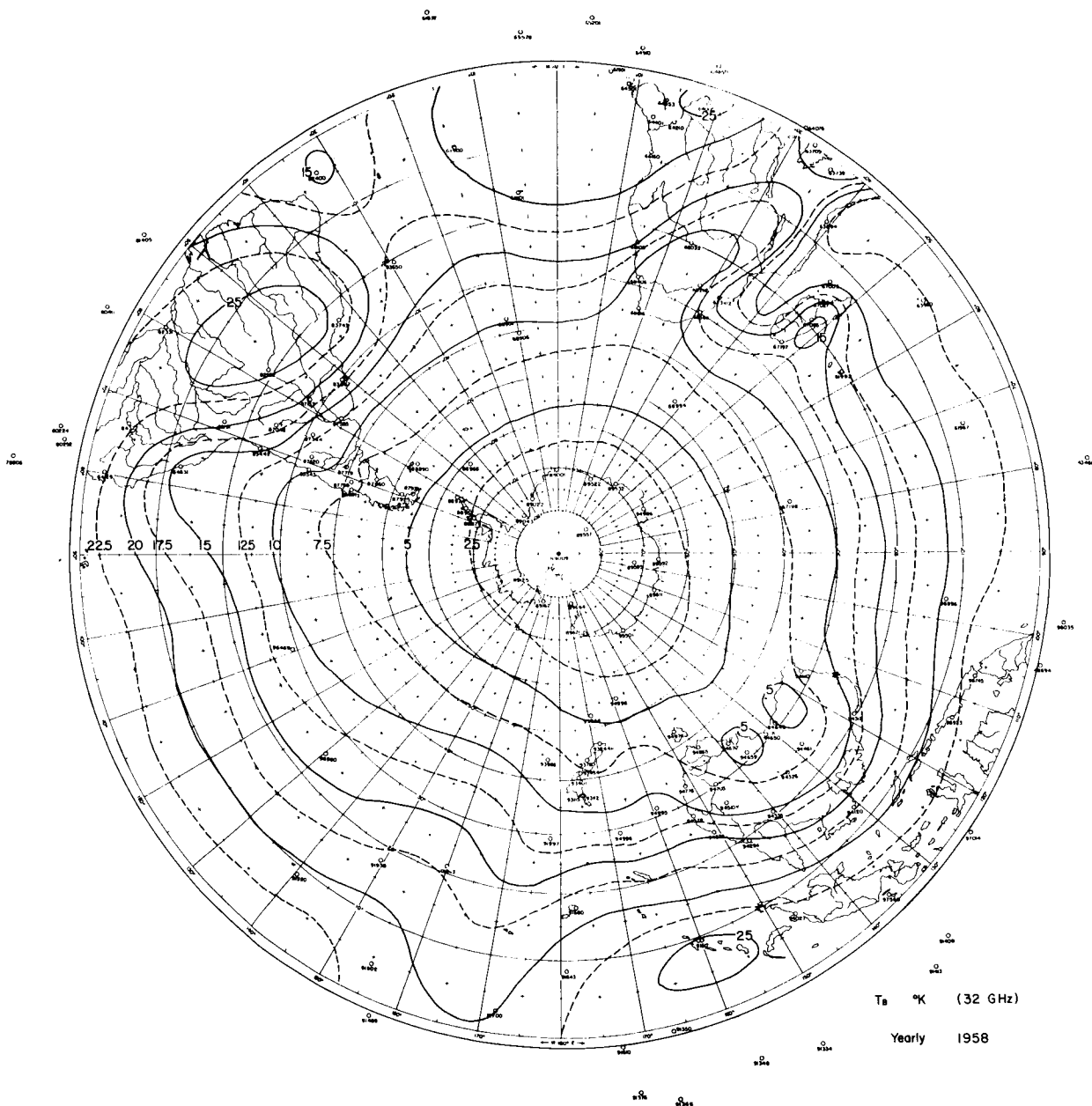


Figure V-39. The mean annual distribution over the southern hemisphere of brightness temperature T_B due to water vapor alone at 32 GHz.

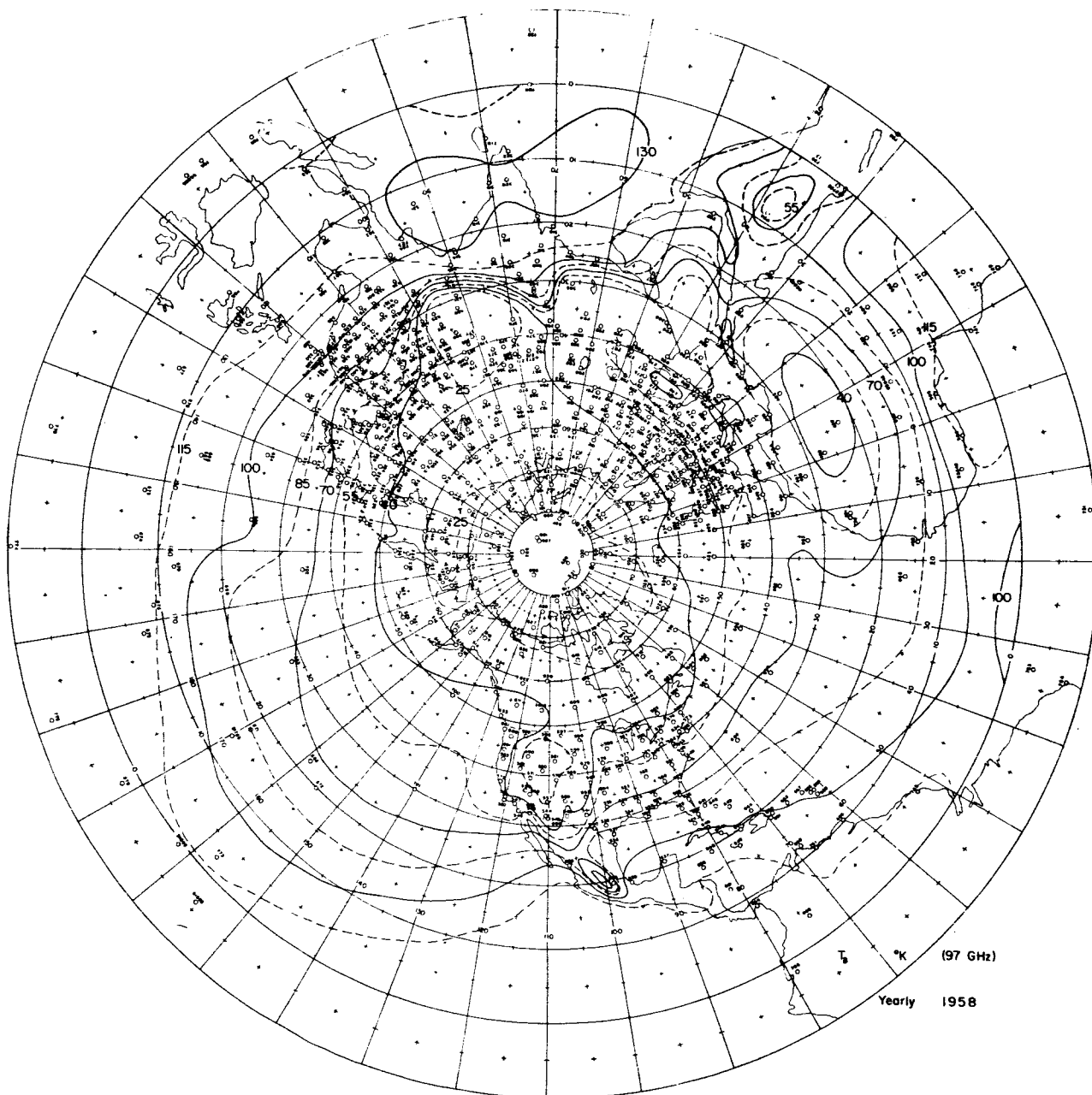


Figure V-40. The mean annual distribution over the northern hemisphere of brightness temperature T_B due to water vapor alone at 97 GHz.

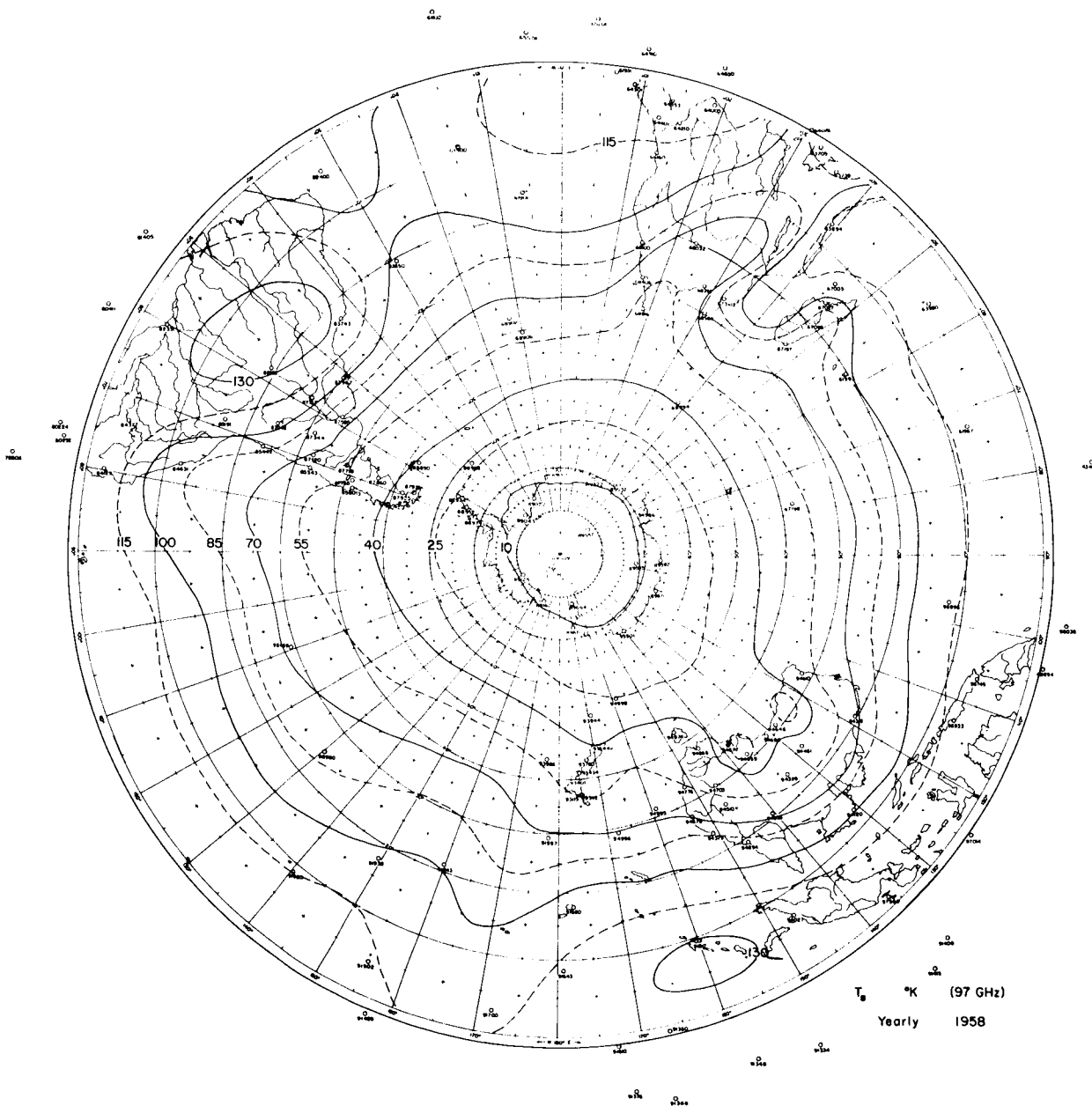


Figure V-41. The mean annual distribution over the southern hemisphere of brightness temperature T_B due to water vapor alone at 97 GHz.

VI. THE VARIABILITY OF LIQUID WATER AND ICE IN THE ATMOSPHERE AND ITS RELATIONSHIP TO RADIOMETRIC OBSERVATIONS

In this Chapter several topics related to radiometric observations through clouds are discussed: First, the distribution of water and ice in individual clouds is reviewed; second, the spatial distribution of these clouds on several scales is discussed; third, the results of several theoretical and experimental radiometric studies of clouds are presented; and fourth, the radiational characteristics of the nine teen cloud models presented in Chapter IV are given at wavelengths from $10\ \mu$ to $10\ \text{cm}$.

A. The Distribution of Water and Ice in the Atmosphere

A discussion of the spatial and temporal distribution of liquid water and ice in the atmosphere is more ambiguous than a similar discussion of water vapor. The reason for this is that there have been no systematic measurements carried out on a global basis to record liquid and frozen water in the atmosphere. No economical method to easily measure the water content of clouds has been available.

Because of the lack of quantitative information about the large scale statistical distribution of cloud water content, it will be more convenient to discuss the features of individual clouds and cloud formations first and then speculate as to how these are related to the statistical patterns on a synoptic and planetary scale.

(1.) Ice Clouds

Several forms of ice clouds exist. The most common are cirrus clouds, the physical details of which were discussed in Chapter III. The density of cirrus clouds usually does not exceed 0.5g/m^3 and normally is less than 0.1g/m^3 . The thickness of cirrus can range from a few hundred meters to several thousand meters. It can be found at many altitudes, but most consistently at and below the tropopause.

The total precipitable water represented by cirrus is low. (A cirrus cloud 5 kilometers thick and 0.1g/m^3 average density would contribute only 0.5 gm/cm^2 to the total precipitable water.) The effectiveness of cirrus as an absorber and scatterer at microwave frequencies is reduced approximately one order of magnitude from the same mass in liquid droplet form. (This can be seen by comparing Figures III-16 and III-17.) The importance of cirrus, therefore, to microwave observations is not as great as the importance of liquid water clouds. However, as one moves into the infrared region, say below 400μ , cirrus rapidly becomes a very important consideration to earth observations.

There is a growing body of information that cirrus occurs more often and over greater areal extent than was suspected some years ago. Very thin cirrus which covers the dome of the sky many times cannot be detected visually from the surface. However, discrepancies between the radiance expected at the surface from water vapor and ozone above have

led to at least one measurement program which gives credence to the possibility that cirrus is more widespread than has been indicated by visual observations (see Hall 1968).

Over the tropics extensive sheets of cirrus are very common and are perhaps more normal than cirrus free areas. Cirrus associated with frontal systems commonly cover areas with linear dimensions as large as 2400 by 800 km. Transcontinental flights across the U.S. have shown conditions where visible cirrus has existed over three quarters of the continental area (Valley, 1965). Further, data from the SIRS infrared temperature and water vapor sounding experiment on NIMBUS has tentatively shown that as much as 70-80 percent of the observations are contaminated with clouds of one kind or another, much of which is thin cirrus.

Snow and hail play a more uncertain role in the radiation picture at microwave frequencies. Dry snow and dry hail have many of the attributes of cirrus, being less effective than an equal amount of liquid water in absorbing and scattering radiation. The exact role of snow is complicated because no comprehensive theory exists which can rigorously handle the complex geometrical shapes which occur in snowflakes.

When snow, or for that matter hail, begins to melt it becomes a very complex multiple layered dielectric which can have a scattering and absorption cross-section at least equal and probably greater than water of equivalent drop size and mass. No attempt in this study is made

to model these complex particles.

(2.) Stratiform Water Clouds

Gentle, uniform vertical motion over a wide area gives rise to stratiform clouds. Their common names are related to their height of occurrence or other special identifying features. Stratus clouds are usually low, very uniform, of medium density, and not too thick. Alto-stratus clouds occur at medium levels (>2000 m) and many times comes in multiple layers. They are an important source of uniform, continuous rain and snow. Nimbo-stratus clouds are normally associated with warm frontal conditions and produce heavy, continuous rain. Each of these types shows characteristic densities, drop size distributions and ranges of total precipitable water.

Liquid water densities as measured in clouds are reviewed in Fletcher (1966). Table VI-1 below is a condensation of the results compiled in Chapter 1 of that reference.

Table VI-1. Cloud Liquid Water Characteristics

<u>Cloud Type</u>	<u>Average Liq. Dens.</u>	<u>Aver. Max. Dens.</u>	<u>Measured Absolute Max. Dens.</u>
1. Stratus) Strato-cumulus) Alto-Stratus)	0.25 g/m ³	0.64 g/m ³	0.88 g/m ³
2. Alto-cumulus)	0.14	0.37	0.70
3. Cumulus	0.38	0.91	1.71
4. Cumulo-nimbus	0.51	1.72	~10.0

From the table one can see that stratiform clouds in general have less average liquid water density and a much more restricted range of

measured values than do the cumuliform type of clouds. These densities immediately throw some light on the integrated amount of liquid water to expect from stratiform clouds. If the average density of 0.25 g/m^3 is taken for an example, then it requires a cloud of this average density ten kilometers thick to provide an integrated value of 0.25 g/cm^2 . Contrast this with the average precipitable water in vapor form over the globe of 2.6 g/cm^2 .

The drop size distribution for stratiform clouds has not been studied as extensively as for cumuliform clouds. In general droplet sizes tend to be larger in stratiform clouds, fewer in number, and more spread toward larger drop sizes than cumuliform drop size distributions. Figure VI-1 presents the results of one set of measurements on the drop size distributions from different types of clouds on an arbitrary drop number density scale. The curves are quoted in Fletcher but were prepared by Diem (1948). Nimbostratus shows up as a broad distribution with a broad maximum near 10μ and a significant number of droplets out as far as 40μ . The mean fair weather cumulus curve shows a much more peaked and narrow distribution. (It should be noted that the distributions depend somewhat upon the sampling technique. No system known operates without a bias toward some part of the size spectrum.)

Significant stratus clouds appear much more frequently in mid-latitudes than in the tropics. They are characteristic of the large moving storms which are found most frequently in these latitudes. They can be

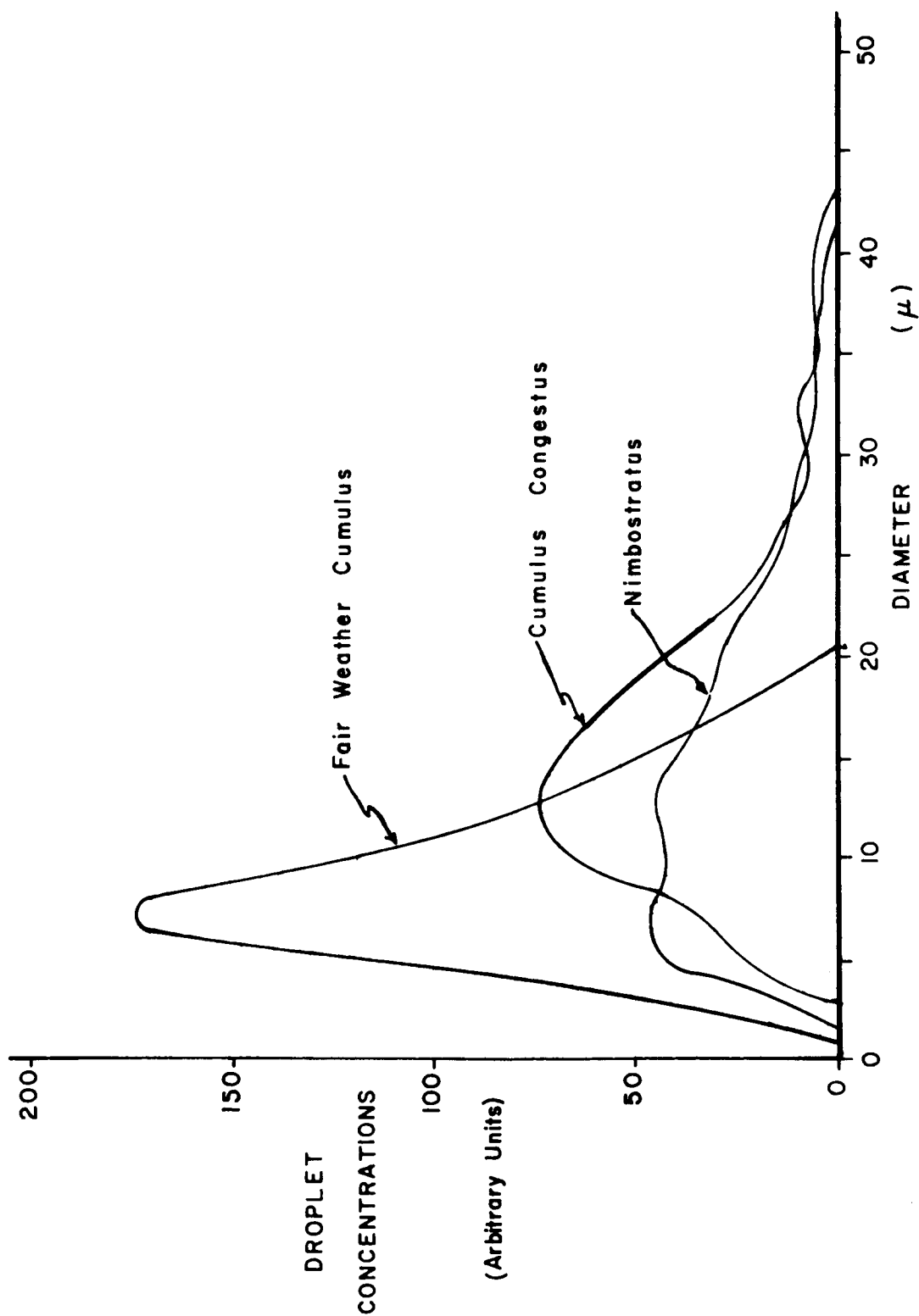


Figure VI-1. Relative droplet size distributions for fair weather cumulus, cumulus congestus and nimbostratus (Niemi, 1948).

hundreds of miles in extent. They will not, however, be of even thickness and density over such large areas. It is impossible to accurately correlate the visual image of a cloud sheet with its water content. Infrared temperature measurements of the tops of clouds give some information in some cases but can only help to make a more intelligent guess about the density and integrated value of the liquid water content.

(3.) Cumuliform Clouds

Cumulus type clouds originate from convective processes and therefore tend to be localized with primary development in the vertical. They ordinarily show higher densities than stratiform clouds, much more variability, and are the forms of clouds which produce the maximum integrated liquid water.

The density of cloud liquid water in cumulus clouds, carefully distinguishing this form from raindrops, is normally below 1 gm/m^3 , as indicated in Table VI-1. Great variability, however, occurs within a cloud in both the horizontal and vertical directions both in droplet concentration and liquid water concentration. Generally, however, judging from the work of Warner (1955) and aufm Kampe and Weickmann (1957) the liquid water content in a cumulus cloud increases to within one or two thousand feet of the top.

To provide some feel for the variability of the water content and drop concentration through cumulus clouds Table VI-2 is presented. It is

Cloud No.	Cloud Base (ft)	Cloud Top (ft)	Traverse Height (ft)	Sample No.							
				1	2	3	4	5	6	7	8
1	2200	9000	6250	(28 0.46	42 0.11	24 0.57	75 1.40	4 0.25	5 0.03		
2	800	6000	1800	(63 0.05	43 0.14	55 0.18	133 0.45	117 0.44	74 0.25	82 0.38	
3	3600	8500	7000	(66 0.66	79 0.74	58 0.71	82 1.00	70 0.71	238 2.14	57 0.62	128 1.50
4	2500	6500	5600	(107 1.29	19 0.20	19 0.25	14 0.11	10 0.10	15 0.26	6 0.06	14 0.05
5	2500	7500	6500	(82 0.15	59 0.13	52 0.13	73 0.17	199 0.63	140 0.41	77 0.13	67 0.17
6	7200	12000	9800	(24 0.02	231 0.15	141 0.15	505 0.74	117 0.17	270 0.35	127 0.19	177 0.26

Table VI-2. Measured droplet concentrations in particles/cm³ (upper number) and liquid water concentrations in gm/m³ (lower number) at points 200 m apart through various cumulus clouds.

abridged from a similar table presented in Squires (1958). The most important points to notice from this table are that any model cloud which uses a single drop size distribution and a smooth or invariant liquid water density will not conform to the observed facts. Nevertheless, the single distribution approach has already been adopted in Chapter IV for the cloud modeling as a matter of practicality. When one analyzes the effect of the variable drop size distribution, it is apparent that two parameters which must be modeled correctly to predict the microwave spectrum are the average liquid water content as a function of temperature, and the concentration of drops in the size range which causes scattering.

Maximum cloud liquid water concentrations occur in thunderstorms, but from measurements taken in these clouds it is very doubtful that rain can be separated from the cloud component. Cumulus congestus clouds, which are clearly non-precipitating, have shown densities as high as 6 gm/m^3 (aufm Kampe and Weickmann, 1957). It is conceivable, therefore, that the maximum density one can expect in cloud form is somewhere near 6 to 8 gm/m^3 .

The maximum precipitable water in cloud droplet form favors cumulus clouds again because of their great vertical development. Thunderstorms have been observed to top out above 20 km. If they hold one half the maximum liquid water density over the lower half of their vertical extent and one eighth of this on the average in the top half, the total precipi-

table water in cloud droplet form would be 5 gm/cm^2 . This would be in addition to water vapor and liquid water in the form of raindrops. This contrasts with values below 1 gm/cm^2 for most stratiform clouds even when they are raining.

(4.) Rain

Rain in the form of droplets above 100μ and below 1 cm potentially represents the greatest concentration of liquid water in the atmosphere. However, it is highly variable depending upon the rain rate. Rain falling from thin stratiform clouds at a rate of several millimeters per hour will have a density of approximately one-tenth gm/m^3 (Crane, 1966). Whereas, rain rates in the middle of well developed thunderstorms will approach 300 mm/hr. (Valley, 1965) and exhibit water densities in excess of 10 gm/m^3 . 25.4 millimeters 1 hour (1 inch) of falling rain in stagnant air would mean a density of approximately 1.15 gm/m^3 .

The integrated water content in raindrop form in a vertical column is highly variable. In stratiform clouds one would expect less total water than in cumulus clouds. A uniform 25.4 mm/hr rain from stratiform clouds might expect to contribute 0.5 to 1 gm/cm^2 of total liquid water in a vertical column depending upon the depth of the cloud and the vigor of the updrafts. Through the core of a well developed thunderstorm as much as 6 to 7 gm/cm^2 of rain water can be suspended in the violent updrafts which are characteristic of cumulonimbus clouds.

The statistical global distribution of cloud liquid water and rain is unknown. However, the distribution must be something like that for

water vapor shown in Figure V-3. The reasons are similar: warm moist air is found, in general, closer to the equator and at lower altitudes. Therefore, when one finally averages in time and around latitude circles, one should find more cloud and rain drops suspended in the atmosphere closer to the equator and at lower altitudes. It is entirely likely, however, that there will be some height at which the average suspended water will be a maximum because of the fact most clouds do not intercept the surface.

In an attempt to bring some of the numbers into focus about the relationship between scale sizes of clouds, rain formations and the precipitable water retained in the atmosphere by these forms Figure VI-2 has been drawn. Like Figure V-17 it is an attempt to relate the expected maximum precipitable water in the atmosphere in cloud and rain drop form to the scale size on which these maxima might be found. Like Figure V-17, it is hypothetical and based solely on the information represented by the references quoted and the experience of the authors in modeling clouds.

B. Radiometric Studies of Clouds

Several recent theoretical and experimental study programs concerning clouds show results which are important to review for the present purposes. They provide insights into three questions: (1) What is the effect of height on the absorption and emission of clouds? (2) What emission characteristics would a real extended cloud check exhibit? (3) At what frequencies do different cloud types begin to become opaque?

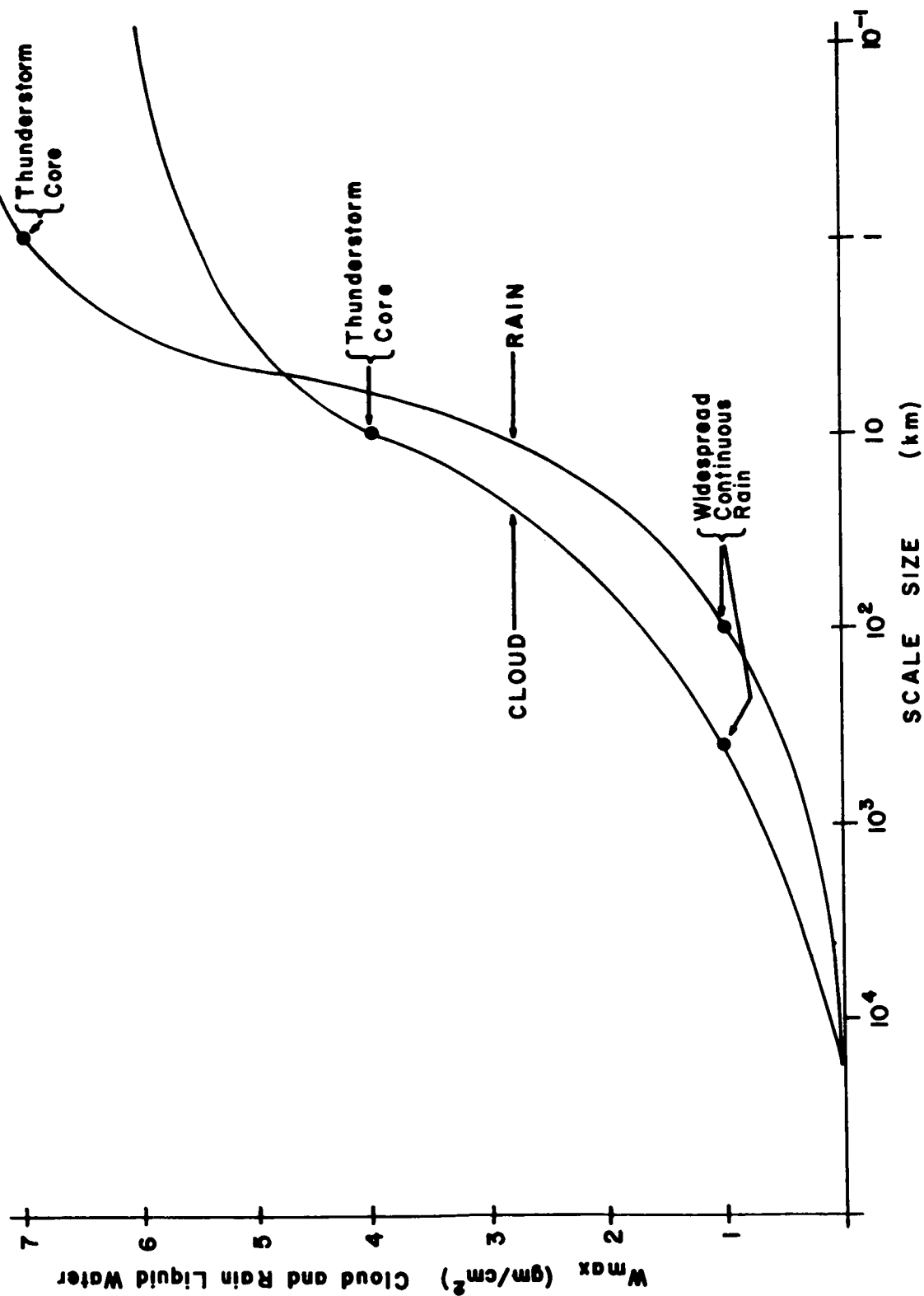


Figure VI-2. Hypothetical curves describing the maximum precipitable water in cloud droplet and rain droplet forms as a function of scale size.

(1.) Cloud Weighting Function

To assess the dependence of cloud height on cloud absorption Figure VI-3 is presented. It is taken from Reifenstein and Gaut (1971). This Figure represents the vertical distribution of an absorption weighting function for frequencies below 50 GHz and which have absorption properties described by the Rayleigh absorption expression given in Chapter III. It may be expressed as

$$WF_3(\lambda, z) = \frac{\tau_{\text{cloud}}(T, P, \lambda)}{W(z)} \quad \text{neper (gm/cm}^2\text{)}^{-1} \quad (6-1)$$

in which WF_3 is the weighting function for total cloud opacity at the wavelength λ and at the height z given in nepers $(\text{gm/cm}^2)^{-1}$. τ_{cloud} is the total opacity of the cloud in nepers at height z where the temperature is T °K and the pressure P millibars, and W is the total liquid water content through the cloud in gm/cm^2 .

The computation of τ_{cloud} is discussed in some depth in Chapters III and IV and it is shown there that the Rayleigh approximation is inversely proportional to temperature. This shows up clearly in Figure VI-3. One can think of the curves in the figure corresponding to the cloud opacity abscisses as being the measured opacity of a cloud with 1 gm/cm^2 of total liquid water in the vertical moved upward through the atmosphere. At each level, the cloud takes on the temperature of the surroundings and because of this has a different opacity at each level

The important points to notice are that: (1) at 19.35 GHz the range

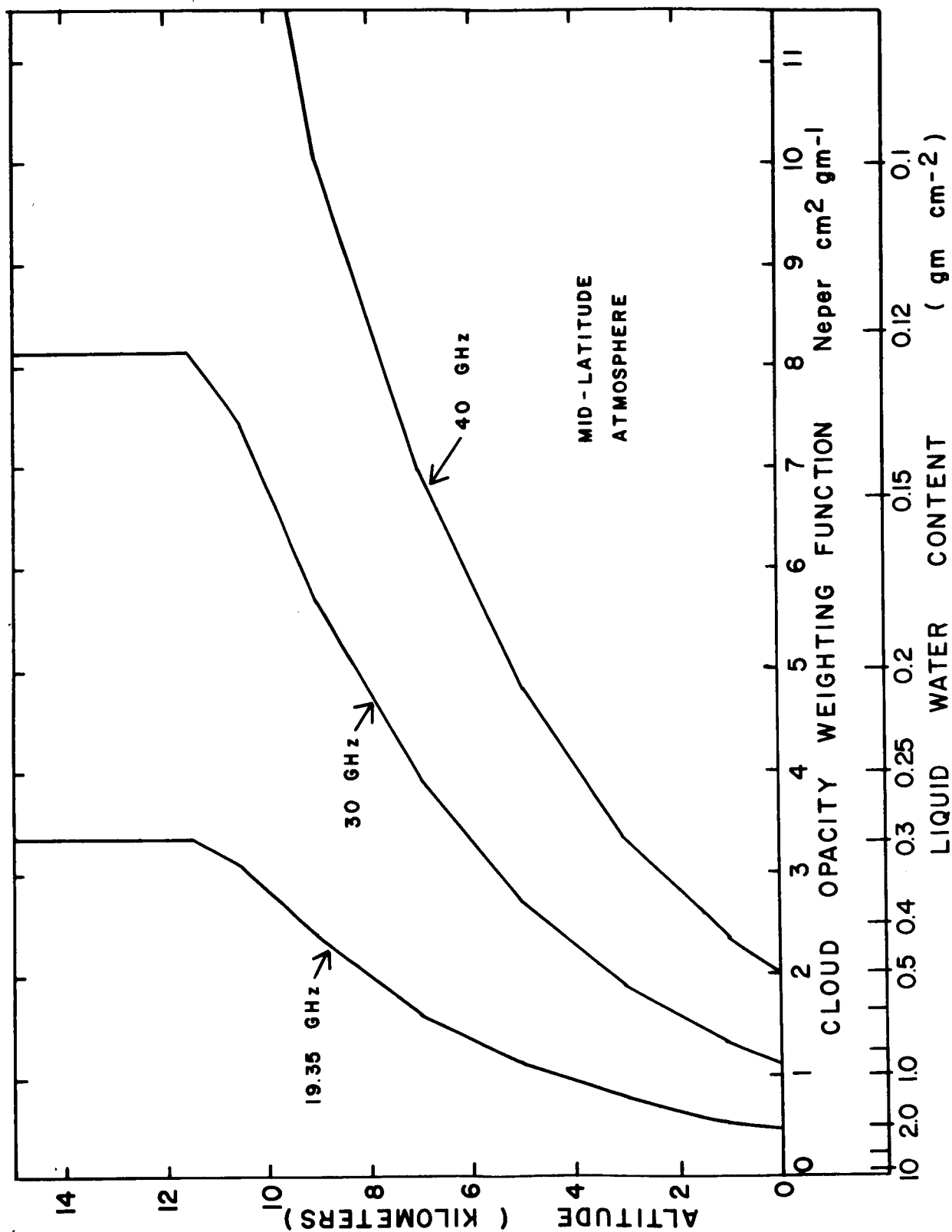


Figure VI-3. Cloud opacity weighting functions in the mid-latitude atmosphere for three frequencies. (Reifenstein & Gaut, 1971)

of values for a mid-latitude atmosphere is less than three, while at 40 GHz the range is a factor of five in the midlatitude atmosphere;

- (2) the colder the cloud the more effectively it absorbs; and
- (3) the effect is exaggerated for higher frequencies and for viewing angles away from the nadir.

The lower abscissa on Figure VI-3 is an adaptation of the weighting function concept. If one assumes that the curves in the figure represent one neper of total opacity, then the scale at the bottom of the figure corresponds to the total liquid water which would be needed for a total opacity of one neper at the temperature found in the model atmosphere at the height on the ordinate scale.

An example to illustrate the information contained in Figure VI-3 is the following: If a cloud were found at the 5 km level, then at 40 GHz, if the cloud has a total liquid water content of 1 gm/cm^2 , the total opacity is 5 nepers (21.7 dB), given by the upper abscissa scale. If instead of assuming that the cloud holds 1 gm/cm^2 of liquid water we assume that the cloud has a total opacity of 1 neper, then the cloud holds 0.2 gm/cm^2 of total water in cloud droplet form, shown on the lower abscissa scale.

(2.) Radiometric Properties of Model Clouds

As an extension of the weighting function concept, Figure VI-4 from Reifenstein and Gaut (1971) is presented. Here the concept of the 1 neper (4.35dB) curves for cloud liquid water content are drawn again, this time for 19.35 GHz viewing the zenith, 37 GHz viewing the zenith and

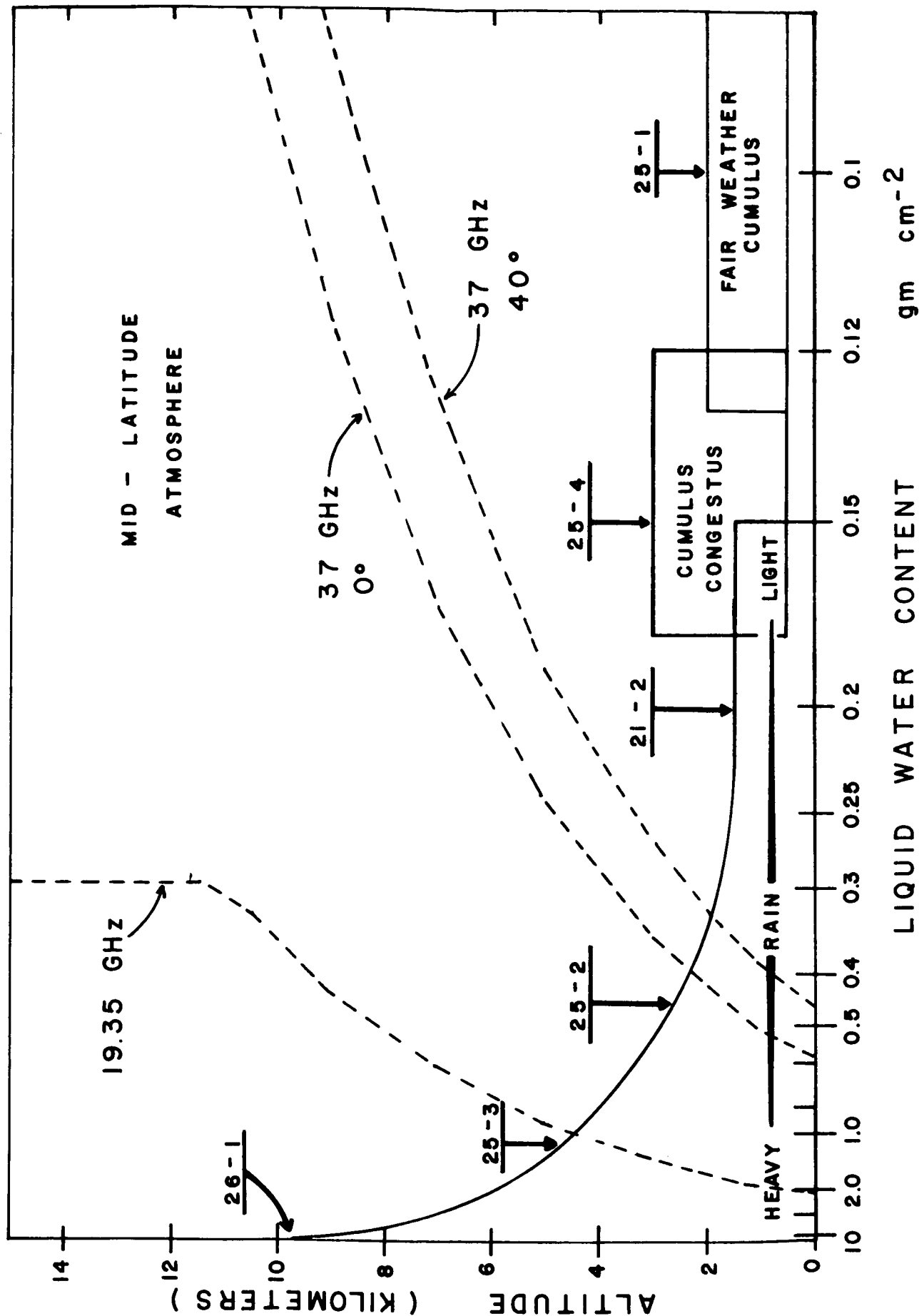


Figure VI-4. Liquid water content for which the opacity is unity as a function of frequency and nadir angle, with typical cloud types shown for reference. (Reifenstein&Gaut,1971)

37 GHz viewing at a 40° angle from the zenith. The equivalent total water for the one neper opacity is given on the abscissa. Included on the graph are representations of several of the cloud models given in Chapter IV. The boxes include a range of values for liquid water content over a range of heights. The purpose is to give some idea where clouds and rain become opaque. This can be seen to happen for total liquid water conditions beyond about 0.3 gm/cm^2 at 40 GHz.

Another curve taken from Reifenstein and Gaut (1971) is shown in Figure VI-5 and is shown as an example of what the emission from clouds do to observations over a calm ocean at 288°k. The viewing angle is 40° away from the nadir and two polarizations are evaluated at 30, 35, and 40 GHz. Drastic saturation effects of the low lying stratus begin to show at total liquid water contents beyond about 0.2 gm/cm^2 corresponding to a cloud with 2 gram/m^3 average liquid water density 1 km thick. This is a heavy cloud but not unreasonable. The conclusion is that low lying stratus will remain mostly transparent below 40 GHz (<1dB) but probably cumulus clouds will appear mostly quite opaque (>1dB).

A final set of curves from Reifenstein and Gaut (1971) are given in Figure VI-6. These are derived by differentiating curves like those given in VI-5 to obtain dT_B/dW and multiplying by W. This sensitivity curves is therefore given by

$$S = W \frac{dT_B}{dW} \quad (6-2)$$

Several features of these curves are interesting to note. First, their amplitude depends only upon the contrast between the background

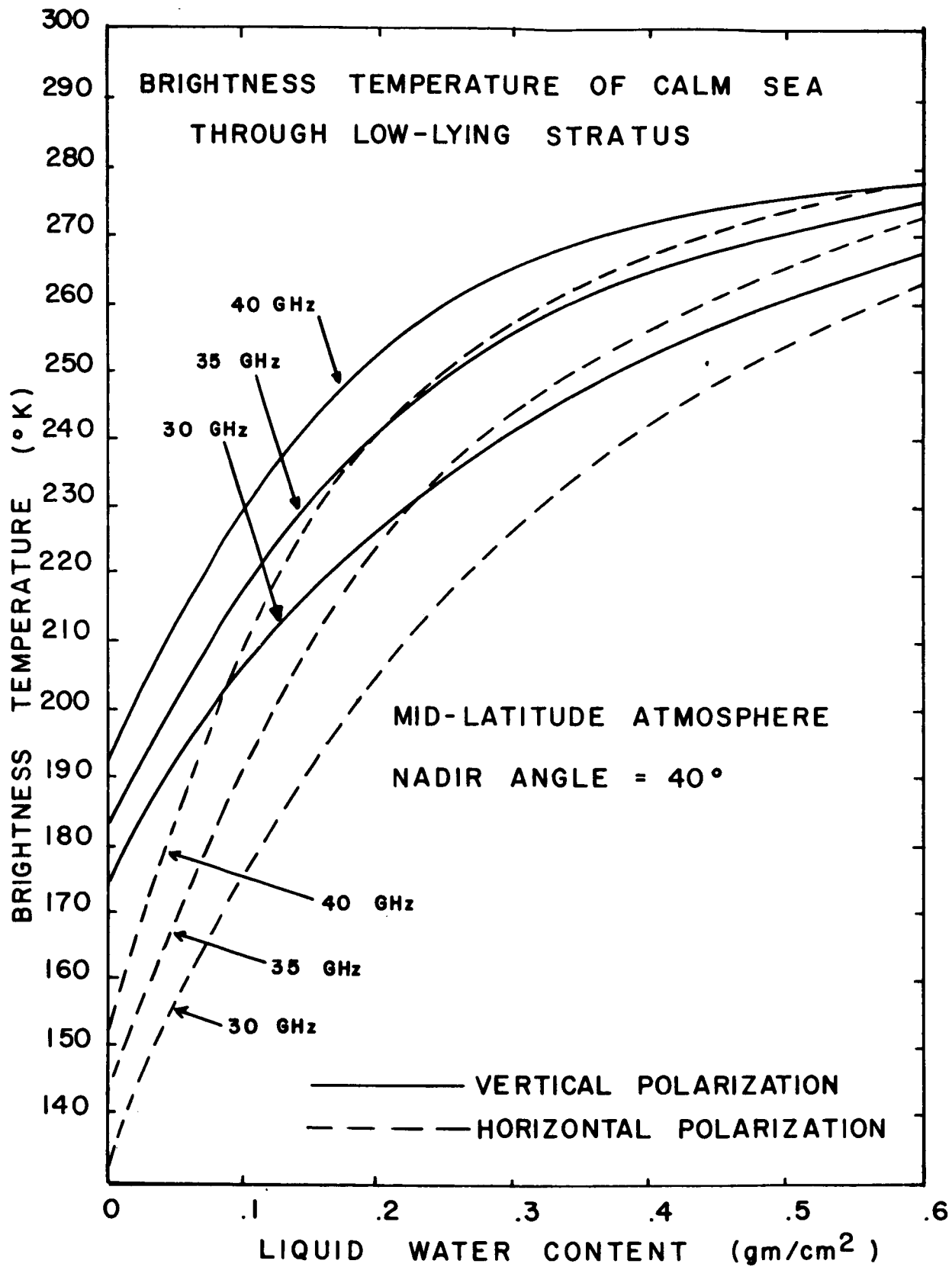


Figure VI-5. Brightness temperature of the calm sea surface through low-lying stratus in the mid-latitude atmosphere, for three frequencies, as a function of cloud liquid water content. (Reifenstein&Gaut, 1971)

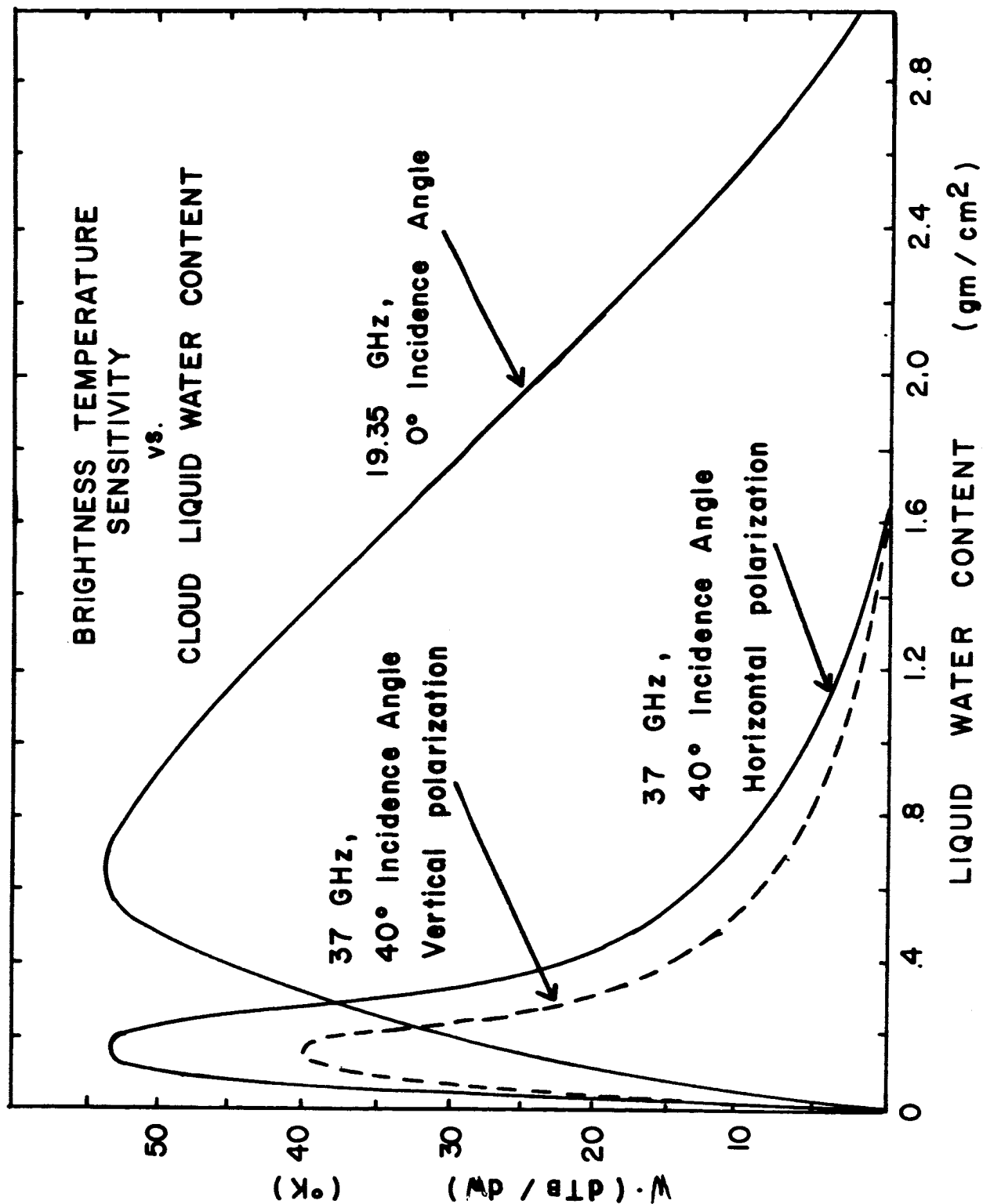


Figure VI-6. The function $W \cdot (dT_B / dW)$ vs. cloud liquid water content at 19.35 GHz and 37 GHz. (Reifenstein & Gaut, 1971.)

brightness temperature (sky or surface) and the saturated temperature of the cloud. Second, the width of the curves depend only upon the frequency chosen, the viewing geometry, and the saturation temperature in a very simple way. The peak of the curves occur at total liquid water values which are exactly one half the values which cause 1 neper opacities.

The sensitivity curves are very useful to determine the properties of clouds which a given radiometer configuration can "see". Three properties can be determined: (1) the minimum liquid water content which can be detected; (2) the maximum liquid water content for which a 100% change can be detected; (3) the minimum percentage change in liquid water which can be detected for any given total liquid water.

For an example, consider the following: a radiometer has an over-all system noise fluctuation of 2° K. A signal to noise ratio of 5 is needed to determine liquid water content of a cloud. Therefore a 10^0 change in signal is required. For the 19.35 GHz curve in Figure VI-6, the liquid water which initially gives a 10^0 signal is 0.16 gm/cm^2 . If one moves across to the right side of the 19.35 GHz curve where it again intersects the 10^0 ordinate value, at about 2.6 gm/cm^2 , this is the last value for which a 100% or greater change in the water content can be detected. Finally, one can determine what water content change can be detected for a given total water content by the following analysis: Using 0.4 gm/cm^2 as the total water content for an example read a value of approximately

50° change for a 100% change of water content. Therefore, if 10° is the needed change for detection, then one fifth of a 100% change in the water content is detectable or 0.04 gm/cm².

(3.) Radiometric Observations of Oceanic Clouds

In order to give some insight into actual radiometric measurements of clouds over an ocean surface Figure VI-7 has been included from Gaut and Reifenstein (1970). It is a trace from the output of a 19.35 GHz radiometer viewing the nadir from the NASA Convair 990 aircraft. Figure VI-7 is from a flight over the Gulf of Mexico which included a flight path which carried the airplane over a cumulonimbus buildup.

Case 1 is over very low patchy stratocumulus and represents values very close to clear conditions over the ocean. Case 2 represents a building cell probably in the cumulus congestus stage. The cloud was modeled to have a vertical extent of 7000 feet and an average density of 6 gm/m³. The integrated water content was computed to be 1.38 gm/cm². This latter number is probably more accurate than the average density and thickness, which combination gives the integrated value. Measurements of the cumulonimbus gave brightness temperatures which were close to if not at saturation temperature for the cloud (270°K). Scattering processes were no doubt important and therefore the recovery of liquid water content is doubtful.

The trace at the top of the Figure is the temperature measured by an infrared radiometer viewing in the 10-12μ window. Flight levels,

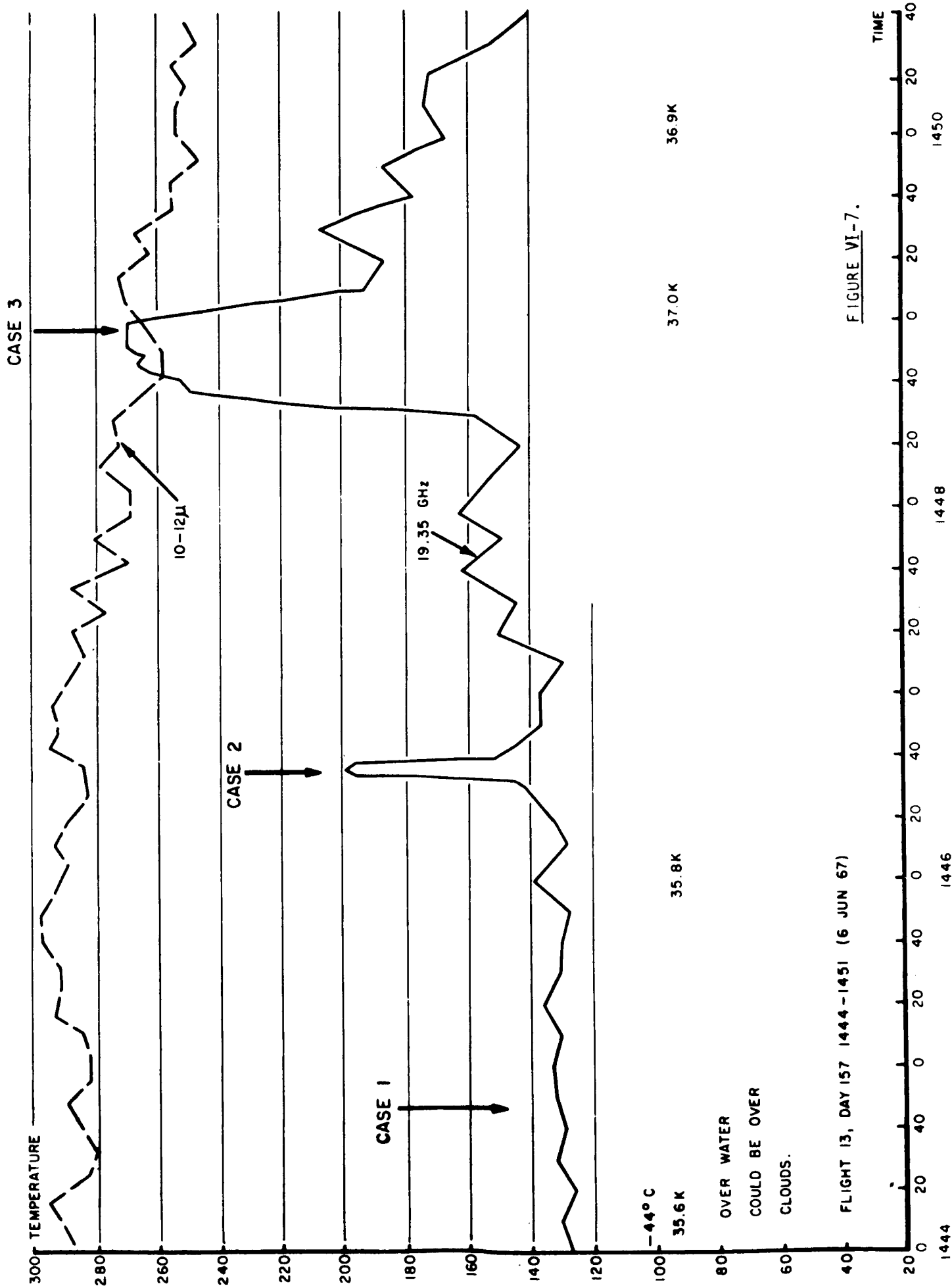


FIGURE VI-7.

ambient temperatures, and certain remarks are included in the bottom half of the graph. Time of observation and therefore distance is the abscissa, brightness temperature the ordinate.

C. Absorption, Scattering and Other Characteristics of the Clouds in the Cloud Catalogue

There is no way to summarize the effects of clouds on radiometric observations from space in the same convenient world wide map format as presented in Chapter V for water vapor. The next best approach in our opinion to this is to establish many representative types of clouds, as was done in Chapter IV, and give enough data so that if the clouds of a region are known, something can be said about their radiometric characteristics.

In Appendix C, all of the pertinent scattering and absorption data pertaining to the 19 cloud models introduced in Chapter IV are summarized layer by layer. From this information the absorption and scattering behavior can be plotted if desired, as a function of wavelength from 10 cm to 10 μ . Of particular interest will be the scattering and absorption depths as a function of wavelength because this curve will establish where the opacity of a given cloud configuration becomes too great for a given observational purpose.

The information included in the tables of Appendix C are computed at a temperature of 298⁰K because, even though the dielectric constant of pure water is known at microwave wavelengths as a function of temperature, this is not true at infrared wavelengths. To be consistent therefore, the whole spectrum was computed at 298⁰K.

VII. CONCLUSIONS AND RECOMMENDATIONS

The most important conclusion from this report is that we now have the tools and understanding to model the majority of conditions which occur in the natural atmosphere for their radiational properties over the spectral region 1 cm to about 200 μ . Linked to accurate statistical information about the atmosphere, excellent planning information can be generated for any purpose: communications, earth observations, or noise energy.

The outstanding weak points are: (1) a lack of definitive data for the complex index of refraction for ice as a function of temperature, especially in the middle infrared region; (2) lack of experimental data for the water vapor spectrum at wavelengths shorter than 300 microns; (3) a lack of statistical information about the distribution of liquid water and ice suspended in the atmosphere over the globe, or for that matter over a single geographical location; and (4) lack of extensive correlative information linking cloud types and characteristics with cloud water content.

Recommendations which would further our knowledge in this general area of absorption, scattering and emission by the atmosphere are embodied in the following thoughts:

1. Experimental work could be profitably devoted to establishing the index of refraction of ice over the entire spectral region of interest at representative temperatures found in the atmosphere.

2. Careful laboratory experiments to establish the validity of the computed absorption coefficient beyond 1000 GHz are needed.
3. Field measurements at one location with a water vapor-cloud radiometer to establish a statistical link between cloud type and cloud water content would be very useful to begin the job of gathering cloud opacity data world wide.
4. Careful studies of the simultaneous cloud water content measurements, infrared and visual images from NIMBUS E and F would be a very useful study to perform.
5. In the time between now and launch of NIMBUS E there should be an optimum method developed to invert the water vapor-cloud data from NIMBUS E.
6. Conversion of the M.I.T. Planetary Circulations Library data on atmospheric water vapor to a more detailed analysis of the statistical attenuation properties of various regions and the globe should be done for more accurate planning purposes.
7. The theoretical methods developed in this study should be continued in detail, from where they now have been carried, on out to $10\ \mu$, establishing or identifying optimum band models which are economical in computer

time for the infrared part of the spectrum.

8. The needs of NASA should be established for the type of information which can be generated by the methods outlined in this report and exact procedures established to compute the needed information.

REFERENCES

- Atlas, D., R. M. Cunningham, R. J. Donaldson, Jr., G. Kanta and P. Newman (1965): "Some Aspects of Electromagnetic Wave Propagation" in Handbook of Geophysics and Space Environments, Shea L. Valley, ed., Air Force Cambridge Research Laboratories, Bedford, Mass.
- aufm Kampe, H. J. and H. K. Weickmann (1957): "Physics of Clouds," Meteor. Monographs, 3, 182.
- Becker, G. E. and S. H. Autler, (1946): "Water Vapor Absorption of Electromagnetic Radiation in the Centimeter Wave-Length Range," Phys. Rev. 70, Nos. 5 and 6.
- Blau, H. H., R. P. Espinola, E. C. Reifstein, III (1966): "Near Infrared Scattering by Sunlit Terrestrial Clouds." Applied Optics, 5, 4, p. 555.
- Born, M., and E. Wolf, (1964): Principles of Optics, Pergamon, Oxford.
- Burch, D. E. (1968): "Absorption of Infrared Radiant Energy by CO₂ and H₂O III. Absorption by H₂O between 0.5 and 36 cm⁻¹ (278μ-2 cm)", J. Opt. Soc. Am., 58, 1383.
- Chandrasekhar, S., (1950): Radiative Transfer, Clarendon, Oxford
- Crane, R. K. (1966): "Microwave Scattering Parameters for New England Rain." M.I.T. (Lincoln Laboratory Technology Report 426), Lexington, Massachusetts.
- Debye, P. (1909): Ann. Phys., 30, 57.
- Debye, P. (1929): Polar Molecules, (Dover Publications, Inc., New York 1959).
- Deirmendjian, D. (1964): "Scattering and Polarization Properties of Water Clouds and Hazes in the Visible and Infrared." Applied Optics, 3, 2, p. 187.
- Diem, M. (1948): "Messungen der Grösse von Wolkenelementen II", Met. Rundschau, 1, 261.
- Fletcher, N. H. (1966): The Physics of Rainclouds. Cambridge University Press.
- Frenkel, L. and D. Woods, (1966): "The Microwave Absorption by H₂O Vapor and Its Mixtures with Other Gases between 100 and 300 Gc/s,"² Proc. IEEE 54, 4.
- Gaut, N. E., (1967): "Studies of Atmospheric Water Vapor by Means of Passive Microwave Techniques," Ph.D. Thesis, Department of Meteorology, Massachusetts Institute of Technology, July 17, 1967.

- Gaut, N. E. (1968): "Studies of Atmospheric Water Vapor by Means of Passive Microwave Techniques," M.I.T. (Research Laboratory of Electronics Tech. Report 467), Cambridge, Mass.
- Gaut, N. E. and E. C. Reifstein, III (1969): "Determination of Atmospheric and Cloud Properties from Analysis of Convair 990 Data," Environmental Research & Technology, Inc., Tech. Rept. P002.
- Golstein, H. (1951): in Propagation of Short Radio Waves, D. E. Kerr, Ed.,
- Gross, E. P., (1955): "Shape of Collision-Broadened Spectral Lines", Phys. Rev., 97, 395.
- Hall, F. F., Jr. (1968): "The Effect of Cirrus Clouds on 8-13 μ Infrared Sky Radiance," Appl. Optics, 7, 891.
- Herman, B. M., and L. J. Battan (1961): Quart., J. Roy Meteor. Soc. 87, 223.
- Herzberg, G. (1966): Molecular Spectra and Molecular Structure: II. Infrared and Raman Spectra of Polyatomic Molecules (D. Van Nostrand Co., Princeton, N. J. especially see Chap. V.
- Hulst, H. C., van de (1957): Light Scattering by Small Particles, Wiley, New York.
- Irvine, W. M., and J. B. Pollack (1968): "Infrared Optical Properties of Water and Ice Spheres" Icarus 8, 324.
- Laws, J. O. and D. A. Parsons (1943): "The Relation of Rain Drop-size to Intensity," Am Geoph. Union Trans., Vol. 24 p. 452.
- Lenoir, W. B. (1968): "Microwave Spectrum of Molecular Oxygen in the Mesosphere," J. Geop. Res., 73, 361.
- Lorentz, H. A. (1906): Proc. Amsterdam Acad. Sci. 8, 591.
- Mason, B. J. (1957): The Physics of Clouds. Oxford University Press.
- Mastenbrook, H. J. and D. R. Purdy (1969): "Vertical Distribution of Water Vapor Over Washington D. C., During 1966 and 1967," NRL Report 6891, Naval Research Laboratory, Washington, D. C.
- Mie, G. (1908): Ann. Phys., 25, 377.
- Peixoto, J. P. (1970): "Water Vapor Balance of the Atmosphere from Five Years of Hemispheric Data" Nordic Hydrology, 2, 120.
- Peixoto, J. P. (1971): "Atmospheric Vapor Flux Computations for Hydrological Purposes," (Manuscript in preparation).

- Peixoto, J. P. and A. R. Crisi (1965): "Hemispheric Humidity Conditions During the IGY," Scientific Report No. 6, Planetary Circulations Project, M.I.T. Department of Meteorology.
- Peixoto, J. P. and G.O.P. Obasi (1965): "Humidity Conditions over Africa During the IGY," Scientific Report No. 7, Planetary Circulations Project, M.I.T. Department of Meteorology.
- Plass, G. N., (1966): "Mie Scattering and Absorption Cross Sections for Absorbing Particles," Applied Optics, 2, 279.
- Reifenstein, E. C. III and Gaut, N. E. (1971): "Microwave Properties of Clouds in the Spectral Range 30-40 GHz," Technical Report No. 12, Environmental Research & Technology, Inc., Waltham, Mass.
- Samuelson, R. E., (1967): "The Transfer of Thermal Infrared Radiation in Cloudy Planetary Atmospheres: Application to Venus," Ph.D. dissertation, Georgetown University, Washington, D. C.
- Sissenwine, N., D. D. Grantham, and H. A. Salmela, (1966): "Mid-Latitude Stratospheric Humidity Regime to 30 Km," Interim Notes on Atmospheric Properties No. 73; Air Force Cambridge Research Laboratories, Bedford, Mass.
- Staelin, D. H., (1966): "Measurements and Interpretation of the Microwave Spectrum of the Terrestrial Atmosphere Near 1-centimeter Wavelength," J. Geophys. Research, 71, 2875.
- Starr, V. P., J. P. Peixoto and R. G. McKean (1969): "Pole-to-Pole Moisture Conditions for the IGY" Rev. Pure and Appl. Geoph., 75, 300.
- Stratton, J. (1941): Electromagnetic Theory, McGraw-Hill, New York.
- Squires, P. (1958): "The Spatial Variation of Liquid Water and Droplet Concentration in Cumuli," Tellus, X, 3, 373.
- Townes, C. H. and A. L. Schawlow, (1955): Microwave Spectroscopy (McGraw-Hill Book Company, Inc., New York (1955)).
- Ulab, F. T. and A. W. Straiton (1970): "Atmospheric Absorption of Radio Waves Between 150 and 350 GHz" IEEE Trans Antennas and Propagation, AP-18, 479.
- Valley, S., (ed.) (1965): Handbook of Geophysics and Space Environments. Air Force Cambridge Research Laboratories, Bedford, Massachusetts.
- Van Vleck, J. H. (1947): "Absorption of Microwaves by Water Vapor," Phys. Rev. 71.

Van Vleck, J. H. and V. F. Weisskopf, (1945): "On the Shape of Collision Broadened Lines," Rev. Mod. Phys. 17, Nos. 2 and 3.

Warner, J. (1955): "The Water Content of Cumuliform Cloud," Tellus, 7, 449.

Zolotarev, V.M., A.B. Mikhailov, L.I. Alpecovich, and S.I. Popov, (1969): "Dispersion and Absorption of Liquid Water in the Infrared and Radio Region of the Spectrum," Optics and Spectr., 27, No. 5, p. 430.

Zhevakin, S. A., and A.P. Naumov (1963): Izvestiy Vuzov (Radiofizika) 6, 674.

APPENDIX A

WATER-VAPOR ROTATIONAL SPECTRAL-LINE PARAMETERS

The following table contains the constants used in Eq. 2-5 of Chapter II for the computation of the water vapor rotational spectrum to 1350 GHz. The values tabulated are those compiled by Gaut (1968) for the 54 lowest frequency lines of water vapor. The line designation is given in column 1 in the $J_{K-1,K+1}$ notation (e.g. the $5_{2,3} \rightarrow 6_{1,6}$ transition is designated 5-2,3 \rightarrow 6-1,6). Column 2 contains the line frequency in GHz, column 3 the parity used for the determination of the factor g_{ij} of Eq. 2-5, which is 1 for "EE00" & "OOEE" & 3 for "E00E" or "OEEO" parities. Column 4 gives the line strength S_{ij} , columns 5 and 6 the lower and upper term (energy) values E_i , E_j , and column 7 the line width in air used in Eq. 2-11 for the determination of the spectral line width. The linewidth in water vapor given in column 8 is used for the computation of the factor α in Eq. 2-11 by the following (see Gaut, 1968):

$$\alpha = 0.00460 \left[\frac{(\Delta\nu_{H_2O})}{(\Delta\nu)_0} - 1 \right] \quad (A-1)$$

Finally, column 9 contains the exponent describing the temperature dependence of the linewidth in Eq. 2-11.

WATER-VAPOR ROTATIONAL SPECTRAL LINE PARAMETERS

NLINES= 54

DESIGNATION	FREQ.GHZ	PARITY	STRENGTH	TERM1	TERM2	WDAIR	WDH2O	TEXP
5-2,3	22.23521	E00E	0.0549	446.39	447.17	0.09019	0.47770	0.626
2-2,0	183.31012	F000	0.1015	136.15	142.30	0.09600	0.49370	0.649
9-3,6	323.15845	0E00	0.0870	1283.02	1293.80	0.07652	0.40120	0.420
4-2,2	323.75806	E000	0.0891	315.70	326.50	0.09292	0.50710	0.619
3-2,1	377.41797	F00E	0.1224	212.12	224.71	0.09480	0.52800	0.630
11-2,10	389.70874	F000	0.0680	1525.31	1538.31	0.07020	0.38070	0.330
6-6,6	435.87427	E000	0.0820	1045.14	1059.68	0.05000	0.26480	0.290
5-5,0	437.67285	0E00	0.0987	742.18	756.18	0.05900	0.34800	0.360
6-6,1	441.56982	F00E	0.0820	1045.14	1059.87	0.05023	0.27090	0.332
3-3,0	445.76685	0E00	0.1316	285.46	300.33	0.08247	0.47480	0.510
5-5,1	465.85181	0E0E	0.0990	742.18	757.72	0.06290	0.35210	0.380
4-4,0	470.94800	E000	0.1165	488.19	503.90	0.06900	0.39870	0.380
7-1,7	487.13599	0E0E	0.0330	586.46	602.71	0.08610	0.49260	0.510
7-7,0	498.52734	0E00	0.0770	1394.96	1411.59	0.04240	0.20510	0.320
7-7,1	498.52734	0E0E	0.0720	1394.96	1411.59	0.04240	0.20500	0.340
1-0,1	557.58325	F00E	1.5000	23.76	42.36	0.11115	0.48890	0.645
4-4,1	617.83813	F00E	0.1193	488.19	508.80	0.07606	0.42620	0.600
8-8,0	641.52051	F000	0.0660	1789.36	1810.76	0.03800	0.17200	0.400
8-8,1	641.52051	F00E	0.0660	1789.36	1810.76	0.03800	0.17150	0.400
2-0,2	752.73730	F000	2.0739	70.08	95.19	0.10440	0.46480	0.690
8-3,5	833.07739	0E0E	0.1570	1052.72	1080.51	0.07980	0.42970	0.510
11-2,4	857.95874	F00E	0.0670	1690.74	1719.36	0.05500	0.30900	0.200
9-9,0	859.15796	0E0E	0.0590	2225.87	2254.53	0.03570	0.15350	0.480
9-9,1	859.15796	0E0E	0.0590	2225.87	2254.53	0.03570	0.15350	0.480
3-3,1	912.51807	0E0E	0.1613	285.26	315.70	0.08638	0.46890	0.676
4-3,1	961.38159	0E0E	0.2622	383.93	416.00	0.08262	0.47220	0.560
1-1,1	987.46191	0E0E	0.7557	37.14	70.08	0.10316	0.50690	0.660
12-2,11	1077.39478	E00E	0.0420	1774.85	1810.79	0.06100	0.34760	0.250
3-0,3	1098.37915	F00E	2.1809	136.74	173.38	0.09944	0.55900	0.701
10-2,9	1107.67212	F000	0.0500	1438.19	1475.14	0.06100	0.63100	0.250
0-0,0	1113.36792	E000	1.0000	0.0	37.14	0.10034	0.50260	0.689
10-10,0	1142.74609	F000	0.0540	2702.61	2740.73	0.03434	0.12970	0.503
10-10,1	1142.74609	F00E	0.0540	2702.61	2740.73	0.03434	0.12970	0.503
8-1,8	1145.74390	0E0E	0.0250	744.20	782.42	0.08008	0.45630	0.498
2-2,1	1154.13745	F00E	0.3003	134.88	173.38	0.09515	0.54850	0.610
5-4,1	1159.83325	F00E	0.2784	610.34	649.03	0.07131	0.42290	0.399
3-1,2	1161.33203	0E0E	2.5434	173.38	212.12	0.09487	0.50600	0.682
7-6,1	1163.43066	F00E	0.2230	1216.38	1255.19	0.05160	0.29040	0.290
6-5,1	1169.72583	0E0E	0.2520	888.74	927.76	0.06480	0.37400	0.360
7-6,2	1187.11279	F000	0.2230	1216.38	1255.98	0.05420	0.30610	0.300
8-7,1	1208.99658	0E0E	0.1990	1591.11	1631.44	0.04450	0.23810	0.320
8-7,2	1213.19336	0E0E	0.1990	1591.11	1631.58	0.04470	0.24110	0.340
4-1,3	1213.19336	0E0E	3.6547	272.23	315.70	0.09507	0.50910	0.720
2-2,0	1227.86232	0E0E	1.2594	95.19	136.15	0.09792	0.46540	0.670
6-5,2	1227.94507	0E0E	0.2530	888.70	931.33	0.06880	0.26820	0.450
7-3,4	1294.43262	0E0E	0.1840	842.51	885.69	0.08190	0.45770	0.550
9-1,8	1309.72119	0E0E	0.0470	1079.20	1122.89	0.06000	0.34800	0.250
5-3,2	1323.21118	0E0E	0.3117	508.80	552.94	0.08313	0.49390	0.571
9-8,1	1329.80615	F00E	0.1730	2010.19	2054.55	0.03900	0.20770	0.390
9-8,2	1329.80615	F000	0.1730	2010.19	2054.55	0.03900	0.20770	0.390
8-1,7	1342.69653	0E0E	0.0360	882.97	927.76	0.06600	0.37500	0.300
5-1,4	1407.44824	0E0E	4.2239	399.44	446.39	0.09470	0.51230	0.722
10-1,9	1423.33618	0E0E	0.0590	1293.22	1340.70	0.05500	0.32200	0.240
6-3,3	1435.92676	0E0E	0.2580	661.54	709.44	0.08300	0.46420	0.590

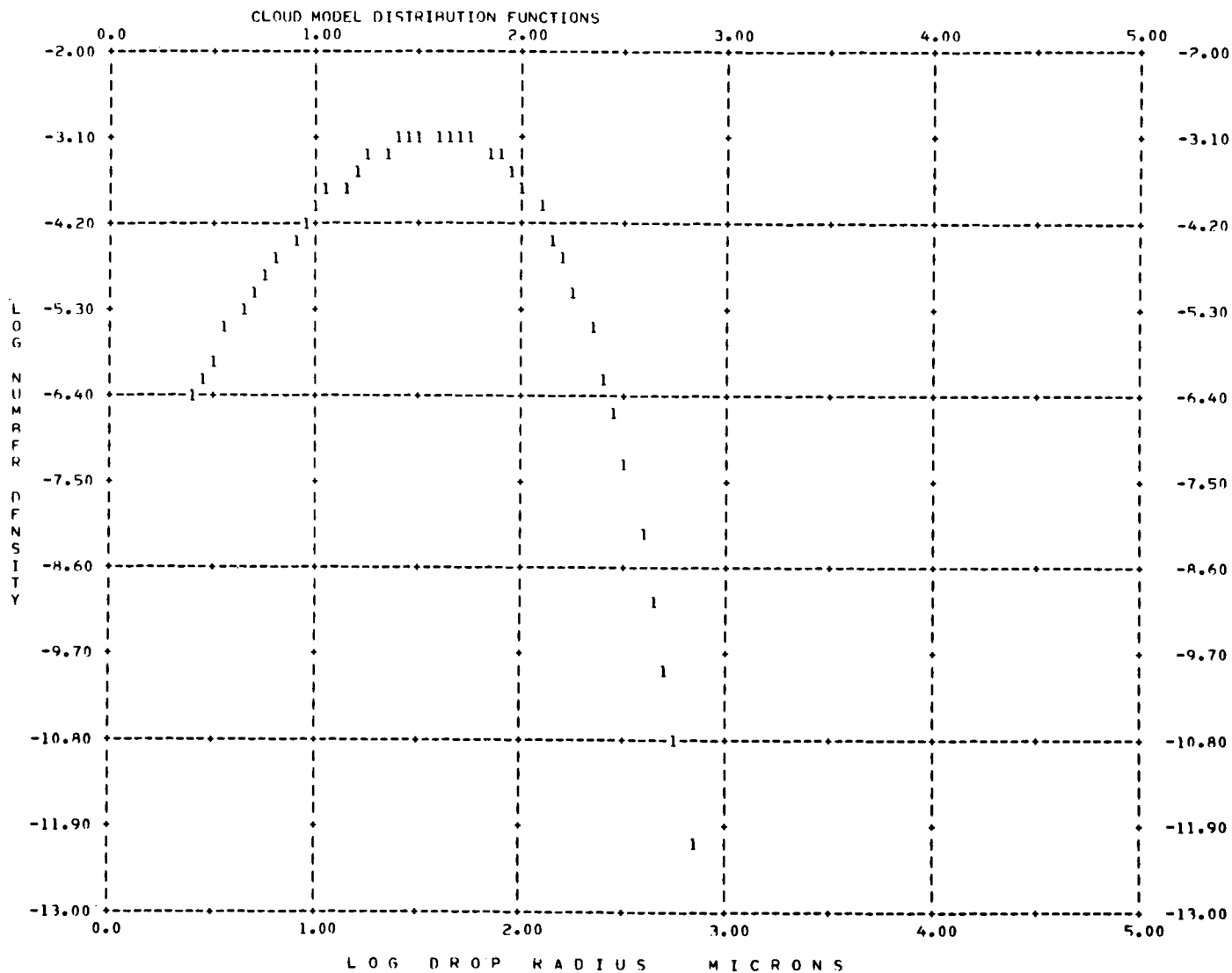
APPENDIX B

CLOUD MODEL DISTRIBUTION FUNCTIONS

The Deirmendjian (1964) distribution functions for the cloud models tabulated in Chapter IV are given on the following pages. For each cloud model, the parameters are tabulated layer-by-layer, followed by a log-log plot of the distribution functions. The base and top height are given in meters in columns 1 and 2, the mass density in column 3, followed by the mode radius, and the shape parameters C_1 and C_2 in columns 4 to 6. Column 7 indicates the composition of each layer, as liquid, rain, or ice. The symbols used to trace the distribution functions in the computer-generated plots refer to the layer numbers of the model.

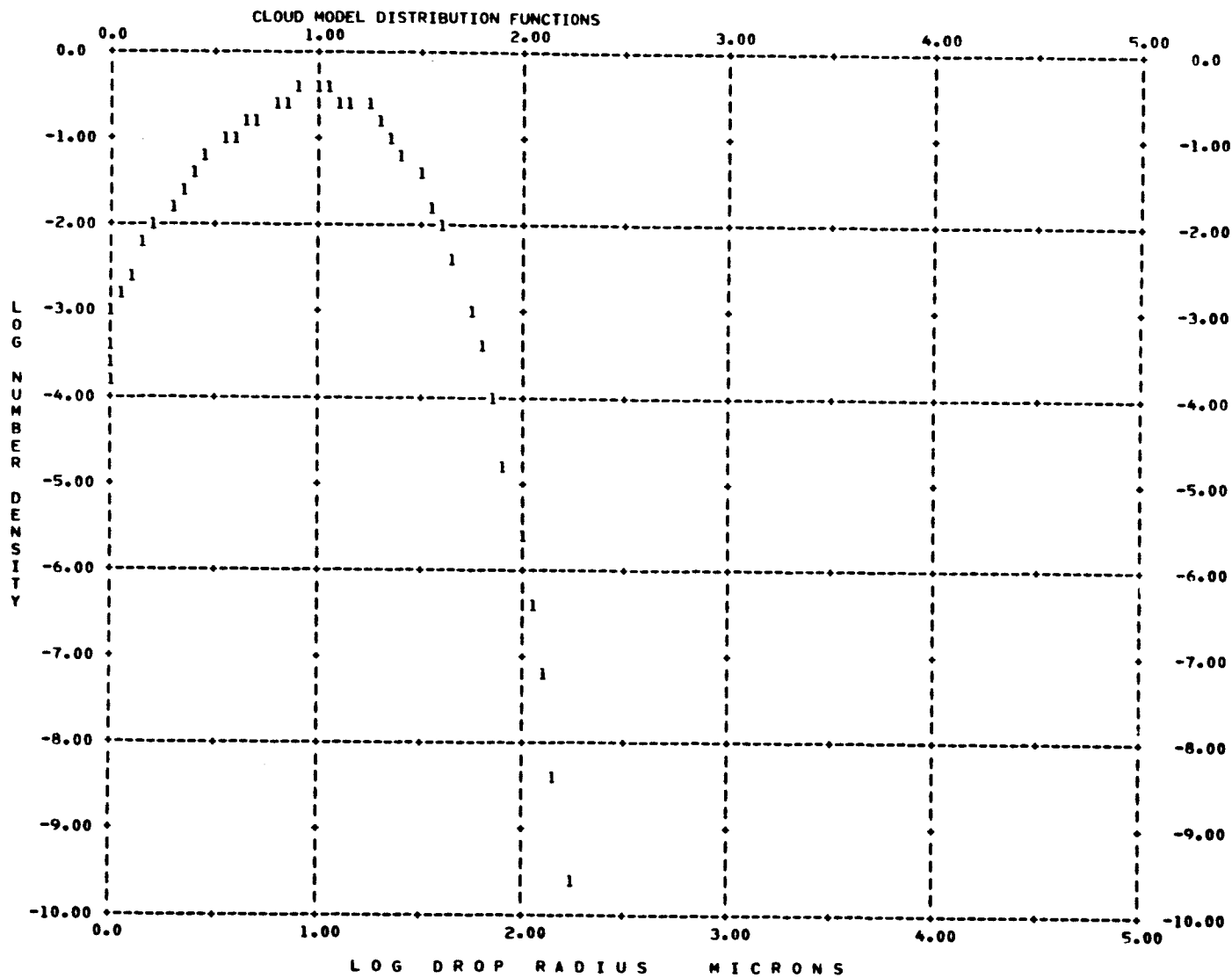
1-M-1 CIRROSTRATUS, MID-LATITUDE, 15-21 KFT

ZBASE METERS	ZTOP METERS	DENSITY G/M**3	R(MODE) MICRON	C1	C2	COMP.
5000.0	7000.0	0.100	40.00	6.00	0.50	ICE

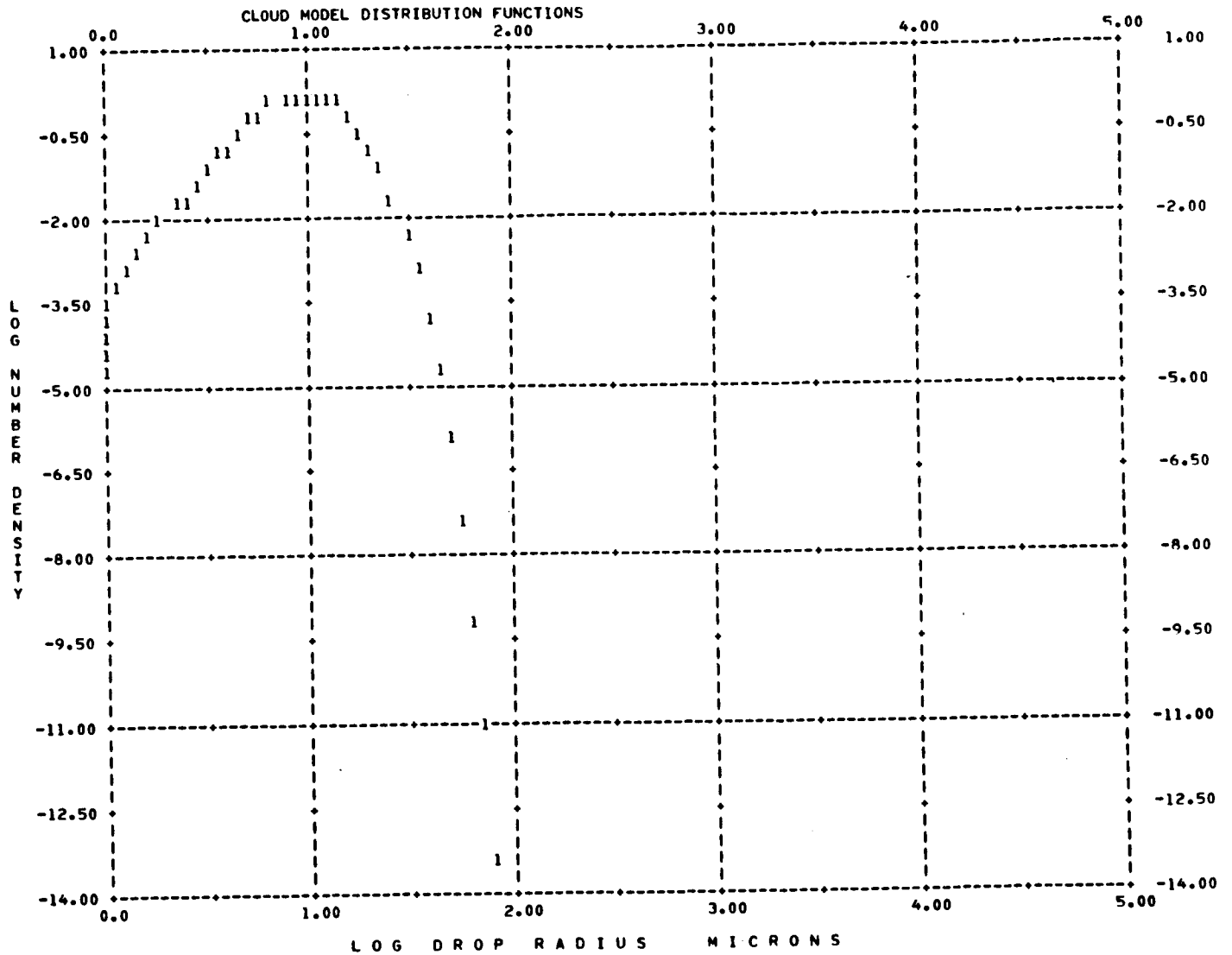


10-1 ALTOCUMULUS 8000-9000 FT

ZBASE METERS	ZTOP METERS	DENSITY G/M**3	R(MODE) MICRON	C1	C2	COMP.
2400.0	2900.0	0.150	10.00	6.00	0.50	LIQ.

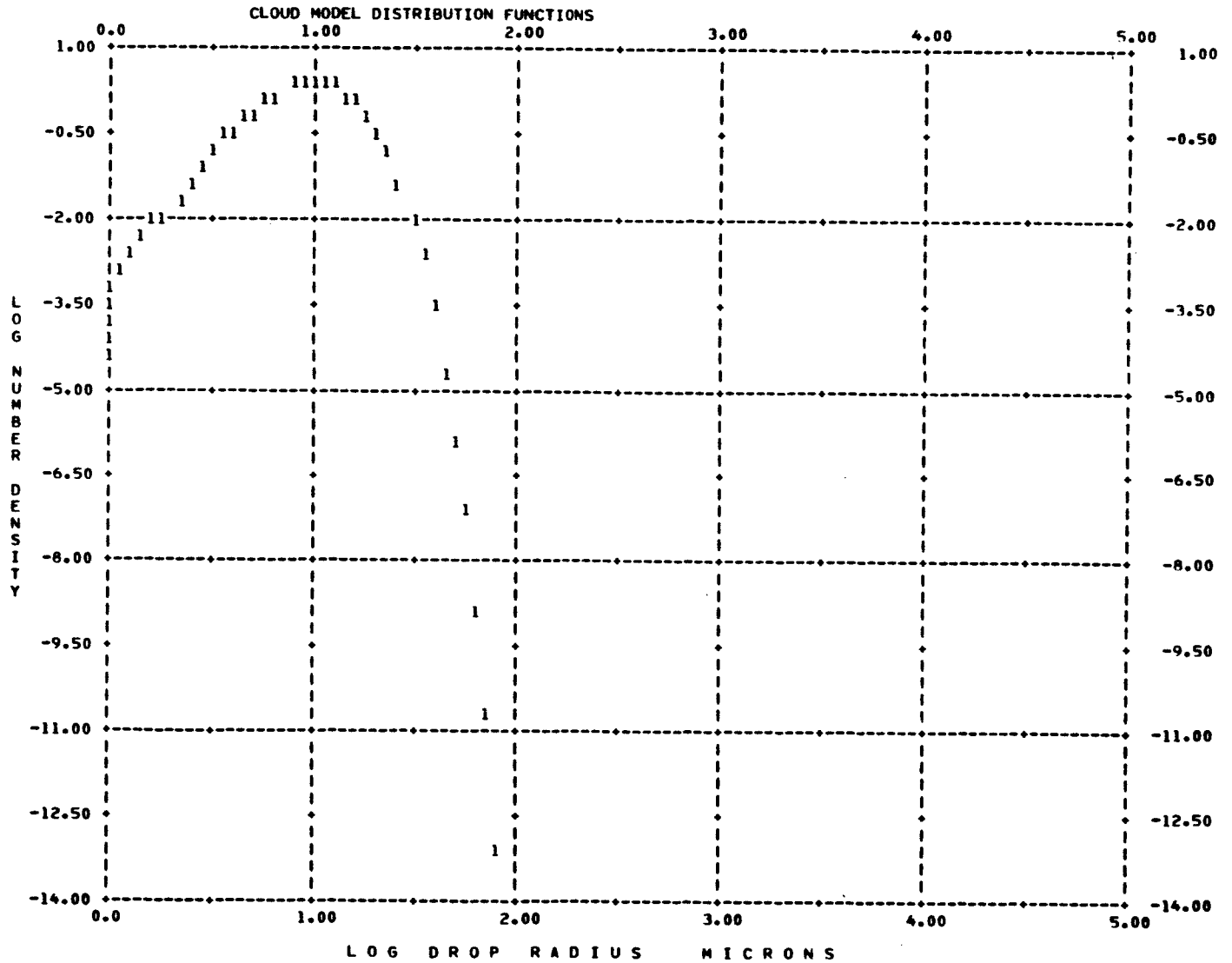


ZBASE METERS	ZTOP METERS	DENSITY G/M**3	R(MODE) MICRON	C1	C2	COMP.
2400.0	2900.0	0.150	10.00	6.00	1.00	LIQ.



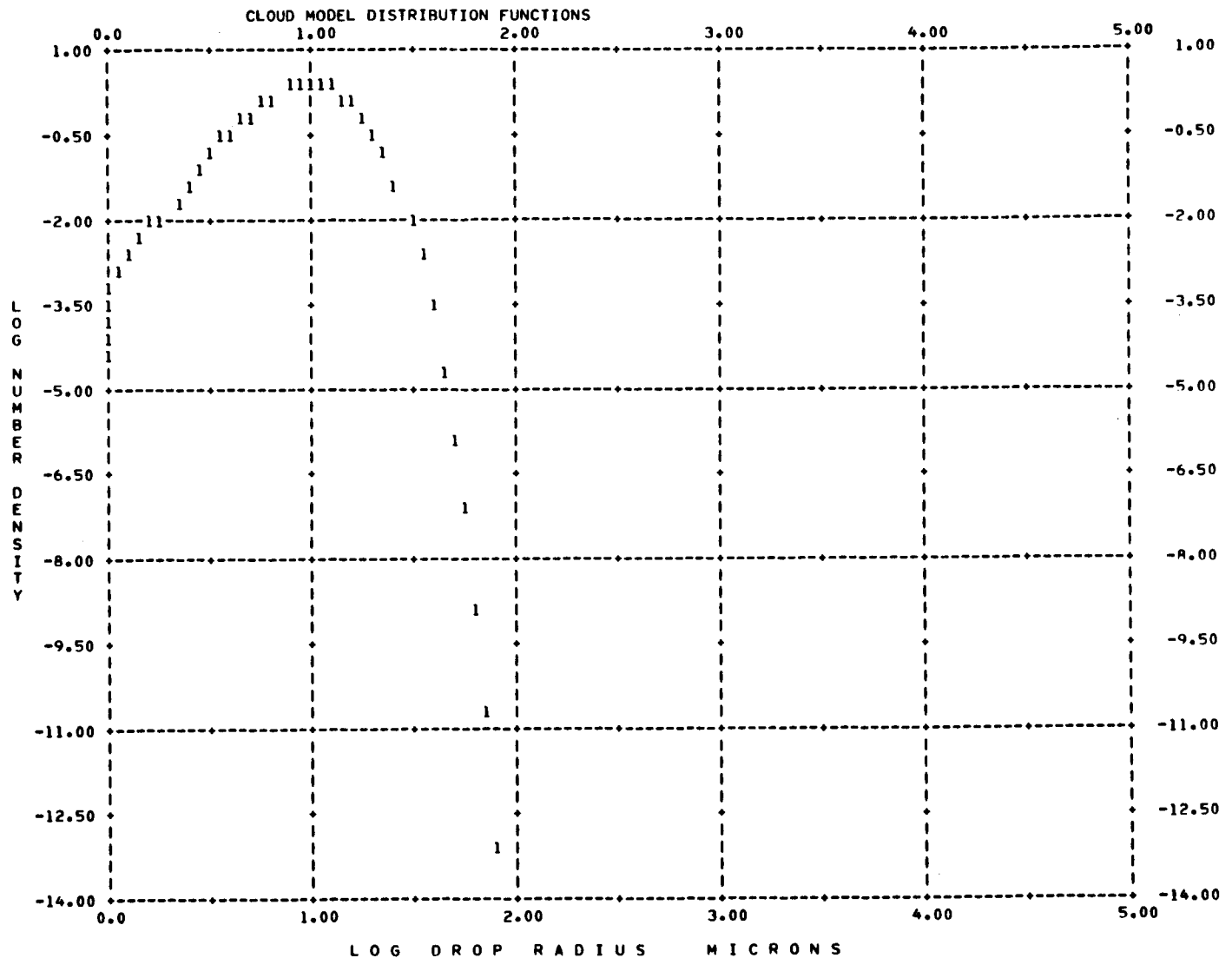
20-1 LOW-LYING STRATUS 500-2000 FT

ZBASE METERS	ZTOP METERS	DENSITY G/M**3	R(MODE) MICRON	C1	C2	COMP.
150.0	650.0	0.250	10.00	6.00	1.00	L10.

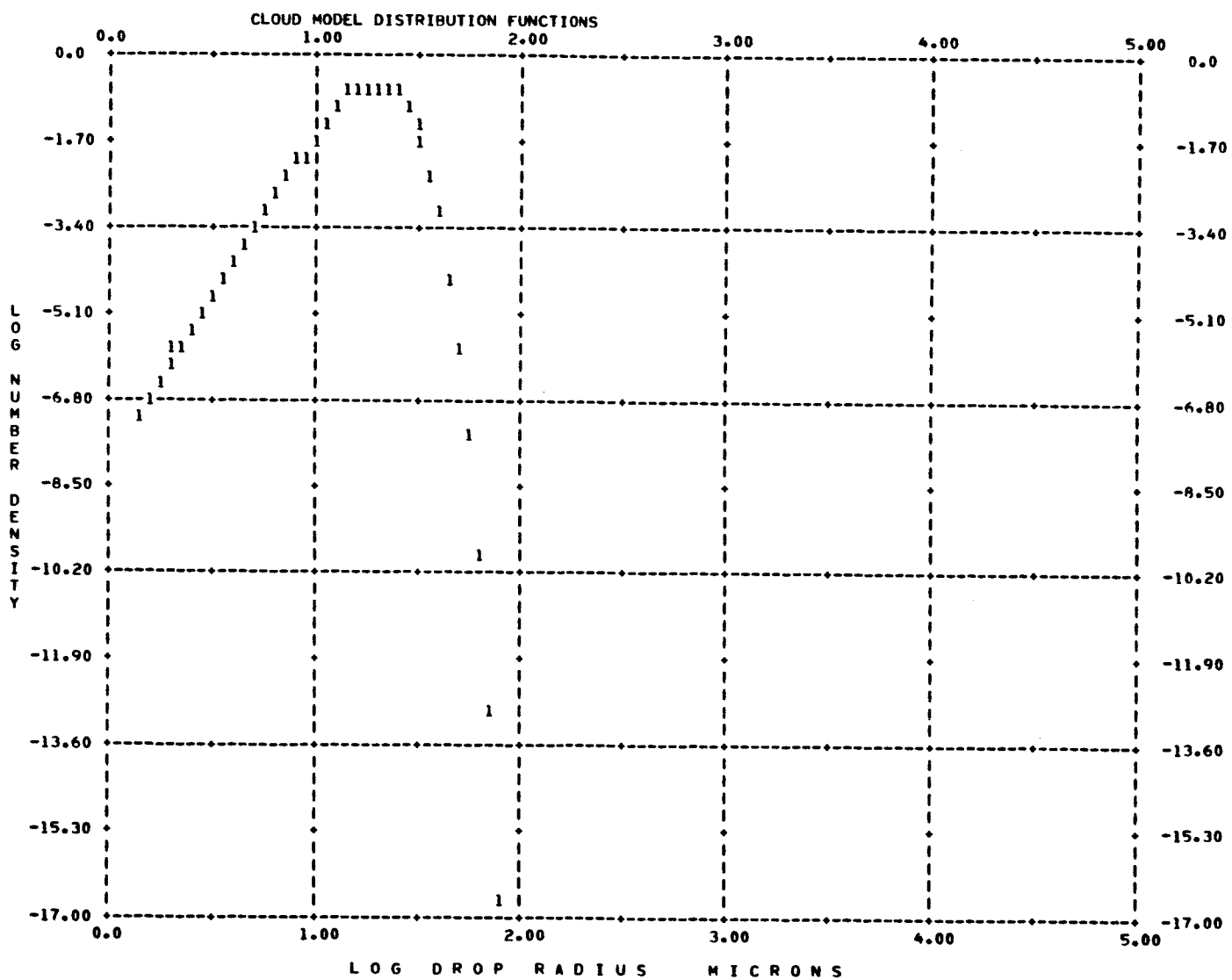


20-2 LOW-LYING STRATUS 1500-3000 FT

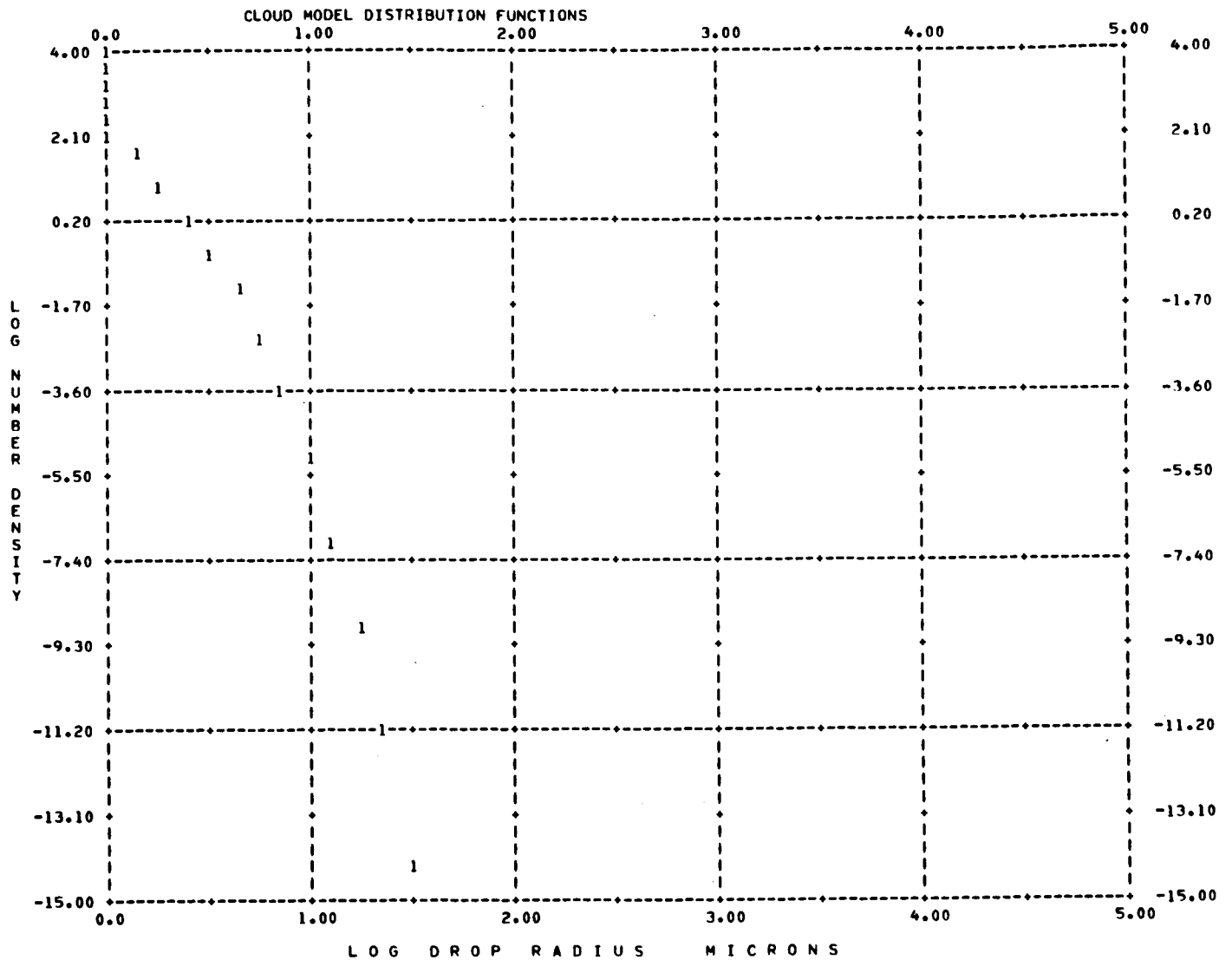
ZBASE METERS	ZTOP METERS	DENSITY G/M**3	R(MODE) MICRON	C1	C2	COMP.
500.0	1000.0	0.250	10.00	6.00	1.00	LIQ.



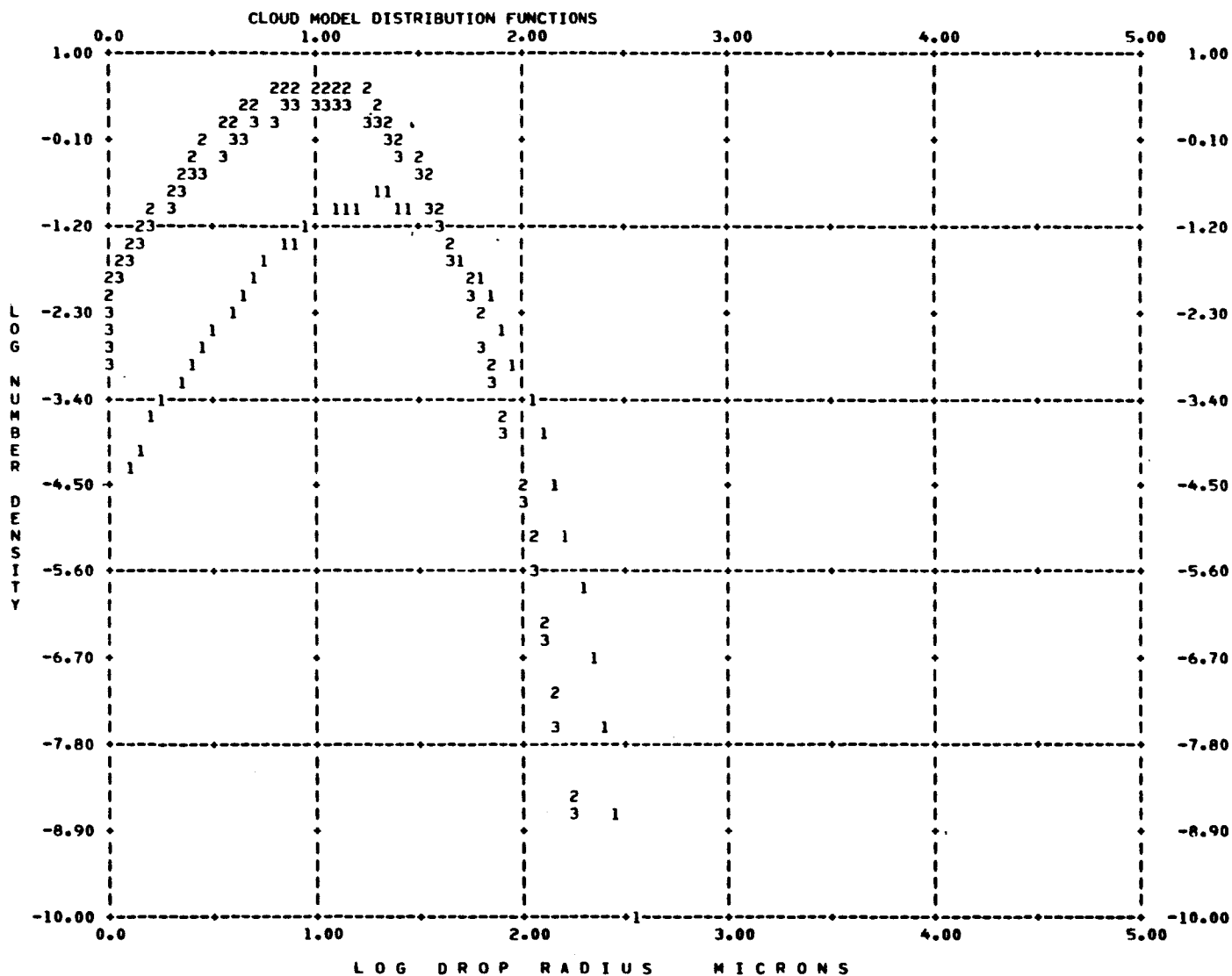
ZBASE METERS	ZTOP METERS	DENSITY G/M**3	R(MODE) MICRON	C1	C2	COMP.
0.0	50.0	0.150	20.00	7.00	2.00	L10.



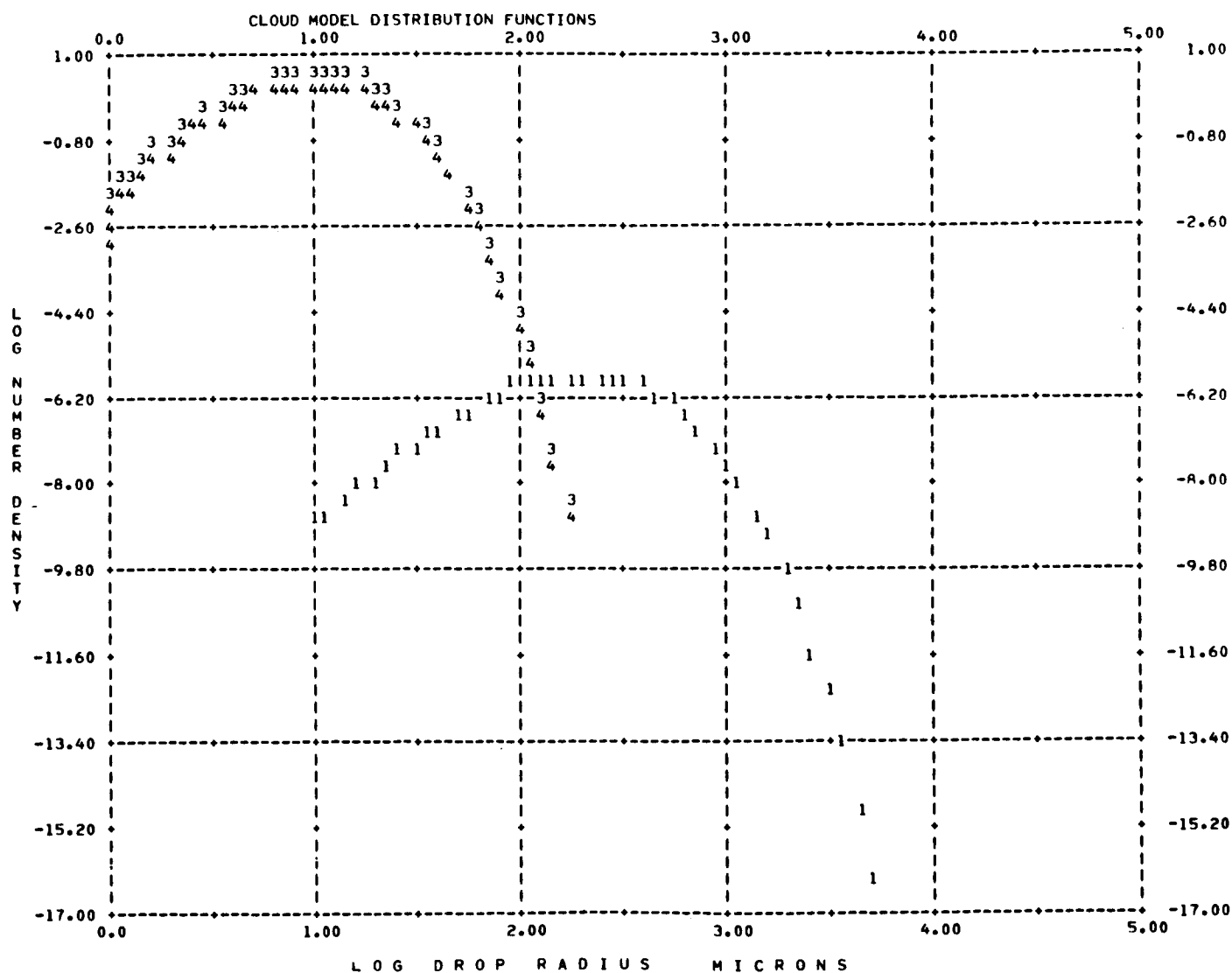
ZBASE METERS	ZTOP METERS	DENSITY G/M**3	R(MODE) MICRON	C1	C2	COMP.
0.0	1500.0	0.001	0.05	1.00	0.50	LIQ.



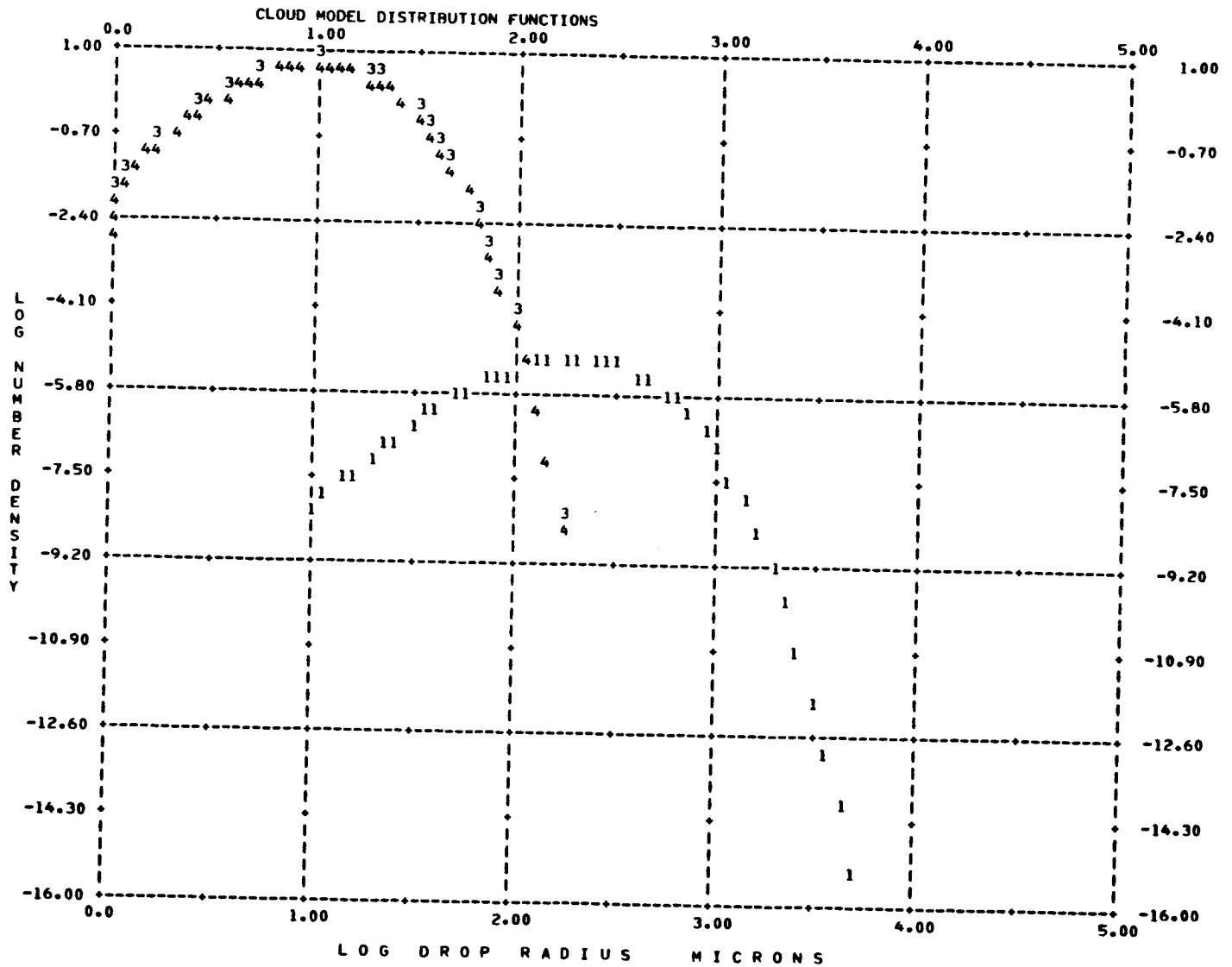
ZBASE METERS	ZTOP METERS	DENSITY G/M**3	R(MODE) MICRON	C1	C2	COMP.
0.0	500.0	1.000	20.00	6.00	0.50	RAIN
500.0	1000.0	2.000	10.00	6.00	0.50	LIQ.
1000.0	1500.0	1.000	10.00	6.00	0.50	LIQ.



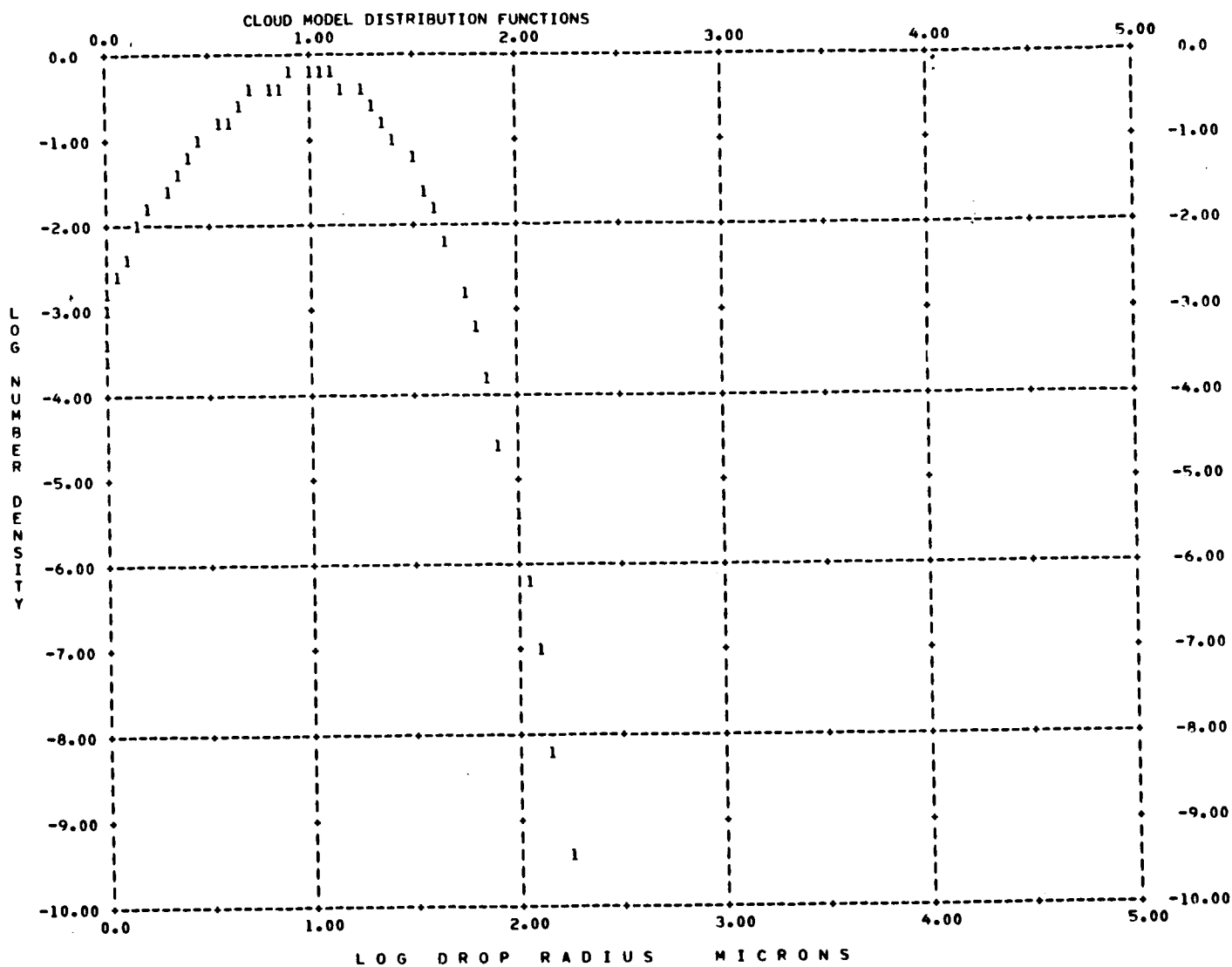
ZBASE METERS	ZTOP METERS	DENSITY G/M**3	R(MODE) MICRON	C1	C2	COMP.
0.0	150.0	0.200	200.00	5.00	0.50	RAIN
150.0	500.0	1.000	10.00	6.00	0.50	LIQ.
500.0	1000.0	2.000	10.00	6.00	0.50	LIQ.
1000.0	1500.0	1.000	10.00	6.00	0.50	LIQ.



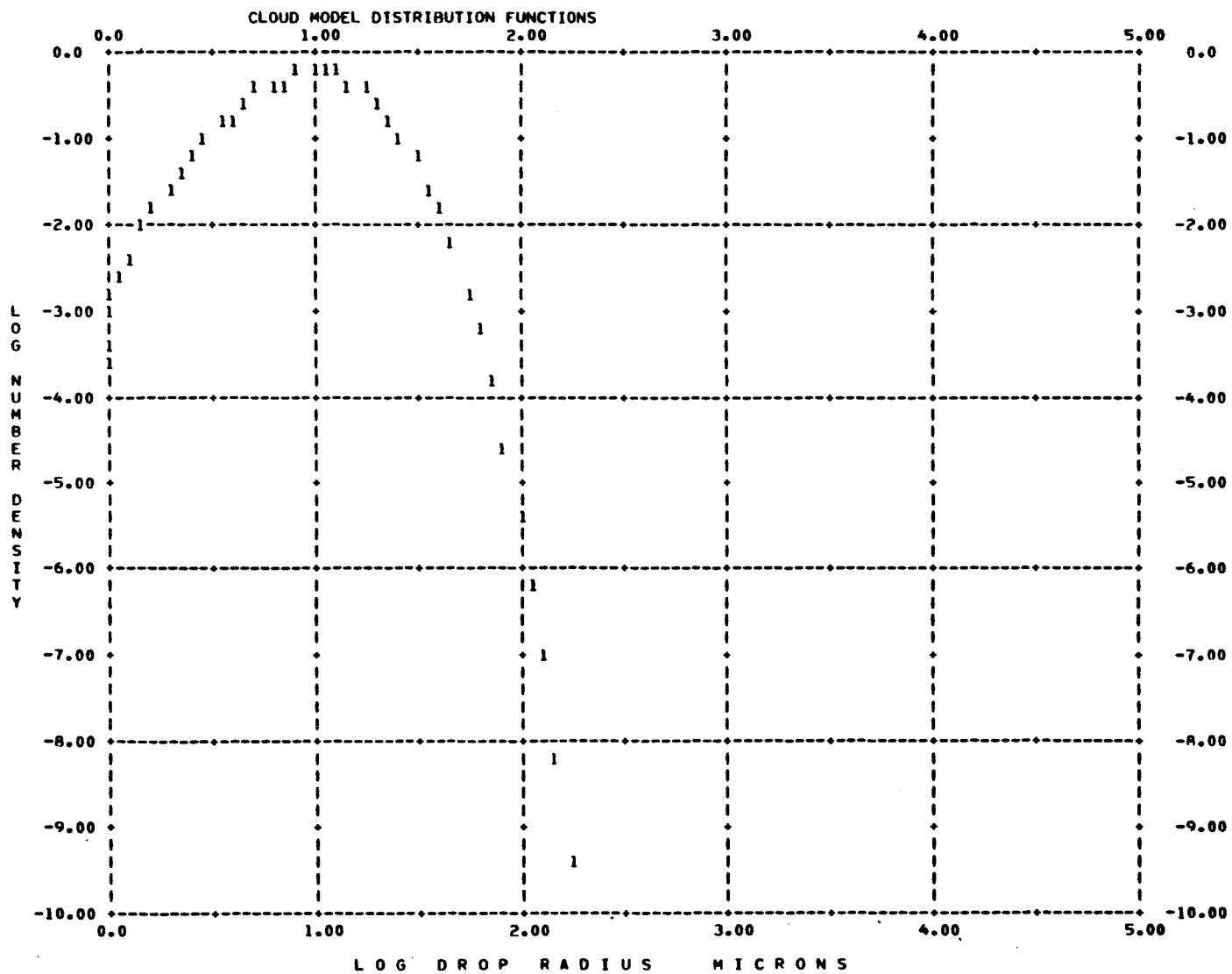
ZBASE METERS	ZTOP METERS	DENSITY G/M**3	R(MODE) MICRON	C1	C2	COMP.
0.0	300.0	1.000	200.00	5.00	0.50	RAIN
300.0	1000.0	2.000	10.00	6.00	0.50	LIQ.
1000.0	2000.0	3.000	10.00	6.00	0.50	LIQ.
2000.0	4000.0	2.000	10.00	6.00	0.50	LIQ.



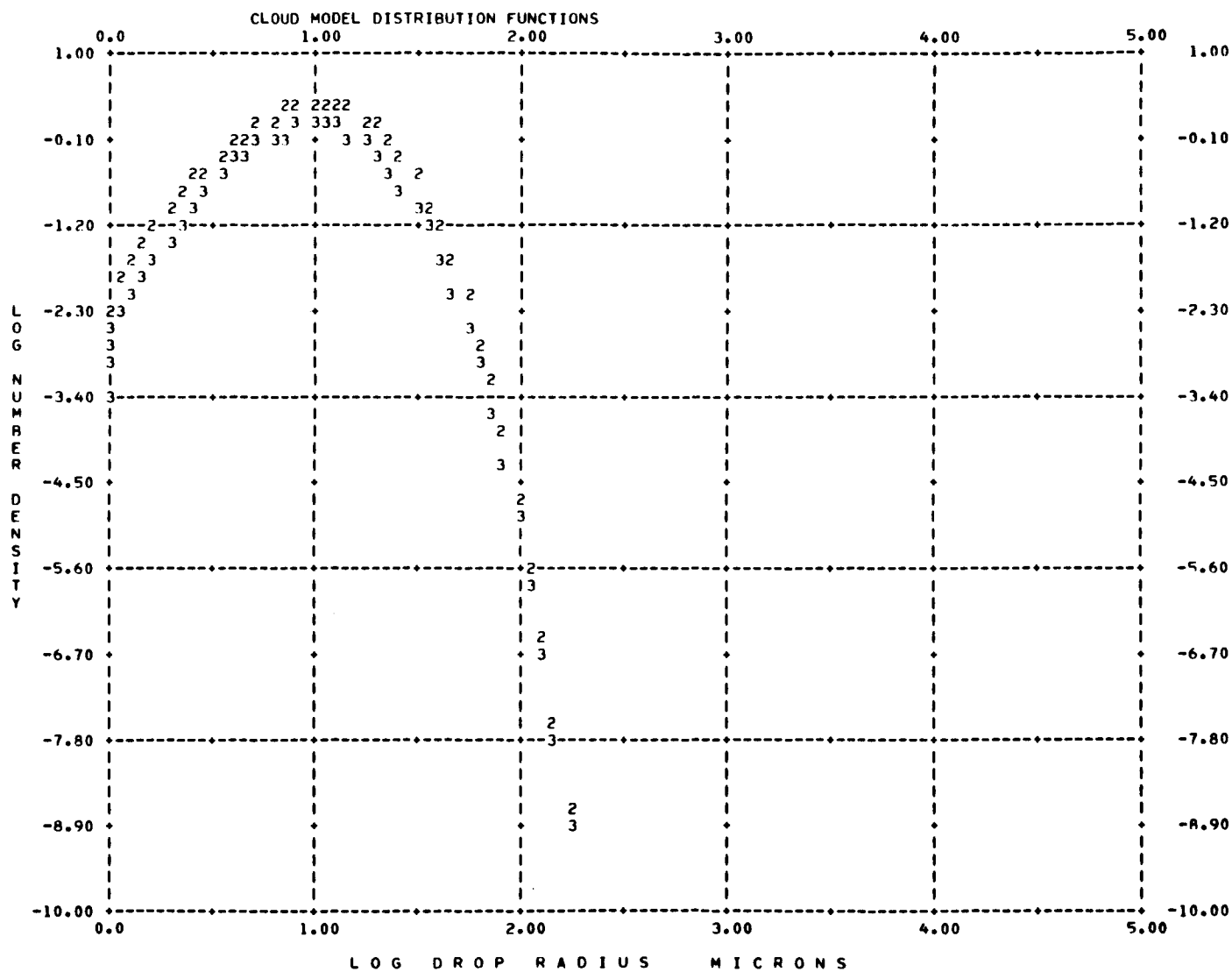
ZBASE METERS	ZTOP METERS	DENSITY G/M**3	R(MODE) MICRON	C1	C2	COMP.
330.0	660.0	0.250	10.00	6.00	0.50	L10.



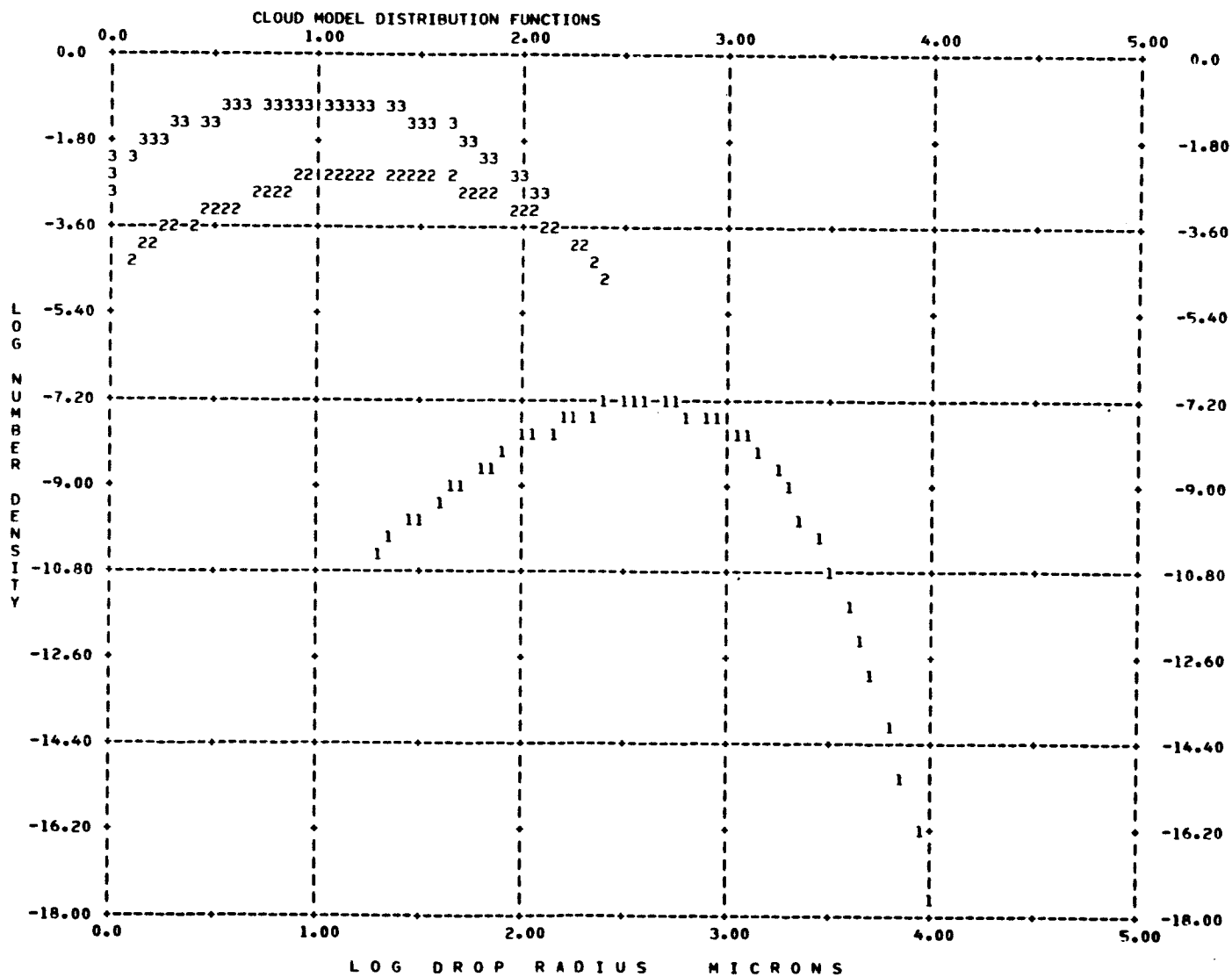
ZBASE METERS	ZTOP METERS	DENSITY G/M**3	R(MODE) MICRON	C1	C2	COMP.
660.0	1320.0	0.250	10.00	6.00	0.50	LIO.



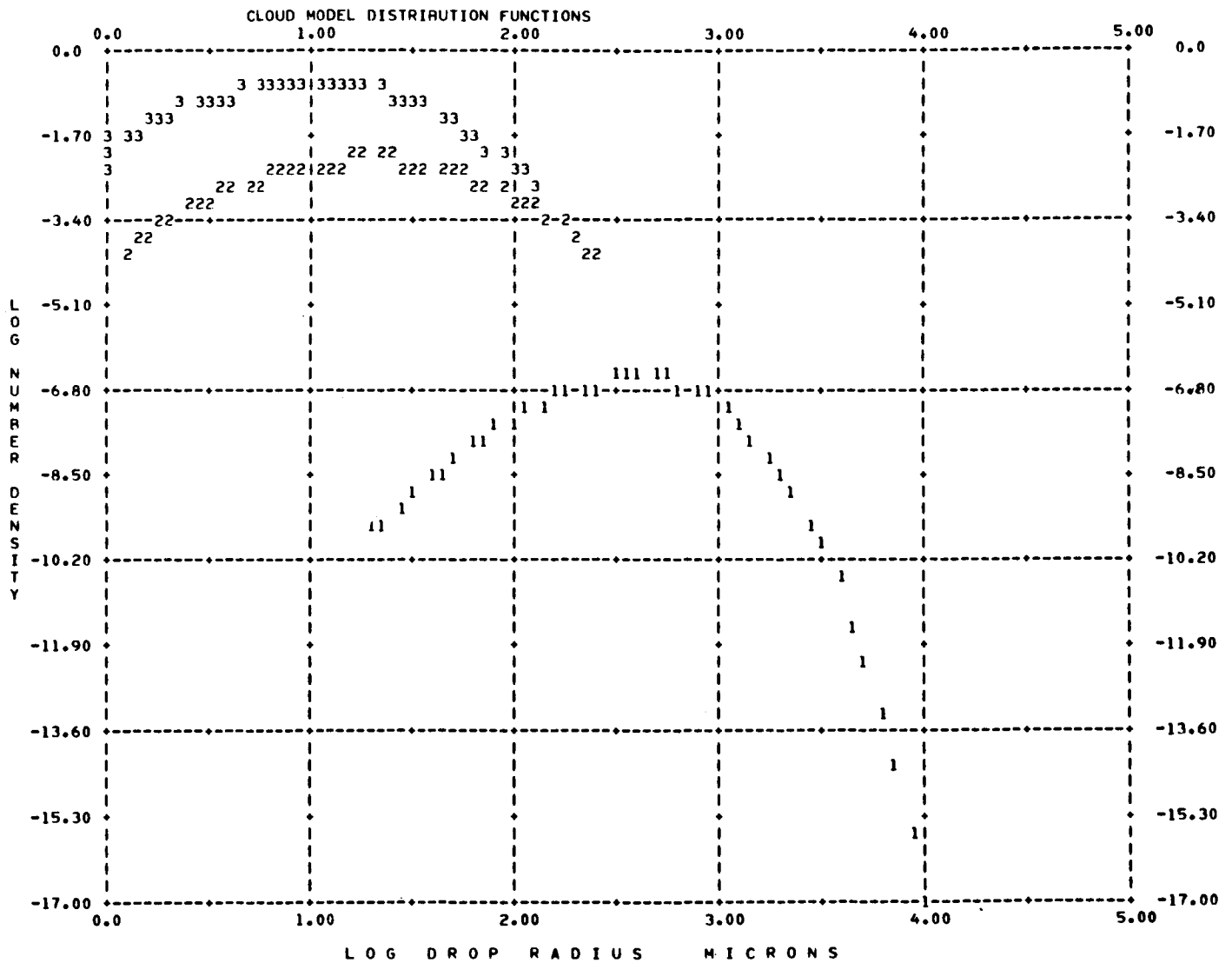
ZBASE METERS	ZTOP METERS	DENSITY G/CM ³	R(MODE) MICRON	C1	C2	COMP.
500.0	1000.0	0.500	10.00	6.00	0.50	LIQ.
1000.0	1500.0	1.000	10.00	6.00	0.50	LIQ.
1500.0	2000.0	0.500	10.00	6.00	0.50	LIQ.



ZHASE METERS	ZTOP METERS	DENSITY G/M**3	R(MODE) MICRON	C1	C2	COMP.
0.0	500.0	0.100	400.00	5.00	0.50	RAIN
500.0	1000.0	1.000	20.00	6.00	0.20	LIO.
1000.0	3000.0	2.000	10.00	6.00	0.20	LIO.

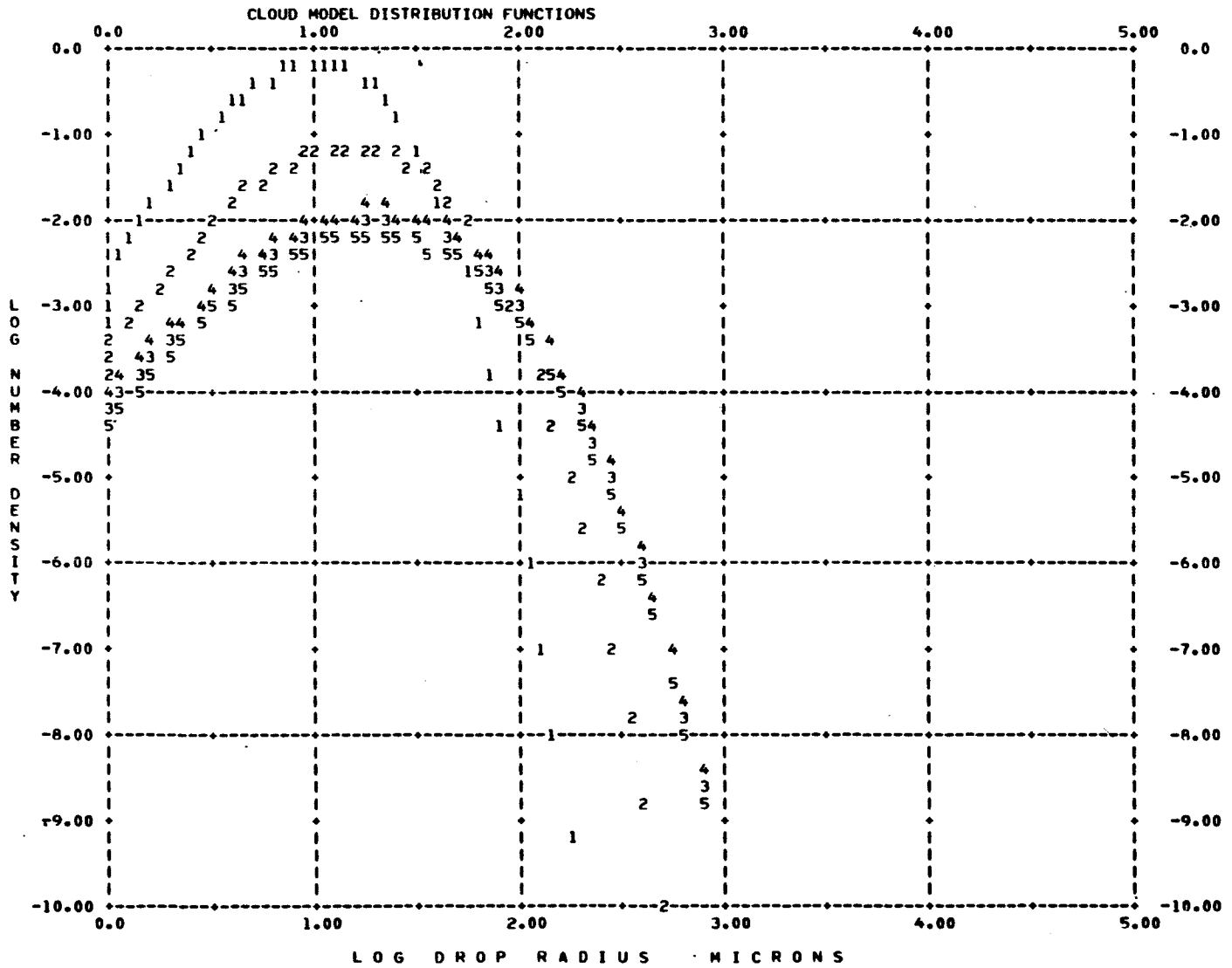


ZBASE METERS	ZTOP METERS	DENSITY G/M**3	R(MODE) MICRON	C1	C2	COMP.
0.0	400.0	0.500	400.00	5.00	0.50	RAIN
400.0	1000.0	2.000	20.00	6.00	0.20	LIQ.
1000.0	4000.0	4.000	10.00	6.00	0.20	LIQ.

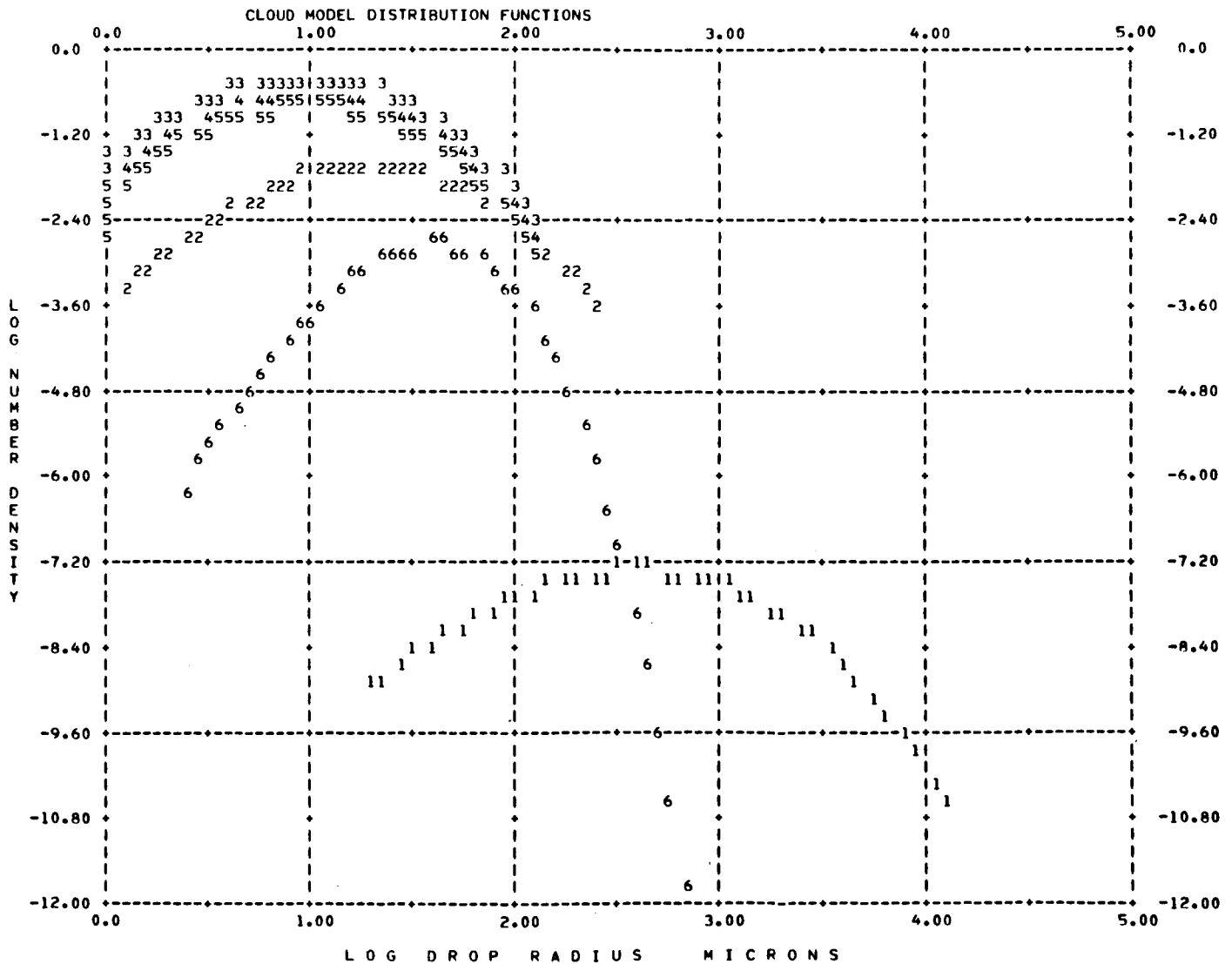


25-4 CUMULUS CONGESTUS.3000-9000 FT

ZBASE METERS	ZTOP METERS	DENSITY G/M**3	R(MODE) MICRON	C1	C2	COMP.
1000.0	1200.0	0.300	10.00	6.00	0.50	L10.
1200.0	1600.0	0.500	15.00	5.00	0.40	L10.
1600.0	2000.0	0.800	20.00	5.00	0.30	L10.
2000.0	2500.0	1.000	20.00	5.00	0.30	L10.
2500.0	3000.0	0.500	20.00	5.00	0.30	L10.



ZBASE METERS	ZTOP METERS	DENSITY G/M**3	R(MODE) MICRON	C1	C2	COMP.
0.0	300.0	6.300	400.00	5.00	0.20	RAIN
300.0	1000.0	7.000	20.00	6.00	0.20	LIQ.
1000.0	4000.0	8.000	10.00	6.00	0.20	LIQ.
4000.0	6000.0	4.000	10.00	6.00	0.20	LIQ.
6000.0	8000.0	3.000	10.00	6.00	0.20	LIQ.
8000.0	10000.0	0.200	40.00	6.00	0.50	ICE



APPENDIX C

COMPUTATIONAL RESULTS FOR CLOUD MODELS

The unit-volume absorption and scattering properties of the cloud models of Chapter IV have been computed using the theory developed in Chapter III. The computation procedures are embodied in the "Radiative Absorption and Scattering Program" (RASP) written for the IBM 360 computer. At each given wavelength, the program evaluates the Mie efficiency factors over the range of drop-size parameters 0.01 to 50 (Figures III-3 through III-11 and, III-13 through III-15), and from these the single-particle cross sections for scattering, absorption, and extinction. For each cloud model, the set of number densities, $N(r)$, are evaluated using Eq. 4-1 of Chapter IV with the given distribution parameters, and the unit-volume coefficients determined by numerical integration of Eq. 3-12 of Chapter III.

The following quantities are tabulated for each layer of a multi-layer distribution, at each given wavelength λ . In columns 2 and 3 are given the mass density and number density of the layer determined by numerical summation over the computed drop distribution. Columns 4 and 5 contain the coefficients for scattering $GAM(S)$ and extinction $GAM(E)$ in neper cm^{-1} . Column 6 contains the extinction coefficient $GAM(E)$ in dB km^{-1} (since both sets of units are often of interest). The Rayleigh extinction coefficient $GAM(R)$ computed using the Staelin approximation formula (Eq. 3-16), is given in Column 7. Finally, the single scattering albedo and penetration depths for single scattering $D(SCAT)$ and extinction $D(EXT)$ are given in columns 8 to 10.

The computed coefficients $GAM(S)$ & $GAM(E)$ for the Cirrus model

1-M-1 make use of the index of refraction for ice at the three wavelengths considered, but the Rayleigh extinction coefficient $GAM(R)$ refers to the equivalent mass density of water droplets with the same particle distribution and temperature. Thus, at 1 cm, the computed extinction coefficient of ice is seen to be two orders of magnitude less than the same mass density of water in a Rayleigh distributed cloud. Ice clouds are often neglected in radiative transfer problems at microwave frequencies for this reason.

Cloud model 26-1 presents a special case with its Cirrus cap. Since the index of refraction data used in the computations for water and ice are at different temperatures, the results for the ice layer have been computed separately and added to the table at the wavelengths 1 cm, 100 μ and 10 μ . In this case, the Rayleigh extinction coefficient corresponds to the same mass density of water at 0°C, instead of 25°C for the water layers.

1-M-1 CIRROSTRATUS, MID-LATITUDE, 15-21 KFT

ZBASE METERS	ZTOP METERS	DENSITY G/M**3	R(MODE) MICRON	C1	C2	COMP.
5000.0	7000.0	0.100	40.00	6.00	0.50	ICE

SUMMARY OF UNIT VOLUME PROPERTIES AT LAMDA= 1.000E 00 CM,TEMP= 273.00 DEG K

LAYER NUMBER	M-DENS. G M**3	N-DENS. CM**3	GAM(S) NEPER/CM	GAM(E) NEPER/CM	GAM(E) DB/KM	GAM(R) DB/KM	ALBEDO	D(SCAT) KM	D(EXT) KM
1	0.1004	0.0564	1.675E-10	2.009E-09	8.739E-04	7.238E-02	0.08337	5.971E 03	4.978E 02

SUMMARY OF UNIT VOLUME PROPERTIES AT LAMDA= 1.000E-02 CM,TEMP= 273.00 DEG K

LAYER NUMBER	M-DENS. G M**3	N-DENS. CM**3	GAM(S) NEPER/CM	GAM(E) NEPER/CM	GAM(E) DB/KM	GAM(R) DB/KM	ALBEDO	D(SCAT) KM	D(EXT) KM
1	0.1004	0.0564	1.319E-05	2.173E-05	9.454E 00	7.238E 02	0.60706	7.580E-02	4.601E-02

SUMMARY OF UNIT VOLUME PROPERTIES AT LAMDA= 1.000E-03 CM,TEMP= 273.00 DEG K

LAYER NUMBER	M-DENS. G M**3	N-DENS. CM**3	GAM(S) NEPER/CM	GAM(E) NEPER/CM	GAM(E) DB/KM	GAM(R) DB/KM	ALBEDO	D(SCAT) KM	D(EXT) KM
1	0.1004	0.0564	8.545E-06	1.694E-05	7.368E 00	7.238E 04	0.50451	1.170E-01	5.904E-02

10-1 ALTOCUMULUS 8000-9000 FT

ZRASE METERS	ZTOP METERS	DENSITY G/M**3	R(MODE) MICRON	C1	C2	COMP.
2400.0	2900.0	0.150	10.00	6.00	0.50	LIO.

SUMMARY OF UNIT VOLUME PROPERTIES AT LAMDA= 1.000E 01 CM,TEMP= 298.00 DEG K

LAYER NUMBR	M-DENS. G M**3	N-DENS. CM**3	GAM(S) NEPER/CM	GAM(E) NEPER/CM	GAM(R) DB/KM	ALBEDO	D(SCAT) KM	D(EXT) KM
1	0.1505	5.4137	1.833E-15	1.678E-09	7.300E-04	5.379E-04	0.0000	5.456E 08
								5.959E 02

SUMMARY OF UNIT VOLUME PROPERTIES AT LAMDA= 1.000E 00 CM,TEMP= 298.00 DEG K

LAYER NUMBR	M-DENS. G M**3	N-DENS. CM**3	GAM(S) NEPER/CM	GAM(E) NEPER/CM	GAM(R) DB/KM	ALBEDO	D(SCAT) KM	D(EXT) KM
1	0.1505	5.4137	2.041E-11	1.611E-07	7.008E-02	5.379E-02	0.00013	4.900E 04
								6.207E 00

SUMMARY OF UNIT VOLUME PROPERTIES AT LAMDA= 1.000E-01 CM,TEMP= 298.00 DEG K

LAYER NUMBR	M-DENS. G M**3	N-DENS. CM**3	GAM(S) NEPER/CM	GAM(E) NEPER/CM	GAM(R) DB/KM	ALBEDO	D(SCAT) KM	D(EXT) KM
1	0.1505	5.4137	1.409E-07	5.555E-06	2.416E 00	5.379E 00	0.02537	7.097E 00
								1.800E-01

SUMMARY OF UNIT VOLUME PROPERTIES AT LAMDA= 1.000E-02 CM,TEMP= 298.00 DEG K

LAYER NUMBR	M-DENS. G M**3	N-DENS. CM**3	GAM(S) NEPER/CM	GAM(E) NEPER/CM	GAM(R) DB/KM	ALBEDO	D(SCAT) KM	D(EXT) KM
1	0.1505	5.4137	5.080E-05	1.138E-04	4.950E 01	5.379E 02	0.44638	1.969E-02
								8.787E-03

SUMMARY OF UNIT VOLUME PROPERTIES AT LAMDA= 1.000E-03 CM,TEMP= 298.00 DEG K

LAYER NUMBR	M-DENS. G M**3	N-DENS. CM**3	GAM(S) NEPER/CM	GAM(E) NEPER/CM	GAM(R) DB/KM	ALBEDO	D(SCAT) KM	D(EXT) KM
1	0.1505	5.4137	6.775E-05	1.154E-04	5.022E 01	5.379E 04	0.58688	1.476E-02
								8.662E-03

PHASE	ZTOP	DENSITY	R(MODE)	C1	C2	COMP.
METERS	METERS	G/M**3	MICRON			
2400.0	2900.0	0.150	10.00	6.00	1.00	LIG.

SUMMARY OF UNIT VOLUME PROPERTIES AT LAMDA= 1.000E 01 CM,TEMP= 298.00 DEG K

LAYER	M-DENS.	N-DENS.	GAM(S)	GAM(E)	GAM(R)	ALBEDO	D(SCAT)	D(EXT)
NUMBER	G M**3	CM**3	NEPER/CM	DB/KM	DR/KM		KM	KM
1	0.1504	15.1663	2.621E-16	1.677E-09	7.294E-04	5.374E-04	0.0000	3.915E 09
								5.964E 02

SUMMARY OF UNIT VOLUME PROPERTIES AT LAMDA= 1.000E 00 CM,TEMP= 298.00 DEG K

LAYER	M-DENS.	N-DENS.	GAM(S)	GAM(E)	GAM(R)	ALBEDO	D(SCAT)	D(EXT)
NUMBER	G M**3	CM**3	NEPER/CM	DB/KM	DR/KM		KM	KM
1	0.1504	15.1663	2.671E-12	1.585E-07	6.895E-02	5.374E-02	0.0002	3.483E 05
								6.309E 00

SUMMARY OF UNIT VOLUME PROPERTIES AT LAMDA= 1.000E-01 CM,TEMP= 298.00 DEG K

LAYER	M-DENS.	N-DENS.	GAM(S)	GAM(E)	GAM(R)	ALBEDO	D(SCAT)	D(EXT)
NUMBER	G M**3	CM**3	NEPER/CM	DB/KM	DR/KM		KM	KM
1	0.1504	15.1663	1.987E-08	5.094E-06	2.216E 00	5.374E 00	0.00370	5.300E 01
								1.963E-01

SUMMARY OF UNIT VOLUME PROPERTIES AT LAMDA= 1.000E-02 CM,TEMP= 298.00 DEG K

LAYER	M-DENS.	N-DENS.	GAM(S)	GAM(E)	GAM(R)	ALBEDO	D(SCAT)	D(EXT)
NUMBER	G M**3	CM**3	NEPER/CM	DB/KM	DR/KM		KM	KM
1	0.1504	15.1663	4.878E-05	1.272E-04	5.533E 01	5.374E 02	0.38349	2.050E-02
								7.861E-03

SUMMARY OF UNIT VOLUME PROPERTIES AT LAMDA= 1.000E-03 CM,TEMP= 298.00 DEG K

LAYER	M-DENS.	N-DENS.	GAM(S)	GAM(E)	GAM(R)	ALBEDO	D(SCAT)	D(EXT)
NUMBER	G M**3	CM**3	NEPER/CM	DB/KM	DR/KM		KM	KM
1	0.1504	15.1663	1.252E-04	1.930E-04	8.396E 01	5.374E 04	0.64887	7.984E-03
								5.181E-03

20-1

ZHASE METERS	ZTOP METERS	DENSITY G/CM**3	R(MODE) MICRON	C1	C2	COMP.
150.0	650.0	0.250	10.00	6.00	1.00	LIO.

SUMMARY OF UNIT VOLUME PROPERTIES AT LAMDA= 1.000E 01 CM,TEMP= 298.00 DEG K

LAYER	M-DENS.	N-DENS.	GAM(S)	GAM(E)	GAM(P)	D(SCAT)	D(EXT)		
NUMBER	G M**3	C M**3	NEPER/CM	DB/KM	DB/KM	KM	KM		
1	0.2507	25.2771	4.368E-16	2.795E-09	1.216E-03	8.957E-04	0.00000	2.289E 09	3.578E 02

SUMMARY OF UNIT VOLUME PROPERTIES AT LAMDA= 1.000E 00 CM*TEMP= 298.00 DEG K

LAYER NUMBER	M-DENS. G M**3	N-DENS. CM**3	GAM(S) NEPER/CM	GAM(E) NEPER/CM	GAM(E) DB/KM	GAM(R) DB/KM	ALBEDO	D(SCAT) KM	D(EXT) KM
1	0.2507	25.2771	4.786E-12	2.642E-07	1.149E-01	8.957E-02	0.00002	2.090E 05	3.785E 00

SUMMARY OF UNIT VOLUME PROPERTIES AT $\lambda_{MD} = 1.000E-01$ CM, $TEMP = 298.00$ DEG K

LAYER NUMBER	M-DENS. G M**-3	N-DENS. CM**-3	GAM(S) NEPER/CM	GAM(E) NEPER/CM	GAM(E) DR/KM	GAM(R) DR/KM	ALBEDO	D(SCAT) KM	D(EXT) KM
1	0.2507	25.2771	3.145E-08	8.490E-06	3.693E 00	8.957E 00	0.00370	3.180E 01	1.178E-01

SUMMARY OF UNIT VOLUME PROPERTIES AT LAMDA= 1.000E-02 CM.TEMP= 298.00 DEG K

LAYER NUMBER	M-DENS. G M**-3	N-DENS. CM**-3	GAM(S) NEPER/CM	GAM(E) NEPER/CM	GAM(E) DB/KM	GAM(R) DR/KM	ALBEDO	D(SCAT) KM	D(EXT) KM
1	0.2507	25.2771	8.130E-05	2.120E-04	9.222E 01	8.957E 02	0.38349	1.230E-02	4.717E-03

SUMMARY OF UNIT VOLUME PROPERTIES AT LAMDA= 1.000E-03 CM,TEMP= 298.00 DEG K

LAYER	M-DENS.	N-DENS.	GAM(S)	GAM(E)	GAM(E)	GAM(R)	ALBEDC	DISCAT	D(EXT)
NUMBER	G M**3	CM**3	NEPER/CM	NEPER/CM	DR/KM	DR/KM	KM	KM	KM
1	0.2507	25.2771	2.087E-04	3.217E-04	1.399E 02	8.957E 04	0.6487	4.791E-03	3.108E-03

20-2

ZRASE	ZTOP	DENSITY	R(MODE)	C1	C2	COMP.
METERS	METERS	G/CM**3	MICRON			
500.0	1000.0	0.250	10.00	6.00	1.00	LIO.

SUMMARY OF UNIT VOLUME PROPERTIES AT LAMDA= 1.000E 01 CM,TEMP= 298.00 DEG K

LAYER NUMBER	M-DENS. G M**-3	N-DENS. CM**-3	GAM(S) NEPER/CM	GAM(E) NEPER/CM	GAM(E) DB/KM	GAM(R) DR/KM	ALBEDO	D(SCAT) KM	D(EXT) KM
1	0.2507	25.2771	4.368E-16	2.795E-09	1.216E-03	8.957E-04	0.00000	2.289E 09	3.578E 02

..... OF UNIT VOLUME PROPERTIES AT LAMDA# 1.000E 00 CM,TEMP= 298.00 DEG K

LAYER NUMBER	M-DENS. G M**3	N-DENS. CM**3	GAM(S) NEPER/CM	GAM(E) NEPER/CM	GAM(E) DR/KM	GAM(R) DB/KM	ALBEDO	D(SCAT) KM	D(EXT) KM
1	0.2507	25.2771	4.786E-12	2.642E-07	1.149E-01	8.957E-02	0.00002	2.090E 05	3.785E 00

SUMMARY OF UNIT VOLUME PROPERTIES AT LAMDA= 1.000E-01 CM.TEMP= 298.00 DEG K

LAYER	M-DENS.	N-DENS.	GAM(TS)	GAM(E)	GAM(E)	GAM(E)	GAM(P)	ALBEDO	D(SCAT)	D(EXT)
NUMBER	G M**-3	CM**-3	NEPER/CM	NEPER/CM	DB/KM	DB/KM	DB/KM		KM	KM
1	0.2507	25.2771	3.145E-08	8.490E-06	3.693E 00	8.957E 00	0.00370	3.180E 01	1.178E-01	

SUMMARY OF UNIT VOLUME PROPERTIES AT LAMDA= 1.000E-02 CM,TEMP= 298.00 DEG K

LAYER	M-DENS.	N-DENS.	GAM(S)	GAM(E)	GAM(E)	GAM(E)	GAM(H)	ALBEDO	O(SCAT)	O(EXT)
NUMBER	G M**3	CM**3	NEPER/CM	NEPER/CM	DB/KM	DB/KM	DB/KM		KM	KM
1	0.2507	25.2771	8.130E-05	2.120E-04	9.222E 01	8.957E 02	0.38349	1.230E-02	4.717E-03	

SUMMARY OF UNIT VOLUME PROPERTIES AT $\lambda_{MDA} = 1.000E-03$ CM, TEMP= 298.00 DEG K

LAYER	M-DENS.	N-DENS.	GAM(S)	GAM(E)	NEPER/CM	GAM(E)	GAM(E)	GAM(R)	ALBEDO	D(SCAT)	D(EXT)
NUMBER	G M**3	CM**3	NEPER/CM	NEPER/CM	DB/KM	DB/KM	DB/KM	DB/KM		KM	KM
1	0.2507	25.2771	2.087E-04	3.217E-04	1.399E 02	8.957E 04	0.64887	4.791E-03	3.108E-03		

20-3 FOG LAYER, GROUND TO 150 FT

ZBASE METERS	ZTOP METERS	DENSITY G/M**3	R(MODE) MICRON	C1	C2	COMP.
0.0	50.0	0.150	20.00	7.00	2.00	L10.

SUMMARY OF UNIT VOLUME PROPERTIES AT LAMDA= 1.000E 01 CM,TEMP= 298.00 DEG K

LAYER NUMBER	M-DENS. G M**3	N-DENS. CM**3	GAM(S) NEPER/CM	GAM(E) NEPER/CM	GAM(E) DB/KM	GAM(R) DB/KM	ALBEDO	D(SCAT) KM	D(EXT) KM
1	0.1503	3.3171	7.201E-16	1.675E-09	7.287E-04	5.370E-04	0.00000	1.389E 09	5.969E 02

SUMMARY OF UNIT VOLUME PROPERTIES AT LAMDA= 1.000E 00 CM,TEMP= 298.00 DEG K

LAYER NUMBER	M-DENS. G M**3	N-DENS. CM**3	GAM(S) NEPER/CM	GAM(E) NEPER/CM	GAM(E) DB/KM	GAM(R) DB/KM	ALBEDO	D(SCAT) KM	D(EXT) KM
1	0.1503	3.3171	7.943E-12	1.600E-07	6.961E-02	5.370E-02	0.00005	1.259E 05	6.249E 00

SUMMARY OF UNIT VOLUME PROPERTIES AT LAMDA= 1.000E-01 CM,TEMP= 298.00 DEG K

LAYER NUMBER	M-DENS. G M**3	N-DENS. CM**3	GAM(S) NEPER/CM	GAM(E) NEPER/CM	GAM(E) DB/KM	GAM(R) DB/KM	ALBEDO	D(SCAT) KM	D(EXT) KM
1	0.1503	3.3171	5.154E-08	5.250E-06	2.284E 00	5.370E 00	0.00982	1.940E 01	1.905E-01

SUMMARY OF UNIT VOLUME PROPERTIES AT LAMDA= 1.000E-02 CM,TEMP= 298.00 DEG K

LAYER NUMBER	M-DENS. G M**3	N-DENS. CM**3	GAM(S) NEPER/CM	GAM(E) NEPER/CM	GAM(E) DB/KM	GAM(R) DB/KM	ALBEDO	D(SCAT) KM	D(EXT) KM
1	0.1503	3.3171	6.169E-05	1.328E-04	5.779E 01	5.370E 02	0.46440	1.621E-02	7.527E-03

SUMMARY OF UNIT VOLUME PROPERTIES AT LAMDA= 1.000E-03 CM,TEMP= 298.00 DEG K

LAYER NUMBER	M-DENS. G M**3	N-DENS. CM**3	GAM(S) NEPER/CM	GAM(E) NEPER/CM	GAM(E) DB/KM	GAM(R) DB/KM	ALBEDO	D(SCAT) KM	D(EXT) KM
1	0.1503	3.3171	6.683E-05	1.176E-04	5.115E 01	5.370E 04	0.56843	1.496E-02	8.505E-03

20-4 HAZE, HEAVY

```

=====
| ZBASE | ZTOP | DENSITY | R(MODE) | C1 | C2 | COMP. |
| METERS | METERS | G/M**3 | MICRON | | | |
+-----+-----+-----+-----+-----+-----+-----+
| 0.0 | 1500.0 | 9.001 | 0.05 | 1.00 | 0.50 | LIQ. |
+-----+-----+-----+-----+-----+-----+

```

SUMMARY OF UNIT VOLUME PROPERTIES AT LAMDA= 1.000E 01 CM,TEMP= 298.00 DEG K

```

=====
| LAYER | M-DENS. | N-DENS. | GAM(S) | GAM(E) | GAM(E) | GAM(R) | ALBEDO | DISCAT | D(EXT) |
| NUMBER | G M**3 | CM**3 | NEPER/CM | NEPER/CM | DB/KM | DB/KM | | KM | KM |
+-----+-----+-----+-----+-----+-----+-----+
| 1 | 0.0010 | 2018.4150 | 2.034E-21 | 1.130E-11 | 4.915E-06 | 3.621E-06 | 0.00000 | 4.917E 14 | 8.851E 04 |
+-----+-----+-----+-----+-----+-----+

```

SUMMARY OF UNIT VOLUME PROPERTIES AT LAMDA= 1.000E 00 CM,TEMP= 298.00 DEG K

```

=====
| LAYER | M-DENS. | N-DENS. | GAM(S) | GAM(E) | GAM(E) | GAM(R) | ALBEDO | DISCAT | D(EXT) |
| NUMBER | G M**3 | CM**3 | NEPER/CM | NEPER/CM | DB/KM | DB/KM | | KM | KM |
+-----+-----+-----+-----+-----+-----+-----+
| 1 | 0.0010 | 2018.4150 | 2.009E-17 | 1.054E-09 | 4.586E-04 | 3.621E-04 | 0.00000 | 4.978E 10 | 9.485E 02 |
+-----+-----+-----+-----+-----+-----+

```

SUMMARY OF UNIT VOLUME PROPERTIES AT LAMDA= 1.000E-01 CM,TEMP= 298.00 DEG K

```

=====
| LAYER | M-DENS. | N-DENS. | GAM(S) | GAM(E) | GAM(E) | GAM(R) | ALBEDO | DISCAT | D(EXT) |
| NUMBER | G M**3 | CM**3 | NEPER/CM | NEPER/CM | DB/KM | DB/KM | | KM | KM |
+-----+-----+-----+-----+-----+-----+-----+
| 1 | 0.0010 | 2018.4150 | 1.425E-13 | 3.278E-08 | 1.426E-02 | 3.621E-02 | 0.00000 | 7.018E 06 | 3.050E 01 |
+-----+-----+-----+-----+-----+-----+

```

SUMMARY OF UNIT VOLUME PROPERTIES AT LAMDA= 1.000E-02 CM,TEMP= 298.00 DEG K

```

=====
| LAYER | M-DENS. | N-DENS. | GAM(S) | GAM(E) | GAM(E) | GAM(R) | ALBEDO | DISCAT | D(EXT) |
| NUMBER | G M**3 | CM**3 | NEPER/CM | NEPER/CM | DB/KM | DB/KM | | KM | KM |
+-----+-----+-----+-----+-----+-----+-----+
| 1 | 0.0010 | 2018.4150 | 7.927E-10 | 3.367E-07 | 1.465E-01 | 3.621E 00 | 0.00235 | 1.261E 03 | 2.970E 00 |
+-----+-----+-----+-----+-----+-----+

```

SUMMARY OF UNIT VOLUME PROPERTIES AT LAMDA= 1.000E-03 CM,TEMP= 298.00 DEG K

```

=====
| LAYER | M-DENS. | N-DENS. | GAM(S) | GAM(E) | GAM(E) | GAM(R) | ALBEDO | DISCAT | D(EXT) |
| NUMBER | G M**3 | CM**3 | NEPER/CM | NEPER/CM | DB/KM | DB/KM | | KM | KM |
+-----+-----+-----+-----+-----+-----+-----+
| 1 | 0.0010 | 2018.4150 | 1.674E-07 | 8.505E-07 | 3.700E-01 | 3.621E 02 | 0.19678 | 5.975E 00 | 1.176E 00 |
+-----+-----+-----+-----+-----+-----+

```


21-1 DRIZZLF,0.2 MM/HP

LAYER NUMBER	ZTOP METERS	DENSITY G/CM**3	R(MODE) MICRON	C1	C2	COMP.
1	0.0	1.000	20.00	6.00	0.50	RAIN
2	500.0	2.000	10.00	6.00	0.50	LIQ.
3	1000.0	1.000	10.00	6.00	0.50	LIQ.

SUMMARY OF UNIT VOLUME PROPERTIES AT LAMDA= 1.000E 01 CM,TEMP= 298.00 DEG K

LAYER NUMBER	M-DENS. G CM**3	N-DENS. CM**3	GAM(S) NEPER/CM	GAM(E) NEPER/CM	GAM(E) DB/KM	GAM(R) DR/KM	ALBEDO	D(SCAT) KM	D(EXT) KM
1	1.0035	4.5114	9.882E-14	1.119E-08	4.868E-03	3.586E-03	0.0001	1.012E 07	8.937E 01
2	2.0070	72.1829	2.444E-14	2.238E-08	9.734E-03	7.172E-03	0.0000	4.092E 07	4.469E 01
3	1.0035	36.0914	1.222E-14	1.119E-08	4.867E-03	3.586E-03	0.0000	8.184E 07	8.938E 01

SUMMARY OF UNIT VOLUME PROPERTIES AT LAMDA= 1.000E 00 CM,TEMP= 298.00 DEG K

LAYER NUMBER	M-DENS. G CM**3	N-DENS. CM**3	GAM(S) NEPER/CM	GAM(E) NEPER/CM	GAM(E) DB/KM	GAM(R) DR/KM	ALBEDO	D(SCAT) KM	D(EXT) KM
1	1.0035	4.5114	1.097E-09	1.110E-06	4.828E-01	3.586E-01	0.0099	9.113E 02	9.009E-01
2	2.0070	72.1829	2.721E-10	2.148E-06	9.344E-01	7.172E-01	0.0013	3.675E 03	4.655E-01
3	1.0035	36.0914	1.361E-10	1.074E-06	4.672E-01	3.586E-01	0.0013	7.350E 03	9.311E-01

SUMMARY OF UNIT VOLUME PROPERTIES AT LAMDA= 1.000E-01 CM,TEMP= 298.00 DEG K

LAYER NUMBER	M-DENS. G CM**3	N-DENS. CM**3	GAM(S) NEPER/CM	GAM(E) NEPER/CM	GAM(E) DB/KM	GAM(R) DR/KM	ALBEDO	D(SCAT) KM	D(EXT) KM
1	1.0035	4.5114	7.617E-06	5.296E-05	2.304E 01	3.586E 01	0.14383	1.313E-01	1.888E-02
2	2.0070	72.1829	1.879E-06	7.406E-05	3.222E 01	7.172E 01	0.02537	5.323E-01	1.350E-02
3	1.0035	36.0914	9.354E-07	3.703E-05	1.611E 01	3.586E 01	0.02537	1.065E 00	2.700E-02

21-1 DRIZZLE,0.2 MM/HR

ZBASE METERS	ZTOP METERS	DENSITY G/M**3	R(MODE) MICRON	C1	C2	COMP.
0.0	500.0	1.000	20.00	6.00	0.50	RAIN
500.0	1000.0	2.000	10.00	6.00	0.50	L10.
1000.0	1500.0	1.000	10.00	6.00	0.50	L10.

SUMMARY OF UNIT VOLUME PROPERTIES AT LAMDA= 1.000E-02 CM,TEMP= 298.00 DEG K

LAYER NUMBER	M-DENS. G M**3	N-DENS. CM**3	GAM(S) NEPER/CM	GAM(E) NEPER/CM	GAM(E) DB/KM	GAM(R) DB/KM	ALBEDC	D(SCAT) KM	D(EXT) KM
1	1.0035	4.5114	2.107E-04	4.425E-04	1.925E 02	3.586E 03	0.47604	4.747E-03	2.260E-03
2	2.0070	72.1829	6.773E-04	1.517E-03	6.600E 02	7.172E 03	0.44638	1.476E-03	6.591E-04
3	1.0035	36.0914	3.387E-04	7.587E-04	3.300E 02	3.586E 03	0.44638	2.953E-03	1.318E-03

SUMMARY OF UNIT VOLUME PROPERTIES AT LAMDA= 1.000E-03 CM,TEMP= 298.00 DEG K

LAYER NUMBER	M-DENS. G M**3	N-DENS. CM**3	GAM(S) NEPER/CM	GAM(E) NEPER/CM	GAM(E) DB/KM	GAM(R) DB/KM	ALBEDC	D(SCAT) KM	D(EXT) KM
1	1.0035	4.5114	1.829E-04	3.534E-04	1.537E 02	3.586E 05	0.51766	5.467E-03	2.830E-03
2	2.0070	72.1829	9.033E-04	1.539E-03	6.696E 02	7.172E 05	0.58688	1.107E-03	6.497E-04
3	1.0035	36.0914	4.517E-04	7.696E-04	3.348E 02	3.586E 05	0.58688	2.214E-03	1.299E-03

21-2 STEADY RAIN 3 MM/HR

ZBASE METERS	ZTOP METERS	DENSITY G/M**3	R(MODE) MICRON	C1	C2	COMP.
0.0	150.0	0.200	200.00	5.00	0.50	RAIN
150.0	500.0	1.000	10.00	6.00	0.50	LIO.
500.0	1000.0	2.000	10.00	6.00	0.50	LIO.
1000.0	1500.0	1.000	10.00	6.00	0.50	LIO.

SUMMARY OF UNIT VOLUME PROPERTIES AT LAMDA= 1.000E 01 CM,TEMP= 298.00 DEG K

LAYER NUMBER	M-DENS. G M**3	N-DENS. CM**3	GAM(S) NEPER/CM	GAM(E) NEPER/CM	GAM(E) DB/KM	GAM(R) DB/KM	ALBEDO	D(SCAT) KM	D(EXT) KM
1	0.2008	0.0007	3.782E-11	2.774E-09	1.207E-03	7.177E-04	0.01364	2.644E 04	3.605E 02
2	1.0035	36.0914	1.222E-14	1.119E-08	4.867E-03	3.586E-03	0.00000	8.184E 07	8.938E 01
3	2.0070	72.1829	2.444E-14	2.238E-08	9.734E-03	7.172E-03	0.00000	4.092E 07	4.469E 01
4	1.0035	36.0914	1.222E-14	1.119E-08	4.867E-03	3.586E-03	0.00000	8.184E 07	8.938E 01

SUMMARY OF UNIT VOLUME PROPERTIES AT LAMDA= 1.000E 00 CM,TEMP= 298.00 DEG K

LAYER NUMBER	M-DENS. G M**3	N-DENS. CM**3	GAM(S) NEPER/CM	GAM(E) NEPER/CM	GAM(E) DB/KM	GAM(R) DB/KM	ALBEDO	D(SCAT) KM	D(EXT) KM
1	0.2008	0.0007	3.908E-07	1.450E-06	6.309E-01	7.177E-02	0.26941	2.559E 00	6.895E-01
2	1.0035	36.0914	1.361E-10	1.074E-06	4.672E-01	3.586E-01	0.00013	7.350E 03	9.311E-01
3	2.0070	72.1829	2.721E-10	2.148E-06	9.344E-01	7.172E-01	0.00013	3.675E 03	4.655E-01
4	1.0035	36.0914	1.361E-10	1.074E-06	4.672E-01	3.586E-01	0.00013	7.350E 03	9.311E-01

SUMMARY OF UNIT VOLUME PROPERTIES AT LAMDA= 1.000E-01 CM,TEMP= 298.00 DEG K

LAYER NUMBER	M-DENS. G M**3	N-DENS. CM**3	GAM(S) NEPER/CM	GAM(E) NEPER/CM	GAM(E) DB/KM	GAM(R) DB/KM	ALBEDO	D(SCAT) KM	D(EXT) KM
1	0.2008	0.0007	3.994E-06	7.684E-06	3.343E 00	7.177E 00	0.51979	2.504E-01	1.301E-01
2	1.0035	36.0914	9.394E-07	3.703E-05	1.611E 01	3.586E 01	0.02537	1.065E 00	2.700E-02
3	2.0070	72.1829	1.879E-06	7.406E-05	3.222E 01	7.172E 01	0.02537	5.323E-01	1.350E-02
4	1.0035	36.0914	9.394E-07	3.703E-05	1.611E 01	3.586E 01	0.02537	1.065E 00	2.700E-02

21-2 STEADY RAIN 3 MM/HR

ZBASE METERS	ZTOP METERS	DENSITY G/M**3	R(MODE) MICRON	C1	C2	COMP.
0.0	150.0	0.200	200.00	5.00	0.50	RAIN
150.0	500.0	1.000	10.00	6.00	0.50	LIQ.
500.0	1000.0	2.000	10.00	6.00	0.50	LIQ.
1000.0	1500.0	1.000	10.00	6.00	0.50	LIQ.

SUMMARY OF UNIT VOLUME PROPERTIES AT LAMDA= 1.000E-02 CM,TEMP= 298.00 DEG K

LAYER NUMBER	M-DENS. G M**3	N-DENS. CM**3	GAM(S) NEPER/CM	GAM(E) NEPER/CM	GAM(E) DB/KM	GAM(R) DR/KM	ALBEDO	D(SCAT) KM	D(EXT) KM
1	0.2008	0.0007	3.453E-06	6.081E-06	2.645E 00	7.177E 02	0.56777	2.896E-01	1.644E-01
2	1.0035	36.0914	3.387E-04	7.587E-04	3.300E 02	3.586E 03	0.44638	2.953E-03	1.318E-03
3	2.0070	72.1829	6.773E-04	1.517E-03	6.600E 02	7.172E 03	0.44638	1.476E-03	6.591E-04
4	1.0035	36.0914	3.387E-04	7.587E-04	3.300E 02	3.586E 03	0.44638	2.953E-03	1.318E-03

SUMMARY OF UNIT VOLUME PROPERTIES AT LAMDA= 1.000E-03 CM,TEMP= 298.00 DEG K

LAYER NUMBER	M-DENS. G M**3	N-DENS. CM**3	GAM(S) NEPER/CM	GAM(E) NEPER/CM	GAM(E) DB/KM	GAM(R) DR/KM	ALBEDO	D(SCAT) KM	D(EXT) KM
1	0.2008	0.0007	2.950E-06	5.835E-06	2.538E 00	7.177E 04	0.50561	3.390E-01	1.714E-01
2	1.0035	36.0914	4.517E-04	7.696E-04	3.348E 02	3.586E 05	0.58688	2.214E-03	1.299E-03
3	2.0070	72.1829	9.033E-04	1.539E-03	6.696E 02	7.172E 05	0.58688	1.107E-03	6.497E-04
4	1.0035	36.0914	4.517E-04	7.696E-04	3.348E 02	3.586E 05	0.58688	2.214E-03	1.299E-03

C1-3 STEADY RAIN, 15 MM/HK

ZBASE METERS	ZTOP METERS	DENSITY G/M**3	R(MODE) MICRON	C1	C2	COMP.
0.0	300.0	1.000	200.00	5.00	0.50	RAIN
300.0	1000.0	2.000	10.00	6.00	0.50	LIO.
1000.0	2000.0	3.000	10.00	6.00	0.50	LIO.
2000.0	4000.0	2.000	10.00	6.00	0.50	LIO.

SUMMARY OF UNIT VOLUME PROPERTIES AT LAMDA= 1.000E 01 CM,TEMP= 298.00 DEG K

LAYER NUMBER	M-DENS. G M**3	N-DENS. CM**3	GAM(S) NEPER/CM	GAM(E) NEPER/CM	GAM(E) DB/KM	GAM(R) DB/KM	ALBEDO	D(SCAT) KM	D(EXT) KM
1	1.0042	0.0033	1.891E-10	1.387E-08	6.033E-03	3.589E-03	0.01364	5.288F 03	7.211E 01
2	2.0070	72.1829	2.444E-14	2.238E-08	9.734E-03	7.172E-03	0.00000	4.092E 07	4.469E 01
3	3.0105	108.2743	3.666E-14	3.356E-08	1.460E-02	1.076E-02	0.00000	2.728E 07	2.979E 01
4	2.0070	72.1829	2.444E-14	2.238E-08	9.734E-03	7.172E-03	0.00000	4.092E 07	4.469E 01

SUMMARY OF UNIT VOLUME PROPERTIES AT LAMDA= 1.000E 00 CM,TEMP= 298.00 DEG K

LAYER NUMBER	M-DENS. G M**3	N-DENS. CM**3	GAM(S) NEPER/CM	GAM(E) NEPER/CM	GAM(E) DB/KM	GAM(R) DB/KM	ALBEDO	D(SCAT) KM	D(EXT) KM
1	1.0042	0.0033	1.954E-06	7.252E-06	3.155E 00	3.589E-01	0.26941	5.118E-01	1.379E-01
2	2.0070	72.1829	2.721E-10	2.148E-06	9.344E-01	7.172E-01	0.00013	3.675E 03	4.655E-01
3	3.0105	108.2743	4.082E-10	3.222E-06	1.402E 00	1.076E 00	0.00013	2.450E 03	3.104E-01
4	2.0070	72.1829	2.721E-10	2.148E-06	9.344E-01	7.172E-01	0.00013	3.675E 03	4.655E-01

SUMMARY OF UNIT VOLUME PROPERTIES AT LAMDA= 1.000E-01 CM,TEMP= 298.00 DEG K

LAYER NUMBER	M-DENS. G M**3	N-DENS. CM**3	GAM(S) NEPER/CM	GAM(E) NEPER/CM	GAM(E) DB/KM	GAM(R) DB/KM	ALBEDO	D(SCAT) KM	D(EXT) KM
1	1.0042	0.0033	1.997E-05	3.842E-05	1.671E 01	3.589E 01	0.51979	5.007E-02	2.603E-02
2	2.0070	72.1829	1.879E-06	7.406F-05	3.222F 01	7.172E 01	0.02537	5.323E-01	1.350E-02
3	3.0105	108.2743	2.918E-06	1.111E-04	4.833E 01	1.076E 02	0.02537	3.548E-01	9.001E-03
4	2.0070	72.1829	1.879E-06	7.406E-05	3.222E 01	7.172E 01	0.02537	5.323E-01	1.350E-02

21-3 STEADY RAIN, 15 MM/HR

ZBASE METERS	ZTOP METERS	DENSITY G/M**3	R(MODE) MICRON	C1	C2	COMP.
0.0	300.0	1.000	200.00	5.00	0.50	RAIN
300.0	1000.0	2.000	10.00	6.00	0.50	L10.
1000.0	2000.0	3.000	10.00	6.00	0.50	L10.
2000.0	4000.0	2.000	10.00	6.00	0.50	L10.

SUMMARY OF UNIT VOLUME PROPERTIES AT LAMDA= 1.000E-02 CM,TEMP= 298.00 DEG K

LAYER NUMBER	M-DENS. G M**3	N-DENS. CM**3	GAM(S) NEPER/CM	GAM(E) NEPER/CM	GAM(E) DB/KM	GAM(R) DB/KM	ALBEDO.	D(SCAT) KM	D(EXT) KM
1	1.0042	0.0033	1.726E-05	3.041E-05	1.323E 01	3.589E 03	0.56777	5.793E-02	3.289E-02
2	2.0070	72.1829	6.773E-04	1.517E-03	6.600E 02	7.172E 03	0.44638	1.476E-03	6.591E-04
3	3.0105	108.2743	1.014E-03	2.276E-03	9.900E 02	1.076E 04	0.44639	9.843E-04	4.394E-04
4	2.0070	72.1829	6.773E-04	1.517E-03	6.600E 02	7.172E 03	0.44638	1.476E-03	6.591E-04

SUMMARY OF UNIT VOLUME PROPERTIES AT LAMDA= 1.000E-03 CM,TEMP= 298.00 DEG K

LAYER NUMBER	M-DENS. G M**3	N-DENS. CM**3	GAM(S) NEPER/CM	GAM(E) NEPER/CM	GAM(E) DB/KM	GAM(R) DB/KM	ALBEDO	D(SCAT) KM	D(EXT) KM
1	1.0042	0.0033	1.475E-05	2.917E-05	1.269E 01	3.589E 05	0.50561	6.779E-02	3.428E-02
2	2.0070	72.1829	9.033E-04	1.539E-03	6.696E 02	7.172E 05	0.58688	1.107E-03	6.497E-04
3	3.0105	108.2743	1.355E-03	2.309E-03	1.004E 03	1.076E 06	0.58688	7.380E-04	4.331E-04
4	2.0070	72.1829	9.033E-04	1.539E-03	6.696E 02	7.172E 05	0.58688	1.107E-03	6.497E-04

LAYER NUMBER	ZTOP METERS	DENSITY G/M**3	R(MODE) MICRON	C1	C2	COMP.
1	330.0	650.0	0.250	10.00	6.00	0.50
						L10.

SUMMARY OF UNIT VOLUME PROPERTIES AT LAMDA= 1.000E 01 CM,TEMP= 298.00 DEG K

LAYER NUMBER	M-DENS. G M**3	N-DENS. CM**3	GAM(S) NEPER/CM	GAM(E) NEPER/CM	GAM(E) DB/KM	GAM(R) DB/KM	ALBEDO	D(SCAT) KM	D(EXT) KM
1	0.2509	9.0228	3.055E-15	2.797E-09	1.217E-03	8.965E-04	0.0000	3.273E 04	3.575E 02

SUMMARY OF UNIT VOLUME PROPERTIES AT LAMDA= 1.000E 00 CM,TEMP= 298.00 DEG K

LAYER NUMBER	M-DENS. G M**3	N-DENS. CM**3	GAM(S) NEPER/CM	GAM(E) NEPER/CM	GAM(E) DB/KM	GAM(R) DB/KM	ALBEDO	D(SCAT) KM	D(EXT) KM
1	0.2509	9.0228	3.402E-11	2.685E-07	1.168E-01	8.965E-02	0.0013	2.940E 04	3.724E 00

SUMMARY OF UNIT VOLUME PROPERTIES AT LAMDA= 1.000E-01 CM,TEMP= 298.00 DEG K

LAYER NUMBER	M-DENS. G M**3	N-DENS. CM**3	GAM(S) NEPER/CM	GAM(E) NEPER/CM	GAM(E) DB/KM	GAM(R) DB/KM	ALBEDO	D(SCAT) KM	D(EXT) KM
1	0.2509	9.0228	2.348E-07	9.258E-06	4.027E 00	8.965E 00	0.02537	4.258E 00	1.090E-01

SUMMARY OF UNIT VOLUME PROPERTIES AT LAMDA= 1.000E-02 CM,TEMP= 298.00 DEG K

LAYER NUMBER	M-DENS. G M**3	N-DENS. CM**3	GAM(S) NEPER/CM	GAM(E) NEPER/CM	GAM(E) DB/KM	GAM(R) DB/KM	ALBEDO	D(SCAT) KM	D(EXT) KM
1	0.2509	9.0228	8.466E-05	1.897E-04	8.250E 01	8.965E 02	0.44639	1.181E-02	5.272E-03

SUMMARY OF UNIT VOLUME PROPERTIES AT LAMDA= 1.000E-03 CM,TEMP= 298.00 DEG K

LAYER NUMBER	M-DENS. G M**3	N-DENS. CM**3	GAM(S) NEPER/CM	GAM(E) NEPER/CM	GAM(E) DB/KM	GAM(R) DB/KM	ALBEDO	D(SCAT) KM	D(EXT) KM
1	0.2509	9.0228	1.129E-04	1.924E-04	8.370E 01	8.965E 04	0.58688	8.856E-03	5.197E-03

PHASE	7TOP	DENSITY	R(MODE)	C1	C2	COMP.
METEWS	4ETFS	G/MSS3	MICRON			
660.0	1320.0	0.250	10.00	6.00	0.50	LIO.

SUMMARY OF UNIT VOLUME PROPERTIES AT LAMDA= 1.000E 01 CM,TEMP= 298.00 DEG K

LAYER	M-DENS.	N-DENS.	GAM(S)	GAM(E)	GAM(E)	GAM(R)	ALBEDO	D(SCAT)	D(EXT)
NUMBER	G M**3	CM**3	NEPER/CM	NEPER/CM	DB/KM	DB/KM		KM	KM
1	0.2509	9.0228	3.045E-15	2.797E-09	1.217E-03	8.965E-04	0.00000	3.273E 08	3.575E 02

SUMMARY OF UNIT VOLUME PROPERTIES AT LAMDA= 1.000E 00 CM,TEMP= 298.00 DEG K

LAYER	M-DENS.	N-DENS.	GAM(S)	GAM(E)	GAM(E)	GAM(R)	ALBEDO	D(SCAT)	D(EXT)
NUMBER	G M**3	CM**3	NEPER/CM	NEPER/CM	DB/KM	DB/KM		KM	KM
1	0.2509	9.0228	3.402E-11	2.685E-07	1.168E-01	8.965E-02	0.00013	2.940E 04	3.724E 00

SUMMARY OF UNIT VOLUME PROPERTIES AT LAMDA= 1.000E-01 CM,TEMP= 298.00 DEG K

LAYER	M-DENS.	N-DENS.	GAM(S)	GAM(E)	GAM(E)	GAM(R)	ALBEDO	D(SCAT)	D(EXT)
NUMBER	G M**3	CM**3	NEPER/CM	NEPER/CM	DB/KM	DB/KM		KM	KM
1	0.2509	9.0228	2.348E-07	9.258E-06	4.027E 00	8.965E 00	0.02537	4.258E 00	1.080E-01

SUMMARY OF UNIT VOLUME PROPERTIES AT LAMDA= 1.000E-02 CM,TEMP= 298.00 DEG K

LAYER	M-DENS.	N-DENS.	GAM(S)	GAM(E)	GAM(E)	GAM(R)	ALBEDO	D(SCAT)	D(EXT)
NUMBER	G M**3	CM**3	NEPER/CM	NEPER/CM	DB/KM	DB/KM		KM	KM
1	0.2509	9.0228	8.466E-05	1.897E-04	4.250E 01	8.965E 02	0.44639	1.181E-02	5.272E-03

SUMMARY OF UNIT VOLUME PROPERTIES AT LAMDA= 1.000E-03 CM,TEMP= 298.00 DEG K

LAYER	M-DENS.	N-DENS.	GAM(S)	GAM(E)	GAM(E)	GAM(R)	ALBEDO	D(SCAT)	D(EXT)
NUMBER	G M**3	CM**3	NEPER/CM	NEPER/CM	DB/KM	DB/KM		KM	KM
1	0.2509	9.0228	1.129E-04	1.924E-04	8.370E 01	8.965E 04	0.58688	8.956E-03	5.197E-03

25-1 FAIR WEATHER CU. 1500-6000 FT

ZBASE METERS	ZTOP METERS	DENSITY G/M**3	R(MODE) MICRON	C1	C2	COMP.
500.0	1000.0	0.500	10.00	6.00	0.50	LIQ.
1000.0	1500.0	1.000	10.00	6.00	0.50	LIQ.
1500.0	2000.0	0.500	10.00	6.00	0.50	LIQ.

SUMMARY OF UNIT VOLUME PROPERTIES AT LAMDA= 1.000E 01 CM,TEMP= 298.00 DEG K

LAYER NUMBER	M-DENS. G M**3	N-DENS. CM**3	GAM(S) NEPER/CM	GAM(E) NEPER/CM	GAM(R) DB/KM	ALBEDO	D(SCAT) KM	D(EXT) KM
1	0.5018	18.0457	6.110E-15	5.594E-09	2.433E-03	1.793E-03	0.0000	1.637E 08
2	1.0035	36.0914	1.222E-14	1.119E-08	4.867E-03	3.586E-03	0.0000	8.184E 07
3	0.5018	18.0457	6.110E-15	5.594E-09	2.433E-03	1.793E-03	0.0000	1.637E 08

SUMMARY OF UNIT VOLUME PROPERTIES AT LAMDA= 1.000E 00 CM,TEMP= 298.00 DEG K

LAYER NUMBER	M-DENS. G M**3	N-DENS. CM**3	GAM(S) NEPER/CM	GAM(E) NEPER/CM	GAM(R) DB/KM	ALBEDO	D(SCAT) KM	D(EXT) KM
1	0.5018	18.0457	6.803E-11	5.370E-07	2.336E-01	1.793E-01	0.0013	1.470E 04
2	1.0035	36.0914	1.361E-10	1.074E-06	4.672E-01	3.586E-01	0.0013	7.350E 03
3	0.5018	18.0457	6.803E-11	5.370E-07	2.336E-01	1.793E-01	0.0013	1.470E 04

SUMMARY OF UNIT VOLUME PROPERTIES AT LAMDA= 1.000E-01 CM,TEMP= 298.00 DEG K

LAYER NUMBER	M-DENS. G M**3	N-DENS. CM**3	GAM(S) NEPER/CM	GAM(E) NEPER/CM	GAM(R) DB/KM	ALBEDO	D(SCAT) KM	D(EXT) KM
1	0.5018	18.0457	4.697E-07	1.852E-05	8.054E 00	1.793E 01	0.02537	2.129E 00
2	1.0035	36.0914	9.394E-07	3.703E-05	1.611E 01	3.586E 01	0.02537	1.065E 00
3	0.5018	18.0457	4.697E-07	1.852E-05	8.054E 00	1.793E 01	0.02537	2.129E 00

25-1 FAIR WEATHER CU. 1500-6000 FT

ZBASE METERS	ZTOP METERS	DENSITY G/M**3	R(MODE) MICRON	C1	C2	COMP.
500.0	1000.0	0.500	10.00	6.00	0.50	L1Q.
1000.0	1500.0	1.000	10.00	6.00	0.50	L1Q.
1500.0	2000.0	0.500	10.00	6.00	0.50	L1Q.

SUMMARY OF UNIT VOLUME PROPERTIES AT LAMDA= 1.000E-02 CM,TEMP= 298.00 DEG K

LAYER NUMBER	M-DENS. G M**3	N-DENS. CM**3	GAM(S) NEPER/CM	GAM(E) NEPER/CM	GAM(E) DB/KM	GAM(R) DR/KM	ALREDO	DISCAT)	D(EXT)
1	0.5018	18.0457	1.693E-04	3.793E-04	1.650E 02	1.793E 03	0.44638	5.906E-03	2.636E-03
2	1.0035	36.0914	3.387E-04	7.587E-04	3.300E 02	3.586E 03	0.44638	2.953E-03	1.319E-03
3	0.5018	18.0457	1.693E-04	3.793E-04	1.650E 02	1.793E 03	0.44638	5.906E-03	2.636E-03

SUMMARY OF UNIT VOLUME PROPERTIES AT LAMDA= 1.000E-03 CM,TEMP= 298.00 DFG K

LAYER NUMBER	M-DENS. G M**3	N-DENS. CM**3	GAM(S) NEPER/CM	GAM(E) NEPER/CM	GAM(E) DR/KM	GAM(R) DR/KM	ALREDO	DISCAT)	D(EXT)
1	0.5018	18.0457	2.258E-04	3.848E-04	1.674E 02	1.793E 05	0.58688	4.428E-03	2.599E-03
2	1.0035	36.0914	4.517E-04	7.696E-04	3.349E 02	3.586E 05	0.58688	2.214E-03	1.299E-03
3	0.5018	18.0457	2.258E-04	3.848E-04	1.674E 02	1.793E 05	0.58688	4.428E-03	2.599E-03

25-2 CUMULUS WITH RAIN 2.4 MM/HR

ZBASE METERS	ZTOP METERS	DENSITY G/M**3	R(MODE) MICRON	C1	C2	COMP.
0.0	~500.0	0.100	400.00	5.00	0.50	RAIN
500.0	1000.0	1.000	20.00	6.00	0.20	LIO.
1000.0	3000.0	2.000	10.00	6.00	0.20	LIO.

SUMMARY OF UNIT VOLUME PROPERTIES AT LAMDA= 1.000E 00 CM,TEMP= 298.00 DEG K

LAYER NUMBER	M-DENS. G M**3	N-DENS. CM**3	GAM(S) NEPER/CM	GAM(E) NEPER/CM	GAM(E) DB/KM	GAM(R) DB/KM	ALREDO	N(SCAT) KM	D(EXT) KM
1	0.1004	0.0000	5.274E-07	1.097E-06	4.771E-01	3.589E-02	0.48078	1.896E 00	9.117E-01
2	0.5178	0.2032	8.849E-09	7.027E-07	3.057E-01	1.850E-01	0.01259	1.130E 02	1.423E 00
3	1.0355	3.2507	2.184E-09	1.172E-06	5.099E-01	3.700E-01	0.00186	4.579E 02	8.532E-01

SUMMARY OF UNIT VOLUME PROPERTIES AT LAMDA= 1.000E 01 CM,TEMP= 298.00 DEG K

LAYER NUMBER	M-DENS. G M**3	N-DENS. CM**3	GAM(S) NEPER/CM	GAM(E) NEPER/CM	GAM(E) DB/KM	GAM(R) DB/KM	ALREDO	N(SCAT) KM	D(EXT) KM
1	0.1004	0.0000	1.645E-10	2.768E-09	1.204E-03	3.589E-04	0.06088	5.934E 03	3.613E 02
2	0.5178	0.2032	8.844E-13	5.890E-09	2.562E-03	1.850E-03	0.00015	1.131E 04	1.698E 02
3	1.0355	3.2507	1.963E-13	1.155E-08	5.022E-03	3.700E-03	0.00002	5.094E 04	8.662E 01

SUMMARY OF UNIT VOLUME PROPERTIES AT LAMDA= 1.000E-01 CM,TEMP= 298.00 DEG K

LAYER NUMBER	M-DENS. G M**3	N-DENS. CM**3	GAM(S) NEPER/CM	GAM(E) NEPER/CM	GAM(E) DB/KM	GAM(R) DB/KM	ALREDO	N(SCAT) KM	D(EXT) KM
1	0.1004	0.0000	9.889E-07	1.762E-06	7.666E-01	3.589E 00	0.56106	1.011E 00	5.674E-01
2	0.5178	0.2032	2.354E-05	5.722E-05	2.489E 01	1.850E 01	0.41130	4.249E-02	1.747E-02
3	1.0355	3.2507	1.669E-05	7.343E-05	3.194E 01	3.700E 01	0.22728	5.992E-02	1.362E-02

25-2 CUMULUS WITH RAIN 2.4 MM/HR

ZRAE METERS	ZTOP METERS	DENSITY G/M**3	R(MODE) MICRON	C1	C2	COMP.
0.0	500.0	0.100	400.00	5.00	0.50	RAIN
500.0	1000.0	1.000	20.00	6.00	0.20	L10.
1000.0	3000.0	2.000	10.00	6.00	0.20	L10.

SUMMARY OF UNIT VOLUME PROPERTIES AT LAMDA= 1.000E-02 CM,TEMP= 298.00 DEG K

LAYER NUMBER	M-DENS. G M**3	N-DENS. CM**3	GAM(S) NEPER/CM	GAM(E) NEPER/CM	GAM(E) DB/KM	GAM(R) DB/KM	ALREDC	D(SCAT) KM	D(EXT) KM
1	0.1004	0.0000	8.532E-07	1.478E-06	6.428E-01	3.589E 02	0.57741	1.172E 00	6.767E-01
2	0.5178	0.2032	3.979E-05	7.771E-05	3.381E 01	1.850E 03	0.51198	2.513E-02	1.287E-02
3	1.0355	3.2507	1.597E-04	3.309E-04	1.439E 02	3.700E 03	0.48254	6.263E-03	3.022E-03

SUMMARY OF UNIT VOLUME PROPERTIES AT LAMDA= 1.000E-03 CM,TEMP= 298.00 DEG K

LAYER NUMBER	M-DENS. G M**3	N-DENS. CM**3	GAM(S) NEPER/CM	GAM(E) NEPER/CM	GAM(E) DB/KM	GAM(R) DB/KM	ALBEDO	D(SCAT) KM	D(EXT) KM
1	0.1004	0.0000	7.375E-07	1.459E-06	6.345E-01	3.589E 04	0.50561	1.356E 00	6.856E-01
2	0.5178	0.2032	3.347E-05	6.606E-05	2.874E 01	1.850E 05	0.50665	2.988E-02	1.514E-02
3	1.0355	3.2507	1.409E-04	2.724E-04	1.185E 02	3.700E 05	0.51717	7.098E-03	3.671E-03

25-3 CUMULUS WITH RAIN 12 MM/HR

ZBASE METERS	ZTOP METERS	DENSITY G/M**3	R(MODE) MICRON	C1	C2	COMP.
0.0	400.0	0.500	400.00	5.00	0.50	RAIN
400.0	1000.0	2.000	20.00	6.00	0.20	LIO.
1000.0	4000.0	4.000	10.00	6.00	0.20	LIO.

SUMMARY OF UNIT VOLUME PROPERTIES AT LAMDA= 1.000E 01 CM,TEMP= 298.00 DEG K

LAYER NUMBER	M-DENS. G M**3	N-DENS. CM**3	GAM(S) NEPER/CM	GAM(E) NEPER/CM	GAM(E) DB/KM	GAM(R) DB/KM	ALBEDO	D(SCAT) KM	D(EXT) KM
1	0.5021	0.0002	8.425E-10	1.384E-08	6.020E-03	1.794E-03	0.06088	1.187E 03	7.226E 01
2	1.0355	0.4063	1.769E-12	1.178E-08	5.124E-03	3.700E-03	0.00015	5.653E 05	8.489E 01
3	2.0711	6.5014	3.924E-13	2.309E-08	1.004E-02	7.401E-03	0.00002	2.547E 06	4.331E 01

SUMMARY OF UNIT VOLUME PROPERTIES AT LAMDA= 1.000E 00 CM,TEMP= 298.00 DEG K

LAYER NUMBER	M-DENS. G M**3	N-DENS. CM**3	GAM(S) NEPER/CM	GAM(E) NEPER/CM	GAM(E) DB/KM	GAM(R) DB/KM	ALBEDO	D(SCAT) KM	D(EXT) KM
1	0.5021	0.0002	2.637E-06	5.484E-06	2.386E 00	1.794E-01	0.48078	3.793E-01	1.823E-01
2	1.0355	0.4063	1.770E-08	1.405E-06	6.114E-01	3.700E-01	0.01259	5.650E 01	7.115E-01
3	2.0711	6.5014	4.368E-09	2.344E-06	1.020E 00	7.401E-01	0.00186	2.290E 02	4.266E-01

SUMMARY OF UNIT VOLUME PROPERTIES AT LAMDA= 1.000E-01 CM,TEMP= 298.00 DEG K

LAYER NUMBER	M-DENS. G M**3	N-DENS. CM**3	GAM(S) NEPER/CM	GAM(E) NEPER/CM	GAM(E) DB/KM	GAM(R) DB/KM	ALBEDO	D(SCAT) KM	D(EXT) KM
1	0.5021	0.0002	4.944E-06	8.812E-06	3.833E 00	1.794E 01	0.56106	2.023E-01	1.135E-01
2	1.0355	0.4063	4.707E-05	1.144E-04	4.979E 01	3.700E 01	0.41130	2.124E-02	8.737E-03
3	2.0711	6.5014	3.338E-05	1.469E-04	6.388E 01	7.401E 01	0.22728	2.996E-02	6.810E-03

25-3 CUMULUS WITH RAIN 12 MM/HR

ZHASE METERS	ZTOP METERS	DENSITY G/M**3	R(MODE) MICRON	C1	C2	COMP.
0.0	400.0	0.500	400.00	5.00	0.50	RAIN
400.0	1000.0	2.000	20.00	6.00	0.20	LIO.
1000.0	4000.0	4.000	10.00	6.00	0.20	LIO.

SUMMARY OF UNIT VOLUME PROPERTIES AT LAMDA= 1.000E-02 CM,TEMP= 298.00 DEG K

LAYER NUMBER	M-DENS. G M**3	N-DENS. CM**3	GAM(S) NEPER/CM	GAM(E) NEPER/CM	GAM(E) DB/KM	GAM(R) DB/KM	ALREDC	D(SCAT) KM	D(EXT) KM
1	0.5021	0.0002	4.266E-06	7.388E-06	3.214E 00	1.794E 03	0.57741	2.344E-01	1.353E-01
2	1.0355	0.4063	7.958E-05	1.554E-04	6.761E 01	3.700E 03	0.51198	1.257E-02	6.434E-03
3	2.0711	6.5014	3.193E-04	6.618E-04	2.979E 02	7.401E 03	0.48254	3.131E-03	1.511E-03

SUMMARY OF UNIT VOLUME PROPERTIES AT LAMDA= 1.000E-03 CM,TEMP= 298.00 DEG K

LAYER NUMBER	M-DENS. G M**3	N-DENS. CM**3	GAM(S) NEPER/CM	GAM(E) NEPER/CM	GAM(E) DB/KM	GAM(R) DB/KM	ALREDC	D(SCAT) KM	D(EXT) KM
1	0.5021	0.0002	3.688E-06	7.293E-06	3.173E 00	1.794E 05	0.50561	2.712E-01	1.371E-01
2	1.0355	0.4063	6.694E-05	1.321E-04	5.748E 01	3.700E 05	0.50665	1.494E-02	7.568E-03
3	2.0711	6.5014	2.918E-04	5.448E-04	2.370E 02	7.401E 05	0.51717	3.549E-03	1.836E-03

25-4 CUMULUS CONGESTUS, 3000-9000 FT

ZBASE METERS	ZTOP METERS	DENSITY G/M**3	R(MODE) MICRON	C1	C2	COMP.
1000.0	1200.0	0.300	10.00	6.00	0.50	LIO.
1200.0	1600.0	0.500	15.00	5.00	0.40	LIO.
1600.0	2000.0	0.800	20.00	5.00	0.30	LIO.
2000.0	2500.0	1.000	20.00	5.00	0.30	LIO.
2500.0	3000.0	0.500	20.00	5.00	0.30	LIO.

SUMMARY OF UNIT VOLUME PROPERTIES AT LAMDA= 1.000E 01 CM,TEMP= 298.00 DEG K

LAYER NUMBER	M-DENS. G M**3	N-DENS. CM**3	GAM(S) NEPER/CM	GAM(E) NEPER/CM	GAM(E) DB/KM	GAM(R) DB/KM	ALBEDO	D(SCAT) KM	D(EXT) KM
1	0.3011	10.8274	3.666E-15	3.356E-09	1.460E-03	1.076E-03	0.0000	2.728E 08	2.979E 02
2	0.5023	2.1599	1.112E-13	5.607E-09	2.439E-03	1.795E-03	0.0002	8.994E 06	1.784E 02
3	0.8031	0.5379	2.675E-12	9.125E-09	3.969E-03	2.870E-03	0.00029	3.738E 05	1.096E 02
4	1.0038	0.6724	3.344E-12	1.141E-08	4.962E-03	3.587E-03	0.00029	2.990E 05	8.767E 01
5	0.5019	0.3362	1.672E-12	5.703E-09	2.481E-03	1.794E-03	0.00029	5.981E 05	1.753E 02

SUMMARY OF UNIT VOLUME PROPERTIES AT LAMDA= 1.000E 00 CM,TEMP= 298.00 DEG K

LAYER NUMBER	M-DENS. G M**3	N-DENS. CM**3	GAM(S) NEPER/CM	GAM(E) NEPER/CM	GAM(E) DB/KM	GAM(R) DB/KM	ALBEDO	D(SCAT) KM	D(EXT) KM
1	0.3011	10.8274	4.082E-11	3.222E-07	1.402E-01	1.076E-01	0.00013	2.450E 04	3.104E 00
2	0.5023	2.1599	1.191E-09	5.671E-07	2.467E-01	1.795E-01	0.00210	8.398E 02	1.763E 00
3	0.8031	0.5379	2.907E-08	1.197E-06	5.207E-01	2.870E-01	0.02429	3.440E 01	8.354E-01
4	1.0038	0.6724	3.634E-08	1.496E-06	6.509E-01	3.587E-01	0.02429	2.752E 01	6.683E-01
5	0.5019	0.3362	1.817E-08	7.481E-07	3.254E-01	1.794E-01	0.02429	5.503E 01	1.337E 00

25-4 CUMULUS CONGESTUS, 3000-9000 FT

ZBASE METERS	ZTOP METERS	DENSITY G/M**3	R(MODE) MICRON	C1	C2	COMP.
1000.0	1200.0	0.300	10.00	6.00	0.50	L10.
1200.0	1600.0	0.500	15.00	5.00	0.40	L10.
1600.0	2000.0	0.800	20.00	5.00	0.30	L10.
2000.0	2500.0	1.000	20.00	5.00	0.30	L10.
2500.0	3000.0	0.500	20.00	5.00	0.30	L10.

SUMMARY OF UNIT VOLUME PROPERTIES AT LAMDA= 1.000E-01 CM, TEMP= 298.00 DEG K

LAYER NUMBER	M-DENS. G M**3	N-DENS. CM**3	GAM(S) NEPER/CM	GAM(E) NEPER/CM	GAM(E) DB/KM	GAM(R) DB/KM	ALBEDO	D(SCAT) KM	D(EXT) KM
1	0.3011	10.8274	2.819E-07	1.111E-05	4.833E 00	1.076E 01	0.02537	3.548E 00	9.001E-02
2	0.5023	2.1599	6.696E-06	3.180E-05	1.383E 01	1.795E 01	0.21059	1.493E-01	3.145E-02
3	0.8031	0.5379	2.964E-05	7.742E-05	3.368E 01	2.870E 01	0.38293	3.373E-02	1.292E-02
4	1.0038	0.6724	3.706E-05	9.677E-05	4.209E 01	3.587E 01	0.38293	2.699E-02	1.033E-02
5	0.5019	0.3362	1.853E-05	4.838E-05	2.105E 01	1.794E 01	0.38293	5.397E-02	2.067E-02

SUMMARY OF UNIT VOLUME PROPERTIES AT LAMDA= 1.000E-02 CM, TEMP= 298.00 DEG K

LAYER NUMBER	M-DENS. G M**3	N-DENS. CM**3	GAM(S) NEPER/CM	GAM(E) NEPER/CM	GAM(E) DB/KM	GAM(R) DB/KM	ALBEDO	D(SCAT) KM	D(EXT) KM
1	0.3011	10.8274	1.016E-04	2.276E-04	9.900E 01	1.076E 03	0.44639	9.843E-03	4.394E-03
2	0.5023	2.1599	9.231E-05	1.932E-04	8.406E 01	1.795E 03	0.47771	1.083E-02	5.175E-03
3	0.8031	0.5379	7.050E-05	1.402E-04	6.100E 01	2.870E 03	0.50278	1.418E-02	7.132E-03
4	1.0038	0.6724	8.813E-05	1.753E-04	7.625E 01	3.587E 03	0.50278	1.135E-02	5.705E-03
5	0.5019	0.3362	4.406E-05	8.764E-05	3.812E 01	1.794E 03	0.50278	2.269E-02	1.141E-02

25-4 CUMULUS CONGESTUS, 3000-9000 FT

ZHASE METERS	ZTOP METERS	DENSITY G/M**3	R(MODE) MICRON	C1	C2	COMP.
1000.0	1200.0	0.300	10.00	6.00	0.50	L10.
1200.0	1600.0	0.500	15.00	5.00	0.40	L10.
1600.0	2000.0	0.800	20.00	5.00	0.30	L10.
2000.0	2500.0	1.000	20.00	5.00	0.30	L10.
2500.0	3000.0	0.500	20.00	5.00	0.30	L10.

SUMMARY OF UNIT VOLUME PROPERTIES AT LAMDA= 1.000E-03 CM, TEMP= 298.00 DEG K

LAYER NUMBER	M-DENS. G M**3	N-DENS. CM**3	GAM(S) NEPER/CM	GAM(E) NEPER/CM	GAM(E) DB/KM	GAM(R) DB/KM	ALBEDO	D(SCAT) KM	D(EXT) KM
1	0.3011	10.8274	1.355E-04	2.309E-04	1.004E 02	1.076E 05	0.58688	7.380E-03	4.331E-03
2	0.5023	2.1599	8.213E-05	1.577E-04	6.861E 01	1.795E 05	0.52071	1.218E-02	6.340E-03
3	0.8031	0.5379	5.952E-05	1.172E-04	5.100E 01	2.870E 05	0.50772	1.680E-02	8.530E-03
4	1.0038	0.6724	7.440E-05	1.465E-04	6.375E 01	3.587E 05	0.50772	1.344E-02	6.824E-03
5	0.5019	0.3362	3.720E-05	7.327E-05	3.187E 01	1.794E 05	0.50772	2.688E-02	1.365E-02

26-1 CUMULONIMBUS W. RAIN 150 MM/HR

ZBASE METERS	ZTOP METERS	DENSITY G/M**3	R(MODE) MICRON	C1	C2	COMP.
0.0	300.0	6.300	400.00	5.00	0.20	RAIN
300.0	1000.0	7.000	20.00	6.00	0.20	LIO.
1000.0	4000.0	8.000	10.00	6.00	0.20	LIO.
4000.0	6000.0	4.000	10.00	6.00	0.20	LIO.
6000.0	8000.0	3.000	10.00	6.00	0.20	LIO.
8000.0	10000.0	0.200	40.00	6.00	0.50	ICE

SUMMARY OF UNIT VOLUME PROPERTIES AT LAMDA= 1.000E 01 CM,TEMP= 298.00 DEG K

LAYER NUMBER	M-DENS. G M**3	N-DENS. CM**3	GAM(S) NEPER/CM	GAM(E) NEPER/CM	GAM(E) DB/KM	GAM(R) DB/KM	ALBEDO	D(SCAT) KM	D(EXT) KM
1	4.9066	0.0001	9.440E-07	4.044E-06	1.759E 00	1.753E-02	0.23342	1.059E 00	2.473E-01
2	3.6244	1.4222	6.192E-12	4.123E-08	1.793E-02	1.295E-02	0.00015	1.615E 05	2.425E 01
3	4.1421	13.0028	7.953E-13	4.618E-08	2.009E-02	1.480E-02	0.00002	1.273E 06	2.165E 01
4	2.0711	6.5014	3.924E-13	2.309E-08	1.004E-02	7.401E-03	0.00002	2.547E 06	4.331E 01
5	1.5533	4.8761	2.945E-13	1.732E-08	7.533E-03	5.551E-03	0.00002	3.396E 06	5.774E 01
6	0.2007	0.1128				1.448E-03			

SUMMARY OF UNIT VOLUME PROPERTIES AT LAMDA= 1.000E 00 CM,TEMP= 298.00 DEG K

LAYER NUMBER	M-DENS. G M**3	N-DENS. CM**3	GAM(S) NEPER/CM	GAM(E) NEPER/CM	GAM(E) DB/KM	GAM(R) DB/KM	ALBEDO	D(SCAT) KM	D(EXT) KM
1	4.9066	0.0001	1.382E-05	2.083E-05	9.060E 00	1.753E 00	0.66345	7.237E-02	4.801E-02
2	3.6244	1.4222	6.194E-08	4.919E-06	2.140E 00	1.295E 00	0.01259	1.614E 01	2.033E-01
3	4.1421	13.0028	8.736E-09	4.688E-06	2.039E 00	1.480E 00	0.00186	1.145E 02	2.133E-01
4	2.0711	6.5014	4.368E-09	2.344E-06	1.020E 00	7.401E-01	0.00186	2.290E 02	4.266E-01
5	1.5533	4.8761	3.276E-09	1.758E-06	7.648E-01	5.551E-01	0.00186	3.053E 02	5.688E-01
6	0.2007	0.1128	3.350E-10	4.018E-09	1.748E-03	1.448E-01	0.08337	2.980E 03	2.489E 02

* VALUE3 ADDED FOR ICE AT TEMP=273 DEG K

ZBASE METERS	ZTOP METERS	DENSITY G/M**3	R(MODE) MICRON	C1	C2	COMP.
0.0	300.0	6.300	400.00	5.00	0.20	RAIN
300.0	1000.0	7.000	20.00	6.00	0.20	LIO.
1000.0	4000.0	8.000	10.00	6.00	0.20	LIO.
4000.0	6000.0	4.000	10.00	6.00	0.20	LIO.
6000.0	8000.0	3.000	10.00	6.00	0.20	LIO.
8000.0	10000.0	0.200	40.00	6.00	0.50	ICE

SUMMARY OF UNIT VOLUME PROPERTIES AT LAMDA= 1.000E-01 CM,TEMP= 298.00 DEG K

LAYER NUMBER	M-DENS. G M**3	N-DENS. CM**3	GAM(S) NEPER/CM	GAM(E) NEPER/CM	GAM(E) DB/KM	GAM(R) DB/KM	ALBEDO	D(SCAT) KM	D(EXT) KM
1	4.9066	0.0001	1.143E-05	1.877E-05	8.165E 00	1.753E 02	0.60905	8.747E-02	5.328E-02
2	3.6244	1.4222	1.648E-04	4.006E-04	1.742E 02	1.295E 02	0.41130	6.070E-03	2.496E-03
3	4.1421	13.0028	6.675E-05	2.937E-04	1.279E 02	1.480E 02	0.22728	1.498E-02	3.405E-03
4	2.0711	6.5014	3.338E-05	1.469E-04	6.388E 01	7.401E 01	0.22728	2.996E-02	6.810E-03
5	1.5533	4.8761	2.503E-05	1.101E-04	4.791E 01	5.551E 01	0.22728	3.995E-02	9.080E-03
6	0.2007	0.1128				1.448E 01			

SUMMARY OF UNIT VOLUME PROPERTIES AT LAMDA= 1.000E-02 CM,TEMP= 298.00 DEG K

LAYER NUMBER	M-DENS. G M**3	N-DENS. CM**3	GAM(S) NEPER/CM	GAM(E) NEPER/CM	GAM(E) DB/KM	GAM(R) DB/KM	ALBEDO	D(SCAT) KM	D(EXT) KM
1	4.9066	0.0001	1.018E-05	1.757E-05	7.643E 00	1.753E 04	0.57963	9.818E-02	5.691E-02
2	3.6244	1.4222	2.785E-04	5.440E-04	2.366E 02	1.295E 04	0.51198	3.590E-03	1.838E-03
3	4.1421	13.0028	6.387E-04	1.324E-03	5.758E 02	1.480E 04	0.48254	1.566E-03	7.555E-04
4	2.0711	6.5014	3.193E-04	6.618E-04	2.879E 02	7.401E 03	0.48254	3.131E-03	1.511E-03
5	1.5533	4.8761	2.395E-04	4.963E-04	2.159E 02	5.551E 03	0.48254	4.175E-03	2.015E-03
6	0.2007	0.1128	2.638E-05	4.346E-05	1.891E 01	1.448E 03	0.60706	3.790E-02	2.301E-02

* VALUES ADDED FOR ICE AT TEMP=273 DEG K

26-1 CUMULONIMBUS W. RAIN 150 MM/HR

ZHASE METERS	ZTOP METERS	DENSITY G/M**3	R(MODE) MICRON	C1	C2	COMP.
0.0	300.0	6.300	400.00	5.00	0.20	RAIN
300.0	1000.0	7.000	20.00	6.00	0.20	LIO.
1000.0	4000.0	8.000	10.00	6.00	0.20	LIO.
4000.0	6000.0	4.000	10.00	6.00	0.20	LIO.
6000.0	8000.0	3.000	10.00	6.00	0.20	LIO.
8000.0	10000.0	0.200	40.00	6.00	0.50	ICE

SUMMARY OF UNIT VOLUME PROPERTIES AT LAMDA= 1.000E-03 CM,TEMP= 298.00 DEG K

LAYER NUMBER	M-DENS. G M**3	N-DENS. CM**3	GAM(S) NEPER/CM	GAM(E) NEPER/CM	GAM(E) DB/KM	GAM(R) DB/KM	ALBEDG	D(SCAT) KM	D(EXT) KM
1	4.9066	0.0001	8.845E-06	1.749E-05	7.609E 00	1.753E 06	0.50561	1.131E-01	5.717E-02
2	3.6244	1.4222	2.343E-04	4.624E-04	2.012E 02	1.295E 06	0.50665	4.268E-03	2.162E-03
3	4.1421	13.0028	5.635E-04	1.090E-03	4.740E 02	1.480E 06	0.51717	1.775E-03	9.178E-04
4	2.0711	6.5014	2.818E-04	5.448E-04	2.370E 02	7.401E 05	0.51717	3.549E-03	1.836E-03
5	1.5533	4.8761	2.113E-04	4.086E-04	1.777E 02	5.551E 05	0.51717	4.732E-03	2.447E-03
6 *	0.2007	0.1128	1.709E-05	3.388E-05	1.474E 01	1.448E 05	0.50451	5.850E-01	2.952E-02

* VALUES ADDED FOR ICE AT TEMP=273 DEG K